

**Effect of Water on Copper Electrodeposition from  
Water-containing Deep Eutectic Solvents**

**A Thesis submitted by**

**Priscila Estefania Valverde Armas**

**For the Degree of Doctor of Philosophy**

**Department of Chemical and Process Engineering  
University of Strathclyde**

**January 2019**

## **Declaration of Authenticity and Author's Rights**

This thesis is the result of the author's original research. It has been composed by the author and has not been previously submitted for examination, which has led to the award of a degree.

The copyright of this thesis belongs to the author under the terms of the United Kingdom Copyright Acts as qualified by University of Strathclyde Regulation 3.50. Due acknowledgement must always be made of the use of any material contained in, or derived from, this thesis.

Signed:

Date: January 23, 2019

## ABSTRACT

Metal electrodeposition is mostly based on aqueous systems which sometimes require the addition of chemicals that can be hazardous for the environment. Due to growing environmental regulations, Ionic Liquids (ILs) have been investigated as an alternative electrochemical media for this process. Amongst a variety of ILs, deep eutectic solvents (DESs) formulated from choline chloride and hydrogen bond donors have exhibited the most promising characteristics to be exploitable at large scale. Some of these characteristics are the tolerance to water, low volatility and toxicity, and reasonable cost. Despite these properties, DESs are viscous and the diffusivity of electroactive species is correspondingly low. This imposes mass transport constraints reflected in low deposition rates compared to either high-temperature ILs or aqueous systems. This study therefore examined if the use of water addition alleviated these problems and investigated the effect of water content on various aspects of metal electrodeposition from hydrated DES systems.

‘Ethaline’ was the DES focus of this study since it exhibits one of the highest conductivity and lowest viscosity amongst DESs. Cu electroplating had been particularly common as it is used extensively in the electronics and microelectronic industry. Since there is a large body of existing studies on Cu electrodeposition from both ILs and aqueous systems, it can be used to benchmark metal electrodeposition from hydrated DES systems. Thereby, the ‘electrolyte’ used in this work comprised of the cupric chloride salt (0.2 M  $\text{CuCl}_2 \cdot 2\text{H}_2\text{O}$ ) dissolved in ethaline.

Since ethaline is a hygroscopic substance, the ability of the electrolyte to incorporate water from the atmosphere was quantified using Karl Fischer titration. It was found that the electrolyte could incorporate water from 3 to 15 wt% over a month. Using these water amounts, the speciation of Cu (II) complexes, viscosity and conductivity were investigated. The behaviour of Cu (II) reduction from ethaline and the electrochemical window of ethaline were examined as a function of water content. Thereafter, Cu electrodeposition was performed from water-containing electrolytes using steel disks. The uniformity, morphology and microstructure features of Cu electrodeposits were assessed using SEM, EBSD and XRD techniques. One of the key

technical issues to be resolved before practical DES-based plating systems can be deployed is the characterisation of the anode reaction. Therefore, the anodic reaction occurring at the soluble copper anode during the electrodeposition of Cu from the water-containing electrolytes was also studied.

The diffusion limiting currents for Cu (II) reduction from ethaline were found to increase three times as water content increased from 1 to 15 wt%, e.g. from 6 to 18.5 mA cm<sup>-2</sup>. This occurred with minimal influence on the speciation of Cu (II) complexes, electrochemical window and deposit characteristics. This finding could be mostly attributed to the improved diffusivity of electroactive species brought about by water. This was therefore a beneficial effect since faster plating rates were achievable from hydrated DES systems than that of low water-containing ones. Cu electrodeposits were found to exhibit poor homogeneity despite the fact that increasing amounts of water increased the conductivity of the medium. Importantly, the addition of water was not detrimental to the current efficiency of the process, microstructure and purity of the Cu coatings.

The analysis of the anodic reaction using a Cu soluble anode showed that the dominant anodic species were the Cu (I) complexes whereas the solution was depleted of the higher valency species, Cu (II) complexes. In the electrolyte, the apparent dissolution valency ( $n'$ ) was typically less than unity, corresponding to an observed mass loss greater than that expected from Faraday's law. Moreover,  $n'$  showed a marked dependence on the electrode rotation rate, Cu (II) concentration, and water content. These observations were consistent with a corrosion reaction occurring in parallel with the anodic dissolution. The most likely corrosion process was identified to be the comproportionation reaction:  $[\text{CuCl}_4]^{2-} + \text{Cu} \rightarrow 2[\text{CuCl}_2]^-$ .

This study therefore determined a simple model for the electro-dissolution of Cu from hydrated DES systems and showed that the influence of water content was not detrimental to the electrolyte properties, electrodeposition process, and electrodeposits. Hence, the addition of water content can be considered to be a simple way to improve the rate of electrodeposition from DES systems with no particular downside.

## ACKNOWLEDGEMENTS

I would like to express my gratitude to the following people:

- My primary supervisor Prof. Sudipta Roy for her guidance throughout this project, her encouragement to engage in activities that have helped me to develop as a researcher and for involving me in research collaborations.
- My secondary supervisor Dr. Todd Green for his valuable guidance in this study and for sharing his enthusiasm and knowledge in the laboratory.
- The scholarship by the Secretariat of Higher Education, Science, Technology and Innovation (SENESCYT) of Ecuador for funding this study.
- Dr. Jan Sefcik, Dr. Elke Prasad and Dr. Thomas McGlone for helping me to get access to the facilities at the Continuous Manufacturing and Crystallisation Centre (CMAC) of Strathclyde University to perform titration measurements.
- Dr. Yi-Chieh Chen and Mr. Nicolau Dehanov from the Department of Chemical and Process Engineering for training me to use the UV-Vis-NIR spectrophotometer.
- Mr. James Kelly from the Department of Mechanical Engineering for the induction in grinding/polishing techniques.
- Dr. Ashleigh Fletcher and Dr. Chris Price from the Department of Chemical and Process Engineering for their valuable advice.
- The studentship support of the COST Action Division MP1407 under the scheme of ‘Short Term Scientific Mission’ to perform EBSD analysis.
- Dr. Himanshu Lalvani for granting me access to the Advanced Forming Research Centre (AFRC) of Strathclyde University as well as Dr. Ryan O’Neill and Mrs.

Kornelia Kondziolka for their assistance with the preparation of the specimens for the EBSD analysis.

- Professor Uta Klement for welcoming me in her research group at Chalmers University of Technology to perform EBSD analysis and Mr. Antonio Mulone for his help with the measurements.
- Mr. Jim Murphy, Mr. Christopher Jones and all the technical staff in the mechanical workshop as well as the administrative staff of the Department of Chemical and Process Engineering for their assistance.
- All the students in my research group and office for the friendly atmosphere, especially Christine, Eleni, Shaon, John and Mohammed for the enjoyable conversations.
- Mrs. Silvia Piccinini for her valuable advice.
- My friends Davide, Valerie, Yuemin, and Teresa who supported and encouraged not only in blissful but also in gloomy moments.
- My parents Belgica, Hector, Monica, Xavier and my cousin Ariana for their love and encouragement throughout this process.
- My stepfather Celso who departed this life being a brilliant husband and did not doubt that I could culminate my studies.
- My aunt Lourdes who helped me to find hope through music and departed this life.
- My fiancé Cristhyan for his exceptional support and fondness along this journey.

## CONTENTS

<b>ABSTRACT</b> .....	i
<b>ACKNOWLEDGEMENTS</b> .....	iii
<b>LIST OF FIGURES</b> .....	x
<b>LIST OF TABLES</b> .....	xxi
<b>LIST OF NOMENCLATURE</b> .....	xxiii
<b>LIST OF ABBREVIATIONS</b> .....	xxviii
<b>1. Chapter - Introduction</b> .....	1
<b>1.1 Background</b> .....	2
<b>1.2 Ionic Liquids</b> .....	4
1.2.1 Definition and brief history of ionic liquids .....	5
1.2.2 Types of ionic liquids .....	7
1.2.3 Chloroaluminate and water-air stable ionic liquids .....	7
1.2.4 Nomenclature of chloroaluminate and water- air stable ionic liquids .....	10
<b>1.3 Properties of chloroaluminate and water-air stable ionic liquids</b> .....	11
1.3.1 Thermal properties .....	11
1.3.2 Physico-chemical properties .....	12
1.3.2.1 Viscosity .....	13
1.3.2.2 Conductivity .....	14
1.3.3 Electrochemical properties .....	16
1.3.3.1 Electrochemical window .....	16
1.3.4 Limitations of chloroaluminate and water-air stable ionic liquids .....	19
<b>1.4 Deep Eutectic Solvents</b> .....	20
1.4.1 Definition of deep eutectic solvents .....	20
1.4.2 Type I eutectics .....	24
1.4.3 Type II eutectics .....	27
1.4.4 Type III eutectics .....	28
1.4.5 Physico-chemical properties .....	32
1.4.5.1 Density .....	32
1.4.5.2 Viscosity .....	36
1.4.5.3 Conductivity .....	42

1.4.6	Electrochemical properties	44
1.4.6.1	Electrochemical window	44
1.4.7	General electroplating from deep eutectic solvent systems	48
1.4.7.1	Ni	49
1.4.7.2	Cr	53
1.4.7.3	Zn	55
<b>1.5</b>	<b>Aims and Objectives of Current Work</b>	<b>58</b>
<b>2.</b>	<b>Chapter - Literature Review</b>	<b>60</b>
<b>2.1</b>	<b>Electrodeposition of Cu from DESs</b>	<b>61</b>
2.1.1	Speciation of Cu	61
2.1.1.1	Speciation of Cu in chloroaluminate and water-air stable ionic liquids	61
2.1.2	Speciation of Cu in DESs	66
2.1.2.1	Effect of water on Cu speciation in DESs	67
2.1.3	Mechanism of Cu electrodeposition	69
2.1.3.1	Diffusion coefficients of Cu species	78
2.1.4	Electrodeposition of Cu from DES systems	79
2.1.5	Effect of Cu salt on physico-chemical properties of DESs	84
<b>3.</b>	<b>Chapter - Fundamentals</b>	<b>89</b>
<b>3.1</b>	<b>Electrodeposition process</b>	<b>90</b>
<b>3.2</b>	<b>Thermodynamics of electrodeposition</b>	<b>92</b>
3.2.1	Electrode potential	92
3.2.2	Nernst equation	92
3.2.3	Overpotential	94
<b>3.3</b>	<b>Kinetics of electrodeposition</b>	<b>95</b>
<b>3.4</b>	<b>Mass transfer in electrodeposition</b>	<b>97</b>
<b>3.5</b>	<b>Rotating disk electrode</b>	<b>100</b>
3.5.1	Current distribution at a Rotating Disk Electrode	105
3.5.2	Primary current distribution	106
3.5.3	Secondary current distribution	109



3.5.3.1	Secondary current distribution for linear polarisation	109
3.5.3.2	Secondary current distribution for Tafel polarisation	111
3.5.4	Wagner number	113
<b>4.</b>	<b>Chapter – Experimental</b>	<b>115</b>
<b>4.1</b>	<b>Measurement of water content</b>	<b>116</b>
4.1.1	Karl Fischer titration principle	116
4.1.2	Materials and apparatus of Karl Fischer titration	118
4.1.3	Experimental procedure of Karl Fischer titration	119
4.1.4	Near-Infrared spectroscopy principle	120
4.1.5	Materials and apparatus of NIR spectroscopy	122
4.1.5.1	Experimental procedure of NIR spectroscopy	123
<b>4.2</b>	<b>Monitoring of Cu speciation on water-containing electrolyte</b>	<b>124</b>
4.2.1	Ultraviolet Visible spectroscopy principle	124
4.2.2	Materials and apparatus of UV-Vis spectroscopy	128
4.2.3	UV-Vis test procedure	129
<b>4.3</b>	<b>Physicochemical and electrochemical properties as a function of water content</b>	<b>130</b>
4.3.1	Electrolyte preparation	130
4.3.2	Density, viscosity and conductivity	130
4.3.3	Electrochemical window	131
<b>4.4</b>	<b>Electrodeposition of Cu from water-containing electrolyte</b>	<b>132</b>
4.4.1	Divided electrochemical cell	132
4.4.2	Electrode preparation	135
4.4.3	Experimental procedure to determine ohmic drop	135
4.4.4	Experimental procedure to examine limiting currents	138
4.4.5	Experimental procedure to determine kinetic parameters	138
4.4.6	Experimental procedure of electrodeposition experiments	138
4.4.6.1	Experimental procedure to determine current efficiency by gravimetric method	139
4.4.6.2	Experimental procedure to determine current efficiency by stripping method	140

<b>4.5 Material analysis</b>	142
4.5.1 SEM, EDX and EBSD operating principle	142
4.5.2 Experimental procedure for SEM, EDX and EBSD analysis	146
4.5.2.1 Metallographic preparation of specimens	147
4.5.3 XRD operating principle	150
4.5.4 Experimental procedure of XRD analysis	153
<b>4.6 Anodic dissolution of copper</b>	154
4.6.1 Materials and apparatus	154
4.6.2 Experimental procedure to ascertain the dissolution valency	155
4.6.3 Dissolution valency as a function of current density, concentration of species and rotation speed	156
4.6.4 Experimental procedure to determine complex species as a function of anodic charge	157
<b>5. Chapter – Results and Discussion: Physico-chemical and electrochemical properties as a function of water content</b>	158
<b>5.1 Measurement of water content</b>	159
5.1.1 Water content in ethaline and electrolyte by KF titration	159
5.1.2 Water content in the electrolyte by NIR spectroscopy	161
5.1.3 Incorporation of water by ethaline and the electrolyte as a function of time	164
<b>5.2 Monitoring of Cu speciation as a function of water content in DESs</b>	166
5.2.1 Speciation of Cu in aqueous systems	166
5.2.2 Speciation of Cu in DES systems	168
<b>5.3 Physico-chemical properties as a function of water content</b>	171
5.3.1 Density as a function of water content	171
5.3.2 Viscosity as a function of water content	173
5.3.3 Conductivity as a function of water content	175
5.3.4 Electrochemical window as function of water content	177

<b>6. Chapter – Results and Discussion: Electrodeposition of Cu from water-containing electrolyte</b>	183
<b>6.1 Polarisation experiments</b>	184
6.1.1 Electrochemical behaviour of Cu in DES system	184
6.1.2 Effect of water on limiting current	189
<b>6.2 Effect of water on kinetics of Cu electrodeposition</b>	192
6.2.1 Reduction potential and standard heterogeneous rate constant	192
6.2.2 Prediction of deposit uniformity from the water-containing electrolytes	202
<b>6.3 Material analysis</b>	205
6.3.1 Electrodeposition of Cu from water-containing electrolyte	205
6.3.2 Morphology of electrodeposits produced from water-containing electrolyte	212
6.3.3 Chemical composition of Cu electrodeposits	218
6.3.4 Grain size of deposits obtained from the water-containing electrolytes	220
<b>7. Chapter – Results and Discussion: Anodic reactions and Cu corrosion from water-containing electrolyte</b>	224
7.1.1 Anodic species product of the electro-dissolution process in DES system	225
7.1.2 Dissolution valency and apparent dissolution valency in DES system	229
7.1.3 Mechanism of corrosion reaction of Cu in DES system	234
7.1.4 Prediction of the production rate of Cu (I) species in the electrolyte	240
<b>8. Chapter - Conclusions and Future Work</b>	244
<b>8.1 Conclusions</b>	245
<b>8.2 Future work</b>	250
<b>Appendices</b>	251
<b>References</b>	272

## LIST OF FIGURES

Figure 1.1 Structure of the dialkylimidazolium cation that forms a eutectic mixture with $\text{AlCl}_3$ . .....	6
Figure 1.2 Scheme of the quaternization reaction of 1-alkylimidazoles. Adapted from [23]. .....	8
Figure 1.3 Common cations that are used to synthesise haloaluminate ILs. ....	8
Figure 1.4 Common anions that are used to synthesise water-air stable ILs. ....	10
Figure 1.5 Schematic of an electrochemical window showing the anodic and cathodic limits defined at arbitrary current densities. ....	16
Figure 1.6 Electrochemical window of a) dry and b) wet $[\text{BMIM}]^+[\text{BF}_4]^-$ using a Pt electrode ( $d= 50 \mu\text{m}$ ) at a scan rate of $100 \text{ mV s}^{-1}$ . The liquid was exposed to water-saturated argon atmosphere. Adapted from [42]. ....	17
Figure 1.7 Cyclic voltammetry in chloroaluminate IL using a) GC, b) W and c) Pt electrode at $50 \text{ mVs}^{-1}$ at $40 \text{ }^\circ\text{C}$ . The continuous curves correspond to the dry liquid whereas the dotted curves represent the liquid + added water. Adapted from [3]. ....	18
Figure 1.8 Phase diagram of a two-component system showing the eutectic point. Adapted from [44]. ....	20
Figure 1.9 Gibbs free energy curves of a binary system when reaching the eutectic temperature. The blue curve corresponds to the liquid phase while the green and orange curves are the solid phases. Adapted from [44]. ....	21
Figure 1.10 General representation of deep eutectic solvents. ....	22
Figure 1.11 Schematic of the complexation of the anion by the HBD occurring in DESs. Adapted from [46]. ....	22
Figure 1.12 Cell potential measurement of the $\text{ChCl}: 2\text{ZnCl}_2$ system at $60 \text{ }^\circ\text{C}$ . ....	26
Figure 1.13 Synthesis of choline chloride. Adapted from [52]. ....	28
Figure 1.14 Structure of choline chloride. ....	28
Figure 1.15 Formation of the DES ethaline ( $\text{ChCl}: 2 \text{ EG}$ ). Adapted from [54]. ....	29
Figure 1.16 Chemical structures of ethanolamine and phenol acting as HBDs. ....	33
Figure 1.17 Structure of halide salts $\text{ChCl}$ (left) and methyltriphenylphosphonium bromide (right). ....	33
Figure 1.18 Chemical structures of HBDs such as ethylene glycol, malonic acid and glutaric acid. ....	34

Figure 1.19 Chemical structures of HBDs such as ethylene glycol and glycerol. ....	34
Figure 1.20 Schematic of the molten salts before (left) and after (right) fusion. Adapted from [72]. ....	37
Figure 1.21 Vacancy model or quasi-lattice model showing Schottky defects and b) the formation of holes. Adapted from [72]. ....	37
Figure 1.22 Formation of holes in molten salts. Adapted from [72]. ....	38
Figure 1.23 Fluidity of liquids as a function of the probability $[P(r < R)]$ of finding holes of suitable sizes for an ion to move in for $[BMIM]^+[PF_6]^-$ , NaCl, H <sub>2</sub> O, benzene and butanol. Adapted from [77]. ....	39
Figure 1.24 Conductivity and viscosity as a function of the mole composition of the oxalic acid in choline chloride. Adapted from [51]. ....	41
Figure 1.25 Energy for activation of viscous flow as a function of solvent to hole radius ratio. Adapted from [51]. ....	42
Figure 1.26 Cyclic voltammograms of a) ChCl: 2 EG, b) ChCl: 2 1,2-propylene, c) ChCl: 2 1,3-propanediol and ChCl: 2 urea using a Hg electrode at a scan rate of 50 $mVs^{-1}$ at 40-60 °C. Adapted from [86]. ....	45
Figure 1.27 Cyclic voltammograms of a) ChCl: 2 urea, b) ChCl: 2 EG, c) ChCl: malonic acid using a Pt electrode ( $A = 0.031 \text{ cm}^2$ ), Ag wire as the reference electrode at a scan rate of $50 \text{ mV s}^{-1}$ at 20 °C. Adapted from [23]. ....	46
Figure 1.28 Linear sweep voltammetry of ethaline using a Pt electrode, a Ag wire as the reference electrode at a scan rate of $30 \text{ mV s}^{-1}$ at 25 °C. Adapted from [87]. ....	47
Figure 1.29 a) Cyclic voltammetry of ChCl: 2 urea (solid line) and 0.2 M of Ni (II) species dissolved in ChCl: 2 urea (dashed line) using a Cu electrode at $20 \text{ mV s}^{-1}$ at 65 °C. b) SEM image of Ni coating obtained from reline. Adapted from [93]. ....	50
Figure 1.30 Cyclic voltammetry of 0.2 M Ni (II) in ChCl: 2 urea containing a) 0, b) 200, c) 400, d) 800, and e) $1200 \text{ mg L}^{-1}$ of nicotinic acid using a Cu electrode at $20 \text{ mV s}^{-1}$ at 65 °C. Adapted from [93]. ....	50
Figure 1.31 SEM image of Ni coating in ChCl: 2 urea containing 0.2 M $NiCl_2 \cdot 6H_2O$ with a) 400 and b) $1200 \text{ mg L}^{-1}$ of nicotinic acid using a Cu electrode at a scan rate of $20 \text{ mV s}^{-1}$ at 65 °C. Adapted from [93]. ....	51
Figure 1.32 SEM image of Ni film fabricated from 0.0114 M $NiCl_2 \cdot 6H_2O$ in ethaline at 25 °C (left) and image of the appearance of the deposit (right). Adapted from [90]. ....	51
Figure 1.33 SEM images of Ni films fabricated at 80 °C from a) from Watts bath and b) ethaline using a Ni electrode. The concentration of Ni (II) species was 0.0114 M. Adapted from [90]. ....	52

Figure 1.34 Voltammetry of ChCl: 2 CrCl <sub>3</sub> ·6H <sub>2</sub> O system using a Pt electrode at a scan rate of 20 mV s <sup>-1</sup> at 60 °C. Adapted from [50].	54
Figure 1.35 SEM image of Cr film using a Ni electrode fabricated from ChCl: 2 CrCl <sub>3</sub> ·6H <sub>2</sub> O system at 60 °C. Adapted from [50].	54
Figure 1.36 Cyclic voltammetry of 0.5 M ZnCl <sub>2</sub> shown as the dotted line in a) ChCl: 2 urea and b) ChCl: 2 EG using a Pt electrode (d= 0.5 mm) at a scan rate of 20 mV s <sup>-1</sup> at 40 °C. The solid line corresponds to the voltammetry of SnCl <sub>2</sub> which is not included in this work. Adapted from [98].	56
Figure 2.1 Structure of the hexa-aquacopper ion formed in aqueous solutions between Cu and molecules of water.	61
Figure 2.2 Potentiometric titration curve of Cu (I) species in MEIC-AlCl <sub>3</sub> IL at 40 °C. Adapted from [99].	62
Figure 2.3 Spectrum of Cu (II) species in the basic [EMIM] <sup>+</sup> [BF <sub>4</sub> ] <sup>-</sup> IL. The concentration of Cu (II) species was 1.63 mM. Adapted from [100].	64
Figure 2.4 UV-Vis absorption spectra of hydrated cupric salt (black curve) and anhydrous cupric salt (red curve) in ethaline using a concentration of 0.2 mM of Cu (II) species. Adapted from [102].	67
Figure 2.5 UV-Vis absorption spectra of 0.1 M Cu (II) species dissolved in ChCl containing increasing amounts of water. Adapted from [101].	68
Figure 2.6 Cyclic voltammetry of Cu (I) species electrochemically produced in acidic [EMIM] <sup>+</sup> [Cl] <sup>-</sup> -AlCl <sub>3</sub> using a Pt electrode and a scan rate of 50 mV s <sup>-1</sup> at 40 °C. Adapted from [104].	69
Figure 2.7 Cyclic voltammetry of 0.1 M Cu (II) species in both reline and ethaline using a Pt electrode at different scan rates at 20 °C. Adapted from [102].	72
Figure 2.8 Polarisation data for the reduction of 0.05 M CuCl <sub>2</sub> ·2H <sub>2</sub> O in ethaline using a Pt electrode at a scan rate of 30 mV s <sup>-1</sup> , rotation speed of 700 rpm at 25 °C. Adapted from [87].	73
Figure 2.9 Polarisation data for the reduction of CuCl <sub>2</sub> ·2H <sub>2</sub> O in ethaline using concentrations of a) 0.05 M and b) 0.20 M using a Pt electrode (A= 0.031 cm <sup>2</sup> ), scan rate of 30 mV s <sup>-1</sup> , rotation speed of 700 rpm (black curve) and 1300 rpm (red curve), and at 25 °C. Adapted from [87].	75
Figure 2.10 Cyclic voltammetric data for the reduction of Cu (II) species from aqueous chloride system (0.05 M CuCl <sub>2</sub> + 1.5 NaCl) using a stationary Pt electrode and a scan rate of 5 mV s <sup>-1</sup> at 25 °C. Adapted from [106].	77
Figure 2.11 a) Appearance of the fresh electrolyte ChCl: 2 EG containing 0.45 M of Cu (II) species, and b) appearance of the electrolyte after 6 h of plating. Adapted from [109].	80

Figure 2.12 Cu coating obtained from $\text{CuCl}_2 \cdot 2 \text{EG}$ containing 0.45 M of Cu (II) species using a brass substrate. The deposit was obtained under potentiostatic conditions at -0.6 V vs. Ag wire RE at 25 °C. Adapted from [109].	81
Figure 2.13 Cu coating obtained from the sulphate aqueous system (0.6 M $\text{Cu}^{2+}$ + 2.0 M $\text{H}_2\text{SO}_4$ with no additives) using a steel substrate. The deposit was obtained under galvanostatic conditions by setting the applied current to 40% of $i_{\text{lim}}$ , ( $i_{\text{lim}}=20.32 \text{ mA cm}^{-2}$ measured under stagnant conditions) at 25 °C. Adapted from [110].	81
Figure 2.14 Cu deposits obtained from Cu (II) in ethaline under potentiostatic conditions at 25 °C using different amounts of Cu (II) salt as: a) 0.05 M and 700 rpm, b) 0.20 M and 700 rpm, and c) 0.20 M and 1300 rpm. Adapted from [87].	82
Figure 2.15 Polarisation data of Cu (II) species in ethaline using a Pt electrode ( $A=0.031 \text{ cm}^2$ ), scan rate of $30 \text{ mV s}^{-1}$ , and temperature of 25 °C. Adapted from [87].	83
Figure 2.16 Density of ethaline as a function of the concentration of the $\text{CuCl}_2 \cdot 2\text{H}_2\text{O}$ metal salt from 0 to 0.2 M in the solvent at 20 °C. Adapted from [66].	85
Figure 2.17 Proposed structure of the tetrachloro-cuprate species formed ethaline. Adapted from [87].	85
Figure 2.18 Molar conductivity versus fluidity of Ni (II) species in ethaline as a function of the concentration of Ni (II) species. Adapted from [113].	88
Figure 3.1 Schematic of a basic electrochemical cell with a three electrode configuration for an electrodeposition process. Adapted from [117].	90
Figure 3.2 Nernst diffusion layer model for reactant species near to the vicinity of the electrode surface showing the actual boundary layer thickness ( $\delta$ ) and the Nernst diffusion layer thickness $\delta_N$ . Adapted from [126].	98
Figure 3.3 Concentration profile of reacting species as a function of the distance to the electrode surface. Adapted from [127].	99
Figure 3.4 Schematic of the overpotential curve showing the limiting current density ( $i_{\text{lim}}$ ) as the plateau region of the curve. Adapted from [126].	99
Figure 3.5 Schematic of the cross-section of the RDE showing its basic components and the flow lines followed by the liquid. Adapted from [128].	100
Figure 3.6 Coordinates useful to describe the solution velocity components in the x, r, and $\theta$ directions in the a) cross-section of the RDE and b) the bottom view of the RDE. Adapted from [128].	101
Figure 3.7 Plot of $\ln k_f(E)$ against $(E - E_o')$ from which heterogeneous rate constant and charge transfer coefficient can be calculated.	104

Figure 3.8 Potential distribution and current distribution at two parallel electrodes facing each other within an insulating flow channel. Equipotential surfaces (green) and current curves (red). The current distribution has been evaluated at the two edges of the substrate (e.g. points 1 and -1) whereby the current approaches infinitive values. Adapted from [134].	107
Figure 3.9 Primary current distribution for parallel planar electrodes. Adapted from [134].	107
Figure 3.10 Equipotential lines and current distribution at a rotating disk electrode for the primary current distribution. Adapted from [135].	108
Figure 3.11 Secondary current distribution for linear polarisation at a disk electrode, where $r/r_0 = 0$ is the centre of the electrode and $r/r_0 = 1$ is the edge. $N = \infty$ means that the variation of the concentration is not considered since the electrolyte was assumed to be well-agitated. Adapted from [132].	111
Figure 3.12 Secondary current distribution for Tafel polarisation at a disk electrode of radius $r_0$ . The set of curves corresponds to various values of $Wa$ . $N = \infty$ means that mass transport limitations have been neglected since the electrolyte has been assumed to be well-agitated. Adapted from [132].	114
Figure 4.1 Schematic of the Karl Fischer titration vessel showing the twin Pt electrode for the detection of the end-point of the titration. Adapted from [142].	118
Figure 4.2 Schematic of the KF titration vessel and the automatic burette used to determine water content. Adapted from [142].	119
Figure 4.3 Electromagnetic spectrum showing the UV-Vis and NIR region from 800 to 2500 nm. Adapted from [148].	120
Figure 4.4 NIR vibrational modes of water: stretching and bending vibrations with symmetric and anti-symmetric modes [149].	121
Figure 4.5 a) Demountable quartz magnetic cuvette (125 $\mu\text{m}$ pathlength) used for spectroscopy measurements and b) magnifying glass to check for bubbles.	122
Figure 4.6 Schematic of the incident radiant power and the emerging radiant light after passing through an absorbing solution. Adapted from [151].	124
Figure 4.7 Diagram of a spectrophotometer showing its basic components and instrumentation. Adapted from [151].	125
Figure 4.8 Schematic of the logarithmic relationship between transmittance and absorbance of a solution [151].	126
Figure 4.9 UV-Vis spectrum of 0.20 M Cu (II) species in ethaline acquired with the magnetic cuvette of 125 $\mu\text{m}$ pathlength.	128



Figure 4.10 a) Schematic of the quartz cuvette with a narrow pathlength, e.g. 10 $\mu\text{m}$ and b) UV-Vis spectra of 0.20 M Cu (II) which were not reproducible due to the uncertainties in the thin pathlength of the cuvette.....	129
Figure 4.11 a) Picture of the DHR-2 rheometer and b) flat plate and sample stage of the rheometer. ....	131
Figure 4.12 Schematic of the divided electrochemical cell used for the polarisation and electrodeposition experiments. The three-electrode configuration is also shown. ....	133
Figure 4.13 Schematic of the lab-made reference electrode. ....	134
Figure 4.14 a) Electrode holder components and b) holder assembled to the RDE. ....	134
Figure 4.15 a) Images of the steel disk embedded in bakelite, b) holder after crushing and c) polished steel disk ( $A=1.18 \text{ cm}^2$ , $d = 1.20 \text{ cm}$ ). ....	135
Figure 4.16 a) Schematic of an electrochemical cell showing the uncompensated resistance in an analogue mode to an electronic circuit, b) simplest circuit showing that at a high frequency, the $C_{dl}$ acts a cable. Adapted from [2]. ....	136
Figure 4.17 Example of a Nyquist plot where the Ru can be obtained from the intercept of the real component at the highest applied frequency.....	136
Figure 4.18 Anodic polarisation of Cu in 0.5 M HCl. ....	141
Figure 4.19 Basic operating principle of Scanning Electron Microscope. Adapted from [159]. ....	143
Figure 4.20 Type of emitted electrons depending on the interaction volume of the sample when the electron beam strikes the specimen. Adapted from [157]. ....	144
Figure 4.21 Mechanisms by which electrons are emitted such as a) secondary electrons, b) backscattered electrons and c) X-rays. Adapted from [157]. ....	144
Figure 4.22 Diagram of the basic operating principle of EBSD analysis. Adapted from [157]. ....	145
Figure 4.23 a) EBSD map with its corresponding b) inverse pole figure (IPF) in the growth direction ( $Y_0$ ). ....	146
Figure 4.24 Process of the metallographic preparation of Cu deposits for EBSD analysis. The steps corresponded to: a) deposit before cross-sectioning, b) cutting, c) mounting, d-e) grinding/polishing and f) vibratory polishing. ....	148
Figure 4.25 Prepared specimens from the electrolyte containing 1, 6 and 10 wt% of water for EBSD analysis.....	149

Figure 4.26 SEM image of Cu coating showing the grid of five horizontal and vertical lines in order to apply the line intercept method to calculate grain size [161].	149
Figure 4.27 Schematic of the constructive interference when the beam of X-rays interacts with the electrons of a periodic arrangement of atoms. Adapted from [158].	150
Figure 4.28 Schematic of Bragg's law. Incident X-ray waves with a $\lambda$ wavelength impacts on atoms (P and Q) located at the crystal planes (G-G' and H-H'). The waves are scattered at a certain angle $\theta$ and if the difference between of pathlength between SQ and QT is an integral number, diffraction ensues. Adapted from [158].	151
Figure 4.29 Example of a diffractogram of the crystalline structure of a metal.	152
Figure 5.1 Calibration curve constructed using Karl Fischer titration data using 0.20 M $\text{CuCl}_2 \cdot 2\text{H}_2\text{O}$ in ethaline. The error bars are smaller than the markers.	160
Figure 5.2 NIR spectrum of blank ethaline recorded between 1050 and 2040 nm.	161
Figure 5.3 NIR spectra of the electrolyte with added water (2 to 18 wt%). The inset graphic shows the absolute absorbance at 1950 nm after the contribution of the background was subtracted and the bands being smoothed.	162
Figure 5.4 Calibration curve obtained using NIR data to cross-check the initial concentration of water in the electrolyte.	163
Figure 5.5 Ability of ethaline and the electrolyte to incorporate water with time. The error bars were smaller than the markers.	164
Figure 5.6 Monitoring of the electrolyte for water incorporation over four months to ascertain its approximated saturation point. The error bars were smaller than the markers.	165
Figure 5.7 UV-Vis spectrum of 0.05 M $\text{CuCl}_2 \cdot 2\text{H}_2\text{O}$ dissolved in DI water, cuvette pathlength = 1cm. The inset image shows the colour of this solution.	166
Figure 5.8 UV-Vis spectrum of 5.0 mM $\text{CuCl}_2 \cdot 2\text{H}_2\text{O}$ dissolved in 6 M HCl, cuvette pathlength= 1 cm. The inset image shows the colour of this solution.	167
Figure 5.9 UV-Vis spectrum of 0.05 M Cu (II) in ethaline, cuvette pathlength = 125 $\mu\text{m}$ . The inset image shows the colour of this solution.	168
Figure 5.10 UV-Vis spectra of 0.05 M $\text{CuCl}_2 \cdot 2\text{H}_2\text{O}$ in ethaline containing increasing amounts of water, cuvette pathlength = 125 $\mu\text{m}$ .	169
Figure 5.11 UV-Vis spectra of 0.05 M $\text{CuCl}_2 \cdot 2\text{H}_2\text{O}$ in ethaline solution containing 15 and 35 wt% of $\text{H}_2\text{O}$ , cuvette pathlength 125 $\mu\text{m}$ . The spectrum of Cu (II) species in aqueous solution corresponds to a concentration of 5 mM Cu (II) + 6 M HCl. This latter spectrum was measured in a cuvette of pathlength= 1 cm.	170

Figure 5.12 Density of ethaline and electrolyte measured with increasing amounts of water (1-15 wt%). The measurements were carried out at room temperature.....	171
Figure 5.13 Schematic of the tetrachlorocuprate complex likely to form when $\text{CuCl}_2$ dissolved in ethaline. ....	172
Figure 5.14 Ethaline and electrolyte viscosity with increasing amounts of water, 1-15 wt% at 25 °C. ....	174
Figure 5.15 Conductivity of the electrolyte against the fluidity containing increasing amounts of water (1-15 wt%). ....	176
Figure 5.16 Voltammetry of ethaline containing water from 1 to 15 wt% of water. All the experiments were performed using a Pt electrode at a scan rate of $5 \text{ mV s}^{-1}$ , rotation speed of $\omega = 700 \text{ rpm}$ at 25 °C. ....	178
Figure 5.17 Reaction mechanisms for the formation of acetaldehyde and 2-methyl-1,3-dioxolane via dehydration of ethylene glycol. Adapted from [111]. ....	180
Figure 5.18 Reaction mechanism for the formation of trimethylamine via Hoffman elimination of choline hydroxide in the undivided cell. Adapted from [111]. ....	181
Figure 5.19 Reaction mechanism of trimethylamine via electrochemical reduction of choline hydroxide in the undivided cell. Adapted from [111]. ....	182
Figure 6.1 Cyclic voltammogram of 0.20 M $\text{CuCl}_2 \cdot 2\text{H}_2\text{O}$ in ethaline (1 wt% $\text{H}_2\text{O}$ ) using a stationary Pt electrode ( $A = 0.031 \text{ cm}^2$ ) at 25 °C. The CE was a Pt wire and the RE was a Ag wire. The scan rate was $5 \text{ mV s}^{-1}$ . The red arrows show the direction of the scan that commenced at the rest potential, +0.55 V vs. Ag wire RE. ....	185
Figure 6.2 Linear potential scans of 0.20 M $\text{CuCl}_2 + 0.5 \text{ M NaCl}$ (–) and 0.20 M $\text{CuCl}_2$ in ethaline (–) using a Pt electrode ( $A = 0.031 \text{ cm}^2$ ) at a scan rate of $5 \text{ mV s}^{-1}$ and $\omega = 700 \text{ rpm}$ at 25 °C. For the aqueous system the RE was SCE and Ag wire for the DES system. The red arrow shows the direction of both scans that started from the rest potential. Data are not corrected for ohmic drop. ....	187
Figure 6.3 Cyclic voltammogram of 0.20 M $\text{CuCl}_2$ in ethaline (1 wt% $\text{H}_2\text{O}$ ) using a Pt electrode ( $A = 0.031 \text{ cm}^2$ ). The scan rate was $v = 5 \text{ mV s}^{-1}$ using different rotation speeds of $\omega = 300\text{-}3500 \text{ rpm}$ . The experiments were performed at 25 °C. ....	188
Figure 6.4 Linear potential scan of 0.20 M $\text{CuCl}_2 \cdot 2\text{H}_2\text{O}$ in ethaline using a Pt electrode ( $A = 0.031 \text{ cm}^2$ ) at 25 °C. The scan rate was $5 \text{ mV s}^{-1}$ and $\omega = 700 \text{ rpm}$ . The red arrow shows the direction of scan that commenced (OCP), around +0.60 V vs. Ag wire RE. ....	189
Figure 6.5 Steady-state curves of 0.20 M $\text{CuCl}_2 \cdot 2\text{H}_2\text{O}$ in ethaline as a function of water using a Pt electrode ( $A = 0.031 \text{ cm}^2$ ) at 25 °C. The scan rate was $5 \text{ mV s}^{-1}$ and $\omega = 700 \text{ rpm}$ . The black arrow shows the shift of the reduction potentials. The experiments were performed with ohmic drop correction (80% of measured $R_u$ ). ....	192

Figure 6.6 Cathodic linear scans of 0.2 M CuCl <sub>2</sub> -ethaline system using a Pt electrode (A= 0.031 cm <sup>2</sup> ) with increasing $\omega$ from 700 to 2800 rpm for a) 1 wt% and b) 10 wt% of water. The experiments were performed with ohmic drop correction (80% of R <sub>u</sub> ). .....	193
Figure 6.7 Cathodic potential scans of 0.20 M CuCl <sub>2</sub> ·2H <sub>2</sub> O in ethaline using a Pt electrode (A= 0.031 cm <sup>2</sup> ) at 25 °C. The scan rate was 5 mV s <sup>-1</sup> and $\omega$ = 700 rpm. The highlighted region corresponds from 35 up to 60% of the ascending part of the polarisation curve. The red arrow shows the direction of scan. The experiments were performed with ohmic correction (80% of measured R <sub>u</sub> ). .....	194
Figure 6.8 Plot of $i^{-1}$ vs. $\omega^{-1/2}$ for Cu(II)/Cu(I) step for electrolyte containing a) 1 wt% and b) 15 wt% of water. The scans were performed using a Pt WE (A =0.031 cm <sup>2</sup> ) at differing rotation speed as $\omega$ = 700, 1400, 2100 and 2800 rpm. The experiments were performed with ohmic correction (80% of R <sub>u</sub> ). .....	195
Figure 6.9 Plot of $i^{-1}$ vs. $\omega^{-1/2}$ for Cu(I)/Cu(0) step for electrolyte containing a) 1 wt% and b) 15 wt% of water. The scans were performed using a Pt WE (A =0.031 cm <sup>2</sup> ) at differing rotation speeds such as $\omega$ = 700, 1400, 2100 and 2800 rpm. The experiments were performed with ohmic correction (80% of R <sub>u</sub> ) .....	196
Figure 6.10 Standard heterogeneous rate constant $k^0$ for the first and second reduction reaction with increasing amounts of water in the electrolyte, e.g. 1-15 wt%. .....	199
Figure 6.11 Proposed DES/electrode interface structure for a) low and b) high water content under OCP conditions [193], assuming that the more intense H-bonding occurs between H <sub>2</sub> O and the HBD [176]. Adapted from [193]. .....	200
Figure 6.12 Charge transfer coefficients for the first and second reduction step from 0.2 M CuCl <sub>2</sub> in ethaline with increasing amounts of water (1-15 wt%). .....	201
Figure 6.13 Secondary current distribution for Tafel polarisation at a disk electrode of radius $r_0$ . The distribution profile corresponds to $Wa$ = 0.2. Mass transport limitations are neglected due to the agitation of the electrolyte. Adapted from [132]. .....	203
Figure 6.14 Linear scan of 0.20 M CuCl <sub>2</sub> ·2H <sub>2</sub> O in ethaline using a Pt electrode (A=0.031 cm <sup>2</sup> ) at 25 °C. The scan rate was 5 mV s <sup>-1</sup> and $\omega$ = 700 rpm. The black arrow shows the direction of scan that started at OCP conditions, around +0.60 V.....	205
Figure 6.15 a) Images of Cu coatings deposited at steel substrate (A=1.18 cm <sup>2</sup> ) from 0.20 M CuCl <sub>2</sub> in ethaline with increasing amounts of water, 1-15 wt%. The experiments were performed at 78% of $i_{lim}$ at $\omega$ = 700 rpm at 25 °C. b) Optical images of the deposit centre, magnification x200.....	207
Figure 6.16 a) Image of Cu coating deposited at steel substrate (A= 1.18 cm <sup>2</sup> ) from 0.2 M CuCl <sub>2</sub> in ethaline system with 15 wt%. The experiment was	

performed at 95% of $i_{lim}$ with $\omega = 700$ rpm at 25 °C. b) Optical image close to the deposit centre, magnification x200. ....	208
Figure 6.17 Secondary current distribution for Tafel polarisation at a disk electrode of radius $r_o$ . The distribution profile corresponds to $Wa = 0.2$ . Mass transport limitations are neglected since the electrolyte is assumed to be well-agitated. Adapted from [132]. ....	209
Figure 6.18 Secondary current distribution for Tafel polarisation at a disk of electrode of radius $r_o = 0.6$ cm. The distribution profile corresponds to $Wa = 0.2$ . Adapted from [132]. ....	210
Figure 6.19 SEM micrographs of Cu deposits obtained from $CuCl_2$ in ethaline with increasing amounts of water (1-15 wt%). The experiments were performed using steel disks ( $A = 1.18$ cm <sup>2</sup> ), 78% of $i_{lim}$ , $\omega = 700$ rpm at 25 °C. Magnification x5000. ....	213
Figure 6.20 Winand's diagram illustrating types of electrodeposits that can be produced according to electrolysis conditions such as the ratio of the operational current to the diffusion limiting current density $i/i_{lim}$ and inhibition intensity. Adapted from [206]. ....	214
Figure 6.21 XRD diffractogram of Cu electrodeposits at steel substrate. The $i_{avg} = 78\%$ of $i_{lim}$ . RTCs were calculated using relative intensities of peaks corresponding to (111), (200), (220) and (311) planes. ....	216
Figure 6.22 RTC of electrodeposits fabricated from water-containing electrolyte (1-15 wt%). ....	217
Figure 6.23 EBSD maps of cross-sections of Cu deposits fabricated from electrolyte containing 1, 6 and 10 wt% of H <sub>2</sub> O. Nomenclature refers to the deposit centre (C) and edge (E). All EBSD maps are presented as IPFs in the Y0-direction (growth). ....	221
Figure 6.24 EBSD orientation maps showing the preferred orientation of the grains in the direction of the (101) plane for the deposits obtained with 1 and 6 wt% of H <sub>2</sub> O in the electrolyte. The remaining EBSD maps and IPFs are not shown because the grains are randomly orientated. ....	223
Figure 7.1 UV-Vis spectrum obtained from the anode compartment solution after galvanostatic dissolution of Cu in neat ethaline containing 1 wt% of water. The current density was 2.84 mA cm <sup>-2</sup> and the rotation speed was 700 rpm at 25 °C. The dissolution time varied from 1 to 4 h. The cuvette pathlength was 1 cm. ....	225
Figure 7.2 UV-Vis spectra of two metal salts dissolved in ethaline containing 1 wt% of H <sub>2</sub> O using a) CuCl (10, 20 and 30 mM) and b) CuCl <sub>2</sub> ·2H <sub>2</sub> O (50 mM). The cuvette pathlength was 125 μm. ....	226

Figure 7.3 Plot of $[\text{CuCl}_2]^-$ concentration versus anodic charge, Q in neat ethaline. (■) symbol shows the concentration inferred from the absorbance data and (◆) symbol shows the concentration based on the mass loss of the anode. The solid line indicates the expected value from Faraday's law with $n = 1$ .	227
Figure 7.4 Monitoring of the electrode potential of Cu vs. Ag wire RE during its anodic dissolution in ethaline containing increasing amounts of water (1-15 wt%). The area of the Cu electrode was 1.18 cm <sup>2</sup> . The current density was set to 2.84 mA cm <sup>-2</sup> and the rotation speed was 700 rpm at 25 °C.	228
Figure 7.5 Voltammetric data of 0.20 M CuCl <sub>2</sub> ·2H <sub>2</sub> O in ethaline containing increasing amounts of water using a Pt WE (A=0.031 cm <sup>2</sup> ) with a rotation speed of 700 rpm at 25 °C. The red arrow shows the direction of the scans. The red dots represent the electrode potentials while anodic dissolution of Cu in ethaline occurred.	228
Figure 7.6 The apparent dissolution valency, $n'$ , of the Cu electrode in 0.20 M CuCl <sub>2</sub> ·2H <sub>2</sub> O in ethaline containing 1 wt% H <sub>2</sub> O as a function of the applied current density and electrode rotation rate. (◆) $\omega = 0$ rpm (■) $\omega = 700$ rpm.	230
Figure 7.7 The apparent dissolution valency, $n'$ , of the Cu electrode at 2.85 mA cm <sup>-2</sup> as a function of the Cu(II) concentration and electrode rotation rate in an ethaline solution containing 1 wt% H <sub>2</sub> O. (◆) $\omega = 0$ rpm (■) $\omega = 700$ rpm.	231
Figure 7.8 The apparent dissolution valency, $n'$ , of the Cu electrode at 2.85 mA cm <sup>-2</sup> with a rotation speed of $\omega = 700$ rpm. Symbol (◆) corresponds to 0.20 M Cu (II) and (■) 0.0 M (neat ethaline).	232
Figure 7.9 Polarisation data of 0.2 M CuCl <sub>2</sub> ·2H <sub>2</sub> O in ethaline containing 15 wt% H <sub>2</sub> O at a rotation speed of 700 rpm, showing coupling of the anodic and cathodic processes.	234
Figure 7.10 Schematic of the overall dissolution processes showing contributions from anodic dissolution and the corrosion reaction.	235
Figure 7.11 Corrosion current density, $i_{\text{corr}}$ , extracted from the dissolution valency data plotted as a function of rotation rate and water content (1 – 15 wt% H <sub>2</sub> O).	237
Figure 7.12 Corrosion current density, $i_{\text{corr}}$ , extracted from dissolution valency data as a function of CuCl <sub>2</sub> ·2H <sub>2</sub> O concentration and rotation rate in an ethaline containing a) 1 wt% and b) 15 wt% of H <sub>2</sub> O.	238
Figure 7.13 Production rate of Cu (I) species in the electrolyte (1-15 wt% H <sub>2</sub> O) as a function of time. For comparison, the depletion of Cu (II) ions is shown as the dotted orange curve.	242
Figure 7.14 UV-Vis monitoring of $[\text{CuCl}_2]^-$ stability in ethaline over time using concentrations of Cu (I) species such as a) 10 mM, b) 20 mM, and c) 30 mM.	243

## LIST OF TABLES

Table 1.1 Conductivity of some ILs and aqueous solutions measured at 25 °C.....	14
Table 1.2 EW of ILs before and after being exposed to a water-saturated argon atmosphere, (e.g. 3 wt% of H <sub>2</sub> O). The voltammograms were recorded using a Pt electrode of 50 µm of diameter at a scan rate of 100 mV s <sup>-1</sup> . Adapted from [42]. .....	17
Table 1.3 Categories of eutectic-based ILs according to the complexing agent used [47]. .....	23
Table 1.4 Type I eutectic mixtures formed with ChCl and anhydrous metal salts [4, 48]. .....	25
Table 1.5 Melting point of hydrated metal salts that formed type II eutectics with ChCl. ....	27
Table 1.6 Common HBDs used to formulate DESs with ChCl. ....	30
Table 1.7 Density of DESs formed with ChCl and different HBDs at 25 °C.....	32
Table 1.8 Chemical structures of three halide salts that form DESs and their density values. Adapted from [67]. .....	35
Table 2.1 Water-air stable ILs used to study the speciation of Cu (II) complexes by Hartley's group. Adapted from [91]. .....	65
Table 2.2 Experimental ratio of the limiting current density and experimental ratio of the expected limiting current density for Cu reduction using 0.05 and 0.20 M of Cu (II) species at two rotation speeds, 700 and 1300 rpm. Adapted from [87]. .....	76
Table 2.3 Density and average hole size of the system ChCl: 2 EG + Ni (II) salt as a function of Ni (II) concentration at 25 °C. Adapted from [113]. .....	86
Table 4.1 Measured and calculated Ru of the CuCl <sub>2</sub> -ethaline system with increasing amounts of water from 1 to 15 wt%. The radius of the Pt electrode was 0.1 cm and the distance between the Luggin probe and the WE was ~0.3 cm. ....	137
Table 4.2 Applied current density for each electrodeposition process according to the content of water in the electrolyte. ....	139
Table 5.1 Measurement of water content in ethaline and the electrolyte measured by Karl Fischer titration. ....	159
Table 5.2 Conductivity of the electrolyte as function of water concentration in the system. The measurements were performed at room temperature.....	175
Table 5.3 EW of ethaline with increasing amounts of water. The anodic potential was +0.95 V vs. Ag wire RE that remained unchanged. The anodic and cathodic limits were defined at current densities such as +0.010 and -0.010 mA cm <sup>-2</sup> .....	179

Table 6.1 Dynamic viscosity and limiting currents to calculate diffusion coefficients of Cu (II) and Cu (I) species and the Stokes-Einstein product at each water content. ....	190
Table 6.2 Diffusion coefficients for Cu (I) and Cu (II) species in aqueous systems versus DES systems at 25 °C. ....	191
Table 6.3 Second reduction potentials for the CuCl <sub>2</sub> -ethaline system with increasing amounts of water from 1 to 15 wt%. ....	192
Table 6.4 Formal potential and rate constant for the first and second reduction reactions with increasing amounts of water. ....	197
Table 6.5 The heterogeneous rate constant, $k^0$ , for Cu depositon calculated in earlier studies from DES and aqueous systems. ....	198
Table 6.6 Wagner number as a function of water content in the electrolyte, e.g. 1-15 wt%. The characteristic length $r_0$ of the working electrode was 0.6 cm. ....	203
Table 6.7 Applied current density for each water-containing electrolyte, 1-15 wt%. ....	205
Table 6.8 Estimated thickness at the electrode centre for electrodeposits obtained when water content ranged from 1-15 wt% in the electrolyte. ....	207
Table 6.9 Current efficiency for each electrodeposition experiment performed from the water-containing electrolytes. ....	209
Table 6.10 Comparison of current efficiency yielded by the Wagner number analysis and gravimetric measurements. ....	211
Table 6.11 Exchange current density calculated for each electrodeposition process from the water-containing electrolytes. ....	215
Table 6.12 Chemical composition (EDX results) of Cu deposits fabricated from water-containing electrolyte, 1-15 wt%. The EDX analysis shows the chemical composition in wt%. ....	218
Table 6.13 Average column thickness of electrodeposits fabricated from the electrolyte containing 1, 6 and 10 wt% of water. Cu was deposited at steel disks ( $A=1.18 \text{ cm}^2$ ), using 78% of $i_{lim}$ , $\omega = 700 \text{ rpm}$ at 25 °C. ....	220
Table 7.1 Dissolution valency in water-containing ethaline (1-15 wt%) with constant current density without rotation at 25 °C. The area of the Cu electrode was $1.18 \text{ cm}^2$ . ....	230
Table 7.2 Comparison amongst $i_{corr}$ extracted from the dissolution valency data and $i_{lim}$ measured for the reduction of CuCl <sub>4</sub> <sup>2-</sup> species at various water amounts. The applied anodic current density was $2.85 \text{ mA cm}^{-2}$ , 0.2 M of Cu (II) species and $\omega = 700 \text{ rpm}$ . ....	239



## LIST OF NOMENCLATURE

$a$	Activity of the ion	---
$A$	Absorbance	---
	Area of electrode	$\text{cm}^2$
	Peak amplitude of a wave	m
$b$	Cuvette pathlength	cm
$\bar{c}$	Average speed of molecule	$\text{m s}^{-1}$
$C$	Bulk concentration/analyte concentration	$\text{mol L}^{-1}$
$C_s$	Surface concentration	$\text{mol L}^{-1}$
$C_o$	Concentration of species at stand. conditions	$\text{mol L}^{-1}$
$C_{dl}$	Capacitance of the double layer	$\text{F cm}^{-2}$
$d$	Diameter	cm
$d_{hkl}$	Interplanar spacing of crystal	nm
$D$	Diffusion coefficient	$\text{cm}^2 \text{s}^{-1}$
$D_{hkl}$	Grain size	nm
$e$	Electronic charge ( $1.6021 \times 10^{-19}$ )	C
$E$	Electrode Potential	V
$E^o$	Standard electrode potential	V
$E^{o'}$	Formal potential	V
$E_{\text{cell}}$	Cell potential	V
$E_{\text{cath}}$	Electrode potential of cathode	V
$E_{\text{anod}}$	Electrode potential of anode	V
$E_j$	Junction potential	V
$E_{pa}$	Anodic peak potential	V
$E_{pc}$	Cathodic peak potential	V
$F$	Faraday's constant (96485)	$\text{C mol}^{-1}$
$f$	Frequency	Hz
$i$	Current density	$\text{mA cm}^{-2}$
$i_{\text{avg}}$	Average current density	$\text{mA cm}^{-2}$
$i_{\text{centre}}$	Current density at centre of electrode	$\text{mA cm}^{-2}$
$i_{\text{edge}}$	Current density at edge of electrode	$\text{mA cm}^{-2}$

$i_k$	Kinetic current density	$\text{mA cm}^{-2}$
$i_{lim}$	Limiting current density	$\text{mA cm}^{-2}$
$i_{lim1}$	Limiting current density for 1 <sup>st</sup> step	$\text{mA cm}^{-2}$
$i_{lim2}$	Limiting current density for 2 <sup>nd</sup> step	$\text{mA cm}^{-2}$
$i_p$	Peak current density	$\text{mA cm}^{-2}$
$i_o$	Exchange current density	$\text{mA cm}^{-2}$
$i/i_{avg}$	Current density distribution	---
$i_a$	Anodic current density	$\text{mA cm}^{-2}$
$i_{app}$	Applied anodic current density	$\text{mA cm}^{-2}$
$i_{corr}$	Corrosion current density	$\text{mA cm}^{-2}$
$I$	Applied current	A
$I_{(hkl)m}$	Measured intensity of a chosen plane	---
$I_{(hkl)}^o$	Reference intensity of a powder sample	---
$I_{pa}$	Anodic peak current	mA
$I_{pc}$	Cathodic peak current	mA
$J$	Exchange current density parameter	---
$k$	Boltzmann's constant ( $1.3807 \times 10^{-23}$ )	$\text{J K}^{-1}$
$k^o$	Standard heterogeneous rate constant	$\text{cm s}^{-1}$
$k_f(E)$	Potential-dependent rate constant	$\text{cm s}^{-1}$
$K$	Equilibrium constant	---
$m$	Mass of sample	g
	Mass of deposit	g
$m_{H_2O}$	Mass of water in sample	mg
$m_{actual}$	Measured mass after deposition/dissolution	g
$m_{expected}$	Predicted mass from Faraday's law after deposition/dissolution	g
$M$	Molecular mass	$\text{g mol}^{-1}$
$N$	Flux of ionic species	$\text{mol m}^{-2} \text{s}^{-1}$
$N_{dif}$	Diffusion flux	$\text{mol m}^{-2} \text{s}^{-1}$
$N_{con}$	Convective flux	$\text{mol m}^{-2} \text{s}^{-1}$
$N_{mig}$	Migration flux	$\text{mol m}^{-2} \text{s}^{-1}$

$N_A$	Avogadro's number ( $6.022 \times 10^{23}$ )	$\text{mol}^{-1}$
$N_T$	Total moles of species	mol
$n$	Number of transferred electrons	---
	Integer number in Bragg's law	---
	Dissolution valency	---
$n'$	Apparent dissolution valency	---
$n_o$	Mole number	mol
$P$	Emerging radiant light	$\text{J s}^{-1}$
	Probability of finding a hole of radius $r$	---
$P_o$	Incident radiant light	$\text{J s}^{-1}$
$Q_a$	Anodic charge	C
$Q_c$	Cathodic charge	C
$r$	Average size of hole	nm
	Separation between ions	nm
	Reaction rate (1 <sup>st</sup> order reaction)	$\text{s}^{-1} \text{cm}^{-2}$
	Reaction rate (2 <sup>nd</sup> order reaction)	$\text{mol s}^{-1} \text{cm}^{-2}$
$r_o$	Radius of electrode	cm
$R_p$	Polarisation resistance	$\Omega$
$R_u$	Uncompensated resistance	$\Omega$
$R_{+/-}$	Average radius of solvent molecule	nm
$\text{RTC}_{(hkl)}$	Relative texture coefficient	---
$t$	Plating time	s
$t_{\text{diss}}$	Dissolution time	s
$T$	Temperature	$^{\circ}\text{C}$
	Transmittance	%
	Average thickness of deposits	$\mu\text{m}$
$\text{TC}_{(hkl)}$	Texture coefficient	---
$U_o$	Limiting velocity at the RDE	$\text{cm s}^{-1}$
$V$	Volume of the titrating reagent	mL
	Volume of the solution	L
$W_a$	Wagner number	---
$w_E$	Water equivalent or titer	$\text{mg mL}^{-1}$

$x$	Mole fraction	---
$y$	Degree of dissociation	---
$z$	Electrode gap between Luggin tip and WE	cm
$z^+$	Cation charge	C
$z^-$	Anion charge	C
<b>Greek letters</b>		
$\alpha$	Charge transfer coefficient	---
	Decoupling factor	---
$\beta$	Full width at half maximum peak intensity	nm
$\beta'$	Formation constant	---
$\gamma$	Shear rate	$s^{-1}$
	Surface tension	$N m^{-1}$
	Activity coefficient	---
$\delta$	Thickness of diffusion boundary layer	$\mu m$
	Average current density parameter	---
$\delta_N$	Nernst diffusion boundary layer	$\mu m$
$\Delta G^\circ$	Standard Gibbs free energy in a process	$kJ mol^{-1}$
$\Delta m$	Mass loss	g
$\Delta m_{\text{expected}}$	Expected mass loss	g
$\Delta m_{\text{exp}}$	Experimental mass loss	g
$\varepsilon$	Molar absorptivity	$mol^{-1} cm^{-1}$
$\varepsilon_0$	Vacuum permittivity	$F m^{-1}$
$\eta$	Dynamic viscosity	mPa s
	Overpotential	V
$\eta^{-1}$	Fluidity	$mPa^{-1} s^{-1}$
$\eta_s$	Surface overpotential	V
$\eta_c$	Concentration overpotential	V
$\eta_\Omega$	Ohmic overpotential	V
$\theta$	Bragg's angle	rad, degrees
$\kappa$	Conductivity	$S m^{-1}, \Omega^{-1} cm^{-1}$

$\lambda$	Wavelength	nm
	X-ray wavelength	nm
	Ionic conductivity	$\text{S cm}^2 \text{ mol}^{-1}$
$\Lambda$	Molar conductivity	$\text{S cm}^2 \text{ mol}^{-1}$
$\Lambda^\circ$	Limiting molar conductivity	$\text{S cm}^2 \text{ mol}^{-1}$
$\nu$	Kinematic viscosity	$\text{cm}^2 \text{ s}^{-1}$
	Scan rate	$\text{mV s}^{-1}$
$\xi$	Correction parameter	---
$\rho$	Density	$\text{g cm}^{-3}$
$\sigma$	Collision diameter of molecule	nm
$u_r$	Radial velocity	$\text{cm s}^{-1}$
$u_y$	Disk velocity normal to surface	$\text{cm s}^{-1}$
$u_\phi$	Angular velocity	$\text{rad s}^{-1}$
$\Phi$	Current efficiency	%
$\omega$	Rotation speed	$\text{rad s}^{-1}$ , rpm

## LIST OF ABBREVIATIONS

AC	Alternating current
AcChCl	Acetyl choline chloride
AFRC	Advanced Forming Research Centre
BMIM	Butyl-methylimidazolium
BSE	Backscattered electrons
BuPyCl	Butylpyridinium chloride
CCD	Charge coupled device
CE	Counter electrode
ChCl	Choline chloride
ChCl: 2 EG	Choline chloride: 2 ethylene glycol
CMAC	Continuous Manufacturing and Crystallisation Centre
CV	Cyclic voltammetry
DACl	Diethylenethanol ammonium chloride
DES	Deep Eutectic Solvent
DI	Deionized
EBSD	Electron backscatter diffraction
EDA	Ethylene diamine
EDL	Electrical double layer
EDX	Energy Dispersive X-ray spectroscopy
EG	Ethylene glycol
EMIM	Ethyl-methylimidazolium
EPSR	Empirical potential structure refinement
EtNH <sub>3</sub>	Ethylammonium
EtPyBr	Ethylpyridinium bromide
EW	Electrochemical window
EXAFS	Extended X-ray Absorption Fine Structure
FAB-MS	Fast Atom Bombardment Mass-Spectrometry
FT	Field-oriented texture
FWHM	Full width at half maximum peak intensity
GC-MS	Gas Chromatography-Mass Spectrometry

Gly	Glycerol
HBD	Hydrogen bond donor
ICDD	International Centre for Diffraction Data
IL	Ionic liquid
IPF	Inverse pole figure
IUPAC	International Union of Pure and Applied Chemistry
JCPDS	Joint Committee on Powder Diffraction Standards
KF	Karl Fischer
LSV	Linear sweep voltammetry
MDIM	1-methyl-3-[2,6-(S)-dimethylocten-2-yl]imidazolium
MEIC	1-methyl-3-ethyl-imidazolium chloride
MIM	methyl-imidazolium
MTPBr	Methyltriphenylphosphonium bromide
NA	Nicotinic acid
NIR	Near-Infrared
NMR	Nuclear Magnetic Resonance
OCP	Open circuit potential
PEEK	Polyether ether ketone
PTFE	Polytetrafluoroethylene
RDE	Rotating disk electrode
RE	Reference electrode
REACH	Registration Evaluation Authorisation and Restriction of Chemicals
RTC	Relative texture coefficient
RTILs	Room temperature ionic liquids
SCE	Saturated calomel electrode
SD	Standard deviation
SE	Secondary electrons
SEM	Scanning Electron Microscopy
SHE	Standard hydrogen electrode
SiC	Silicon carbide
TBABr	Tetrabutylammonium bromide
Tf <sub>2</sub> N	Trifluoromethylsulfonyl-amide

UD	Un-oriented dispersion
UV	Ultraviolet
UV-Vis	Ultraviolet-visible
WE	Working electrode
XRD	X-ray Diffraction



## **1. Chapter - Introduction**

# 1. Introduction

---

## 1.1 Background

The electronic industry showed the highest rate of growth in the nineties which has demanded the fabrication of metals and alloys at large scale. Certain metals and alloys show high electrical conductivity, which make them preferred materials to electrically connect electronic components and many of these metals and alloys are manufactured by electrochemical means. Due to the continued search of materials with improved properties, new electrolytes and solutions from which these materials can be produced are being sought, many of which have to comply with growing environmental regulations.

Currently, most of the electroplating sector employs aqueous processes since these exhibit high conductivities, low operational costs and high deposition rates. However, the main limitation of aqueous systems is the narrow electrochemical window of water. Some electronegative metals (e.g. Cr and Zn) cannot be electrodeposited without hydrogen generation, which compromises the properties of the deposits. Also, certain plating solutions require complexing agents that are detrimental to the environment. These drawbacks have given rise to the formulation of non-aqueous solvents known as Ionic Liquids (ILs).

ILs have been defined as mixtures of cations and anions whose melting points are lower than 100 °C and their electrochemical windows are larger than aqueous solutions [1, 2]. The earliest ILs used in electrodeposition studies were prepared from chloroaluminate salts. However, chloroaluminate-based ILs are sensitive to moisture. These solutions react with water, hydrolyse and form compounds such as HCl and oxo-chloroaluminates [3]. This led to the formulation of ILs using hydrophobic anions which are water tolerant and therefore stable under ambient conditions. Nevertheless, it has been found that only ultrapure ILs yield reproducible results. At the moment, electrodeposition from chloroaluminate solvents has to be contained

within glove boxes or inert atmospheres which make them expensive for practical electroplating applications.

A third category of ILs which is being explored is Deep Eutectic Solvents (DESs). These liquids are tolerant to water [4] and thereby stable under atmospheric conditions. Since DESs are formulated using compounds such as ammonium salts, amides, carboxylic acids and alcohols, they are less costly solvents [5]. However, DESs are hygroscopic substances and absorb water unless special precautions are taken [6-9].

Metal electrodeposition from DES systems is often performed either neglecting the content of water content or using low water-containing DES systems (< 1 wt% H<sub>2</sub>O). However, due to their hygroscopic property, metal electrodeposition from DES systems in practice is likely to occur from hydrated electrolytes. Moreover, it appears that addition of water could have both advantages and disadvantages which are important to ascertain. This study is focused on investigating the effect of water content on three important aspects of metal electrodeposition: (i) the electrochemical properties of the hydrated metal-DES system, (ii) the morphological and microstructural features of the electrodeposits obtained from water-containing electrolytes, and (iii) the anodic reaction using a soluble anode during metal electrodeposition from the hydrated DES systems.

## 1.2 Ionic Liquids

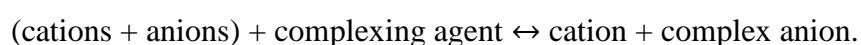
Industrial uses of metal coatings cover a variety of applications such as electrical conductors and corrosion protectors providing mechanical strength, wear resistance and protection against deterioration. As mentioned in the previous section, electrodeposition from aqueous systems are often hindered by: i) limited electrochemical potential window leading to inability to deposit some metals due to water breakdown, ii) hydrogen evolution, iii) poor current efficiency caused by side reactions and iv) consequential deterioration of the deposits properties by incorporation of hydrogen, oxides or hydroxides.

Cr and Zn electroplating are examples of the thermodynamic constraints from aqueous systems [10, 11]. For example, Cr electroplating exhibits low cathodic efficiency (e.g. 10-20%) since it cannot be discharged without evolving H<sub>2</sub> which not only reduces the efficiency of the process, also leads to cracked electrodeposits compromising their properties [10, 11]. In order to avert electrodeposits with poor properties, the use of additional chemicals in Cr aqueous systems is usually required. In a similar fashion, Zn electroplating demands the use of strong additives in order to prevent formation of coatings with poor microstructure. Unfortunately, some of these chemicals are classified as both environmental and health pollutants, which replacement for less hazardous chemicals is regulated in recent years by the European Union directives concerning Registration, Evaluation, Authorisation and Restriction of Chemicals (REACH).

ILs have been proposed to be alternative electrolytes to aqueous systems [12], especially due to their very low vapour pressure and thereby volatility is a minor concern. Complying with environmental regulations has not been the only motivation to study ILs as electrochemical reaction media. There are technical aspects that ILs can improve which are beneficial for electrodeposition processes such as: (i) wider electrochemical potential window, (ii) negligible hydrogen evolution, (iii) deposition of metals that possess negative reduction potentials, (iv) metal deposition with higher current efficiencies, and (v) electrodeposits with improved properties.

### 1.2.1 Definition and brief history of ionic liquids

Ionic liquids (ILs) are substances constituted by cations and anions, i.e. of an ionic nature whose melting temperatures are below 100 °C [1, 13, 14]. The low melting point is achieved by using organic cations associated with inorganic anions that are poorly coordinated. In other words, the anion, generally small, does not interact well with the cation because this is typically large, bulky and asymmetrical. In addition, the irregular shapes of the molecules prevent the ions to pack together in an orderly fashion. When a complexant is added to achieve the liquid phase then the equilibrium on ILs can be defined as:



In this case, the complexing agent interacts with the anion forming a complex anion that causes a delocalization of the charge. This phenomenon weakens the electrostatic interactions and diminishes the energy of the crystal lattice [15]. As a consequence, the melting point of the liquid is lower than the individual components of the mixture. For a substance to be considered as an ionic liquid, it has to be in the liquid state at or below the boiling point of water [13].

In 1914, ethylammonium nitrate ( $[\text{C}_2\text{H}_5\text{NH}_3]^+[\text{NO}_3]^-$ ) was reported by Walden [16] as the first substance that nowadays can be categorised as an ionic liquid. This liquid had a melting point between 12 and 14 °C [16]. After four decades (1954), Hurley and Wier [17] used a mixture of aluminium chloride ( $\text{AlCl}_3$ ) and 1-ethylpyridinium bromide ( $\text{C}_7\text{H}_{10}\text{BrN}$  or EtPyBr) to electrodeposit aluminium at room temperature [17]. However, EtPyBr  $-\text{AlCl}_3$  was liquid only at one specific composition [17]. Moreover, EtPyBr  $-\text{AlCl}_3$  was electrochemically unstable since the bromide ion was prone to oxidation [17].

Osteryoung *et al.* replaced the EtPyBr with *N*-butylpyridinium chloride ( $\text{C}_9\text{H}_{14}\text{ClN}$  or BuPyCl) [18]. Although the resulting system BuPyCl- $\text{AlCl}_3$  was liquid over wider molar compositions, the stability issue remained and the butylpyridinium cation was easily co-reduced while the metal deposition occurred [19]. In the

subsequent years, research concentrated on finding a suitable chloride salt that not only enhanced the electrochemical stability but also lowered the melting point of the liquid at different molar fractions.

Hussey and Wilkes [20] established that amongst some of the quaternary-N and heterocyclic salts, dialkylimidazolium chloride salts showed better physicochemical and electrochemical properties such as viscosity and wider electrochemical window. For example, a mixture of 1-ethyl-3-methylimidazolium chloride ( $C_6H_{11}N_2$  or  $[EMIM]^+[Cl]^-$ ) and  $AlCl_3$  showed a lower viscosity when compared with other melts [21]. In addition, the freezing point of  $[EMIM]^+[Cl]^-$  was lower than room temperature and this mixture was liquid between 0.33 and 0.67 mole fraction of the  $AlCl_3$  [1, 21]. Since the imidazolium cation (Fig. 1.1) was more difficult to reduce, the electrochemical window of the melt was broader than the pyridinium-based IL. This resulted in an improved electrochemical stability of the liquid [21].

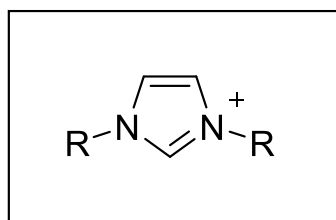


Figure 1.1 Structure of the dialkylimidazolium cation that forms a eutectic mixture with  $AlCl_3$ .

Due to the fact that ILs based on imidazolium salts showed more convenient physico-chemical and electrochemical properties than pyridinium-based ones, intense research has been carried out using these types of salts over the years.

### 1.2.2 Types of ionic liquids

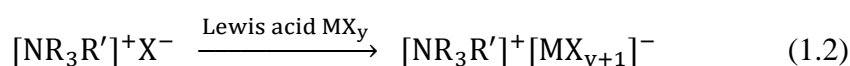
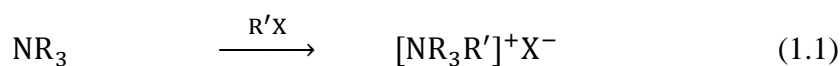
There are three types of ILs which can be differentiated from each other by the type of complexing agent used. The first class of ILs is known as chloroaluminate salts which are composed from cations such as imidazolium, pyridinium, ammonium or phosphonium mixed with aluminium chloride ( $\text{AlCl}_3$ ). These liquids have been extensively studied by Hussey and Wilkes and have attracted the attention of many researchers over the years.

The second type of solvents is known as water-air stable ILs formed with the same cations such as imidazolium, pyridinium, ammonium or phosphonium mixed with discrete or hydrophobic anions. Amongst the most important discrete anions are the tetrafluoroborate ( $[\text{BF}_4]^-$ ) and the hexafluorophosphate ( $[\text{PF}_6]^-$ ) which were reported for the first time in the literature by Wilkes and Zaworotko in 1992 [22].

The third category of ILs is known as Deep Eutectic Solvents (DESs) which are formed by ammonium, phosphonium, or sulphonium cations mixed with hydrogen bond donors (HBDs) such as amides, carboxylic acids or alcohols. The progenitor of these type of ILs was Abbott [4]. More details of each type of ILs will be developed in the following sections.

### 1.2.3 Chloroaluminate and water-air stable ionic liquids

This kind of ILs can be synthesised from two steps. The first step is the formation of the cation, when this is not commercially available. In the second step an anion exchange reaction occurs when the halide salt is added to the salt that contains the cation and haloaluminate anion forms. These reactions are shown in equations (1.1) and (1.2)



Since 1-ethyl-3-methylimidazolium chloride [EMIM][Cl] salt has shown superior properties as explained in section 1.2.1, imidazolium cations are the preferred starting materials to prepare the so-called chloroaluminate ionic liquids. The imidazolium cation can be obtained via a quaternization reaction. This reaction consists of mixing amines with haloalkenes to obtain a compound with unequal chain lengths. For instance, one of the alkyl groups of the obtained product is longer than the other (cf. Fig. 1.2).

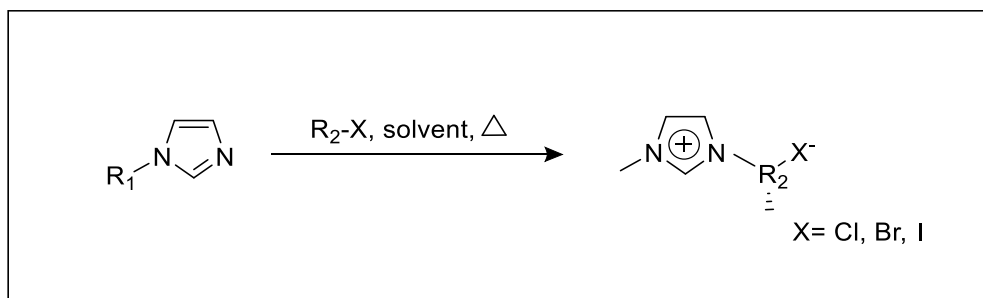


Figure 1.2 Scheme of the quaternization reaction of 1-alkylimidazoles. Adapted from [23].

Also, other common cations such as pyridinium, pyrrolidinium, ammonium, phosphonium and sulfonium (cf. Fig. 1.3) can be obtained with the quaternization reaction to prepare room temperature ILs. The quaternization reaction shown in Fig. 1.2 should be carried out under inert atmosphere to prevent the ingress of water and oxygen because imidazolium salts are hygroscopic.

N-alkyl-pyridinium 	N-alkyl-methyl-pyrrolidinium 	1-alkyl-3-methyl-imidazolium 
Tetra-alkyl-ammonium  $\text{R}_{1,2,3,4} = \text{CH}_3(\text{CH}_2)_n \quad n=1,3,5,7,9$	Tetra-alkyl-phosphonium 	Tri-alkyl-sulfonium 

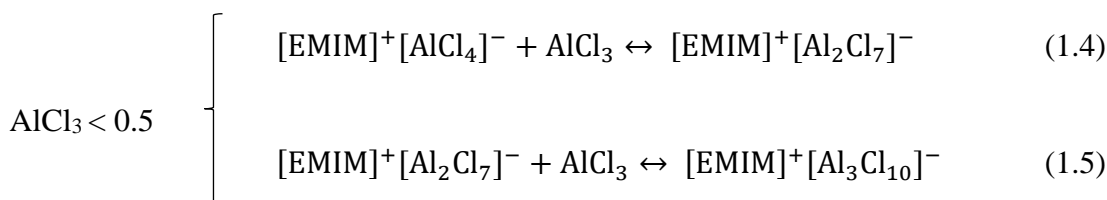
Figure 1.3 Common cations that are used to synthesise haloaluminate ILs.



The second step of the synthesis of ILs refers to a reaction between a halide salt and Lewis acids ( $\text{AlX}_3$ ), where X can be either Cl or Br. The anionic chemistry of chloroaluminate ILs prepared from this method is governed by the proportion of  $\text{AlCl}_3$  to the halide salt. This has led to a nomenclature of ILs divided in three groups, acidic, basic or neutral ILs.

For instance, if the halide salt and the Lewis acid are present in the same molar composition, the melt is neutral. However, when the mole fraction of  $\text{AlCl}_3$  is lower than 0.5, the ionic liquid becomes basic and when the mole fraction of  $\text{AlCl}_3$  becomes greater than 0.5, the liquid is acidic [24]. The acidity or basicity of ILs governs the speciation of metals in solution.

The anionic species that may form depending upon the composition of the liquid are shown in equations (1.3), (1.4) and (1.5). In order to study the chloroaluminate species in the liquid, various techniques have been used such as Raman spectroscopy, Nuclear Magnetic Resonance (NMR) and mass spectrometry.



Unlike chloroaluminate ILs, the second set of ILs was water-air stable ones. These ILs could be prepared and safely stored outside of an inert atmosphere because they are water-insensitive. The most common anions that form water and air stable ILs are shown in Fig 1.4.

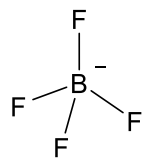
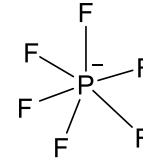
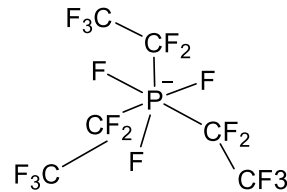
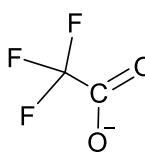
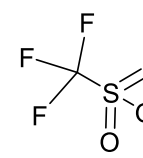
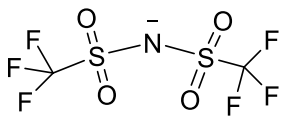
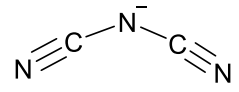
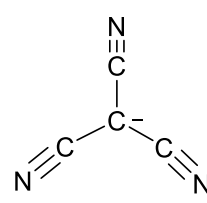
Tetrafluoroborate [BF <sub>4</sub> ] <sup>-</sup> 	Hexafluorophosphate [PF <sub>6</sub> ] <sup>-</sup> 	Tris(pentafluoroethyl) trifluorophosphate [FAP] <sup>-</sup> 
Trifluoroacetate [ATF] <sup>-</sup> 	Trifluoromethanesulfonate [OTF] <sup>-</sup> 	Bis(trifluoromethylsulfonyl) imide [NTF] <sup>-</sup> 
Thiocyanate [SCN] <sup>-</sup> $\text{N}\equiv\text{C}-\text{S}^-$	Dicyanamide [DCA] <sup>-</sup> 	Tricyanomethide [TCM] <sup>-</sup> 

Figure 1.4 Common anions that are used to synthesise water-air stable ILs.

#### 1.2.4 Nomenclature of chloroaluminate and water- air stable ionic liquids

Since ILs are formed by cations and anions, the name of the liquid begins with the cation name followed by the anion. In the case of chloroaluminate ILs, the most used salt is imidazolium and common anions are chlorides or bromides. Since imidazolium salt bears alkyl chains bounded to the cationic structure, the alkyl chain should be stated before the word imidazolium. For example, the name of a typical chloroaluminate ILs is 1-butyl-3-methylimidazolium – chloride, abbreviated as [BMIM]<sup>+</sup>[Cl]<sup>-</sup>.

For water-air stable ILs a similar rule applied. For instance, the name of a common IL is 1-butyl-3-methylimidazolium tetrafluoroborate ([C<sub>8</sub>H<sub>15</sub>ClN<sub>2</sub>]<sup>+</sup>[BF<sub>4</sub>]<sup>-</sup>). Also, the name of this IL can be abbreviated as [BMIM]<sup>+</sup>[BF<sub>4</sub>]<sup>-</sup>, depending of the number of carbons chains that are attached to the cation.

### 1.3 Properties of chloroaluminate and water-air stable ionic liquids

The interest that ILs has attracted in recent years is reflected in numerous publications, the International Union of Pure and Applied Chemistry (IUPAC) has created a database of some thermodynamics, thermochemical and transport properties of ILs [25]. This section will concentrate on the properties of chloroaluminate and water-air stable ILs that are relevant for metal electrodeposition.

#### 1.3.1 Thermal properties

As mentioned in section 1.2, a characteristic of ILs that makes them unique is their low vapour pressure. ILs show negligible vapour pressures at atmospheric condition which make them non-volatile due to their attractive charges [26]. Bier and Dietrich explained that the low vapour pressure of ILs is a result of “a combination of their strong ionic character and low melting points” [27]. Although the vapour pressure of ILs has been measured as nearly zero, it does not mean they cannot be evaporated [28]. Under certain conditions such as low vacuum (0.01 atm) and a temperature of 70 °C, some ILs have been distilled [29]. However, since most of the electrodeposition processes occurs under atmospheric conditions, this is not an issue.

The melting point is another essential thermal property of ILs. Melting point refers to as the temperature where the individual components of an ionic liquid change from the solid to the liquid state. The melting point of ILs depends on ionic radii, cationic and anionic structure length of the side chain bounded to the cation and distribution of the charge [23].

The force that dominates ILs is the Coulombic attractions between the ions. Equation 1.6 shows the Coulombic term.

$$|E| = \frac{Mz^+z^-}{4\pi\epsilon_0 r^2} \quad (1.6)$$

where  $|E|$  is the magnitude of the electric field,  $z^+$  and  $z^-$  refers to the charge of the ions and  $r$  is the separation between the ions, and  $\epsilon_0$  is the vacuum permittivity. When the ions possess larger radii, there is a great ionic separation. This ion separation

diminishes the surface charge density of the crystal lattice, which reduces the electrostatic interactions and the melting point of certain salts. For example, the melting point of the salt [EMIM]<sup>+</sup>[BF<sub>4</sub>]<sup>-</sup> is lower than the one of [EMIM]<sup>+</sup>[Cl]<sup>-</sup> salt because the ionic radius of BF<sub>4</sub><sup>-</sup> is higher (2.29 Å) than Cl<sup>-</sup> ions (1.81 Å).

The melting point of ILs can be also affected by the chemical structure of the cations [30]. For instance, aromatic chemicals as imidazolium and pyridinium exhibited lower melting temperatures (-15 to 20 °C) than non-aromatic substances (29.2 to 104 °C) [30]. The lower melting point with the aromatic cations was attributed to a further delocalisation of the positive charge [30].

Since organic salts have side chains attached to their structures, the effect of chain length was investigated by Seddon *et al.* [31, 32]. The authors used imidazolium tetrafluoroborate salt (water-air stable ILs) with increasing alkyl-chains. It was found that the melting point of the salts were side-chain dependent [31]. For instance, when alkyl-chain lengths increased, the melting points fell progressively.

### 1.3.2 Physico-chemical properties

The physico-chemical properties of ILs depend on the nature and size of the ions, alkyl-chain length and interactive forces between cations and anions. The density of the majority of ILs is reported to be higher than aqueous solutions due to the large size of the ions and the high molecular weight of these compounds. Density values of ILs varied between 1.08 and 1.58 g cm<sup>-3</sup> [33].

ILs based on imidazolium cations exhibited higher densities when changing the anionic species in the following order: Tf<sub>2</sub>N<sup>-</sup> < PF<sub>6</sub><sup>-</sup> < C<sub>2</sub>SO<sub>4</sub><sup>-</sup> < BF<sub>4</sub><sup>-</sup> < Cl<sup>-</sup>. On the contrary, when the alkyl chain length on the imidazolium salt ring increased, the density of the imidazolium-based ILs decreased. Although an explanation for these results has not been offered [34], smaller anions seem to produce greater anion-cation interaction. ILs formed with aromatic cations like pyridinium and imidazolium possessed greater densities than aliphatic ammonium salts.

### 1.3.2.1 Viscosity

Viscosity is an essential property of ILs since it can affect some of the transport properties of the ions in the solution [35]. Viscosity is perhaps the less advantageous property of ILs when compared with the viscosity of aqueous solutions. It has been reported that at 25 °C, imidazolium-based ILs possessed viscosities ranging from 314 mPa s ([HMIM]<sup>+</sup>[BF<sub>4</sub>]<sup>-</sup>) to 35 mPa s ([EMIM]<sup>+</sup>[CF<sub>3</sub>SO<sub>3</sub>]<sup>-</sup>), which are much higher than the viscosity of water which is 1 mPa s at 25 °C.

Okoturo and VanderNoot [36] measured the viscosity of ILs based on AlCl<sub>3</sub> and hydrophobic anions. In the case of Lewis acidic chloroaluminate ILs, the dominant anionic complex was Al<sub>2</sub>Cl<sub>7</sub><sup>-</sup> [20]. Therefore, changes in viscosity were studied as a function of the cationic structure.

The viscosity of chloroaluminate ILs was found to be low when small, symmetrical and cations of low molar mass were used [36]. Cations with higher molar mass but short alkyl chains also produced low-viscous chloroaluminate ILs. On the contrary, the viscosity of the ILs increased when both the molecular weight of the cation was higher and the cationic structure contained functional groups and alkyl chains [36]. It was stated that the viscosity of chloroaluminate ILs was affected by several factors such as: i) the size, ii) the symmetry, iii) and the molecular weight of the cation as well as iv) the entanglement of the chains bounded to the cation, v) hydrogen bond between cations and anions and vi) Van der Waals interactions [36].

The viscosity of ILs based on hydrophobic anions was also investigated as a function of the ionic structure [36]. ILs that contained “large cations bearing ring structures” showed lower viscosities than ILs formed by cations with functional groups. The higher viscosity was ascribed to the further hydrogen bonding brought about by the functional groups such as OH<sup>-</sup> [37].

The effect of the hydrophobic anions on the viscosity of ILs was also investigated. In this study, the cation 1-butyl-3-methylimidazolium was mixed with different hydrophobic anions. It was reported that the more symmetric the anions, the greater the viscosity. The symmetry of the anions and hence the viscosity of the liquid increased in the following order: [Imide] < [CF<sub>3</sub>SO<sub>3</sub>]<sup>-</sup> < [BF<sub>4</sub>]<sup>-</sup> < [SbF<sub>6</sub>]<sup>-</sup> < [PF<sub>6</sub>]<sup>-</sup>.

### 1.3.2.2 Conductivity

The ionic conductivity of chloroaluminate and non-chloroaluminate ILs has been measured to be lower than the conductivity of aqueous solutions. For instance, at room temperature the ionic conductivity of a number of ILs varied from 0.22 to 1.4 S m<sup>-1</sup> whereas the conductivity of some aqueous solutions ranged between 0.29 to 4.51 S m<sup>-1</sup> [38]. Table 1.1 summarises conductivities of some ILs and some of the most important aqueous solutions used for electrodeposition.

Table 1.1 Conductivity of some ILs and aqueous solutions measured at 25 °C.

ILs		Conductivity (S m <sup>-1</sup> )
Cation	Anion	
[BuMePy] <sup>+</sup>	[N(CF <sub>3</sub> SO <sub>2</sub> ) <sub>2</sub> ] <sup>-</sup>	0.22
[BMIM] <sup>+</sup>	[BF <sub>4</sub> ] <sup>-</sup>	0.35
[EMIM] <sup>+</sup>	[N(CF <sub>3</sub> SO <sub>2</sub> ) <sub>2</sub> ] <sup>-</sup>	0.84
[EMIM] <sup>+</sup>	[BF <sub>4</sub> ] <sup>-</sup>	1.40
Aqueous solvents*		Conductivity (S m <sup>-1</sup> )
CuSO <sub>4</sub>		0.29
KCl		0.82
H <sub>2</sub> SO <sub>4</sub>		2.43
HCl		4.51

\*Values of conductivity measured at 20 °C and at 0.5 wt% molar composition of the salt [38-40].

The fact that the conductivity of ILs is lower than conventional aqueous solutions has been attributed to the complex structure of the bulky organic cations, making transport more difficult [41]. On the contrary, aqueous solutions consist of small and simple inorganic ions, which facilitate transport.

The conductivity of ILs was modulated by changing the type of the cation. For example, when different cations were used the conductivity increased in the following fashion: 1-alkyl-3-methylimidazolium > N,N-dialkylpyrrolidinium > tetraalkylammonium [41]. This increment in the conductivity was related to the 'bulkiness' of the cation [42]. The imidazolium cation, for instance, was flatter than the tetraalkylammonium cation which possessed a tetrahedral geometry [42].

However, there were other factors that affected the conductivity of ILs. For instance, Bonhôte *et al.* studied the effect of the ion size and the molecular weight on the conductivity of ILs based on hydrophobic anions [37]. To exemplify, for a given cation, [EMIM]<sup>+</sup> (1-ethyl-3-methylimidazolium) mixed with two different anions such as [TA]<sup>-</sup> and [Tf<sub>2</sub>N]<sup>-</sup> (trifluoroacetate and bis-trifluoromethylsulfonyl-amide, respectively) the [EMIM]<sup>+</sup>[TA]<sup>-</sup> exhibited a higher conductivity than [EMIM]<sup>+</sup>[Tf<sub>2</sub>N]<sup>-</sup> [37]. This was attributed to two factors: i) the smaller size of the TA<sup>-</sup> anion and ii) and its lower molecular weight, e.g. 224.18 g mol<sup>-1</sup> when compared with the molecular weight of the [Tf<sub>2</sub>N]<sup>-</sup> anion, e.g. 391.31 g mol<sup>-1</sup> [37].

### 1.3.3 Electrochemical properties

#### 1.3.3.1 Electrochemical window

The electrochemical window (EW) of a solvent is governed by the chemical structure of the materials and electrode material, temperature, solvent and impurities. The electrochemical window is commonly measured using Linear Sweep Voltammetry (LSV) or Cyclic Voltammetry (CV). These techniques allow sweeping a potential range while recording reduction and oxidation currents. The EW is obtained by subtracting the reduction potential from the oxidation potential as Fig. 1.5 illustrates.

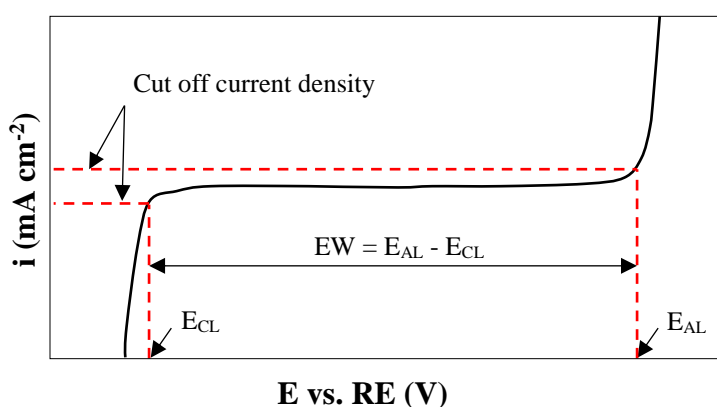


Figure 1.5 Schematic of an electrochemical window showing the anodic and cathodic limits defined at arbitrary current densities.

Since the EW of ILs have been evaluated under a variety of conditions such as different reference electrode, substrate, scan rate, temperature and others, it is not an easy task to establish a comparison amongst them. Generally, cathodic and anodic limits of pure ILs are attributed to the oxidative decomposition of the anion and the reductive decomposition of the cation. EWs of ILs can be as large as 4.4 V in water-air stable ILs and for imidazolium salts as large as 4.0 V.

The impact of water has been demonstrated to be detrimental to the ILs systems because it reduces both the anodic and cathodic limit potentials of the solvent [3, 43]. For example, three ILs such as 1-butyl-3-methylimidazolium tetrafluoroborate ( $\text{BMIM}^+\text{BF}_4^-$ ), 1-butyl-3-methylimidazolium hexafluorophosphate



(BMIM<sup>+</sup>PF<sub>6</sub><sup>-</sup>) and 1-methyl-3-[2,6-(S)-dimethylocten-2-yl]imidazolium tetrafluoroborate (MDIM<sup>+</sup>BF<sub>4</sub><sup>-</sup>) were investigated for water incorporation and its subsequent effect on their EW [43].

The cathodic and anodic limits were measured before and after exposure to a water-saturated atmosphere, as shown in Table 1.2 [43]. The experimental results showed that the EW of the three ILs decreased approximately twofold of the initial value [43]. Fig. 1.6 illustrates the shrinking of the EW of [BMIM]<sup>+</sup>[BF<sub>4</sub>]<sup>-</sup>, which was the IL most affected by the inclusion of water as its EW reduced from 4.15 to 2.10 V [43].

Table 1.2 EW of ILs before and after being exposed to a water-saturated argon atmosphere, (e.g. 3 wt% of H<sub>2</sub>O). The voltammograms were recorded using a Pt electrode of 50 μm of diameter at a scan rate of 100 mV s<sup>-1</sup>. Adapted from [43].

IL	EW (V)	
	Before exposure	After exposure
BMIM <sup>+</sup> PF <sub>6</sub> <sup>-</sup>	4.15	2.10
MDIM <sup>+</sup> BF <sub>4</sub> <sup>-</sup>	3.80	2.00

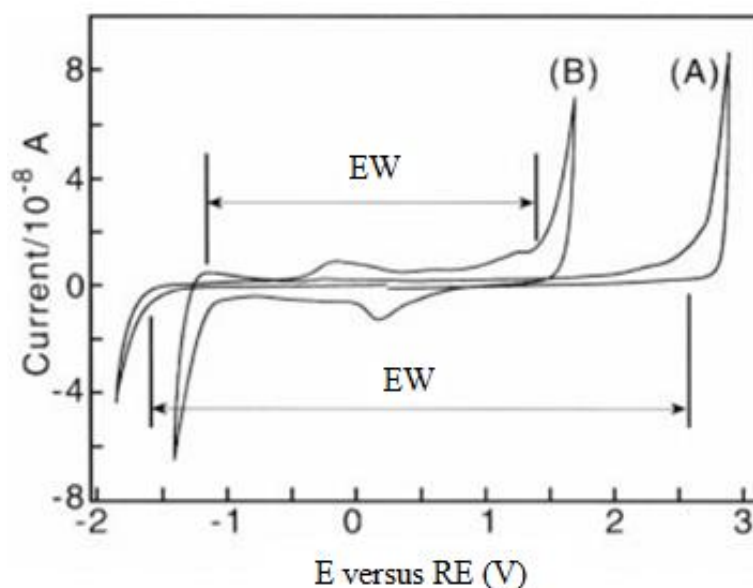


Figure 1.6 Electrochemical window of a) dry and b) wet [BMIM]<sup>+</sup>[BF<sub>4</sub>]<sup>-</sup> using a Pt electrode (d= 50 μm) at a scan rate of 100 mV s<sup>-1</sup>. The liquid was exposed to water-saturated argon atmosphere at 22 °C. Adapted from [43].

Sahami and Osteryoung studied the electrochemical response of the system after its addition to an aluminium chloride-N-n-butylpyridinium chloride, e.g.  $\text{AlCl}_3:2\text{BuPyCl}$  [3]. In this study water was added to the IL system (10.5 mM of  $\text{H}_2\text{O}$ ) and cyclic voltammograms were recorded on three electrodes such as glassy carbon (GC), tungsten (W) and platinum electrode as Fig. 1.7 shows. The cathodic limit was ascribed to the reduction of the  $\text{BuPy}^+$  species and the anodic limit was thought to be the production of chlorine gas [3].

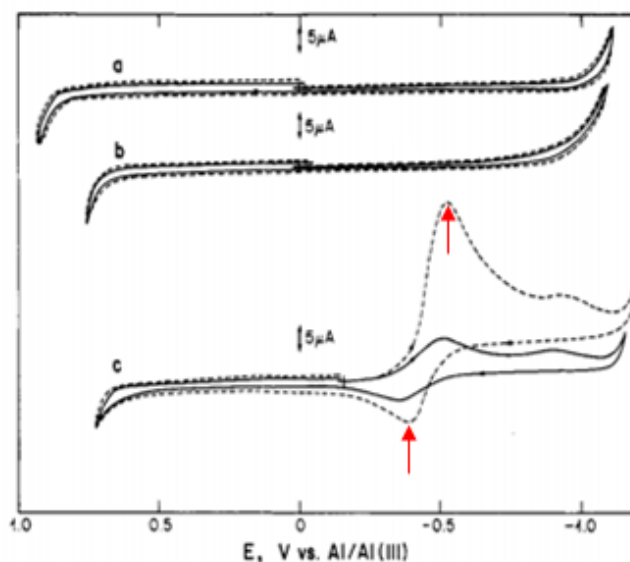


Figure 1.7 Cyclic voltammetry in chloroaluminate IL using a) GC, b) W and c) Pt electrode at  $50 \text{ mVs}^{-1}$  at  $40 \text{ }^\circ\text{C}$ . The continuous curves correspond to the dry liquid whereas the dotted curves represent the liquid + added water. Adapted from [3].

Upon water addition, the cathodic and anodic peak currents already present at Pt electrode increased (cf. dotted voltammogram and red arrows in Fig. 1.7 (c)). The authors performed further experimentation to elucidate which species were being reduced. It was found that when concentrated  $\text{HCl}$  was added to the melt, the electrochemical response was similar to the one obtained when water was present in the IL. After additional experimentation using the rotating disk electrode (RDE), it was concluded that water could react with the aluminium-containing species of the IL to form  $\text{HCl}$ . Besides, the reduction wave observed at the Pt electrode was attributed to the evolution of hydrogen as per reaction  $2\text{HCl} + 2\text{e}^- \rightarrow \text{H}_2 + 2\text{Cl}^-$ . The lack of any reduction wave at GC and W electrodes was thought to be due to the large overpotential for hydrogen evolution at those electrodes.

#### *1.3.4 Limitations of chloroaluminate and water-air stable ionic liquids*

Since the electrodeposition of Al is impossible to achieve from aqueous solutions, one of the main motivations to investigate ILs as alternative electrolytes was to fabricate Al deposits. Although chloroaluminate-based ILs have permitted the electrodeposition of Al, stability issues have delayed their use in practical electroplating applications.

Chloroaluminate-based ILs are known to be hygroscopic chemicals. In addition, these liquids can react with water and breakdown to form poisonous gases such as HCl as per the discussion earlier. The decomposition of these liquids imposes environmental problems as well as health and safety issues.

The limitations of working with chloroaluminate ILs have involved operational and experimental difficulties unless equipment such as glove boxes are utilised to avoid the ingress of water in the ILs.

ILs that are stable under ambient conditions were designed to overcome the operational limitations of chloroaluminate-based ILs. However, when these liquids were exposed to the atmosphere over long periods of time, they also decomposed. For this reason, in order to prevent the breakdown of ILs and obtain reproducible results, the experimental work has continued to require the use of inert atmosphere.

At the moment, the price of some ILs represent an additional constraint for practical applications purposes since they cannot compete with the well-established aqueous solutions. Due to the limitations of chloroaluminate and water/air stable ILs, a new category of ILs was introduced, namely deep eutectic solvents.

## 1.4 Deep Eutectic Solvents

### 1.4.1 Definition of deep eutectic solvents

A third category of ILs was introduced as Deep Eutectic Solvents (DESs). The name ‘eutectic solvents’ was ascribed to these materials to differentiate them from other ILs. Importantly, the term ‘deep’ was attributed to a profound depression of the melting temperature of the mixture, which will be discussed in more detail. Unlike chloroaluminate ILs, DESs do not react with water to form by-products. Due to this fact, DESs do not hydrolyse or decompose under ambient conditions. Thereby, DESs are water-tolerant and stable in the open atmosphere.

One of the objectives of the formulation of ILs has been to improve their thermal properties such as the melting point to obtain liquid materials under 100 °C. If the melting point of a mixture decreases, so does the operating temperature of a process. To reduce the melting point of ILs the scientists have scrutinised the exploitation of mixtures with low eutectic points. As shown in Fig. 1.8, the eutectic point is the temperature at which a liquid phase (L) and solid phases ( $\alpha + \beta$ ) co-exist in equilibrium achieving a eutectic composition [44, 45]. It can also be observed that the eutectic temperature is lower than the melting temperature of the individual components of the mixture [45].

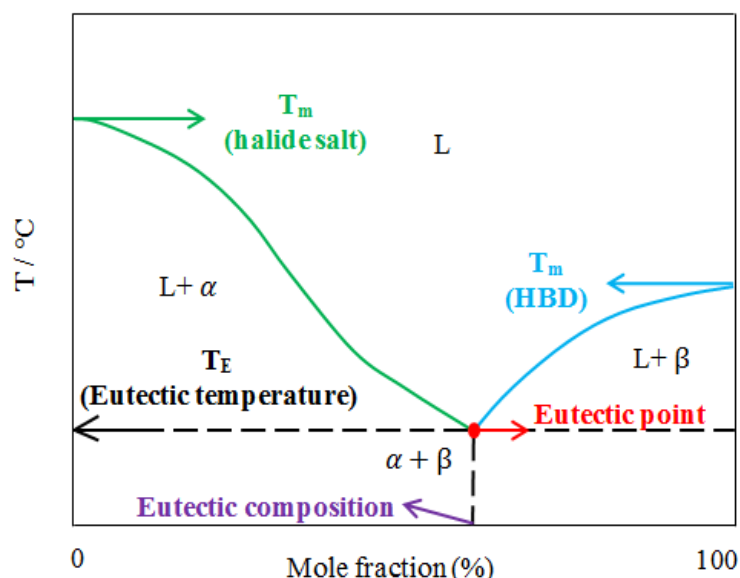


Figure 1.8 Phase diagram of a two-component system showing the eutectic point. Adapted from [45].

From thermodynamics, the eutectic point represents the lowest temperature of the melt at which both the liquid and the solid phase are at equilibrium (minimum Gibbs free energy) [45]. Below the eutectic point, the entire system is in the solid state whereas above it the liquid fraction increases with temperature. To clarify this concept, Gibbs free energy curves are shown in the phase diagram of a binary system (Fig. 1.9), whereby X and Y are the two components of the system. The green curves in Fig. 1.9 correspond to the Gibbs free energy curves of the solid phases ( $\alpha$  and  $\beta$ ) while the blue curve represents the liquid phase [45]. When the eutectic temperature is reached, all phases coexist simultaneously [45]. This is represented by the Gibbs free energy curves of the solid phases sharing the same tangent line than that of the liquid phase (cf. dotted curve in Fig. 1.9).

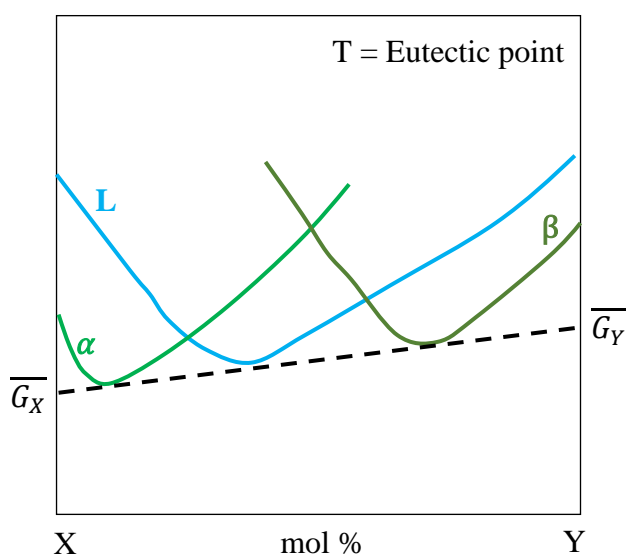


Figure 1.9 Gibbs free energy curves of a binary system when reaching the eutectic temperature. The blue curve corresponds to the liquid phase while the green curves are the solid phases. Adapted from [45].

DESs are represented by the general formula  $\text{Cat}^+\text{X}^-.z\text{Y}$  as shown in Fig. 1.10 where  $\text{Cat}^+$  is the cation,  $\text{X}^-$  is the anion (generally  $\text{Cl}^-$ ), Y refers to the hydrogen bond donor (HBD) and z is the number of molecules of the HBD that is necessary to coordinate the anion.

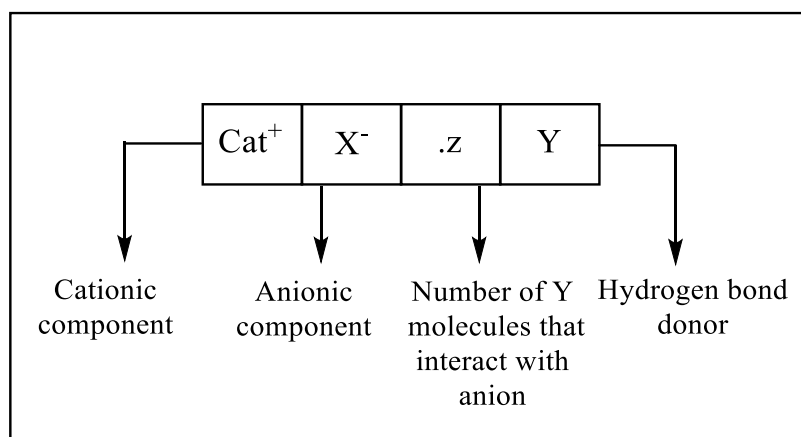


Figure 1.10 General representation of deep eutectic solvents.

Fig. 1.11 illustrates the interactions that arise during the formation of a DES. It is known that the function of the HBD (blue molecule) is to form a hydrogen bond (red dashed lines) with the halide anion ( $\text{Cl}^-$ ). Since the anionic charge of the halide salt is shielded by the HBD, the electrostatic interactions on the crystal lattice are weakened and the depression of the melting point occurs. As an example, the melting temperature of an ammonium salt-urea mixture decreased  $\Delta T=178\text{ }^\circ\text{C}$  relative to the melting point of the individual components [44]. Similarly, the melting point of an ammonium salt-oxalic acid system declined  $272\text{ }^\circ\text{C}$  relative to the melting point of the individual components [46]. The complexation reaction is also shown in equation 1.7 [47].

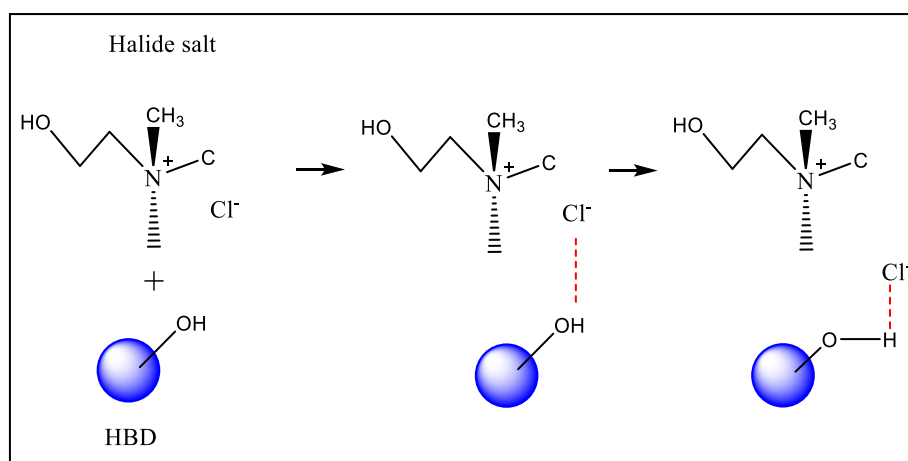
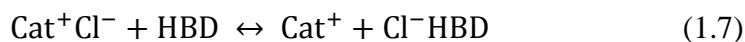


Figure 1.11 Schematic of the complexation of the anion by the HBD occurring in DESs. Adapted from [48].

There are three different classes of eutectic mixtures that fall under the DESs nomenclature. According to the complexing agent used, DESs are classified as type I, II and III eutectics as shown in Table 1. The first category of DESs was formulated from any cationic component such as pyridinium, imidazolium or ammonium mixed with anhydrous metallic salts. The second type of DESs differentiated from the first one because the metal salts possessed water bounded to their structure, and the last classification of DESs involved HBDs such as amides, carboxylic acids, and alcohols. Table 1.3 shows the classification of DESs.

Table 1.3 Categories of eutectic-based ILs according to the complexing agent used [49].

General formula of DESs	Eutectic type	Complexing agent	Example of complexing agents
$\text{Cat}^+ \text{X}^- \cdot z\text{Y}$	I	Anhydrous metal salts, $\text{Y} = \text{MCl}_a$	<ul style="list-style-type: none"> <li>• <math>\text{AuCl}_3</math></li> <li>• <math>\text{CuCl}</math></li> <li>• <math>\text{FeCl}_3</math></li> <li>• <math>\text{InCl}_3</math></li> <li>• <math>\text{SnCl}_2</math></li> <li>• <math>\text{ZnCl}_2</math></li> </ul>
	II	Hydrated metal salts, $\text{Y} = \text{MCl}_a \cdot b\text{H}_2\text{O}$	<ul style="list-style-type: none"> <li>• <math>\text{CaCl}_2 \cdot 6\text{H}_2\text{O}</math></li> <li>• <math>\text{CuCl}_2 \cdot 2\text{H}_2\text{O}</math></li> <li>• <math>\text{CoCl}_2 \cdot 6\text{H}_2\text{O}</math></li> <li>• <math>\text{CrCl}_3 \cdot 6\text{H}_2\text{O}</math></li> <li>• <math>\text{MgCl}_2 \cdot 6\text{H}_2\text{O}</math></li> </ul>
	III	Hydrogen bond donors, $\text{Y} = \text{RZ}$ , where Z: $\text{CONH}_2$ , $\text{COOH}$ , or $\text{OH}$	<ul style="list-style-type: none"> <li>• <math>\text{CH}_4\text{N}_2\text{O}</math> (urea)</li> <li>• <math>\text{C}_2\text{H}_6\text{O}_2</math> (ethylene glycol)</li> <li>• <math>\text{C}_2\text{H}_2\text{O}_4</math> (oxalic acid)</li> <li>• <math>\text{C}_3\text{H}_4\text{O}_4</math> (malonic acid)</li> <li>• <math>\text{C}_3\text{H}_8\text{O}_3</math> (glycerol)</li> </ul>

#### 1.4.2 Type I eutectics

As per discussion in the above section, the earliest DES system was known as type I eutectic and it consists on pyridinium, imidazolium or quaternary ammonium salts mixed with non-hydrated metal salts. A wide range of anhydrous salts were mixed with quaternary ammonium salts to ascertain if liquid materials could be produced either at room temperature or under 100 °C [50]. In this endeavour, more than thirty anhydrous metal salts were tested to find out if liquidus compounds could be obtained. Liquidus materials refer to compounds that are at the liquid state under 100 °C. Some of the anhydrous salts were tested; LiCl, MgCl<sub>2</sub>, AlCl<sub>3</sub>, CaCl<sub>2</sub>, CrCl<sub>3</sub>, FeCl<sub>2</sub>, CoCl<sub>2</sub>, NiCl<sub>2</sub>, and AuCl<sub>3</sub> [4]. However, those metal salts only produced solid mixtures even though the applied temperature was 200 °C [50]. On the other hand, anhydrous metal salts that formed compounds in the liquid state were SnCl<sub>2</sub> [4], ZnCl<sub>2</sub> [4], FeCl<sub>3</sub> and ZnBr<sub>2</sub> [50].

Despite the fact that these liquids were described to be hygroscopic [50], the water content attracted little attention and it was ‘removed’ while heating the system. Type I eutectics were investigated in terms of their phase behaviour, ionic complexation, thermo and physicochemical properties and electrochemical stability.

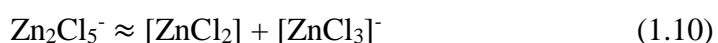
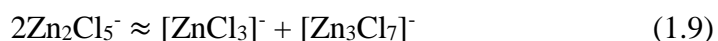
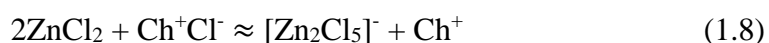
The mixtures of choline chloride with both ZnCl<sub>2</sub> and SnCl<sub>2</sub> in a 1:2 molar ratio were described to exhibit the lowest freezing point, e.g. 25 °C and 45 °C respectively [4]. Likewise, other anhydrous metals showed freezing points of 38 °C (ZnBr<sub>2</sub>) and 65 °C (FeCl<sub>3</sub>) at the same molar composition [50]. It was clarified that the ability of these anhydrous metal salts to form ‘liquidus materials’ relied on their melting temperatures. To exemplify, ZnCl<sub>2</sub> salt has a melting point of 283 °C which is significantly lower than the melting temperature of NiCl<sub>2</sub> salt, e.g. 1001 °C. Table 1.4 lists some of the anhydrous metal salts that were capable to form type I eutectic mixtures and their melting points.



Table 1.4 Type I eutectic mixtures formed with ChCl and anhydrous metal salts [4, 50].

Eutectic system	Melting point of the metal salt (°C)	Anionic complexes
ChCl: 2ZnCl <sub>2</sub>	283	[Zn <sub>2</sub> Cl <sub>5</sub> ] <sup>-</sup> [ZnCl <sub>3</sub> ] <sup>-</sup> [Zn <sub>3</sub> Cl <sub>7</sub> ] <sup>-</sup>
ChCl: 2SnCl <sub>2</sub>	246	[SnCl <sub>3</sub> ] <sup>-</sup> [Sn <sub>2</sub> Cl <sub>5</sub> ] <sup>-</sup>
ChCl: 2FeCl <sub>3</sub>	306	[FeCl <sub>4</sub> ] <sup>-</sup>
ChCl: 2ZnBr <sub>2</sub>	394	[Zn <sub>2</sub> Br <sub>4</sub> Cl] <sup>-</sup>

Using techniques such as Nuclear Magnetic Resonance (NMR) spectroscopy and ion Fast Atom Bombardment Mass-Spectrometry (FAB-MS), a variety of complexes in the eutectic systems were revealed [50]. The anionic species for each eutectic system are listed in Table 1.4. Based on the speciation data, Abbott and colleagues described the reactions that occurred during the formation of the ChCl: 2ZnCl<sub>2</sub> liquid. The reactions are shown in equations 1.8, 1.9 and 1.10.



The potential of the cell was measured as a function of the ZnCl<sub>2</sub> concentration and calculated via the Nernst equation. It was observed that below the 0.63 mole fraction of ZnCl<sub>2</sub>, the experimental cell potential diverged from the calculated one (cf. Fig. 1.12). Apparently, this divergence occurred due to the reduction of the metal concentration in the melt. Since the properties of this liquid were considered to be composition-dependent, they were thereafter investigated.

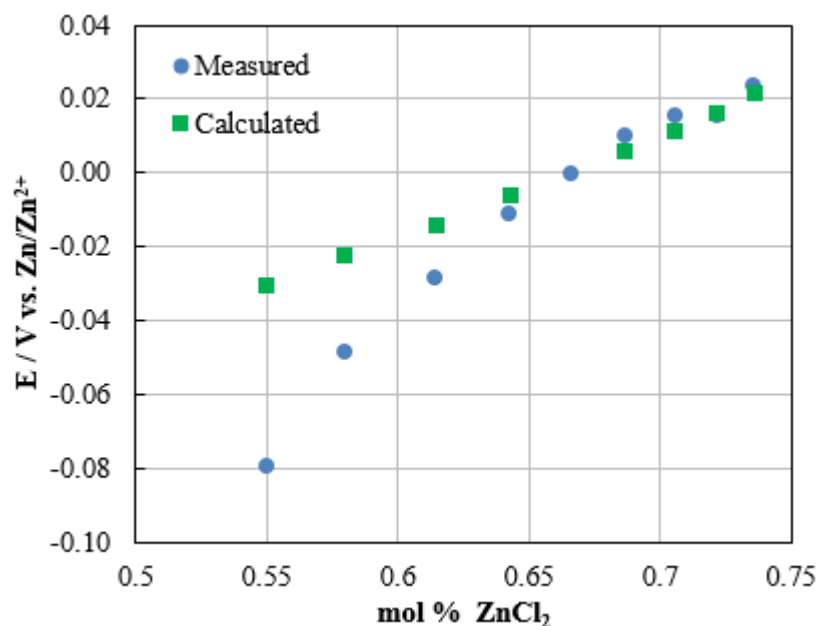


Figure 1.12 Cell potential measurement of the ChCl: 2ZnCl<sub>2</sub> system at 60 °C.

The viscosity of the ChCl: 2ZnCl<sub>2</sub> liquid was measured as a function of temperature and the experimental findings showed that the viscosity of the system ChCl: 2ZnCl<sub>2</sub> was high, e.g. ~7500 mPa s at room temperature. Upon heating up to 90 °C, the viscosity was measured to be ~500 mPa s. It was therefore showed that the viscosity of the type I eutectic mixtures was much greater than the chloroaluminate-based ILs [51].

Also, the EW of the liquids ChCl: 2ZnCl<sub>2</sub> and ChCl: 2SnCl<sub>2</sub> and ChCl: 2FeCl<sub>3</sub> was quantified. It was measured that the largest potential window was offered by the ChCl: 2ZnCl<sub>2</sub> (2.0 V) liquid followed by ChCl: 2SnCl<sub>2</sub> (1.5 V) and ChCl: 2FeCl<sub>3</sub> (0.5 V) [4]. Importantly, chlorine evolution was reported to occur and the cathodic potential was restricted by Sn or Zn deposition [4]. In the case of the ChCl: 2FeCl<sub>3</sub> liquid, the reduction of Fe<sup>3+</sup> to Fe<sup>2+</sup> restricted the cathodic limit [4].

Due to the fact that a limited number of anhydrous metal salts formed DESs, hydrated metal salts were subsequently tested as HBDs.

### 1.4.3 Type II eutectics

Hydrated metallic salts exhibited lower melting points than anhydrous metal salts, as shown in Table 1.4 earlier. This phenomenon occurs because the waters of hydration yielded different crystal structures. For example, the melting temperature of  $\text{CuCl}_2 \cdot 6\text{H}_2\text{O}$  is  $100\text{ }^\circ\text{C}$ , which is much lower than the melting point of the anhydrous salt  $\text{CuCl}_2$ , e.g.  $480\text{ }^\circ\text{C}$ . Due to this fact, the lattice energy of hydrated metal salts tends to be lower than the one of anhydrous chemicals. The presence of moisture in DESs formulated from hydrated salts is unavoidable due to their waters of hydration. Table 1.5 summarises few examples of hydrated salts and their intrinsic melting points.

Table 1.5 Melting point of hydrated metal salts that formed type II eutectics with  $\text{ChCl}$ .

<b>Metal salt</b>	<b>Melting point (<math>^\circ\text{C}</math>)</b>
$\text{CrCl}_3 \cdot 6\text{H}_2\text{O}$	83
$\text{CoCl}_2 \cdot 6\text{H}_2\text{O}$	86
$\text{LaCl}_3 \cdot 6\text{H}_2\text{O}$	91
$\text{CuCl}_2 \cdot 2\text{H}_2\text{O}$	100
$\text{MgCl}_2 \cdot 6\text{H}_2\text{O}$	117

The  $\text{ChCl} : 2\text{CrCl}_3 \cdot 6\text{H}_2\text{O}$  liquids has been explored by Abbot *et al.* [52]. Perhaps the most interesting finding was the hygroscopicity of this liquid. For example, this mixture was reported to adsorb 10 wt% of water at room temperature. The removal of water was studied using thermo-gravimetric analysis; it was found that water molecules were evaporated via two steps. For example, when temperature reached  $85^\circ\text{C}$  three molecules of water per metal was measured to be evaporated; subsequently, the three remaining water molecules were removed at  $180\text{ }^\circ\text{C}$ . Although this analysis demonstrated that waters of hydration were strongly coordinated, few further electrodeposition studies were performed from this type of DES. This lack of interest was the result of previous experiences using chloroaluminate-based ILs, whereby the inclusion of water drastically diminished the EW of the solvent [3].

#### 1.4.4 Type III eutectics

The last category of DESs is known as the type III eutectics. This group forms when the halide anion is complexed by the HBD such as polyamides, polycarboxylic acids or polyalcohols [46]. Amongst these cations, the quaternary ammonium salt choline chloride or 2-hydroxy-ethyl-trimethylammonium chloride ( $C_5H_{14}NOCl$ ) has been the preferred source of cations for the following reasons: (i) choline chloride (ChCl) is a more benign substance classified as a provitamin, (ii) it is manufactured at large scale thereby it is commercially available at a reasonable cost when compared with other starting materials of ILs, and (iii) its preparation involves only mixing and gentle heating. ChCl is synthesised via two step mechanism as shown in Fig. 1.13. Also, the chemical structure of choline chloride is shown in Fig. 1.14.

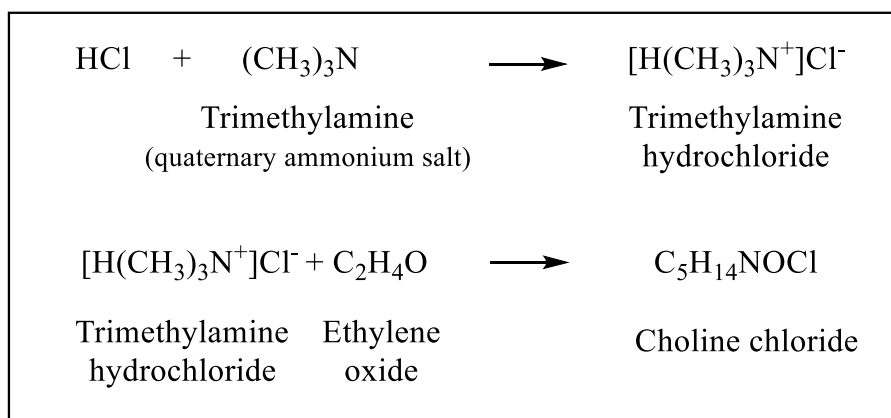


Figure 1.13 Synthesis of choline chloride. Adapted from [53].

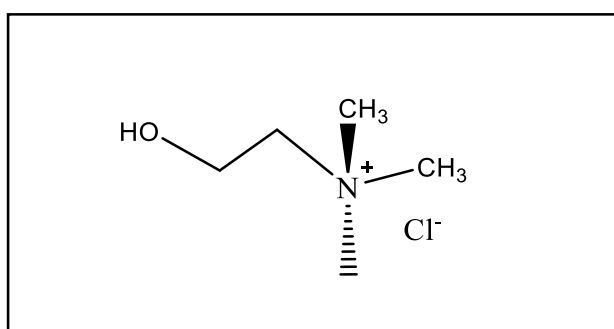


Figure 1.14 Structure of choline chloride.

DESs prepared from HBDs are capable of dissolving a wide range of metals species and metal oxides [5]. It is known that when the HBD is an alcohol, the eutectic mixture exhibits the highest conductivity and the lowest viscosity amongst other DESs, which will be discussed in detail in the upcoming section. Due to this reason, this study focuses on ‘ethaline’. Ethaline is a DES prepared by mixing ChCl with ethylene glycol ( $C_2H_6O_2$ ) in a 1:2 molar ratio. This molar composition has achieved the lowest possible eutectic point for the mixture [54]. The complex that ChCl and ethylene glycol forms is shown in Fig. 1.15.

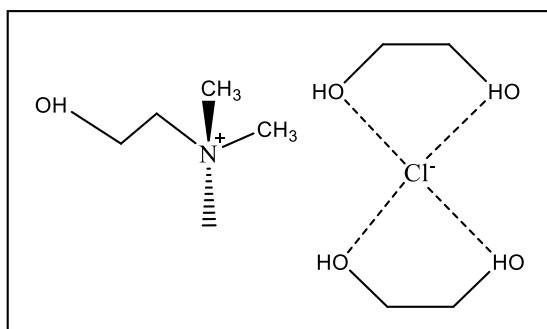
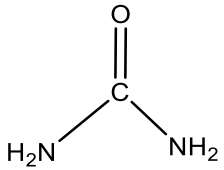
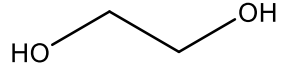
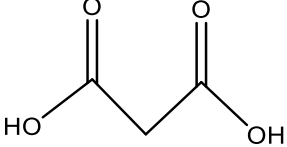
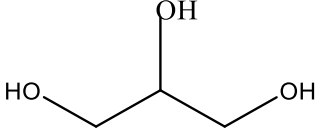
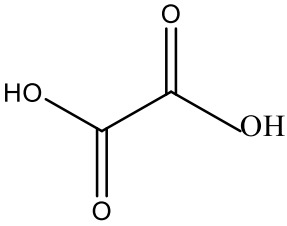
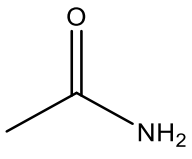
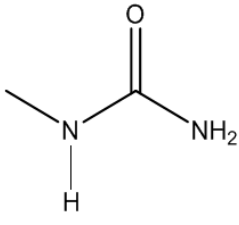
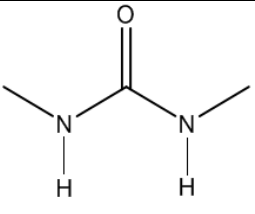
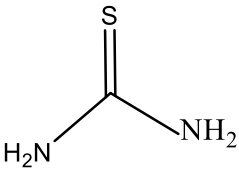
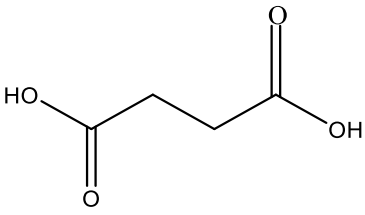
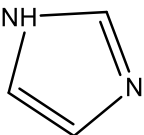
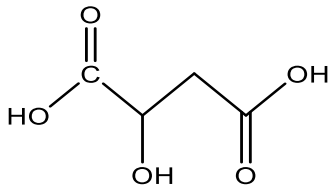
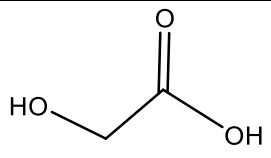

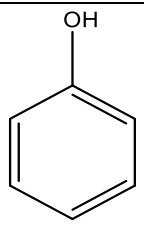


Figure 1.15 Formation of the DES ethaline (ChCl: 2 EG). Adapted from [55].

The name of DESs formulated from ChCl and HBDs depends on the type of HBD used to prepare the liquid and there is no rule or convention to follow. For example, ethaline is the trivial name of the DES derived from ChCl and ethylene glycol. Reline is another example; this is formulated from ChCl and urea. Table 1.6 lists the most common HBDs used to prepare DESs. The term in parenthesis refers to the trivial name (when defined) of some DESs formed between ChCl and HBDs.

Table 1.6 Common HBDs used to formulate DESs with ChCl.

Hydrogen bond donor name	Chemical formula	HBD structure
<b>Urea</b> (reline)	(CH <sub>4</sub> N <sub>2</sub> O)	
<b>Ethylene glycol</b> (ethaline)	(C <sub>2</sub> H <sub>6</sub> O <sub>2</sub> )	
<b>Malonic acid</b> (maline)	(C <sub>3</sub> H <sub>4</sub> O <sub>4</sub> )	
<b>Glycerol</b> (glyceline)	(C <sub>3</sub> H <sub>8</sub> O <sub>3</sub> )	
<b>Oxalic acid</b> (oxaline)	(C <sub>2</sub> H <sub>2</sub> O <sub>4</sub> )	
<b>Acetamide</b>	(C <sub>2</sub> H <sub>5</sub> NO)	
<b>1-methyl urea</b>	(C <sub>2</sub> H <sub>6</sub> N <sub>2</sub> O)	
<b>1,3-dimethyl urea</b>	(C <sub>3</sub> H <sub>8</sub> N <sub>2</sub> O)	

<b>Thiourea</b>	(CH <sub>4</sub> N <sub>2</sub> S)	
<b>Succinic acid</b>	(C <sub>4</sub> H <sub>6</sub> O <sub>4</sub> )	
<b>Imidazole</b>	(C <sub>3</sub> H <sub>4</sub> N <sub>2</sub> )	
<b>Malic acid</b>	(C <sub>4</sub> H <sub>6</sub> O <sub>5</sub> )	
<b>Glycolic acid</b>	(C <sub>2</sub> H <sub>4</sub> O <sub>3</sub> )	
<b>Glutaric acid</b>	(C <sub>5</sub> H <sub>8</sub> O <sub>4</sub> )	
<b>Phenol</b>	(C <sub>6</sub> H <sub>5</sub> OH)	

## 1.4.5 Physico-chemical properties

### 1.4.5.1 Density

The density of DESs has been found to be structure-dependent [5, 56-61]. Since DESs are formed by halide salts and HBDs, the density can change according to the type of halide salt and HBD used in the preparation of the liquid [56, 57]. The effect on density when using different HBDs has been studied while sharing ChCl as the halide salt. Due to their distinctive molecular characteristics, HBDs such as amines, carboxylic acids, alcohol, phenols and others have been examined to elucidate the relationship between the molecular structure and the density. The molecular structure of some HBDs has been already shown in Table 1.6.

The density of DESs formed with HBDs included in Table 1.7 has been measured to decrease in the following order: amines [62] > carboxylic acids [63] > amides [64] alcohols > phenols [60]. The density change has been ascribed to the distinct functional groups, which exist in each molecular structure, to form either weak or strong hydrogen bond interaction [57, 65]. For instance, NH<sub>2</sub> groups can easily link to ions through hydrogen bonding (Cl<sup>-</sup>⋯H–N–H⋯Cl<sup>-</sup>) whereas other groups such as methyl exhibit hydrogen bonding interactions to a lesser extent [49]. Greater hydrogen bonding between the anion of the halide salt and the HBD can cause closer packing of molecules and therefore the density of the solvent increased [66].

Table 1.7 Density of DESs formed with ChCl and different HBDs at 25 °C.

<b>HBD</b>	<b>Density (g cm<sup>-3</sup>)</b>	<b>Ref.</b>
Phenol	1.09	[60]
Ethylene glycol	1.14	[67]
Glutaric acid	1.15	[63]
Glycerol	1.16	[68]
Urea	1.18	[64]
Trifluoroacetamide	1.23	[62]
Malonic acid	1.24	[63]
Oxalic acid	1.27	[63]
Ethanolamine	1.31	[62]



The DES formed with ethanolamine ( $1.31 \text{ g cm}^{-3}$ ) exhibited one of the highest densities amongst the HBDs shown in Table 1.7. This high density was attributed to the fact that ethanolamine include  $\text{NH}_2$  groups on their structure (cf. Fig.1.16) which lead to a dense hydrogen bond network [49] or a more ‘compact’ intermolecular organisation. The contrary effect was observed when phenol was the HBD [60]. For example, when phenol includes a single hydroxyl group, a low density was obtained, (e.g.  $1.09 \text{ g cm}^{-3}$ ) [60]. This was attributed to a less hydrogen bonding due to the aromatic structure of phenol [66].

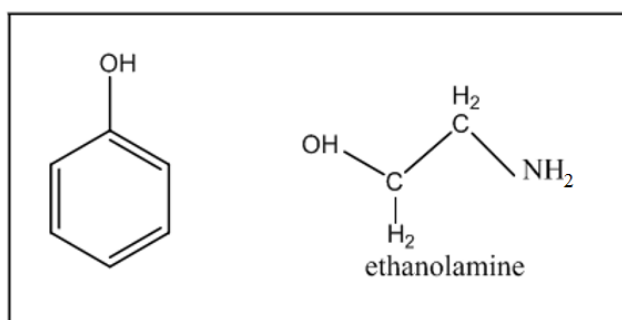


Figure 1.16 Chemical structures of ethanolamine and phenol acting as HBDs.

The influence of different HBDs on density have been assessed not only using  $\text{ChCl}$  as the halide salt but also a phosphonium-based salt [69]. For instance, Kareem *et al.* measured the density of the liquids formed between the halide salt methyltriphenylphosphonium bromide (MTPBr) and ethylene glycol, glycerol and trifluoroacetamide. It was found that the density of the liquid formed with amides was higher ( $1.40 \text{ g cm}^{-3}$ ) than the one formed with alcohols ( $1.23 \text{ g cm}^{-3}$ ). In addition, the density of the DESs formed with MTPBr was higher than the one formed with  $\text{ChCl}$  which was attributed to the bulkier structure of the halide salt (cf. Fig. 1.17).

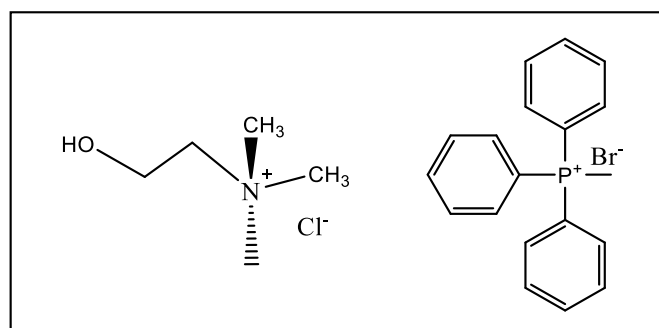


Figure 1.17 Structure of halide salts  $\text{ChCl}$  (left) and methyltriphenylphosphonium bromide (right).

The effect of increasing carbon chain length on DESs density was also investigated using carboxylic acids as HBDs. In that study, oxalic, malonic and glutaric acid were used, and the structure of these molecules is shown in Fig. 1.18. Density was reported to increase (glutaric < malonic < oxalic) as the chain length was shortened which was ascribed to steric effects. Steric effects occur when atoms within the same molecular structure are forced to share the same physical space. The occupancy of the same space causes an “overlapping of electron clouds” which influences the accommodation of the molecules. In other words, due to a steric hindrance, shorter carbon chains of carboxylic acids brought about a more compact arrangement of the molecules which lead to denser DESs.

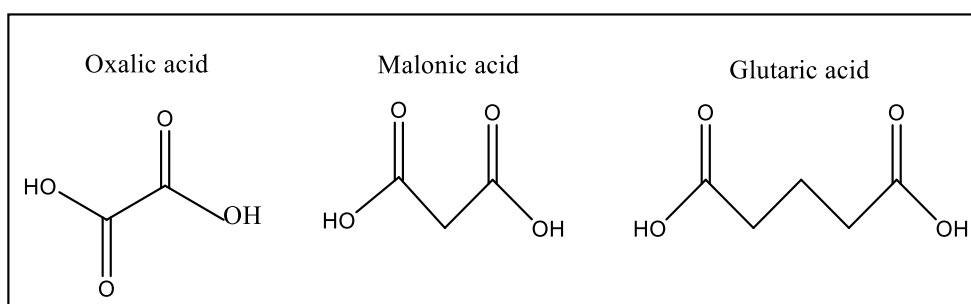


Figure 1.18 Chemical structures of HBDs such as ethylene glycol, malonic acid and glutaric acid.

However, in some cases, such as when using alcohols as HBDs, the density of DESs has been reported to be greater as the number of the hydroxyl group increased in the alcohol structure [68, 70]. For example, the density of the DES formed from glycerol (Gly) was greater than the one using ethylene glycol (EG) [70]. Due to the fact that EG contains two hydroxyl ions whereas glycerol (Gly) possesses three hydroxyl groups as shown in Fig. 1.19, the difference in density was explained by the formation of a dense three-dimensional hydrogen bond network with Gly rather than a two-dimensional structure with EG [70].

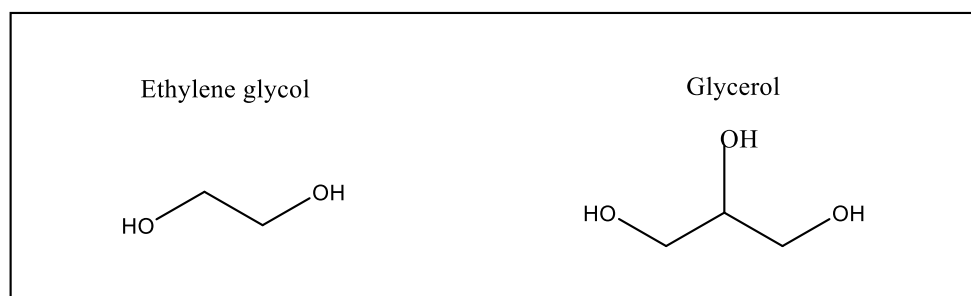
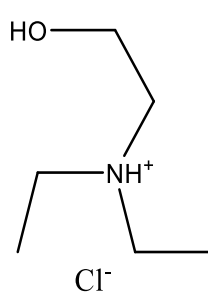
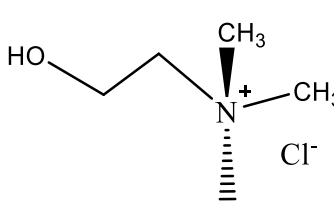
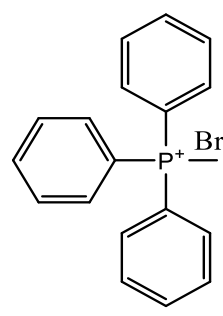


Figure 1.19 Chemical structures of HBDs such as ethylene glycol and glycerol.

Until now, density has been closely related to several factors dictated by the structure of constituting compounds such as: (i) the type of functional groups that each HBD possesses, (ii) the ability of those functional groups to form hydrogen bond, (iii) the length of the carbon chains of HBDs, (iv) the subsequent steric effects and (v) the ability of the hydroxyl groups to form dimensional or three-dimensional hydrogen bond structures.

The density of DESs can be controlled by two other factors. These factors are the type of halide salts used to form the eutectics while sharing the same HBD and the mole fraction of the halide salt to the HBD. Firstly, the type of halide salt used while sharing the same HBD has been evaluated. Shahbaz *et al.* used Gly as the HBD combined with three different halide salts such as choline chloride, N,N diethylenethanol ammonium chloride (DACl) and methyltriphenylphosphonium bromide (MTPBr) (cf. Table 1.8) [68]. The mole fraction of the salt to the HBD was constant throughout the study (0.33:0.67) and density was found to increase in the following order: DACl < ChCl < MTPBr [68]. It was clear that a salt containing the bromide ion leads to DESs of higher density than the ones formulated with chloride ions. This greater density may be the result of a larger ionic radius of the Br<sup>-</sup> ion (0.196 nm) when compared with the ionic radius of the Cl<sup>-</sup> (0.181 nm) [71].

Table 1.8 Chemical structures of three halide salts that form DESs and their density values. Adapted from [68].

HBD	Halide salts		
Gly	<p>DACl</p>  <p>Cl<sup>-</sup></p>	<p>ChCl</p>  <p>Cl<sup>-</sup></p>	<p>MtPBr</p>  <p>Br<sup>-</sup></p>
Density (g cm <sup>-3</sup> )	1.1731	1.1920	1.3064

Secondly, the influence of increasing the mole ratio of the HBD while maintaining the same halide salt has been evaluated. Guo *et al.* used ChCl as the halide salt and changed the concentration of phenol (the HBD) [60]. As the concentration of phenol rose, the density of the DES decreased. For example, while the density of ChCl:2 phenol was measured as  $1.0967 \text{ g cm}^{-3}$ , the density of ChCl:6 phenol decreased to  $1.0852 \text{ g cm}^{-3}$  [60]. The reduction on density was attributed to a weaker Coulombic attraction between the ions which was triggered by the nature of phenol but no further explanation was provided [60].

By contrast, an increased molar fraction of Gly (as the HBD) combined with N,N diethylenethanol ammonium chloride (DACl) produced a greater density of the DES which was ascribed to the high density of Gly itself, e.g.  $1.2610 \text{ g cm}^{-3}$  [68]. Likewise, Gly added to tetrabutylammonium bromide (TBABr) in a mole fraction ranging from 0.67 to 0.85, produced an increment of the density of the DESs [61]. In this study the density was correlated to the way that the molecules wrap together. It was proposed that the manner in which the HBD ‘wraps around the anion’ altered the packing of the molecules, which corresponds to steric effects as discussed earlier [61].

#### 1.4.5.2 Viscosity

Some of the disadvantages of DESs relate to their physicochemical properties such as viscosity and conductivity. In order to understand these properties, it is necessary to recall a basic difference between molten salts and room temperature ionic liquids (RTILs) upon fusion. When molten salts and ILs melt, the formation of empty spaces occur wherein the ions can move into (Fig. 1.20) [72]. Thereby, the fundamental difference between molten salts and RTILs upon fusion is the average size of the voids in these liquids [73].

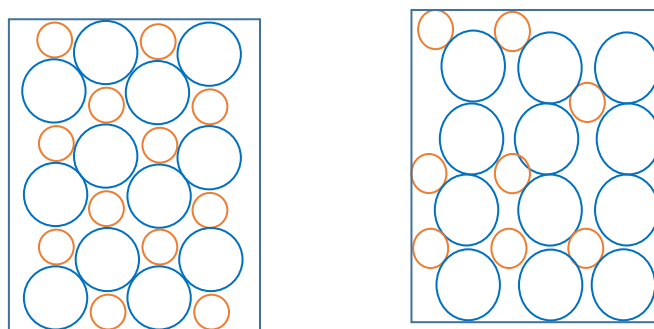


Figure 1.20 Schematic of the molten salts before (left) and after (right) fusion.  
Adapted from [73].

In molten salts, the size of the voids range from 1.5 to 2.5 Å and the dimensions of the ions vary between 1.0 and 2.6 Å [73]. The fact that the voids have a similar size of the ions allows the ions to move through the vacancies of the molten salt. By contrast, because RTILs and DESs possess ionic species with large radii, e.g. ~ 3-4 Å and smaller voids, e.g. ~ 2 Å [29], the ionic motion may be hindered [72]. To exemplify, the average viscosity of the alkyimidazolium molten salts is 14.9 mPa s at 25 °C [74] while the average viscosity of ILs is an order of magnitude higher than that, e.g. 174.5 mPa s [35, 36]. This section summarises the most important models and theories originally developed for molten salts and ILs in order to comprehend ionic motion in DESs.

There are two models that were proposed for molten salts. The models are the vacancy and the hole model. The “vacancy or quasi-lattice model” exhibit voids named as Schottky defects which emerge when ions are detached from the ionic lattice and the volume increases upon fusion. Fig. 1.21 shows the schematic of the vacancy model.

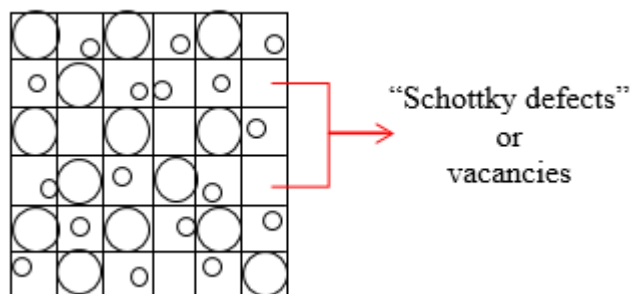


Figure 1.21 Vacancy model or quasi-lattice model showing Schottky defects.  
Adapted from [75].

Fürth proposed the so-called “hole model” which considered that holes are of random size and position that resemble a Swiss cheese [76]. Later, Bockris and Reddy explained the development of the holes as the ejection of the ions from a lattice site [73]. In addition, the size of the holes is associated to the degree of displacement of the ions that occurs due to thermal variation in the local density in the liquid [73]. Besides, not only the size of the holes is random also their location [73]. Fig. 1.22 is an illustration of the emergence of the holes in the liquid. The randomness of the position of the hole arises because thermal variations can occur anywhere [73]. In this line, since holes are not stagnant, they can be conceived as vacancies that are emerging, vanishing and shrinking constantly.

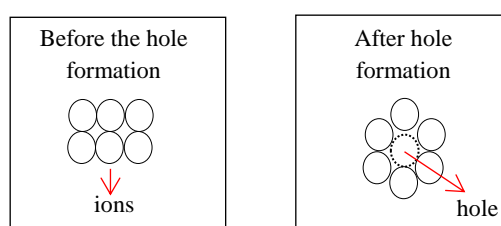


Figure 1.22 Formation of holes in molten salts. Adapted from [73].

The origin of the holes has been explained in molten salts via equation 1.11 which was derived from statistical thermodynamics [73]. This equation correlates the radius of the average hole with the surface tension of the fluid.

$$4\pi r^2 = \frac{3.5kT}{\gamma} \quad (1.11)$$

where  $r$  is the average size of the hole,  $k$  is the Boltzmann constant,  $T$  is the absolute temperature, and  $\gamma$  is the surface tension of the liquid.

Later, the hole model has been used to explain quantitatively the fluid properties of molten salts [73, 76, 77]. This model breaks down when ionic association affected the ionic activity in molten salts [77]. However, in ILs the holes are so small that ionic association can be ignored since the mobility of the ions is minimal [78]. In order to model viscosity in DESs, Abbott has assumed that: (i) there are no thermodynamic restrictions in the formation of the holes because voids merely

exist in the liquid, and (ii) the direction in which the holes travel is contrary to the one of the solvent molecules and ions [79].

Considering these two assumptions, equation 1.12 was determined to account for the probability of finding an empty space of a proper size in which an ion can move or jump on [73].

$$Pdr = \frac{16}{15\sqrt{\pi}} a^{7/2} r^6 e^{-ar^2} dr \quad (1.12)$$

where  $a = 4\pi r/kT$  and  $P$  is the probability of finding a hole of radius  $r$  greater than the average radius of the solvent molecule,  $R_{+/-}$ . In this regard, Abbott has established that the viscosity of ILs is related to the probability of finding a void with an average radius larger than the dimension of the ions, i.e.  $[P(r > R_{+/-})]$  [79]. By plotting the fluidity of ILs based on discrete or hydrophobic anions ( $[BMIM]^+[PF_6]^-$ ) against of the  $(P(r > R_{+/-}))$ , a linear correlation was obtained and this correspondence is shown in Fig. 1.23 [79].

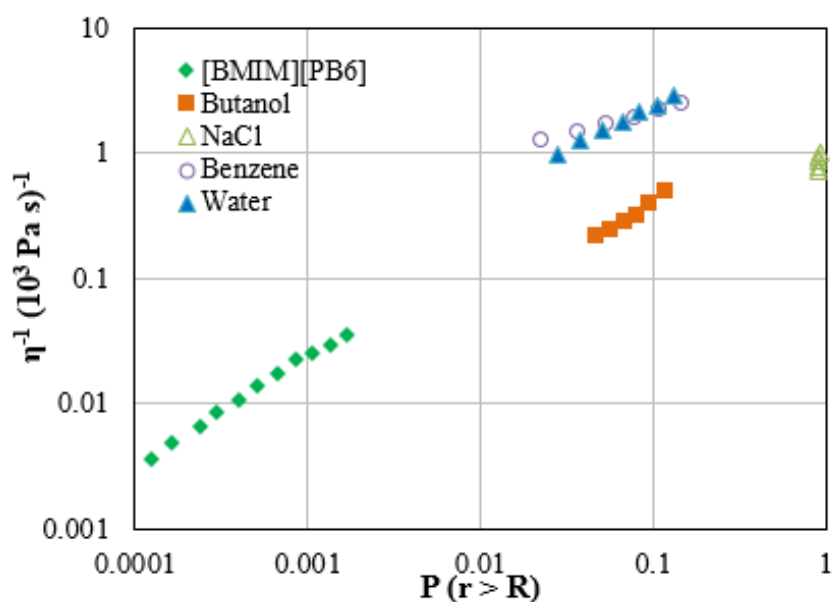


Figure 1.23 Fluidity of liquids as a function of the probability  $[P(r < R)]$  of finding holes of suitable sizes for an ion to move in for  $[BMIM]^+[PF_6]^-$ , NaCl,  $H_2O$ , benzene and butanol. Adapted from [79].

Considering that viscosity of ILs was associated to the probability of the location of a vacancy and that the formation of voids was not limited thermodynamically, the viscosity of ILs was modelled as it behaves like an ideal gas but restricted in motion [79], as equation 1.13 shows.

$$\eta = \frac{M\bar{c}/2.12\sigma}{P(r>R)} \quad (1.13)$$

where  $\eta$  is viscosity,  $M$  is the molecular mass of the IL,  $\bar{c}$  is the average speed of the molecule and  $\sigma$  is the collision diameter of the molecule [79].

At the moment, hole theory was proven to be valid for water-air stable ILs [79]. Nevertheless, in order to prove that hole theory was also applicable to DESs, it was necessary to identify which anionic species was movable. For this purpose, Abbott *et al.* used two eutectic mixtures based on halide salts such ChCl and ethylammonium chloride mixed with amides [80]. In that study, experimental viscosity of the DESs was measured and the results were compared with the viscosity calculated from equation 1.13. On one hand, when the anion ( $\text{Cl}^-$ ) was assumed to move with the amides, poor agreement between experimental and calculated viscosity was obtained [80]. On the other hand, while the ion was supposed to travel freely, a reasonable agreement ensued. This study was the first to determine that hole theory can also be applied to DESs and that  $\text{Cl}^-$  did not move with the HBD.

The viscosity of DESs formed with carboxylic acids as HBDs was also studied. It was reported that viscosity of the liquid was affected by the structure of the carboxylic acid [46]. Viscosity amongst different carboxylic acids was found to increase in the order: phenylpropionic < malonic < oxalic < succinic acid [46]. Viscosity was also affected by the molar ratio of the HBD to the halide salt [46]. For example, the ChCl: oxalic acid liquid was tested to determine the influence of the concentration of the carboxylic acid. Fig. 1.24 demonstrates that the higher the mole fraction of the carboxylic acid in the melt (only when mol % of oxalic acid > 50%), the greater the viscosity of the DES.



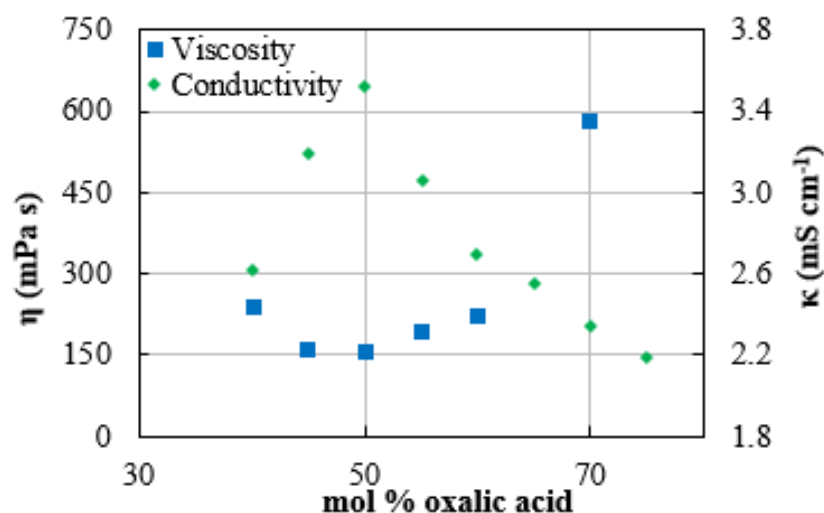


Figure 1.24 Conductivity and viscosity as a function of the mole composition of the oxalic acid in choline chloride. Adapted from [46].

Although viscosity was controlled by the chemical structure and the mole fraction (halide: HBD), the type of salt involved in the DES could not be overlooked. Alomar *et al.* has reported that DESs based on ammonium salts exhibited lower viscosity than DESs based on phosphonium salts [81] for which Garcia *et al.* has suggested that less viscous DESs may be due to larger holes in the liquid [57]. However, surface tension data of DESs, which is scarce, would be necessary to calculate the dimension of the holes in DESs based on ammonium and phosphonium salts.

It has been proposed that the energy for activation of viscous flow ( $E_\eta$ ) of ILs was associated with the ion to hole radius ratio. In order to prove it, the energy for activation of viscous flow of a number of ILs was plotted against the ion to hole ratio. The size of the voids was calculated using equation 1.11 and the size of the ions was computed as the mean of the cation and anion radii. Fig. 1.25 shows that  $E_\eta$  for ILs is high (cf. red circle in Fig 1.25). This large  $E_\eta$  was an indicative of the high energy necessary to form the empty vacancies in ILs. Since the probability of finding a hole is in the order of  $10^{-4}$  to  $10^{-7}$ , the ionic motion is more difficult in ILs [79].

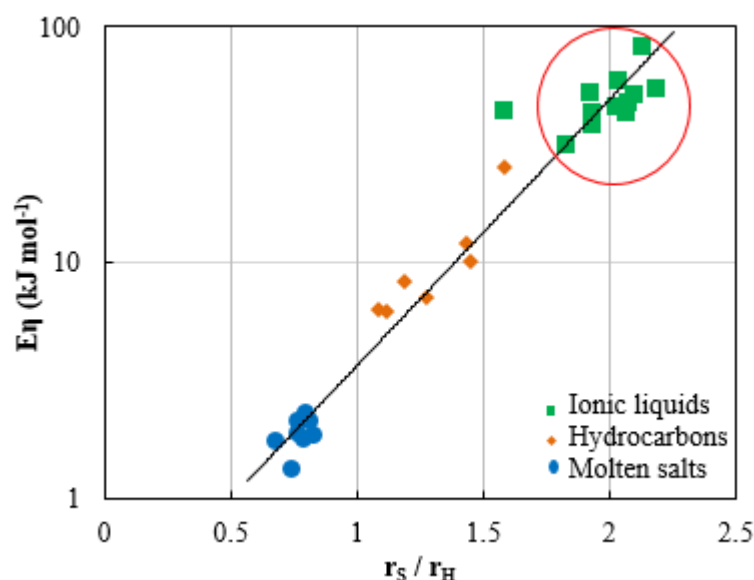


Figure 1.25 Energy for activation of viscous flow as a function of solvent to hole radius ratio. Adapted from [46].

#### 1.4.5.3 Conductivity

One of the first attempts to understand conductivity in non-aqueous solutions was the development of the Fuoss Krauss theory [82], in which the molar conductivity ( $\Lambda$ ) of concentrated quaternary ammonium electrolytes was modelled [82], as shown in equation 1.14.

$$\frac{\Lambda\sqrt{C}}{\Lambda^0} = \sqrt{K_p} + \frac{2c\sqrt{K_p}}{3K_t} \quad (1.14)$$

where  $\Lambda$  is the molar conductivity,  $\Lambda^0$  is the limiting molar conductivity of an electrolyte,  $K_p$  and  $K_t$  are the equilibrium constants for single and triple ion pair dissociation respectively and  $C$  is the bulk concentration of species.

However, obtaining the limiting molar conductivity of concentrated non-aqueous solutions was problematic. For this reason, Walden introduced an empirical correlation between viscosity ( $\eta$ ) and the limiting molar conductivity in room temperature systems [83], as shown in equation 1.15. Additionally, Stokes introduced a decoupling parameter ( $\alpha$ ), which depends on ionic size [84]. The modified equation included the additional  $\alpha$  factor as per equation 1.16 [85]. Walden

correlation is applicable if the ions are at infinite dilution and the ionic interactions can be neglected [83]. However, in ILs the ions are not at infinite dilution and thereby, the empirical Walden correlation may not always be valid.

$$\Lambda_m^o \eta = \text{constant} \quad (1.15)$$

$$(\Lambda_m^o \eta)^\alpha = \text{constant} \quad (1.16)$$

Another approach to obtain an expression of conductivity for ILs at ambient temperature was introduced by Bonhôte *et al.* [37]. The authors used a modified Stokes-Einstein equation [86] to derive a conductivity relationship as shown in equation 1.17.

$$\kappa = \frac{yF^2\rho}{(6\pi N_A M \eta)} [(\xi_+ R_+)^{-1} + (\xi_- R_-)^{-1}] \quad (1.17)$$

where  $y$  is the degree of dissociation,  $F$  is the Faraday constant,  $\rho$  is the density,  $N_A$  is the Avogadro constant,  $M$  is the molar mass of the IL,  $\eta$  is the viscosity,  $\xi_+$  and  $\xi_-$  are correction parameters to account for interactions among ions (which should be obtained for each system), and  $R_+$  and  $R_-$  are the radii of the cation and the anion. However, the main limitation of this model was the inability to determine the correction parameter  $\xi$ . Therefore, this model was not very popular.

More recently, hole theory states that there is a low probability of finding an empty vacancy with a dimension greater than the radius of the ion or solvent molecules for an ion to transfer into [76]. In this regard, Abbott has demonstrated that as a consequence of hole theory, the charge transport in DESs is not limited by the density of charge carriers but governed by the density of the holes [79].

In order to model conductivity, holes are assumed to be at infinite dilution because the probability of finding cavities of suitable dimensions is low as discussed earlier [79]. Stokes-Einstein equation describes the individual migration of the holes in equation 1.18.

$$\lambda_+ = \frac{z^2 F e}{6\pi\eta R_+} \quad (1.18)$$

where  $z$  is the charge on the ion,  $F$  is Faraday constant,  $e$  is the electronic charge, and  $R_+$  is the ionic radius. Since the molar conductivity is given by equation 1.19.

$$\Lambda = \lambda_+ + \lambda_- \quad (1.19)$$

Inserting equation 1.18 in equation 1.19, a relationship for conductivity was derived as shown in equation 1.20 [87].

$$\kappa = \frac{z^2 F e \rho}{6 \pi \eta M} (R_+^{-1} + R_-^{-1}) \quad (1.20)$$

The validity of equation 1.20 was evaluated by plotting the measured and the calculated conductivity data [87]. To construct this plot, cations such as imidazolium, pyridinium, quaternary ammonium and sulfonium were mixed with anions as triflamide, methane sulfonate, trifluoroacetate and others [87]. Since experimental and calculated data showed some agreement, it was established that the model based on holes can predict the conductivity of ILs [87].

In order to evaluate if equation 1.20 is valid for DESs, Abbott *et al.* has tested halide salts as ethylammonium chloride ( $\text{EtNH}_3\text{Cl}$ ), acetyl choline chloride ( $\text{AcChCl}$ ) and  $\text{ChCl}$  mixed with different HBDs such as trifluoroacetamide ( $\text{CF}_3\text{CONH}_2$ ) and urea [80]. The results demonstrated a broad correlation between the calculated conductivity (using equation 1.20) and experimental conductivity existed. To exemplify, the conductivity of the DES  $\text{AcChCl}$ : urea was measured as  $0.017 \text{ mS cm}^{-1}$  while the calculated one was  $0.008 \text{ mS cm}^{-1}$  [80]. At the moment, hole theory is the accepted model to explain the conductivity of DESs.

#### 1.4.6 Electrochemical properties

##### 1.4.6.1 Electrochemical window

The electrochemical window (EW) plays an essential role in electrochemical deposition because it is the potential range wherein the solvent is stable. Stability means that electrochemical reactions involving the solvent or ionic liquid do not occur within a potential range.

Costa *et al.* studied the electrochemical window of DESs formed with ChCl and four different HBDs such as ethylene glycol, propylene glycol, trimethylene glycol and urea, as Fig. 1.26 shows [88]. All potential sweeps were performed using an Hg electrode, with Ag wire as the reference electrode and glassy carbon as the counter electrode [88]. The voltammetric data were recorded using a scan rate of  $50 \text{ mV s}^{-1}$  and at different temperatures. Within the potential window, the voltammograms did not exhibit current peaks which was an indication that charge transfer processes involving the solvent did not occur [88]. The only exception was reline (ChCl: urea) due to the appearance of two peaks near 0 V vs. RE which was attributed to the formation of a film at the Hg working electrode [88]. The study revealed that the largest EW was attained with propylene glycol followed by ethylene glycol, urea and the smallest EW was observed with trimethylene glycol [88].

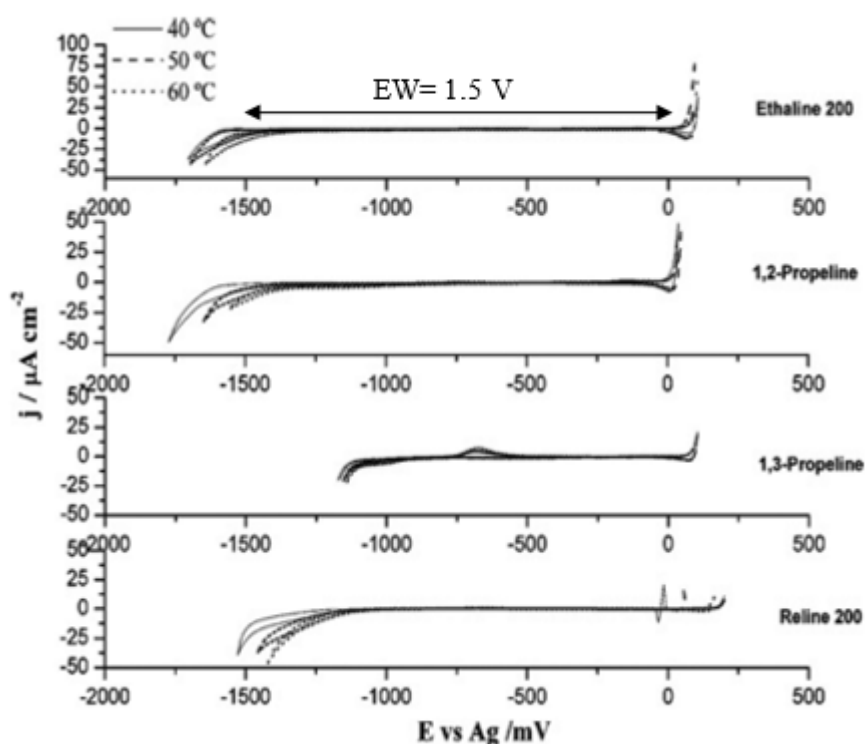


Figure 1.26 Cyclic voltammograms of a) ChCl: 2 EG, b) ChCl: 2 1,2-propylene, c) ChCl: 2 1,3-propanediol and ChCl: 2 urea using a Hg electrode at a scan rate of  $50 \text{ mVs}^{-1}$  at 40-60 °C. Adapted from [88].

The EW of DESs prepared from ChCl and ethylene glycol, urea and malonic acid were also measured using a Pt electrode with Ag wire as the reference electrode at  $50 \text{ mV s}^{-1}$  as Fig.1.27 shows. The potential window of those DESs differed from the values reported by Costa and co-workers, which indicated that the electrochemical window depended on the electrode material. Importantly, the voltammograms in Fig. 1.27 (a) shows that reline breaks down beyond  $-0.4 \text{ V}$  vs. RE as cathodic currents appear (cf. red arrow in Fig. 1.27 a). Similarly, ethaline exhibits a degree of breakdown (cf. red arrow in Fig. 1.27 b) but authors did not comment about such phenomenon.

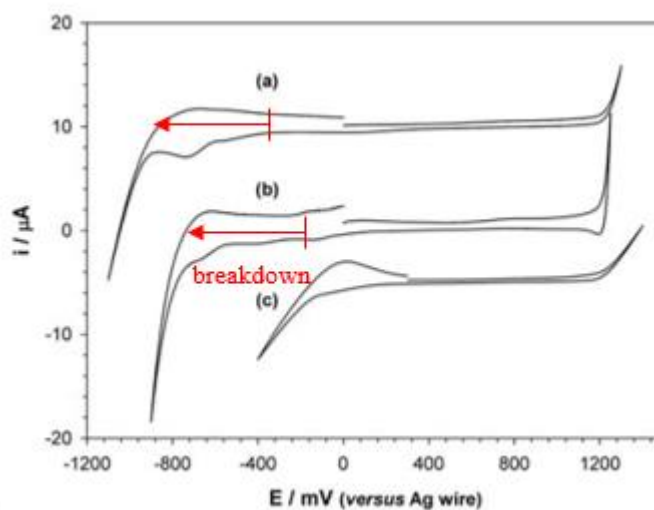


Figure 1.27 Cyclic voltammograms of a) ChCl: 2 urea, b) ChCl: 2 EG, c) ChCl: malonic acid using a Pt electrode ( $A= 0.031 \text{ cm}^2$ ), Ag wire as the reference electrode at a scan rate of  $50 \text{ mV s}^{-1}$  at  $20 \text{ }^\circ\text{C}$ . Adapted from [23]

Ghosh and Roy have scrutinised the potential window of ethaline using a Pt RDE electrode at a scan rate of  $30 \text{ mV s}^{-1}$  at  $25 \text{ }^\circ\text{C}$  using a Ag wire as the reference electrode [89]. Voltammetry of ethaline showed that the EW was similar to the value reported by Costa *et al.* (e.g.  $\sim 1.5 \text{ V}$ ) [88]. Although the cathodic limit was at  $-0.7 \text{ V}$  vs. Ag wire RE, small currents were observed at low potentials such as  $-0.3 \text{ V}$  vs. Ag wire RE (cf. red arrow in Fig. 1.28). This result has indicated that the decomposition of the solvent may start at relatively low overpotentials within the “accepted” electrochemical window, e.g. ( $1.5 \text{ V}$ ) [89].

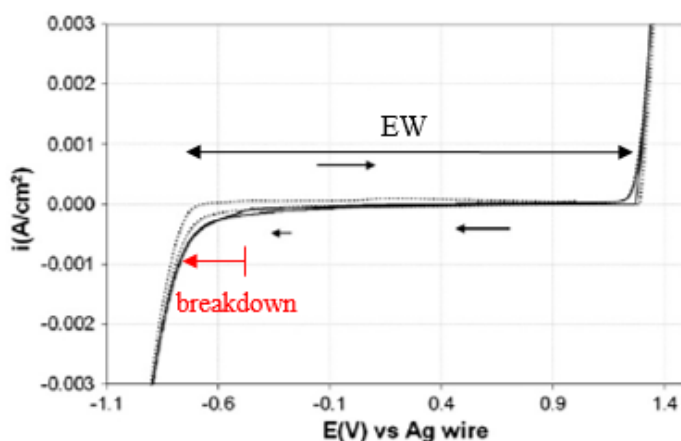


Figure 1.28 Linear sweep voltammetry of ethaline using a Pt electrode, a Ag wire as the reference electrode at a scan rate of  $30 \text{ mV s}^{-1}$  at  $25 \text{ }^\circ\text{C}$ . Adapted from [89].

Some dependence of EW on experimental conditions has been sought from theoretical models. For example, Bagh *et al.* has investigated whether changes in the composition of the DES modified the potential window [90]. Their theoretical analysis examined DESs formulated from ChCl mixed with zinc (II) chloride as the HBD. Firstly, the effect of a change in concentration of HBD on EW was inspected [90]. For example, the mole fraction of  $\text{ZnCl}_2$  was increased from ChCl:  $\text{ZnCl}_2$  to ChCl:  $3 \text{ ZnCl}_2$ , which triggered a shrinking in the potential window from 2.37 to 1.95 V [90].

Secondly, the influence of the type of salt on the EW was evaluated. ChCl was replaced by N,N diethylethanolammonium, which is also an ammonium salt [90]. As a result of the salt change, the EW of the system diminished [90]. Lastly, the ammonium salt was substituted by a phosphonium one, e.g. methyl-triphenylphosphonium bromide [90]. When this replacement occurred, the EW of the system broadened [90]. Even though the results of this investigation have indicated that there is a relationship between the concentration of the HBD, the type of salt and the EW, no insights were offered for these phenomena.

Raising the temperature has also been shown to narrow the EW of some DESs formed between ChCl and HBDs such as ethylene glycol, propylene glycol, trimethylene glycol, and urea [88]. This study demonstrated that despite the fact that higher temperatures can increase the conductivity on DESs, the reduction of the EWs

may be an issue. On the contrary, the EW of DESs formulated from  $\text{ZnCl}_2$  mixed with ammonium or phosphonium salts widened due to the raise of temperature [90]. The underlying causes for this phenomenon appears unknown.

While the electrochemical window of conventional ILs can be as large as 4.4 V, it is clear that the potential window of DESs is smaller. For this reason, sufficiently electropositive metals such as Al cannot be deposited from DESs. However, DESs are still wide enough to electrodeposit a variety of metals such as Ag, Cu, Cr, Zn, Ni, Co, and Sn.

#### *1.4.7 General electroplating from deep eutectic solvent systems*

Industrial deposition of chromium, zinc, nickel and other metals, which provide excellent protection against corrosion, is mostly based on aqueous systems. However, Cr, Zn and Ni aqueous systems use substances such as hexavalent chromium, zinc cyanide, nickel sulphate which are classified as hazardous, toxic and carcinogenic chemicals. Moreover, due to the toxicity issues, the disposal of waste material represents another growing problem. The plating industry has encountered the constraints imposed by REACH on the usage of dangerous substances during the manufacturing process of Cr, Ni, Zn and other metals.

The Registration, Evaluation, Authorisation and Restriction of chemicals (REACH) is the entity that regulates the utilisation of chemicals and their impact in the workforce and in the environment [91]. Since REACH promotes the implementation of alternatives methods to substitute dangerous chemicals [91], DESs have been proposed to be an alternative electrochemical reaction media to aqueous solutions, especially due to their low volatility which averts to the possibility of inhalation by workers or dispersal in the atmosphere by entrainment. However, not only meeting the environmental regulation is a motivation to replace aqueous solvents for DESs. The advantages that DESs may provide are attractive, for example, deposits with improved mechanical properties, averting hydrogen evolution and raising current efficiency of the electrodeposition process are examples of additional motivation to electrodeposit certain metals from DESs.



#### 1.4.7.1 Ni

Ni electrodeposition has been studied using DESs such as ethaline (ChCl: 2 EG) and reline (ChCl: 2 urea). Firstly, it was established that the speciation of Ni in DESs differs from the speciation in aqueous solutions [92]. It is thought that this difference arises due to the dominance of aquo-complex formation in water while the speciation in DESs has been found to be controlled by the anionic component of the solvent [93]. For example, in aqueous solutions the  $[\text{Ni}(\text{H}_2\text{O})_6]^{2+}$  was the dominant species whereas in DESs, Ni(II) was found to be coordinated by three molecules of ethylene glycol forming the  $[\text{Ni}(\text{EG})_3]^{2+}$  complex [93].

The electrochemical behaviour of Ni was studied in reline using a metal concentration of 0.02 M of  $\text{NiCl}_2 \cdot 6\text{H}_2\text{O}$  at room temperature [94]. Ni is reduced via one step mechanism, e.g.  $\text{Ni} + 2e^- \rightarrow \text{Ni}$ . Also, Ni deposits were fabricated from bulk deposition under these operational conditions resulting in powdery black deposits [94]. Moreover, SEM pictures revealed that Ni films were rough and nodular which was stated to be due to the speciation in the melt [94]. However, Yang *et al.* attributed this feature to the high deposition rate at which Ni was electrodeposited since it is known that high currents tend to promote dendritic growth [95].

The use of additives such as nicotinic acid was explored in Ni deposition in order to produce shiner and smoother films [95]. This time, the authors changed two factors, the metal loading was increased to 0.2 M of  $\text{NiCl}_2 \cdot 6\text{H}_2\text{O}$  as well as the temperature from 25 to 65 °C to decrease the viscosity of reline, (e.g. from 1700 to less than 200 mPa s) [95]. The electrochemical behaviour of Ni was recorded using a Cu electrode at a scan rate of 20 mV s<sup>-1</sup> as shown in Fig.1.29 (a). The reduction potential started at -0.67 V and the shoulder at +0.55 V was attributed to the stripping of the metal [95]. Afterwards, Ni films were obtained from reline under galvanostatic conditions, the current was set to 5 mA cm<sup>-2</sup> at 65 °C. The deposits exhibited a morphology of pyramidal clusters as shown in Fig. 1.29 (b) [95]. Besides, another study also reported rough morphology of Ni films from reline at a comparable temperature, e.g. 60 °C [96].

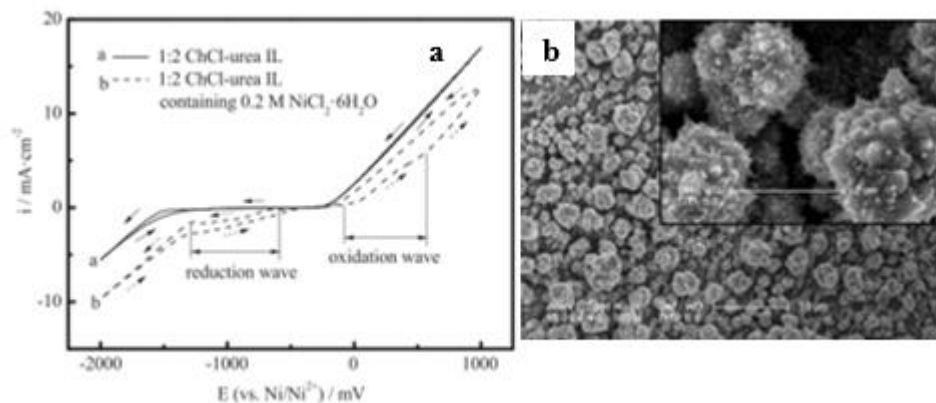


Figure 1.29 a) Cyclic voltammetry of ChCl: 2 urea (solid line) and 0.2 M of Ni (II) species dissolved in ChCl: 2 urea (dashed line) using a Cu electrode at  $20 \text{ mV s}^{-1}$  at  $65^\circ\text{C}$ . b) SEM image of Ni coating obtained from reline. Adapted from [95].

In order to improve the morphology of Ni deposits, nicotinic acid (NA) was used as an additive [95]. It was found that NA inhibited Ni deposition while increasing cathodic polarisation as shown in Fig. 1.30. When NA was added to the solution at  $400 \text{ mg L}^{-1}$ , Ni films with good adherence but a nodular morphology were produced (Fig 1.31 a). Moreover, a higher magnification of the nodules shown needle-like crystals [96]. Although the plating efficiency of the process was 100%, the nodular-like appearance of the deposits remained as Fig. 1.31 (b) illustrates.

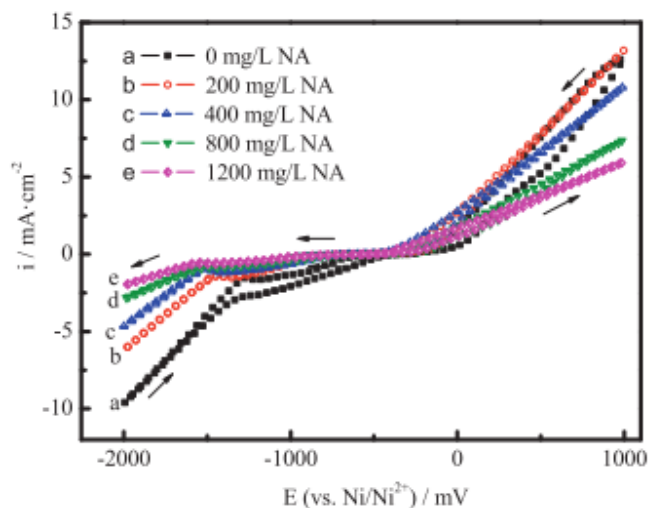


Figure 1.30 Cyclic voltammetry of  $0.2 \text{ M Ni (II)}$  in ChCl: 2 urea containing a) 0, b) 200, c) 400, d) 800, and e)  $1200 \text{ mg L}^{-1}$  of nicotinic acid using a Cu electrode at  $20 \text{ mV s}^{-1}$  at  $65^\circ\text{C}$ . Adapted from [95].

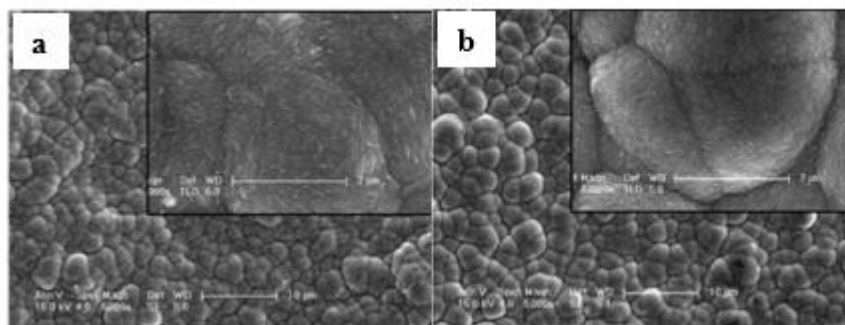


Figure 1.31 SEM image of Ni coating in  $\text{ChCl}: 2 \text{ urea}$  containing  $0.2 \text{ M NiCl}_2 \cdot 6\text{H}_2\text{O}$  with a) 400 and b)  $1200 \text{ mg L}^{-1}$  of nicotinic acid using a Cu electrode at a scan rate of  $20 \text{ mV s}^{-1}$  at  $65 \text{ }^\circ\text{C}$ . Adapted from [95].

Recently, the electrochemical behaviour of Ni was investigated using a concentration of  $0.0114 \text{ M NiCl}_2 \cdot 6\text{H}_2\text{O}$  in ethaline, which is the typical molar content of the Watts Ni aqueous bath [92]. The morphology of Ni deposits was reported to be dull and cracked at room temperature, as shown in Fig. 1.32.

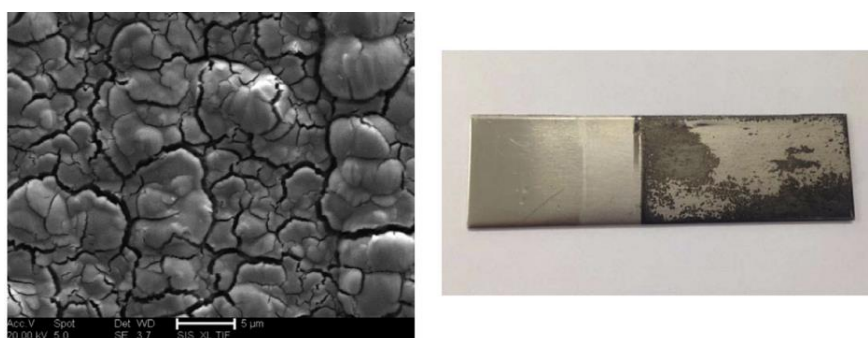


Figure 1.32 SEM image of Ni film fabricated from  $0.0114 \text{ M NiCl}_2 \cdot 6\text{H}_2\text{O}$  in ethaline at  $25 \text{ }^\circ\text{C}$  (left) and image of the appearance of the deposit (right). Adapted from [92].

Since Watts Ni bath operates at  $80 \text{ }^\circ\text{C}$ , the electrochemical behaviour of Ni was explored at this temperature from ethaline [92]. Two important deductions were drawn from the voltammetry data. First, the deposition rate of Ni in ethaline was comparable to the reduction rate on Watts bath in spite of the fact that the viscosity of ethaline ( $16.8 \text{ mPa s}$ ) was greater than the Watts solution ( $0.693 \text{ mPa s}$ ). Second, mass transport did not govern the reduction rate of Ni at  $80 \text{ }^\circ\text{C}$  [92]. Neither does it in Watts bath, as Ni deposition is kinetically controlled. Not only the viscosity but also the speciation of Ni was affected by the rise in temperature [92]. The electroactive species that Ni forms with ethylene glycol was demonstrated to be the



temperature needs further development. Even though nicotinic acid could improve the adhesion of Ni deposits and their morphology, NA can cause serious irritation. Thereby, its implementation in an industrial plating process may be restricted due to the need to use protective equipment. In addition, a nodular morphology of Ni plated films may not be ideal for commercial purposes.

#### 1.4.7.2 Cr

The chemistry of aqueous solutions is based on hexavalent chromium, Cr (VI) which is toxic and the current efficiency of the process is low. Hence, electroplating of Cr from DESs cannot only offer a less toxic chemistry but also the possibility to fabricate Cr deposits with improved properties. For example, in aqueous solutions Cr deposits are affected by the evolution of hydrogen which leads to cracked coatings, low plating efficiencies and hydrogen embrittlement of the substrate.

Since anhydrous Cr metal salt was not soluble in ChCl, the hydrated version of Cr (III) salt was mixed with ChCl [52]. The eutectic composition was found at 1:2 molar ratio of ChCl to  $\text{CrCl}_3 \cdot 6\text{H}_2\text{O}$  and the melting point of the mixture was 13 °C [52]. The main electroactive species in the ChCl:  $2\text{CrCl}_3 \cdot 6\text{H}_2\text{O}$  system was identified to be  $[\text{Cr}(\text{H}_2\text{O})_3\text{Cl}_3]$  [52]. The voltammetry of ChCl:  $2\text{CrCl}_3 \cdot 6\text{H}_2\text{O}$  system was carried out using a Pt electrode at 60 °C as shown in Fig. 1.34. The reduction process of Cr started at potentials  $< 0$  V vs. Cr wire RE in which  $\text{Cr}^{3+}$  was reduced to  $\text{Cr}^{2+}$  [52]. Afterwards, as the cathodic potential become more negative ( $\sim 0.5$  V vs. Cr wire RE), the cathodic current reduced abruptly which was interpreted as a partial passivation of the electrode surface [52]. The authors suggested that Cr(II) species may form an insoluble product on the electrode surface [52]. However, at  $-0.6$  V vs. RE a nucleation loop appeared, which was indicative of Cr deposition. Then, Cr deposition was reported to occur in a two-step mechanism [52]. It is important to mention that Cr (III) processes from aqueous systems are non-toxic but they are still in developing stages.

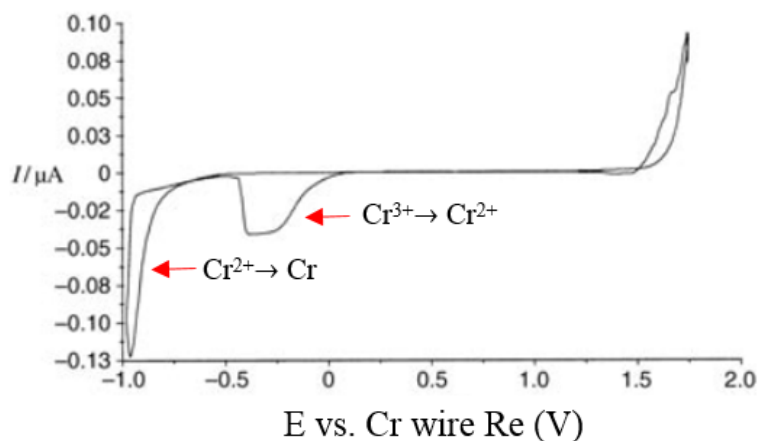


Figure 1.34 Voltammetry of  $\text{ChCl}: 2 \text{CrCl}_3 \cdot 6\text{H}_2\text{O}$  system using a Pt electrode at a scan rate of  $20 \text{ mV s}^{-1}$  at  $60^\circ\text{C}$ . Adapted from [52].

Galvanostatic deposition was carried out at a current density of  $0.345 \text{ mA cm}^{-2}$  using a Ni working electrode over 2 h and at  $60^\circ\text{C}$ . Despite the appearance of Cr deposits (amorphous pale grey) the fact that the deposits were crack-free was the most significant feature [52]. Cr deposits free of cracks (Fig. 1.35) can be attained from aqueous solutions using a variety of complexing agents from which most of them are hazardous. Hence, crack-free deposits are advantages of Cr electrodeposition from DESs [52]. It was also relevant to show that although the metallic salt contained six molecules of water, there was no evidence of water reduction, i.e. hydrogen evolution was not observed during Cr electrodeposition and the current efficiency of the process was  $\Phi = 90\%$  [52].

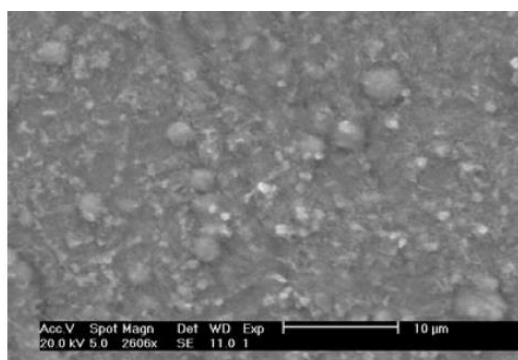


Figure 1.35 SEM image of Cr film using a Ni electrode fabricated from  $\text{ChCl}: 2 \text{CrCl}_3 \cdot 6\text{H}_2\text{O}$  system at  $60^\circ\text{C}$ . Adapted from [52].

### 1.4.7.3 Zn

Zn electroplating from aqueous solutions is a well-established process but exhibits low current efficiency in alkaline aqueous electrolytes [98]. Zn coatings are applied onto iron and steel surfaces to protect them against corrosion. Also, Zn deposits have been used in applications as energy storage devices. However, zinc cyanide,  $\text{Zn}(\text{CN})_2$ , has been classified as a toxic material. Then,  $\text{Zn}(\text{CN})_2$  has been replaced for zinc chloride ( $\text{ZnCl}_2$ ) which is a less toxic material. However, there are disadvantages of  $\text{ZnCl}_2$  aqueous systems; for example, the corrosiveness of the bath and the low throwing power [99]. Moreover, the use of strong additives is compulsory to prevent the formation of dendritic Zn plated films. Zn electroplating from alkaline aqueous solutions also suffers from hydrogen evolution which affects the deposit properties as well as the current efficiency of the plating process [100].

For these reasons, Zn electrodeposition from DESs such as reline and ethaline has been investigated [101]. A 0.5 M  $\text{ZnCl}_2$  solution was prepared in reline (ChCl: 2 urea) and ethaline (ChCl: 2 EG) and the electrochemical response was recorded using a Pt WE, and Ag wire as the RE. The voltammetry experiments were carried out at 40 °C to reduce the viscosity of the solvents [101]. It was established that the electrochemical behaviour of Zn in ethaline was different to its electrochemical response in reline. For example, in ethaline the reduction of Zn started at -0.85 V vs. RE whereas in reline Zn was more difficult to reduce, i.e. the reduction potential of Zn was at -1.00 V vs. RE, as shown in Fig. 1.36.

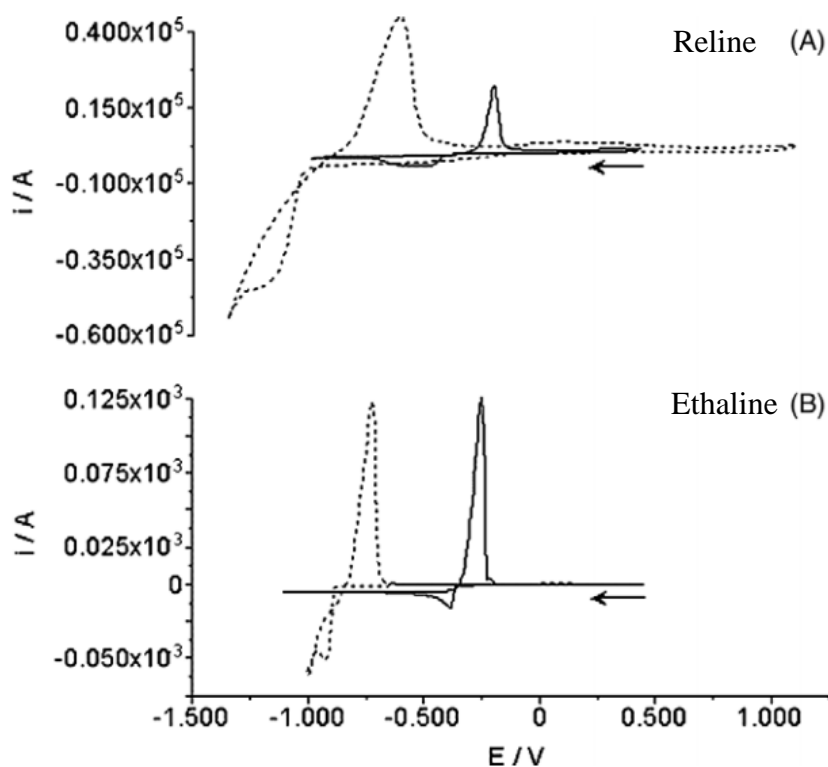


Figure 1.36 Cyclic voltammetry of 0.5 M  $\text{ZnCl}_2$  shown as the dotted line in a)  $\text{ChCl}: 2 \text{ urea}$  and b)  $\text{ChCl}: 2 \text{ EG}$  using a Pt electrode ( $d= 0.5 \text{ mm}$ ) at a scan rate of  $20 \text{ mV s}^{-1}$  at  $40 \text{ }^\circ\text{C}$ . The solid line corresponds to the voltammetry of  $\text{SnCl}_2$  which is not included in this work. Adapted from [101].

The disparity between the reduction potentials was ascribed to different complex electroactive species [101]. While there were three electroactive species of Zn formed in ethaline, i.e.  $\text{ZnCl}_3^-$ ,  $\text{Zn}_2\text{Cl}_5^-$  and  $\text{Zn}_3\text{Cl}_7^-$ , only one complex was detected in reline, e.g.  $\text{ZnCl}_3^-$  [101]. The authors explained that the formation of only one complex in reline occurred due to the greater strength of urea as a ligand than ethylene glycol. As Zn was more easily deposited in ethaline than in reline, it was elucidated that the particular  $\text{ZnCl}_3^-$  complex was more difficult to reduce than the other Zn complexes [101].

The last characteristic of the electrochemical behaviour of Zn in both DESs was that the Zn reduction current was higher in ethaline than in reline [101]. For example, the Zn cathodic current in ethaline was in the order of  $10^{-3} \text{ A cm}^{-2}$  whereas in reline was around  $10^{-5} \text{ A cm}^{-2}$ . The difference in the order of magnitude of the deposition currents was interpreted as the difference on viscosity of both solvents.



For instance, the viscosity of ethaline was measured to be 50 mPa s while the viscosity of reline was much higher, e.g. 1072 mPa s [101].

Rearranging equation 1.22, the authors calculated the ratio of diffusion coefficients of Zn complexes as a function of the viscosity [101].

$$D_1\eta_1 = D_2\eta_2 \quad (1.22)$$

For a diffusion controlled processes, there is another expression that relates the peak reduction currents with the diffusion coefficients as shown in equation 1.23 [101, 102].

$$i_{p, \text{reline}}/i_{p, \text{ethaline}} = \sqrt{\frac{D_{\text{ethaline}}}{D_{\text{reline}}}} \quad (1.23)$$

Using equation 1.23, the authors calculated the ratio of the peak reduction currents obtained with viscosity data and compared this value with the experimental ratio of reduction currents [102]. It was found that only 33% of data could be explained due to the viscosity of the solvent, the remaining difference was ascribed to changes in the surface area of the electrode and different deposition kinetics without further elaboration [101].

Up to now, some of the most important properties of ILs and DESs have been reviewed and metal electrodeposition from DES systems has been discussed. One of the disadvantages of these systems relies on their high viscosity which consequently imposes mass transport constraints. Although the addition of water has been sought as a possible method to overcome this limitation, most of the investigations were performed from dry or low water-containing DES systems. Hence, the influence of water on the metal electrodeposition processes requires thorough investigation.

## 1.5 Aims and Objectives of Current Work

The aim of this study was to systematically investigate the effect of water content on various aspects of metal electrodeposition from the water-containing DES system, which comprised of Cu (II) species dissolved in ethaline. Initially, in order to test if the use of water addition influenced the electrochemical behaviour of Cu (II) reduction from ethaline, mass transport and kinetics properties of Cu electro-reduction from the DES system were investigated. Following this stage, electrodeposition experiments were performed from the water-containing DES system in order to examine the main characteristics of the obtained Cu electrodeposits. The objectives of this work were as follows.

1. Determine the water content that ethaline and copper-containing ethaline solutions (electrolyte) can incorporate over four weeks during their exposure to the atmosphere.
2. Monitor the speciation of the copper-containing ethaline solution as water content increases in the DES system in order to determine at which concentration of water speciation of copper changes in the DES system.
3. Evaluate the effect of water content on the physico-chemical properties of the electrolyte such as density, viscosity and conductivity based on simulated solutions where water was added to match the level of the water content incorporated by the electrolyte over four weeks of monitoring.
4. Measure the electrochemical window of ethaline with increasing amounts of water in order to examine if water can influence the cathodic and anodic potential limits.
5. Determine the effect of water content on the electrochemical behaviour of the copper-containing ethaline solution, by calculating the standard heterogeneous rate constant and ionic mass transfer, as well as the current distribution of Cu electrodeposits from water-containing electrolyte.

6. Examine the morphology of the deposited Cu coatings as well as their microstructure in order to determine grain shape, grain size and preferred orientation as a function of water content in the electrolyte.

The final stage of this work concentrated on the study of the characteristics of the anodic reaction using a soluble copper anode during the electrodeposition of Cu from the water-containing electrolytes by achieving the following:

- (i) Determination of the anodic species product of the electro-dissolution of Cu from the water-containing electrolytes.
- (ii) Calculation of the dissolution valency.
- (iii) Determination of a simple model that explains the anodic dissolution process of Cu from the water-containing electrolytes.

This chapter has summarised some of the basic physico-chemical and electrochemical properties of conventional ILs based on chloroaluminate salts, hydrophobic anions as well as DESs. Also, some electrodeposition processes which are commonly performed from aqueous systems have been discussed based on DES systems. Prior to investigating the effect of water on Cu electrodeposition from DES systems, a literature survey presenting the basic aspects of Cu electrochemical deposition is presented in the next chapter.

## **2. Chapter - Literature Review**

## 2. Literature Review

---

### 2.1 Electrodeposition of Cu from DESs

In chapter one, the electrodeposition of many important metals for the electroplating industry was discussed. In this chapter, the electrodeposition of Cu will be reviewed since as introduced earlier it is a model system which has been extensively studied in aqueous, ILs and DES systems. Thereafter, it will be a useful system to benchmark processes from water-containing DES systems.

#### 2.1.1 Speciation of Cu

##### 2.1.1.1 Speciation of Cu in chloroaluminate and water-air stable ionic liquids

Speciation refers to the complex species that form when a solute is dissolved in a liquid. Metal speciation is important for electrochemical reduction because it controls aspects such as redox potentials, solubility, electro-reduction kinetics, mechanism of electrodeposition and thereby morphology of deposits.

In aqueous solutions, the speciation of metals is dictated by the chemistry of water where the oxygen atoms of the water molecules attach to the central cation to form the metal-aquo complexes. For example, most aqueous copper systems use non-chloride substances so the main species formed are likely to be the hexa-aquacopper ion,  $[\text{Cu}(\text{OH}_2)_6]^{2+}$ . This species exhibits a blue colour in aqueous solutions and Fig. 2.1 shows the structure of the  $[\text{Cu}(\text{OH}_2)_6]^{2+}$  cationic species.

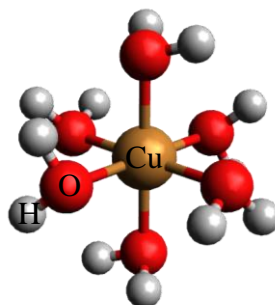


Figure 2.1 Structure of the hexa-aquacopper ion formed in aqueous solutions between Cu and molecules of water.

In ionic liquids (ILs), however, the formation of electroactive species has been reported to be different due to the existence of both anionic and cationic species in the pure solvent. For example, one of the earliest studies to determine Cu speciation in ILs was carried out by Laher and Hussey using a basic chloroaluminate IL, e.g. 1-methyl-3-ethyl-imidazolium chloride mixed with aluminium chloride (MEIC- $\text{AlCl}_3$ ) [103]. This study was in line with other studies where certain transition metals formed stable chloro complexes in basic chloroaluminate ILs [103].

As introduced in section 1.2.3, ILs can be acidic, basic or neutral solvents depending on the molar fraction of  $\text{AlCl}_3$  in the melt. In 1983, Laher and Hussey investigated the formation of both Cu (I) and Cu (II) complex species [103]. Firstly, Cu was electrochemically oxidised from a Cu wire. Due to the fact that the resulting solutions were colourless, potentiometric titration was carried out to elucidate which type of complexes existed in the IL [103]. Fig. 2.2 shows the potentiometric titration curve of Cu (I) species at 40 °C. This graphic shows that when the MEIC- $\text{AlCl}_3$  mixture became basic ( $x_{\text{AlCl}_3} < 0.5$ ), the change in cell potential ( $\Delta E$ ) shifted to more negative values [103]. For example, the  $\Delta E$  varied from 0.4 to -0.6 V and this shift was related to the formation of chloro complex anions in the IL system [103].

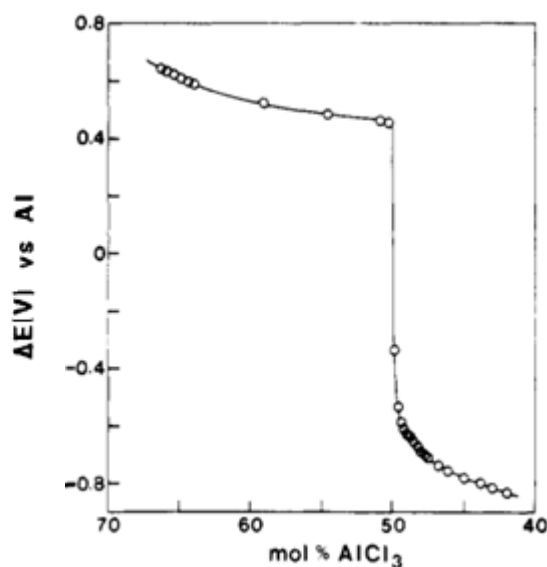


Figure 2.2 Potentiometric titration curve of Cu (I) species in MEIC- $\text{AlCl}_3$  IL at 40 °C. Adapted from [103].

Later, the data of the potentiometric titration versus the mole fraction of the chloride ion was fitted to the equation 2.1 to obtain the stability constants and the type of copper-chloro complexes formed in the solution [103].

$$\Delta E = E_{\text{Cu(I)/Cu}}^{\circ'} + 2.3 \frac{RT}{F} \log x_{\text{Cu(I)}} - 2.3 \frac{RT}{F} \log \sum_{p=1}^m [\beta' (x_{\text{Cl}^-})^p] + E_j \quad (2.1)$$

where,  $E_{\text{Cu(I)/Cu}}^{\circ'}$  is the apparent standard potential of the Cu(I)/Cu redox couple,  $x_{\text{Cu(I)}}$  is the mole fraction of Cu(I) in the mixture,  $x_{\text{Cl}^-}$  is the mole fraction of the chloride ion,  $\beta'$  is the formation constant of the pth Cu (I) complex species and  $E_j$  is the cell liquid-junction potential. The liquid junction potential was neglected in the calculations due to its minor value. Afterwards, the apparent standard potential  $E_{\text{Cu(I)/Cu}}^{\circ'}$  was obtained from the intercept of Nernst plots and a model was proposed that described the stability and the formation of the Cu (I) species in the melt [103]. It was identified that the main electroactive species were complexes such as the  $[\text{CuCl}_2]^-$  and  $[\text{CuCl}_4]^{2-}$  [103]. However, at higher temperature 100 °C, the equilibrium was shifted to favour the formation of the  $[\text{CuCl}_3]^{2-}$  species as described in equation 2.2 [103].



Cu speciation was also studied by Chen and Sun in a water and air stable IL as  $[\text{EMIM}][\text{BF}_4]$  [104]. Since the liquid was a neutral whereby the chloride metal salts were poorly soluble, an excess of 1-ethyl-3-methylimidazolium chloride ( $\text{EMI}\cdot\text{Cl}$ ) was added to the melt to produce a basic mixture (rich in chloride ions) in which the complexation of the metal ions was facilitated [104]. Cu was anodically dissolved from a Cu wire to better control the concentration of the solute in the melt [103, 104]. The diffusion coefficients for Cu (I) species were obtained using the RDE and the Stokes-Einstein product was computed ( $D\eta/T$ ) [104]. Based on this approach, Chen and Sun has suggested that the main Cu (I) species was the  $[\text{CuCl}_3]^-$  complex [104].

Due to the fact that Cu possesses two oxidation numbers, the speciation of Cu (II) species was also investigated [103]. Laher and Hussey deliberately converted Cu (I) to Cu (II) species by coulometric oxidation. Since the cupric solutions exhibited a yellowish colour, Ultraviolet Visible (UV-Vis) spectroscopy was used to identify the stable electroactive species. The spectrum of Cu (II) species in MEIC-AlCl<sub>3</sub> liquid showed two absorption bands, one at 294 and the other at 407 nm [103]. Chen and Sun reported a similar spectrum of cupric species with two maxima absorption bands at 288 and 407 nm using a water-air stable IL as shown in Fig. 2.3 [104].

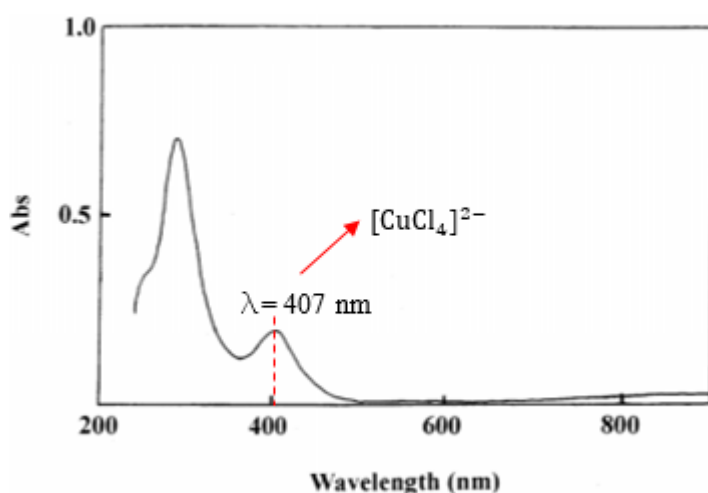


Figure 2.3 Spectrum of Cu (II) species in the basic [EMIM]<sup>+</sup>[BF<sub>4</sub>]<sup>-</sup> IL. The concentration of Cu (II) species was 1.63 mM. Adapted from [104].

The spectrum of Cu (II) species in ILs was associated with the presence of the [CuCl<sub>4</sub>]<sup>2-</sup> complex [103]. This attribute was based on previous Cu (II) speciation studies from other organic solvents, whereby the bands of maximum absorption at 295 and 411 nm were indicative of the existence of the tetrachlorocuprate ion, e.g. [CuCl<sub>4</sub>]<sup>2-</sup> [103]. Furthermore, the molar absorptivity at 407 nm calculated for cupric species in the IL was similar to the value obtained from the organic solutions [103]. Other species such as [CuCl]<sup>+</sup>, CuCl<sub>2</sub> or [CuCl<sub>3</sub>]<sup>-</sup> do not absorb near 407 nm wavelength, which was used as evidence for the sole existence of [CuCl<sub>4</sub>]<sup>2-</sup> complex [103].

Recently, Hartley *et al.* have studied the speciation of cupric ions in ILs based on water-air stable anions. Importantly, this study has considered the inclusion of 5



wt% of water in the speciation of Cu (II) complexes [93]. Extended X-ray Absorption Fine Structure (EXAFS) technique was used because it is a non-invasive technique in which the results are not ambiguous [93]. The effect of both the cation and the anion of the solvent has been scrutinised [93]. Three different hydrated metal salts were used such as copper acetate, copper chloride dehydrate, and copper sulphate pentahydrate mixed with the water tolerant ILs listed in Table 2.1.

Table 2.1 Water-air stable ILs used to study the speciation of Cu (II) complexes by Hartley's group. Adapted from [93].

Name	Abbreviation
1-hexyl-3-methyl-imidazolium chloride	[C <sub>6</sub> MIM][Cl] <sup>-</sup>
1-ethyl-3-methylimidazolium chloride	[C <sub>2</sub> MIM][Cl] <sup>-</sup> or EMIM][Cl] <sup>-</sup>
1-ethyl-3-methylimidazolium thiocyanate	[C <sub>2</sub> MIM][SCN] <sup>-</sup>
1-butyl-3-methyl-imidazolium tetrafluoroborate	[BMIM][BF <sub>4</sub> ] <sup>-</sup>

The effect of the cation on Cu (II) speciation was studied by the comparison of the IL containing the same anion (Cl<sup>-</sup>) and a different alkyl chain, e.g. [C<sub>2</sub>MIM] and [C<sub>6</sub>MIM] [93]. It was reported that the cupric ion was coordinated to four chloride ions when the alkyl chain was short as in the [C<sub>2</sub>MIM]<sup>+</sup>[Cl]<sup>-</sup> liquid. On the contrary, as the alkyl chain extended from two to six, as in the [C<sub>6</sub>MIM]<sup>+</sup>[Cl]<sup>-</sup> liquid, only three chloride ions were found to be attached to the metal ion [93]. The difference of the chloride ligands was suggested to arise due to the lower polarity that ILs with longer alkyl chains possess. Thereby, the stabilisation of complexes with low charge was facilitated forming the [CuCl<sub>3</sub>]<sup>-</sup> instead of [CuCl<sub>4</sub>]<sup>2-</sup> species [93]. There was no evidence that the inclusion of water content (5 wt %) altered the copper-chloro complexes in these ILs [93].

The effect of the anion of the solvent on speciation was also examined. For this purpose, a strong ligand such as thiocyanate [SCN]<sup>-</sup> and weak ligand as tetrafluoroborate [BF<sub>4</sub>]<sup>-</sup> were compared. It was reported that all cupric salts, when dissolved in the IL containing the [SCN]<sup>-</sup> ligand formed a complex of the form [Cu(NCS)<sub>2</sub>(SCN)]<sup>-</sup> and the addition of water did not influence the coordination

number of the cupric ions [93]. By contrast, when  $[\text{BF}_4]^-$  was the anionic ligand, a mixed speciation of Cu was described [93]. For instance, it was identified that two  $\text{Cl}^-$  ions were anchored to the first coordination sphere of Cu whilst the other two detected atoms were thought to be oxygen from water ligands. The proposed electroactive species were either the  $[\text{CuCl}_2(\text{H}_2\text{O})_2]$  or  $[\text{CuCl}_2(\text{BF}_4)_2]$  complexes [93].

At the moment, the speciation of Cu (I) and Cu (II) species has been merely discussed in chloroaluminate and water-air stable ILs. The speciation of Cu in ILs has been demonstrated to depend on several factors such as: (i) the Lewis acidity or basicity of the IL, (ii) the cationic component of the solvent and its alkyl chain and (iii) the strength of the anion of the solvent. Regarding this latter factor, if the strength of the ligand was weaker; the coordination sphere of the metal ion is influenced by water content. However, most of the studies on Cu speciation from conventional ILs were carried out with a relatively low content of water, and hence this was relatively rare.

### 2.1.2 Speciation of Cu in DESs

De Vreese *et al.* studied the speciation of Cu (II) species using a type II eutectic solvent [105]. As discussed in section 1.4.3 type II eutectics are formed by mixing a halide salt directly with a hydrated metal salt. This work employed EXAFS technique to establish the complexes of the copper-containing DES. The Fourier transform signal of the EXAFS spectrum indicated that the cupric ions were fully coordinated with chloride ions, which suggested the presence of the  $[\text{CuCl}_4]^{2-}$  species [105].

Similarly, Hartley *et al.* systematically investigated the speciation of both the Cu (I) and Cu (II) complexes in the DES formed with  $\text{ChCl}$  and HBDs such as polyalcohols and amines [93]. In the case of Cu (I) species, the anhydrous salt, e.g.  $\text{CuCl}$  was dissolved in each HBD to a concentration of 0.1 M and the EXAFS spectrum was matched to a mixture of  $[\text{CuCl}_2]^-$  and  $[\text{CuCl}_3]^{2-}$  complexes [93]. Besides, the speciation of the Cu (II) complexes was explored with both hydrated

( $\text{CuCl}_2 \cdot 2\text{H}_2\text{O}$ ) and its analogous anhydrous metal salt ( $\text{CuCl}_2$ ). In spite of the waters of hydration (i.e.  $\sim 0.34$  wt%), the anionic species in both systems was identified to be the tetrachloro complex,  $[\text{CuCl}_4]^{2-}$  [93].

These results were in good agreement with the findings of De Vreese *et al.* [105] and Abbott *et al.* [106]. The latter study examined the speciation of Cu (II) species using UV-Vis spectroscopy. As shown in Fig. 2.4 no fundamental difference was observed between the absorption spectra of the hydrated and the anhydrous cupric salt [106]. Moreover, as in imidazolium-based ILs, the absorption band at 406 nm was indicative of the presence of the  $[\text{CuCl}_4]^{2-}$  complex [103].

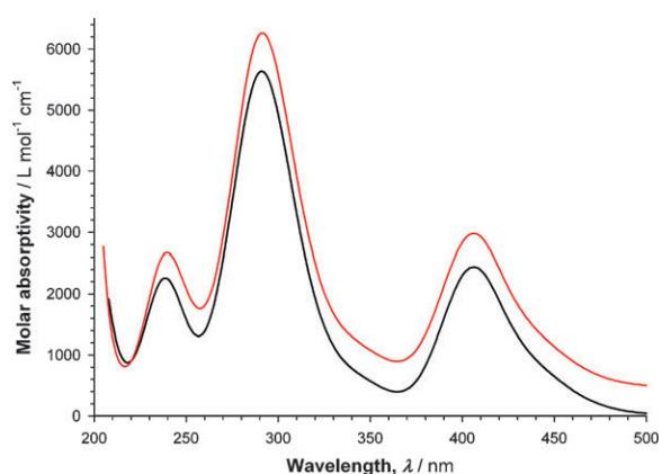


Figure 2.4 UV-Vis absorption spectra of hydrated cupric salt (black curve) and anhydrous cupric salt (red curve) in ethaline using a concentration of 0.2 mM of Cu (II) species. Adapted from [106].

#### 2.1.2.1 Effect of water on Cu speciation in DESs

De Vreese's group not only established the structure of the Cu (II) species in the  $\text{CuCl}_2 \cdot 2\text{H}_2\text{O}$ -ethaline melt, they also scrutinised the influence of water in this system [105]. A set of ChCl mixed with different water content, e.g. 100, 95, 84, 73, 62, 49, 39 and 27 wt% was prepared and the concentration of Cu (II) species was set to 0.1 M. By combining UV-Vis method and EXAFS techniques; changes in Cu (II) speciation were discerned [105].

It was found that, up to 39 wt% of water concentration the tetrachlorocuprate complex remained as the main electroactive species in the solvent [105]. Nevertheless, between 49 and 62 wt% of H<sub>2</sub>O at least one or two Cl<sup>-</sup> ions were displaced by the water molecules, which triggered the formation of a mixed chloro-aqua complexes [105]. It is interesting to note that a water content of 40 wt%, the Cl<sup>-</sup> ion was substituted by oxygen in imidazolium-based ILs in a separate study [107]. Finally, if the sample contained H<sub>2</sub>O ≥ 73 wt%, the cupric metal ion was almost entirely hydrated [105].

These data were supported by other techniques such as UV-Vis spectroscopy. Fig. 2.5 shows the absorption spectra of the ChCl: 2CuCl<sub>2</sub>·2H<sub>2</sub>O with increasing amounts of water. Qualitatively one notices that, up to 39 wt% of water no significant changes in the absorption bands at 291 and 406 nm were recorded [105]. Nonetheless, at 62 wt% of H<sub>2</sub>O, the molar absorptivity of the [CuCl<sub>4</sub>]<sup>2-</sup> species substantially decreases from 2300 to less than 500 L mol<sup>-1</sup> cm<sup>-1</sup>, which implied that this species may disappear in the liquid while other species could form [105]. For 95 wt% of water, a new absorption band at 250 nm appeared which was indicative of a coordination sphere of Cu<sup>2+</sup> fully hydrated [105].

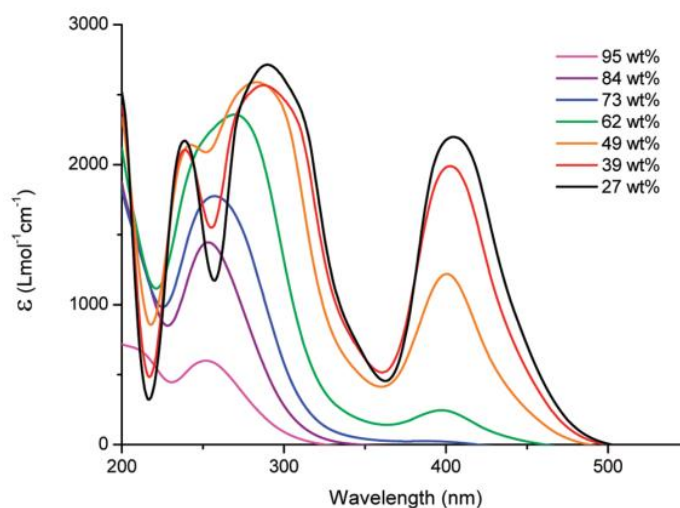


Figure 2.5 UV-Vis absorption spectra of 0.1 M Cu (II) species dissolved in ChCl containing increasing amounts of water. Adapted from [105].

A second line of investigation by Hartley *et al.* was the scrutiny of the speciation of Cu in DESs based on alcohols. There, the concentration of water was

limited to 5 wt%. The EXAFS results demonstrated that at this water content, the  $[\text{CuCl}_4]^{2-}$  complex remained as the dominant electroactive species in the system [93]. Therefore, the debate on the impact of water on the speciation of Cu using ethaline or other DESs over a range of water concentration is still open.

### 2.1.3 Mechanism of Cu electrodeposition

One of the earliest studies to establish the electrodeposition mechanism of Cu from ILs was carried out by Tierney group in 1998 [108]. Their work involved the use of the Lewis acid chloroaluminate IL,  $[\text{EMIM}][\text{Cl}]-\text{AlCl}_3$ , in which Cu was electrochemically dissolved from a Cu wire to a concentration of 0.025 M. The authors corroborated that Cu (I) species were the product of anodic dissolution as the experimental weight loss was comparable to the expected one from the charge calculation [108]. Also, they used cyclic voltammetry which is a useful technique to record the current response of the system while a potential range is swept in the forward and backward direction. Fig. 2.6 shows the voltammetry response of the system carried out using a Pt electrode at a scan rate of  $50 \text{ mV s}^{-1}$  at  $40 \text{ }^\circ\text{C}$  within a  $\text{N}_2$ -filled glove box [108].

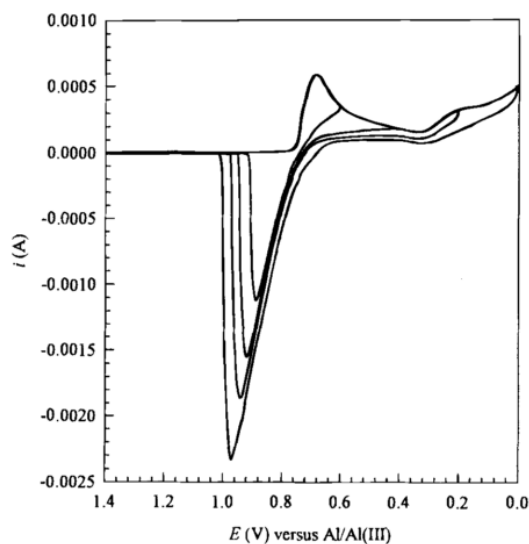


Figure 2.6 Cyclic voltammetry of Cu (I) species electrochemically produced in acidic  $[\text{EMIM}]^+[\text{Cl}]^--\text{AlCl}_3$  using a Pt electrode and a scan rate of  $50 \text{ mV s}^{-1}$  at  $40 \text{ }^\circ\text{C}$ .

Adapted from [108].

The cyclic voltammogram of Fig. 2.6 shows that when the sweep started at +0.30 V vs. RE, a single reduction peak emerged at +0.69 V vs. RE and the corresponding stripping peak appeared at +0.90 V vs. RE [108]. In order to obtain the number of electrons transferred in the redox reaction, the Nernst relationship was used as shown in equation 2.3.

$$E_{\text{eq}} = E^{o'} + \frac{RT}{nF} \ln \left( \frac{a_{\text{Ox}}}{a_{\text{Red}}} \right) \quad (2.3)$$

where,  $E_{\text{eq}}$  is the equilibrium potential,  $E^{o'}$  is the formal potential,  $R$  is the gas constant,  $T$  is the absolute temperature,  $n$  is the number of transferred electrons,  $F$  is Faraday's constant,  $a_{\text{Ox}}$  is the activity of the oxidised species and  $a_{\text{Red}}$  is the activity of reduced species.

The Nernst equation shows that when  $E_{\text{eq}}$  is plotted against  $\ln \left( \frac{a_{\text{Ox}}}{a_{\text{Red}}} \right)$  then the slope of the curve should be 0.059 V for one electron transfer at 25 °C, and the formal potential is given by the intercept of the curve. Their results corroborated that the redox peaks at +0.69 and +0.90 V vs. RE were due to a one electron transfer reaction [108]. Additionally, it was established that the reduction reaction of Cu (I) species in the acidic  $[\text{EMIM}]^+[\text{Cl}]^- \text{-AlCl}_3$  liquid was mass transport-controlled due to the fact that the diffusion limiting currents of the Cu(I)/Cu redox couple were found to be concentration-dependent [108].

Sun and Chen also studied the mechanism of Cu deposition from  $[\text{EMIM}]^+[\text{BF}_4]^-$  which is an IL tolerant to water [104]. They proved that Cu (I) species were products of anodic dissolution via charge analysis. Cyclic voltammetry was performed using a Pt WE and the scan rate was 50 mV s<sup>-1</sup> at 30 °C. The voltammogram showed two redox couples; for example, the first couple appeared at +0.25/+0.20 V vs. RE and the second one at -0.55/-0.50 V vs. RE [104]. In order to establish from which step the deposition of Cu proceeded, potentiostatic deposition was carried out [104]. It was determined that Cu deposition occurred below -0.55 V vs. RE.

Despite the fact that Cu was proven to be oxidised to Cu (I) species from charge analysis, the cyclic voltammograms exhibited two reduction steps [104]. This

phenomenon was associated to the oxidation of Cu (I) to Cu (II) species due to the presence of dissolved oxygen in the liquid [104]. Qualitatively, it was observed that the colour of the solution changed from transparent to yellowish, which was typical of Cu (II) species solvated in chloride media. In order to corroborate that Cu (I) was oxidised to Cu (II) by O<sub>2</sub>, the voltammograms were carried out under a dry argon atmosphere [104]. In spite of using Ar gas, the solution turned yellow after several hours. The authors suggested that even small amounts of dissolved O<sub>2</sub> could induce the oxidation of Cu(I) species [104], and did not attribute it to the oxidation of Cu (I) into Cu (II) species. It remains debatable whether or not O<sub>2</sub> is responsible for the oxidation of Cu (I) since no focused examinations of O<sub>2</sub> solubility in both ILs and DESs are available.

The mechanism of Cu deposition was studied using DESs for the first time in 2008 [102]. The DES system comprised 1 M CuCl<sub>2</sub> in glyceline (ChCl: 2 glycerol) and the experiments were performed using a Pt electrode and a scan rate of 200 mV s<sup>-1</sup> at 40 °C. The voltammograms revealed two separate steps whereby the first cathodic peak potential was at +0.61 V vs. Ag RE, which corresponded to the reduction of Cu (II) to Cu (I) species and it was associated to a quasi-reversible process due to the separation of the peaks ( $\Delta E = 89$  mV) [102]. The voltammogram showed a second reduction step Cu (I)/Cu (0) whose peak potential was at -0.22 V vs. Ag RE and it was attributed to show an irreversible behaviour. A useful comparison was possible using the aqueous chloride system of 1 M CuCl<sub>2</sub> + KCl, where the cathodic peak current was found to be 16 times higher than the one recorded from the DES system. This phenomenon was mostly ascribed to differences in viscosity of both systems. For instance, using the relationship shown in equation 1.23 presented earlier [101] and the Walden's rule, a new correlation was proposed

$$\text{to hold } \left( \frac{i_{p \text{ water}}}{i_{p \text{ glyceline}}} = \sqrt{\frac{\eta_{\text{glyceline}}}{\eta_{\text{water}}}} \right) [102].$$

Using the experimental viscosity of both glyceline and water, the ratio of the peak currents showed a reasonable agreement with the experimental ratio. It was therefore reported that the diffusion of Cu (II) species in glyceline was affected by the high viscosity of the liquid being slower than in aqueous systems.

Similarly, in order to prove the mechanism of Cu deposition from DES systems, two types of DESs were used [106], one derived from amines, e.g. reline (ChCl: urea) and the other from alcohols, e.g. ethaline (ChCl: 2 ethylene glycol) [106]. There the source of metal ions was  $\text{CuCl}_2 \cdot 2\text{H}_2\text{O}$  because it was believed that DESs did not react with water and its presence was not an issue [106]. The electrode configuration system consisted of Pt as the working and counter electrode and a Ag wire as the reference electrode. The concentration of Cu (II) species was set to 0.1 M and all the experimentation was carried out at 20 °C [106].

Although the Cu-DES system contained 10% v/v of  $\text{H}_2\text{O}$ , no difference was found in the polarisation data of Cu when using conventional ILs and DESs [106]. Cu exhibited the same reduction potentials from both reline and ethaline. For instance, as shown in Fig. 2.7 two reduction and two oxidation waves were recorded. The first reversible potential at +0.43 V vs. Ag wire RE was attributed to the reduction of Cu(II) to Cu(I) species and the subsequent potential at -0.45 V vs. Ag wire RE was related to the reduction of Cu(I) to Cu(0) [106].

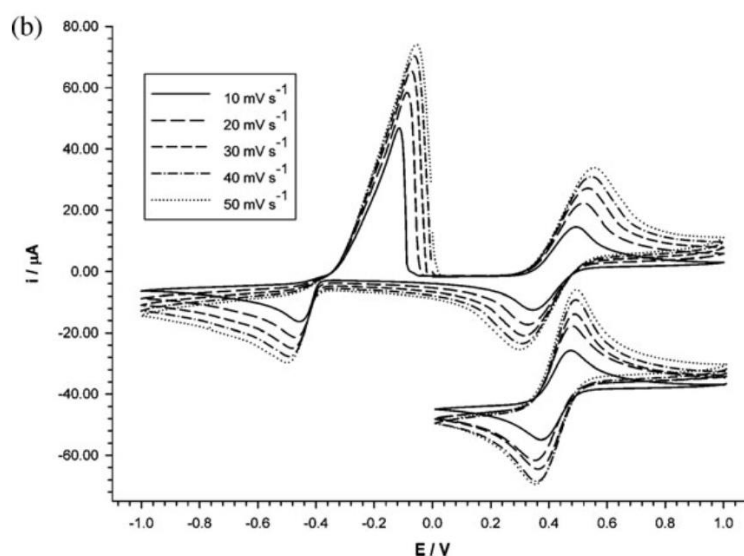


Figure 2.7 Cyclic voltammetry of 0.1 M Cu (II) species in both reline and ethaline using a Pt electrode at different scan rates at 20 °C. Adapted from [106].

Ghosh and Roy analysed the electrochemical behaviour of Cu in ethaline in more detail [89]. They dissolved  $\text{CuCl}_2 \cdot 2\text{H}_2\text{O}$  salt in ethaline to prepare solutions of different concentrations, e.g. 0.05 M and 0.2 M so the behaviour of Cu at low and high metal content was assessed [89]. The  $\text{CuCl}_2 \cdot 2\text{H}_2\text{O}$  salt was selected because the



plating industry may prefer this type of salt rather than a more expensive anhydrous metal salt [89]. Pt was used as the working electrode, the counter electrode was a Pt mesh and the reference electrode was a Ag wire. The potential was swept from the rest potential, which was about +0.6 V to -0.7 V at a scan rate of 30 mV s<sup>-1</sup>. Also, the electrode was rotated at 700 and 1300 rpm in order to evaluate the effect of the agitation on the polarisation behaviour of Cu. The experiments were performed at 25 °C using a thermostatic bath [89].

Fig. 2.8 shows the voltammetry response of Cu using 0.05 M CuCl<sub>2</sub>·2H<sub>2</sub>O in ethaline. Two separate waves were observed in the Cu-DES system and each reduction wave corresponded to a one electron transfer step as equations 2.5 and 2.6 show [89]. The first reduction reversible potential was observed at +0.50 V versus Ag RE followed by the second wave where the reduction potential appeared at -0.40 V vs. Ag RE [89]. These potentials were similar to the ones reported by the Abbott's group in 2009 [106]. The deposition mechanism of Cu from DESs occurred via a two-step mechanism due to the stabilisation of Cu (I) ions in the liquid [109]. This phenomenon arises when a high concentration of chloride is present in the reaction media, which facilitates the complexation of Cu (I) by the Cl<sup>-</sup> ions. This complexation was feasible to occur due to the high concentration of chlorides in ethaline, e.g. 4.8 M.

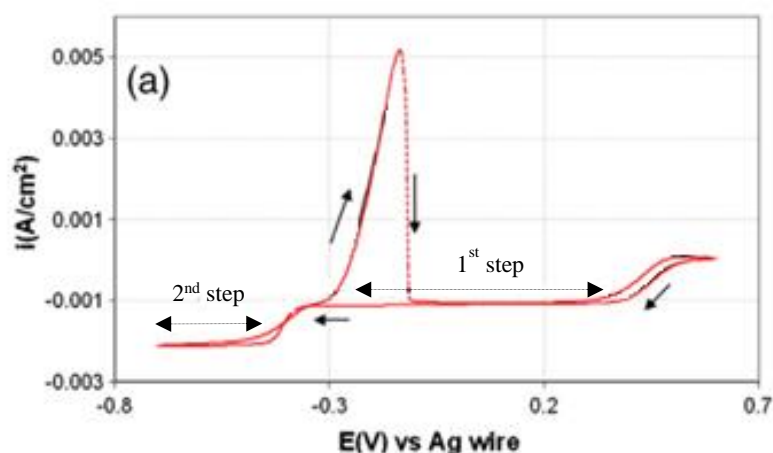
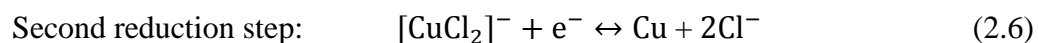
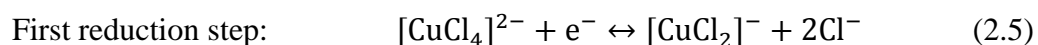


Figure 2.8 Polarisation data for the reduction of 0.05 M CuCl<sub>2</sub>·2H<sub>2</sub>O in ethaline using a Pt electrode at a scan rate of 30 mV s<sup>-1</sup>, rotation speed of 700 rpm at 25 °C. Adapted from [89].



It is important to clarify that the  $[\text{CuCl}_4]^{2-}$  and  $[\text{CuCl}_2]^-$  complexes will be referred in the text as Cu (II) and Cu (I) species for brevity.

Fig. 2.9 illustrates two characteristics of the electrochemical behaviour of Cu in ethaline. Firstly, two ‘flat’ or plateau currents appeared which are typical of the region where the rate of mass transfer of ions to the electrode surface has reached its limit. This current density whereby the plateau is formed is known as the limiting current density ( $i_{\text{lim}}$ ). Both limiting current densities increased in magnitude when the concentration of Cu (II) species was increased from 0.05 to 0.20 M. For example, the first plateau current using 0.05 M of Cu (II) species was measured to be  $\sim 1.0 \text{ mA cm}^{-2}$  while at 0.20 M it increased to  $3.5 \text{ mA cm}^{-2}$ . Increasing the rotation speed, from 700 to 1300 rpm, caused that both limiting currents in the DES system increased. Such responses indicated that both the first and the second reduction steps were controlled by the mass transport of metal ions towards the electrode surface. The relationship between the  $i_{\text{lim}}$  with the concentration of metal ions and the rotation speed is given by the Levich relationship, which is described in section 3.5.

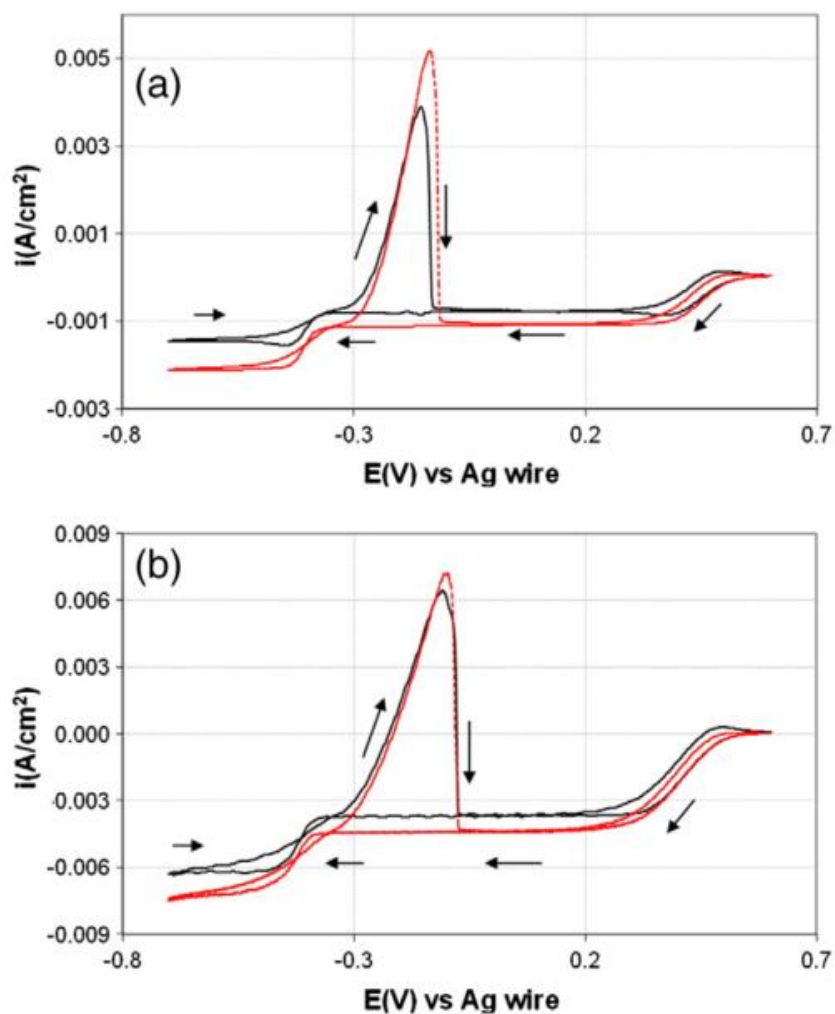


Figure 2.9 Polarisation data for the reduction of  $\text{CuCl}_2 \cdot 2\text{H}_2\text{O}$  in ethaline using concentrations of a) 0.05 M and b) 0.20 M using a Pt electrode ( $A = 0.031 \text{ cm}^2$ ), scan rate of  $30 \text{ mV s}^{-1}$ , rotation speed of 700 rpm (black curve) and 1300 rpm (red curve), and at  $25 \text{ }^\circ\text{C}$ . Adapted from [89].

Ghosh and Roy quantitatively proved that both reduction steps were mass transport-controlled [89]. They compared the ratios of the experimental limiting current versus the expected limiting current using the Levich equation [89]. Table 2.2 summarises the ratios of the limiting currents at 700 and 1300 rpm from the solutions at 0.05 M and 0.20 M concentration of cupric ions. The figures of the experimental and calculated ratios of Table 2.2 indicated that the reduction of Cu in ethaline was limited by the transport of metal ions to surface of the electrode [89], which was analogous to the reduction behaviour of Cu in chloroaluminate-based ILs reported by Tierney's group earlier [108].

Table 2.2 Experimental ratio of the limiting current density and experimental ratio of the expected limiting current density for Cu reduction using 0.05 and 0.20 M of Cu (II) species at two rotation speeds, 700 and 1300 rpm. Adapted from [89].

Concentration of Cu (II) (M)	$\omega$ (rpm)	Experimental ratio of $i_{lim}$	Expected ratio of $i_{lim}$
0.05	700	1.00	1.00
	1300	1.42	1.36
0.20	700	4.28	4.00
	1300	5.00	5.44

Now that the electrochemical response of copper complexes from DES systems has been introduced, it is instructive to compare it with the behaviour of Cu (II) deposition from aqueous chloride systems. Fig. 2.10 shows the cyclic voltammetric response of 0.05 M CuCl<sub>2</sub> + 1.5 NaCl solution using a stationary Pt electrode and a scan rate of 5 mV s<sup>-1</sup> at 25 °C. Two well-defined reduction steps can be identified, corroborating that Cu (II) reduction from ethaline exhibited a similar mechanism of electron-transfer reaction than that of the aqueous chloride system.

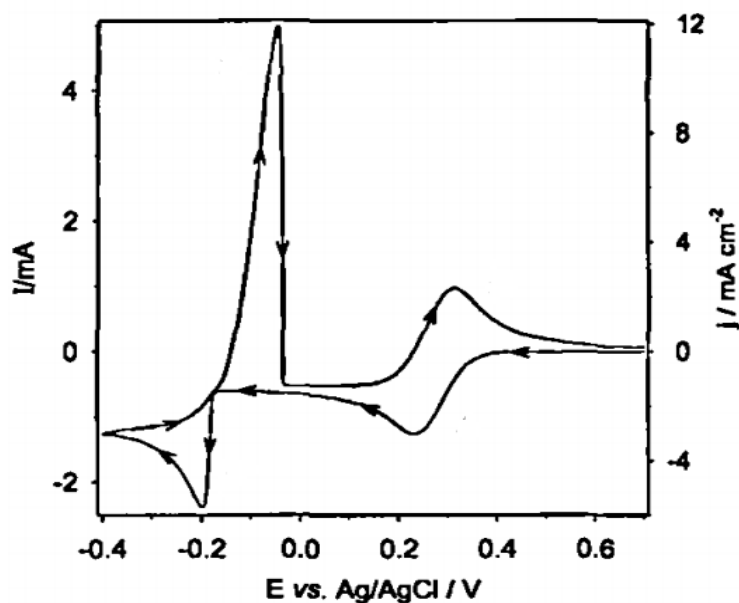


Figure 2.10 Cyclic voltammetric data for the reduction of Cu (II) species from aqueous chloride system (0.05 M CuCl<sub>2</sub> + 1.5 M NaCl) using a stationary Pt electrode and a scan rate of 5 mV s<sup>-1</sup> at 25 °C. Adapted from [110].

However, a notable difference between DES and aqueous systems was the plating rate. For example, the diffusion limiting current achieved in DESs was reported to be -6.0 mA cm<sup>-2</sup> for 0.2 M Cu (II) species using a rotation speed of 700 rpm [89], while in the aqueous chloride system based on a diffusion coefficient of  $6.0 \times 10^{-6} \text{ cm}^2 \text{ s}^{-1}$ ,  $\nu = 0.011 \text{ cm}^2 \text{ s}^{-1}$ , 0.2 M of Cu (II) concentration, and  $\omega = 700 \text{ rpm}$  [110] the limiting current was calculated to be 111.3 mA cm<sup>-2</sup>. This difference accounted as a limitation of DES systems since lower deposition rates were attained when compared with aqueous systems. Viscosity has been identified to be the main limiting factor on the mass transport of electroactive species in DES systems, owing to the higher viscosity of DESs compared to aqueous systems. For example, the viscosity of DESs has been measured to range from 36 mPa s in diol-based DESs up to 1200 mPa s in anhydrous metal-based DESs as compared to 1-2 mPa s for aqueous systems.

### 2.1.3.1 Diffusion coefficients of Cu species

A second parameter influencing limiting current (and hence plating rates) is the diffusion coefficient. Diffusion coefficients of electroactive species in DESs have been measured in order to understand the mobility of ions in this electrochemical medium. As discussed in section 2.1.3, Cu is known to be reduced from DESs via a two-step mechanism, where the first reduction wave corresponds to the reduction of Cu (II) to Cu (I) complexes followed by the deposition step. The diffusion coefficient of Cu (II) species has been studied by numerous researchers [67, 106, 109, 111] compared to Cu (I) species, which is due to the electrochemical reversibility of the first reduction reaction simply due to the ease of measurement.

Since the first reduction step was treated as reversible, the diffusion coefficient of Cu (II) species from DESs has been calculated using the Randles-Sevcik relationship shown in equation 2.10. This equation correlates the anodic and cathodic peak potentials with the square root of the scan rate. For a process controlled by diffusion, the variation of the peak currents should be a linear plot and the slope provides the diffusion coefficient.

$$i_p = 2.69 \times 10^5 n^{3/2} A D^{1/2} \nu^{1/2} C \quad (2.10)$$

where  $n$  is the number of transferred electrons,  $A$  is the area of the working electrode,  $D$  is the Diffusion coefficient,  $\nu$  is the scan rate and  $C$  is the bulk concentration of species. The diffusion coefficient of Cu (II) was measured to be in the range of  $10^{-7} \text{ cm}^2 \text{ s}^{-1}$  for ethaline [67, 106] while in reline it was found to be an order of magnitude smaller, e.g.  $10^{-8} \text{ cm}^2 \text{ s}^{-1}$  [106, 109, 111]. Such a difference was attributed to the higher viscosity of reline than the viscosity of ethaline [89, 106]. The diffusion coefficient of Cu (II) species measured in aqueous system was on a scale of  $10^{-6} \text{ cm}^2 \text{ s}^{-1}$ , which is one or two order or magnitude higher than in DES systems. This limitation has been explained by the bulkier structure of DESs and the low probability of void formation for an ion to move (as discussed in sections 1.4.5.1 and 1.4.5.2).

#### 2.1.4 Electrodeposition of Cu from DES systems

Popescu *et al.* examined the deposition of Cu using four different DESs such as ethaline, reline, oxaline and maline [111]. For each DES system, they used different deposition currents (from 0.1 to 0.2 mA cm<sup>-2</sup>), deposition time (20, 30, 40 and 50 minutes) as well as differing concentration of anhydrous cupric salt CuCl<sub>2</sub> (0.1, 0.2 and 0.5 M). A graphite plate acted as the working electrode, the counter electrode was Si plate, and the experiments were performed at 80 °C. From the reline system, the quality of Cu deposits was described as poor because it appeared dull, scratchy and non-homogeneous.

In maline DES, Cu deposits were described to look homogeneous when the concentration of Cu (II) species and the current density was low, e.g. 0.2 M of Cu (II) and 5.0 mA cm<sup>-2</sup>. Similarly, electrodeposits obtained from the DES ethaline were homogeneous and shiny using a concentration of 0.5 M and a low current density of 5.0 mA cm<sup>-2</sup>. Although the appearance of deposits was described in text, little evidence was presented in the publication [111].

Electrodeposition of Cu using oxides such as Cu (I) oxide as the primary source of metal ions was carried out by Tsuda *et al.* [112]. Since metal oxides such as CuO and Cu<sub>2</sub>O were soluble in DESs, the electrochemistry of Cu<sub>2</sub>O in a ChCl:2urea system was scrutinised. The concentration of water in this electrolyte was measured to be low, e.g. 20 ppm. Moreover, due to the fact that reline is a hygroscopic substance, the experimentation was carried out within a glove-box [112]. The concentration of the solute was 0.06 M Cu (I). Additionally, the working electrode was a Ni disk rotated at 1000 rpm and the deposition was conducted at a constant potential, e.g. -0.20 V. The obtained deposits were dense, compact but nodular [112].

Up to this point, the electrodeposition studies of Cu were carried out either with anhydrous salts or within glove boxes to avoid the incorporation of H<sub>2</sub>O. The limitation of expense encouraged other researchers to examine cases where copper

deposition proceeded where the system was exposed to the surroundings and employed hydrated cupric salts.

Gu *et al.* examined the electrodeposition of Cu from the ethaline-hydrated cupric salt system. This system may be of more interest for a practical plating process [113]. They deposited Cu from a plating bath containing 0.45 M of Cu (II) species using a brass WE and the counter electrode was a copper-phosphorus alloy plate. The deposition experiments were carried out under potentiostatic conditions, e.g. -0.6 V for 2 h at 25 °C. During 6 h of Cu deposition from the same electrolyte, no evidence of instabilities was observed. After this time, however, the solution turned greenish and a 'sludgy' material was observed [113] as Fig. 2.11 (b) shows. Contrary to previous studies, the electrolyte was reported to be unstable [113].



Figure 2.11 a) Appearance of the fresh electrolyte ChCl: 2 EG containing 0.45 M of Cu (II) species, and b) appearance of the electrolyte after 6 h of plating. Adapted from [113].

Gu *et al.* also examined the surface of Cu films which was described as rough exhibiting some cracks as Fig. 2.12 shows. A higher magnification revealed that small grains grew on top of Cu protrusions [113]. In order to improve the morphology of the deposits, ethylene diamine (EDA) was added to the electrolyte [113]. Although Cu electrodeposits with better qualities were reported to be fabricated when EDA was added to the electrolyte, the underlying cause of the instability of the electrolyte was not well-understood [113].



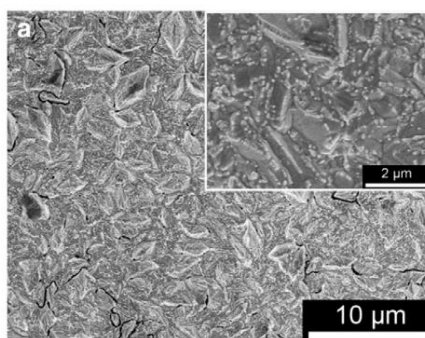


Figure 2.12 Cu coating obtained from ChCl: 2 EG containing 0.45 M of Cu (II) species using a brass substrate. The deposit was obtained under potentiostatic conditions at -0.6 V vs. Ag wire RE at 25 °C. Adapted from [113].

As a mode of comparison, Cu electrodeposit obtained from an aqueous sulphate system is presented in Fig. 2.13. The sulphate aqueous system comprised of 0.6 M Cu (II) + 2.0 M H<sub>2</sub>SO<sub>4</sub> without additives. The appearance of the deposit obtained from the aqueous system was reported to be granular exhibiting well-defined boundaries [114]. Also, the grain size of the deposit was measured to be 11.52 μm [114] whereas the deposits obtained from the DES system was characterised by grains sized as ~2.0 μm [113]. It was therefore noted that electrodeposits possessing finer grains can be obtained from DES systems compared to aqueous systems.

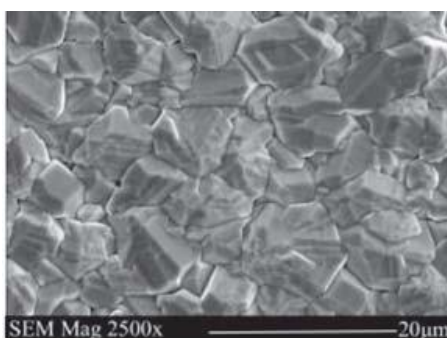


Figure 2.13 Cu coating obtained from the sulphate aqueous system (0.6 M Cu<sup>2+</sup> + 2.0 M H<sub>2</sub>SO<sub>4</sub> with no additives) using a steel substrate. The deposit was obtained under galvanostatic conditions by setting the applied current to 40% of  $i_{lim}$ , ( $i_{lim}$ =20.32 mA cm<sup>-2</sup> measured under stagnant conditions) at 25 °C. Adapted from [114].

Cu was deposited from  $\text{CuCl}_2 \cdot 2 \text{EG}$  system using both the potentiostatic and galvanostatic methods [89]. Firstly, the potential deposition was chosen to be at  $-0.6 \text{ V}$  because it is a potential value near to the second limiting current density whereby the highest rate of plating can be achieved [89]. In this work, hydrated cupric salt was used and the concentration was fixed to  $0.05 \text{ M}$  and  $0.20 \text{ M}$ . The working electrode was a steel disc, the counter electrode was a Pt mesh and the reference electrode was a Ag wire [89]. The temperature of the electrolyte was maintained at  $25 \text{ }^\circ\text{C}$  with a jacketed cell, and the plating time was fixed to  $1 \text{ h}$ . The electrolyte was also agitated using two rotation regimes, e.g.  $700$  and  $1300 \text{ rpm}$  [89].

The results of the potentiostatic experiments showed that Cu deposition was feasible under the experimental conditions [89]. However, it was pointed out that a low metal concentration, e.g. ( $0.05 \text{ M}$ ) was not suitable for electrodeposition since thin and poor deposits were attained (cf. Fig. 2.14 a). Later, Cu deposition with a fixed concentration of  $0.20 \text{ M}$  was tested at  $700$  and  $1300 \text{ rpm}$  [89]. A denser deposit was achieved using a rotation rate of  $700 \text{ rpm}$  (Fig. 2.14 b). If the agitation was greater, Cu films roughened as Fig. 2.14 (c) shows.

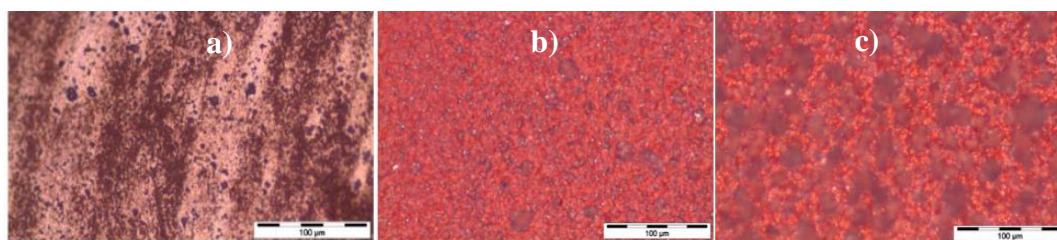


Figure 2.14 Cu deposits obtained from  $\text{Cu}(\text{II})$  in ethaline under potentiostatic conditions at  $25 \text{ }^\circ\text{C}$  using different amounts of  $\text{Cu}(\text{II})$  salt as: a)  $0.05 \text{ M}$  and  $700 \text{ rpm}$ , b)  $0.20 \text{ M}$  and  $700 \text{ rpm}$ , and c)  $0.20 \text{ M}$  and  $1300 \text{ rpm}$ . Adapted from [89].

Once potentiostatic deposition was proven, the deposition of Cu under galvanostatic regime was studied. Fig. 2.15 shows both limiting current densities ( $i_{\text{lim}1}=3.2 \text{ mA cm}^{-2}$  and  $i_{\text{lim}2}=6.0 \text{ mA cm}^{-2}$ ) that correspond to the first and subsequent second reduction steps. Based on the positive results of the potentiostatic deposition, the limiting current was set at the  $78\%$  of  $i_{\text{lim}}$ . It is essential to remind that above  $i_{\text{lim}1}$  only reduction of cupric to cuprous ions proceeded.

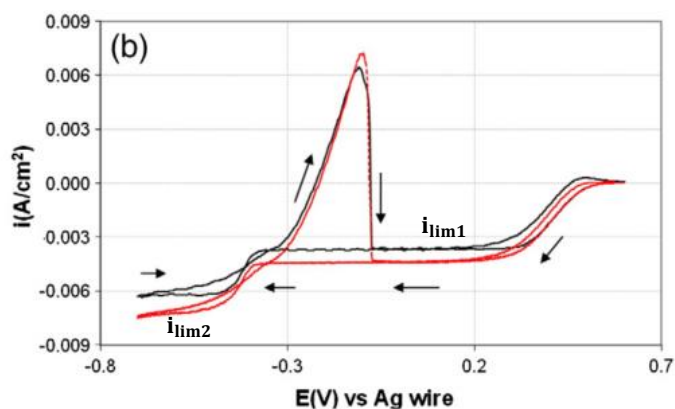


Figure 2.15 Polarisation data of Cu (II) species in ethaline using a Pt electrode ( $A=0.031 \text{ cm}^2$ ), scan rate of  $30 \text{ mV s}^{-1}$ , and temperature of  $25 \text{ }^\circ\text{C}$ . Adapted from [89].

Cu deposits fabricated under those conditions were dense and consisted of small grains. The current efficiency of the process was measured gravimetrically and it was 95%. Nevertheless, the chemical composition of the deposits showed that small amounts of chlorine and carbon were entrapped in the film (around 2 wt% each). This has been attributed to a certain extent of electrolyte decomposition as evidenced in section 1.4.6.1 where tiny currents appeared at low negative potentials within the electrochemical window of ethaline [89, 115].

The stability of the electrolyte was monitored over a month, during which a cumulative value of 27 h of plating was performed [89]. It was ascertained that some fluctuations in the cell potential occurred when an inert counter electrode was used [89]. The authors explained that the decrease of cupric ions in the mixture brought about such instability. When the researchers attempted to replenish the metal ions in solution, it was found that the system stabilised. A notable observation was the evolution of a gas at the anode [89]. However, no attempts of collection and analysis of gaseous compounds were conducted. Therefore, it was assumed that  $\text{O}_2$  evolution occurred due to the adsorption of water from atmosphere, as has been proposed by Haerens *et al.* [115].

It was found that when a soluble Cu anode was used in the plating process, no perturbations in the system were detected [89]. However, a brownish powdery layer on top of the melts was observed within the electrochemical cell. The researchers

proposed that the efficiency of Cu electro-dissolution was higher compared to the efficiency of electrodeposition, which may trigger a higher dissolution rate of the soluble anode [89]. Thereby, the solubility limit of Cu could have been exceeded which may lead to separation of copper chlorides or copper oxides [89].

#### 2.1.5 Effect of Cu salt on physico-chemical properties of DESs

As discussed in previous sections, the mechanism of Cu reduction from the DES system and the obtained deposits are dependent of the speciation and physico-chemical properties of the electrolyte. In this section, the effect of the addition of metal salt in DESs is described.

Ghosh *et al.* performed a comprehensive study about the effect of the metal salt on the physicochemical properties of ethaline [67]. Properties such as density, viscosity and conductivity were evaluated as a function of the concentration of the hydrated metal salt over a range of temperature from 20 to 55 °C [67]. However, only the data corresponding to room temperature will be reviewed since that is relevant to the present study.

The density of ethaline was measured as a function of the concentration of the  $\text{CuCl}_2 \cdot 2\text{H}_2\text{O}$  salt in the liquid as Fig. 2.16 shows [67]. As the metal loading increased, the density of ethaline was found to be 2% higher than the density of 'neat' ethaline. For example, the density of neat ethaline increased from 1.1360 to 1.1549  $\text{g cm}^{-3}$  when the metal ions reached a concentration of 0.2 M in the solvent [67]. This change in density was attributed to the formation of chloro-cupro complexes in ethaline as per discussion in section 2.1.2.

The tetrachloro-cuprate complex  $[\text{CuCl}_4]^{2-}$  'added' to the structure of ethaline which may create a denser arrangement of the molecules as illustrated in Fig. 2.17 [67]. Other studies have examined the density of a type II eutectic system ( $\text{ChCl}:\text{CrCl}_3 \cdot 6\text{H}_2\text{O}$ ) by increasing the molar fraction of the hydrated metal salt [52, 116]. The results have shown a similar tendency of density to increase, i.e. the higher the

content of Cr (III) ions, the greater the density [52, 116]. In effect, this showed that addition of hydrated copper salt “structured” the melt with a resulting denser liquid.

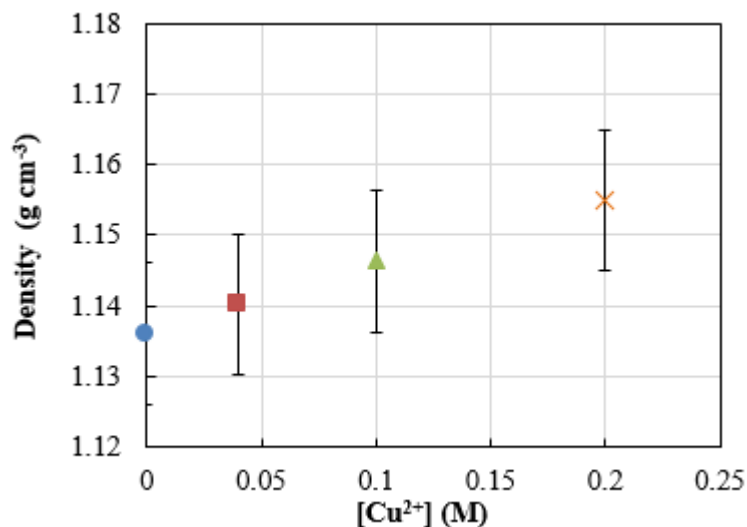


Figure 2.16 Density of ethaline as a function of the concentration of the  $\text{CuCl}_2 \cdot 2\text{H}_2\text{O}$  metal salt from 0 to 0.2 M in the solvent at 20 °C. Adapted from [67].

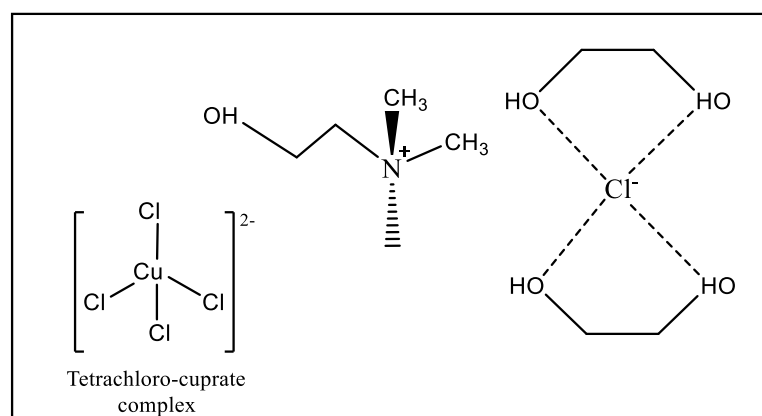


Figure 2.17 Proposed structure of the tetrachloro-cuprate species formed in ethaline. Adapted from [89].

Kityk et al. have also quantified the effect of the salt content in the density of ethaline [117]. It has been reported that the addition of metal ions in the solvent caused an increment on the density [117] which is in agreement with Ghosh *et al.* study [67]. They dissolved  $\text{NiCl}_2 \cdot 6\text{H}_2\text{O}$  in ethaline at different concentrations and measured the density, viscosity, conductivity, and surface tension of the liquid at 25 °C [117]. As summarised in Table 2.3, the density of the mixture increased 8% as the

content of Ni<sup>2+</sup> ions increased from 0 to 1.0 M. The authors explained this increment as the presence of additional hydrogen bonds due to Ni (II) complexation; [Ni(EG)<sub>3</sub>]<sup>2+</sup> discussed in section 1.4.7.1 [117]. Using equation 1.12 (cf. section 1.4.5.2) the authors demonstrated that the higher the concentration of Ni (II) species, the smaller the size of the holes, as presented in Table 2.3. This was believed to trigger a slow ionic mobility [117].

Table 2.3 Density and average hole size of the system ChCl: 2 EG + Ni (II) salt as a function of Ni (II) concentration at 25 °C. Adapted from [117].

DES	[Ni <sup>2+</sup> ] (M)	Density (g cm <sup>-3</sup> )	Average hole size (10 <sup>-10</sup> m)
Ethaline	0.0	1.1162	1.57
	0.1	1.1262	1.43
	0.2	1.1333	1.42
	0.5	1.1634	1.40
	1.0	1.2090	1.35

While the density of ethaline has been demonstrated to be affected by the addition of metal salts. The viscosity and conductivity of ethaline have not been influenced by the inclusion of Cu (II) species [67]. For instance, upon the dissolution of CuCl<sub>2</sub>·2H<sub>2</sub>O at a concentration of 0.2 M, the viscosity of the solvent was measured to be 61 mPa s while the viscosity of ‘neat’ ethaline was measured as 58 mPa s [67]. Likewise, no difference was found in the conductivity of the mixture because it ranged from 0.95 to 1.02 S m<sup>-1</sup>[67]. Since the values of the viscosity and conductivity were within the experimental error, e.g. 6%, it was determined that these properties were not affected by the chemical composition of the cupric salt in the system [67].

Comparable results have been published by Xing *et al.* In their work, the viscosity and conductivity of ethaline were unaffected as CuCl<sub>2</sub>·2H<sub>2</sub>O salt was dissolved in the matrix [118]. Barron has attributed this phenomenon to the ethylene glycol being a relatively ‘weak’ hydrogen bond donor (HBD) with already larger size of holes if compared with other HBDs like urea [119]. Thereby, ethaline with a less

robust network of hydrogen bond may be less susceptible to the inclusion of a metal salt [118, 119].

Conversely, other studies – where ethylene glycol was the HBD – have determined that both viscosity and conductivity were influenced by the addition of metal salts [117, 119]. To exemplify, when Ni (II) and Zn (II) metal salts have been added to ethaline, the viscosity increased whereas the conductivity of the system decreased. In the case of Ni (II) species, the effect of metal ions on viscosity was related to the hole theory [117] (discussed in section 1.4.5.2).

Ionic motion in the Ni-DES system was described to be more difficult due to the following reasons: (i) by dissolving increasing concentrations of Ni (II) from 0.0 to 1.0 M, it was found that the average size of the holes systematically shrunk, e.g. from 1.57 to 1.35 Å, (ii) molecular structure calculations yielded an average radius size of 8.94 Å for the  $[\text{Ni}(\text{EG})_3]^{2+}$  complex, which was six times greater than the average radius of the holes in ‘neat’ ethaline [117]. Thus, the viscosity of the Ni (II)-ethaline system was attributed to be limited by the availability of voids with proper dimensions for an ion to move [117].

Correspondingly, the decreased conductivity was modelled using hole theory [117]. Using equation 1.21 introduced in section 1.4.5.3, the relationship for molar conductivity was rearranged as equation 2.12 [117].

$$\Lambda = \frac{z^2 F e}{6 \pi \eta} (R_+^{-1} + R_-^{-1}) \quad (2.12)$$

If the molar conductivity is controlled by the availability of cavities in the solvent, equation 2.12 must be satisfied, i.e. a linear relationship has to be obtained when plotting the molar conductivity against the fluidity of the system ( $1/\eta$ ). Fig. 2.18 shows that most of the molar conductivity data followed a linear relationship as per addition of Ni (II) salt [117]. Thus, it has been determined that charge transport in the  $\text{ChCl}: 2 \text{EG} + \text{Ni (II)}$  system was governed by the mobility of the ions in lieu of the number of charge carriers [117]. The red symbols in Fig. 2.16 correspond to ‘neat’ ethaline without the addition of Ni (II) salt. It was observed that the slope of

'neat ethaline' differs from the slope of the other liquids. The authors associated this disparity to different charge carriers that exist in pure ethaline.

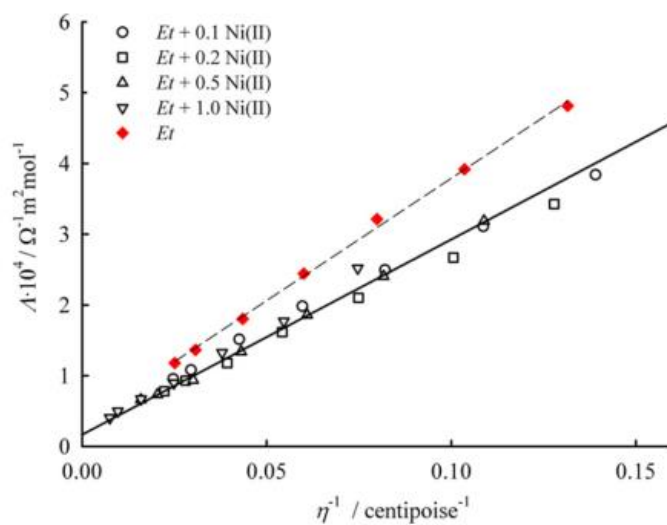


Figure 2.18 Molar conductivity versus fluidity of Ni (II) species in ethaline as a function of the concentration of Ni (II) species. Adapted from [117].



### **3. Chapter - Fundamentals**

### 3. Experimental

---

#### 3.1 Electrodeposition process

Fig. 3.1 illustrates a basic representation of an electrochemical cell for the electrodeposition of metals. This diagram shows a three electrode configuration; the working electrode, the counter electrode, and the reference electrode immersed in the electrolyte solution. These electrodes are connected through external cables to a power supply. Once the power supply starts providing electrons, the dissolved metal ions in the electrolyte ( $M^{n+}$ ) undergo a reduction reaction at the surface of the working electrode due to the gain of electrons [120]. The basic reduction reaction is shown in equation 3.1.



While the reduction reaction yields the formation of the solid phase of the targeted metal at the working electrode, a soluble counter electrode is being oxidized simultaneously in order to replenish the electrolyte solution with metal ions [120].

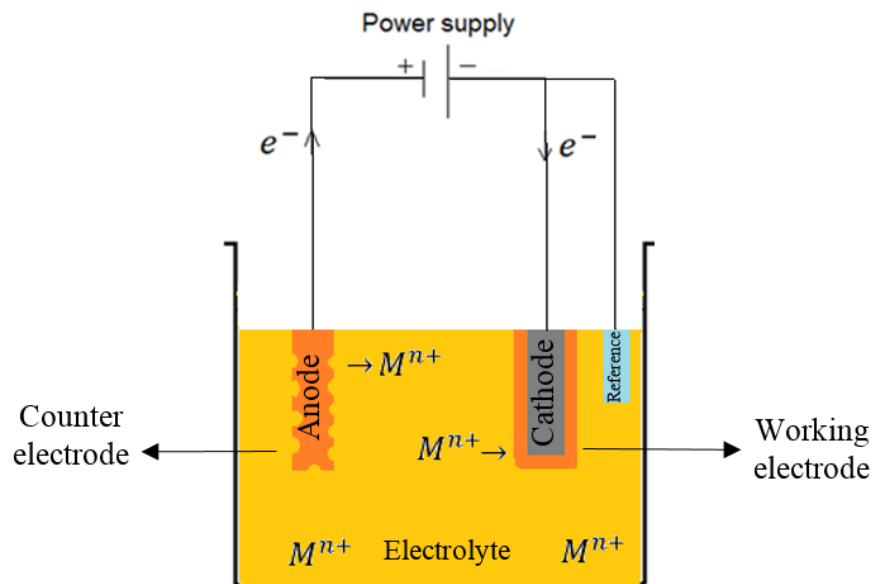
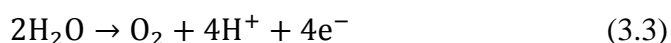


Figure 3.1 Schematic of a basic electrochemical cell with a three electrode configuration for an electrodeposition process. Adapted from [121].

Usually, a soluble counter electrode is made of the same material as the metal to be reduced [122]. Using such a dissolvable anode, allows the oxidation reaction to replenish the metal ions that are consumed during the reduction reaction [122], as equation 3.2 shows.



On the other hand, if the counter electrode is an inert material, the oxidation reaction will proceed with a breakdown of the electrolyte [122]. In aqueous systems, the oxidation reaction corresponds to the evolution of O<sub>2</sub> as equation 3.3 shows (assuming acidic medium) [123]. In systems where the electrolyte includes other inorganic or organic compounds (e.g. ILs or DESs), the oxidation reaction is more difficult to ascertain since a variety of reactions is possible.



Until now, this section describes the electrodeposition mechanism as a simple process. However, the electrodeposition process occurs as a series of stages that includes: mass transport of the cations towards the electrode interface from the bulk solution via, (i) convective movement of the cations towards the hydrodynamic boundary layer at the cathode surface, (ii) diffusion of the cations through the boundary layer. Then (iii) adsorption of the cations onto the cathode surface and the subsequent (iv) reduction of the adsorbed cations, and (v) inclusion of these reduced metal in nuclei or incorporation in the crystal lattice. The fulfillment of these steps is a requirement.

## 3.2 Thermodynamics of electrodeposition

### 3.2.1 Electrode potential

In an electrochemical cell, the cathode and the anode exhibit an electrode potential, which arises at the interface when the electrode comes into contact with the electrolyte [124]. The electrode potential is the potential difference between an electrode and a reference electrode. The difference between the cathodic and anodic electrode potentials is known as the cell potential [124], shown in equation 3.4.

$$E_{\text{cell}} = E_{\text{cath}} - E_{\text{anod}} \quad (3.4)$$

where  $E_{\text{cell}}$  is the cell potential,  $E_{\text{cath}}$  is the electrode potential of the cathode and  $E_{\text{anod}}$  is the electrode potential of the anode. The feasibility of a metal to undergo either an oxidation or a reduction reaction is assessed by measuring the standard electrode potential ( $E^{\circ}$ ) [124]. Conventionally,  $E^{\circ}$  is obtained when all the components of a system are under their standard state [124]. The standard state is achieved when the concentration of the reactant is typically 1.0 M and the measurements are carried out under a pressure of 1 atm at 25 °C. Since it is not possible to measure the electrode potential in isolation, a reference electrode bearing a fixed potential is used. In the literature, the reduction potentials were measured against the standard hydrogen electrode (SHE) and by convention the SHE possesses a potential of zero volts. In the particular case of Cu reduction, the cathodic half-cell standard potential was measured to be +0.34 V vs. SHE as equation 3.5 shows.



### 3.2.2 Nernst equation

Another important potential is the equilibrium potential ( $E_{\text{eq}}$ ) which is achieved in the absence of current. The  $E_{\text{eq}}$  denotes that all the components in the electrochemical system are in equilibrium with each other, which means that the oxidation and reduction reaction rates are equal to each other [125]. The equilibrium potential is calculated using the Nernst relationship shown in equation 3.6.

$$E_{\text{eq}} = E^{\circ} + \frac{RT}{nF} \ln \left( \frac{a_{\text{Ox}}}{a_{\text{Red}}} \right) \quad (3.6)$$

where  $E_{\text{eq}}$  is the equilibrium potential which is equal to the standard potential  $E^{\circ}$  only under standard conditions (e.g.  $a_{\text{Ox}} = a_{\text{Red}} = 1$ ),  $R$  is the gas constant,  $T$  is the absolute temperature,  $n$  is the number of transferred electrons,  $F$  is the Faraday's constant and  $a$  refers to the activity of the ions in the electrolyte. Ox refers to the oxidized species while Red refers to the reduced ones. However, since the activity of an ion is somewhat difficult to measure, it is expressed in terms of the activity coefficient as shown in equation 3.7.

$$a = \gamma \frac{C}{C_0} \quad (3.7)$$

where  $\gamma$  is the activity coefficient,  $C$  is the concentration of species in the bulk electrolyte, and  $C_0$  is the concentration under standard conditions (1.0 M). The replacement of equation 3.7 in equation 3.6 yields equation 3.8 (a) and 3.8 (b).

$$E_{\text{eq}} = E^{\circ} + \frac{RT}{nF} \ln \left( \frac{\gamma_{\text{Ox}} C_{\text{Ox}}}{\gamma_{\text{Red}} C_{\text{Red}}} \right) \quad (3.8a)$$

$$E_{\text{eq}} = E^{\circ} + \frac{RT}{nF} \left( \ln \frac{\gamma_{\text{Ox}}}{\gamma_{\text{Red}}} \right) + \frac{RT}{nF} \left( \ln \frac{C_{\text{Ox}}}{C_{\text{Red}}} \right) \quad (3.8b)$$

Often a formal potential of a redox reaction ( $E^{o'}$ ) is given by equation 3.9.

$$E^{o'} = E^{\circ} + \frac{RT}{nF} \left( \ln \frac{\gamma_{\text{Ox}}}{\gamma_{\text{Red}}} \right) \quad (3.9)$$

This allows one to define Nernst equation in terms of activity coefficients as presented in equation 3.10.

$$E_{\text{eq}} = E^{o'} + \frac{RT}{nF} \left( \ln \frac{C_{\text{Ox}}}{C_{\text{Red}}} \right) \quad (3.10)$$

Equation 3.10 is associated to the electrode potential for a system under ideal conditions [125]. Nonetheless, the electrode potential of a real system is likely to differ from that shown in equation 3.10 due to some factors such as (i) presence of species other than the electroactive ones, (ii) side reactions and (iii) external characteristics of the electrochemical cell which all could influence the electrode potential.

### 3.2.3 Overpotential

The overpotential can be understood as the energy needed to overcome the equilibrium between the electrode and the metal ions so that a redox reaction is driven [125]. For a reduction reaction to occur, the equilibrium has to be disturbed. Such a perturbation is feasible through the application of a potential ( $E$ ) to the working electrode. Due to this applied potential, a difference between the electrode potential and the equilibrium potential arises, which is known as the overpotential ( $\eta$ ) [125]. Whether a reduction or anodic reaction occurs is determined by the overpotential. A negative overpotential indicates the flow of a cathodic current and thereby the reduction reaction proceeds. By contrast, an anodic reaction occurs when the resulting overpotential is positive [125]. Equation 3.11 shows the relationship between the applied potential and the equilibrium potential leading to the overpotential.

$$\eta = E - E_{eq} \quad (3.11)$$

Since the electrodeposition process involves many steps, an overpotential for each individual stage arises. These overpotentials are the surface overpotential, the concentration overpotential, the ohmic overpotential and the charge transfer overpotential [126]. A brief description of each overpotential follows. The surface overpotential ( $\eta_s$ ) is caused by the rate of the surface reactions. This type of overpotential depends on the properties of the electrode surface [126]. The concentration overpotential ( $\eta_c$ ) occurs due to the mass transport of metal ions from the bulk solution to the electrode surface [126]. This depends on the surface concentration of the reactant. The ohmic overpotential ( $\eta_\Omega$ ) depends on the resistance through the solution, which is correlated to the ionic conductivity of the electrolyte [126]. Equation 3.12 accounts for the total overpotential as a result of the contribution of the individual overpotentials just described.

$$\eta = \eta_s + \eta_c + \eta_\Omega \quad (3.12)$$

### 3.3 Kinetics of electrodeposition

Electrode kinetics refers to how fast the reactions are occurring at the electrode interface which includes charge transfer movement across the electrical double layer and electron exchange [75]. The fundamental equation that describes electrochemical kinetics is the well-known Butler-Volmer equation [75], shown in relation 3.13.

$$i = i_o \left[ \exp \left\{ \frac{\alpha_a n F}{RT} \eta_s \right\} - \exp \left\{ - \frac{\alpha_c n F}{RT} \eta_s \right\} \right] \quad (3.13)$$

where  $i$  is the current density,  $i_o$  is the exchange current density,  $\alpha_a$  and  $\alpha_c$  are the charge transfer coefficients for anode and cathode reactions,  $F$  is the Faraday's constant  $R$  is the gas constant,  $T$  is the absolute temperature and  $\eta_s$  is the surface overpotential needed to drive the redox reaction.

Butler-Volmer equation demonstrates that the current density depends on the exchange current density and exponentially on the applied overpotential. In practice, however two limiting cases are popular. For example, for a low value of overpotential ( $< 0.01$  V), the exponential terms of the Butler-Volmer equation is simplified to equation 3.14 [75]. This relationship is indicative of a linear correlation between the current density and the overpotential.

$$i = i_o \left( \frac{nF}{RT} \eta_s \right) \quad (3.14)$$

On the contrary, when the overpotential increases, the exponential term of the Butler-Volmer equation becomes relevant. For instance, in the cathodic direction, the first exponential term is negligible and Butler-Volmer relation is expressed as per equation 3.15 [75].

$$i = -i_o \exp \left( - \frac{\alpha n F}{RT} \eta_s \right) \quad (3.15)$$

For a high enough overpotential, a special case known as the Tafel equation applies [75]. For example, by taking the logarithm on both sides of equation 3.15 yields equation 3.15 (a) and 3.15 (b).

$$\ln|i| = \ln \left[ i_o \exp \left( - \frac{\alpha n F}{RT} \eta_s \right) \right] \quad (3.15a)$$

$$\eta_S = \frac{RT}{\alpha nF} \ln i_o - \frac{RT}{\alpha nF} \ln|i| \quad (3.15b)$$

Expressing the logarithm in base 10 ( $\log_{10}$ ) of both sides of equation 3.15 (b) yields equation 3.16.

$$\eta_S = \frac{2.303RT}{\alpha nF} \log i_o - \frac{2.303RT}{\alpha nF} \log|i| \quad (3.16)$$

If the constants of equation 3.16 are expressed as 'a' and 'b', equation 3.17 (a) and 3.17 (b) are obtained.

$$a = \frac{2.303 RT}{\alpha nF} \log i_o \quad (3.17a)$$

$$b = \frac{2.303 RT}{\alpha nF} \quad (3.17b)$$

The overpotential equation 3.18 is known as the Tafel relationship. Tafel equation demonstrates that when a large overpotential holds, the current density and the overpotential follow the linear relationship shown in equation 3.18 from which kinetic parameters can be obtained [75].

$$\eta_S = a - b \log|i| \quad (3.18)$$

Up to now, kinetics of electrodeposition has been discussed in terms of the Butler-Volmer equation that predicts that the current density increases exponentially with the overpotential. Nevertheless, in a real electrodeposition process the exponential curve can depart from the expected exponential behaviour since it reaches a plateau region. Such a phenomenon arises due to mass transport limitations. In that case, charge transfer considerations are not sufficient to explain the voltammetric behaviour and mass transfer becomes relevant.



### 3.4 Mass transfer in electrodeposition

The mass transfer of the electroactive species from the bulk solution to the electrode is important since the rate of reaction at the electrode surface depends on the supply of metal ions [127]. Mass transport occurs in various modes such as diffusion, convection and migration, which individually contribute to an overall flux of species [127], as the Nernst – Planck relation shows in equation 3.19.

$$J_i(x) = \underbrace{-D_i \frac{\partial c_i(x)}{\partial x}}_{\text{Diffusion}} - \underbrace{\frac{z_i F}{RT} D_i C_i \frac{\partial \phi(x)}{\partial x}}_{\text{Migration}} + \underbrace{C_i v(x)}_{\text{Convection}} \quad (3.19)$$

where  $J_i(x)$  is the flux of ionic species at distance  $x$  from the surface,  $D_i$  is the diffusion coefficient,  $\frac{\partial c_i(x)}{\partial x}$  is the concentration gradient at distance  $x$ ,  $\frac{\partial \phi(x)}{\partial x}$  is the potential gradient,  $z_i$  and  $C_i$  are the charge and concentration of species  $i$ ,  $v(x)$  is the velocity which a volume element in solution moves along the axis.

The migration term depends on the movement of charged species due to a potential field, i.e. anions migrate to the positive electrode whereas the cations move to the negative electrode [127]. The flux by convection refers to the transport of species controlled by the hydrodynamic motion of the liquid [127]. There are two types of convection; natural convection which exists due to density gradient and molecular vibration, and forced convection which is granted through external means of agitation. Diffusion occurs due to a gradient in concentration, i.e. species move from a region containing a high concentration of them to a more dilute region. The diffusion flux is proportional to that gradient and depends on a concentration boundary layer or diffusion layer formed at the vicinity of the electrode [127]. This diffusion layer arises due to the difference between the rate of transport of ions and the rate of reaction at the electrode surface.

The schematic in Fig. 3.2 shows the diffusion layer thickness which depends on the change in concentration of reactant species near the electrode surface. It can be observed that the actual thickness of the diffusion layer ( $\delta$ ) is placed where the concentration of the reactant species starts to differ from that of the bulk

concentration. In order to estimate the thickness of the diffusion layer, a model was developed by Nernst who established that there are two regions in the vicinity of the electrode surface [128]. The closest region corresponds to a stagnant diffusion layer whereby diffusion is the only mode of transport of reactant species. Outside this layer, the bulk solution is well stirred and convection dominates over the remaining modes of transport.

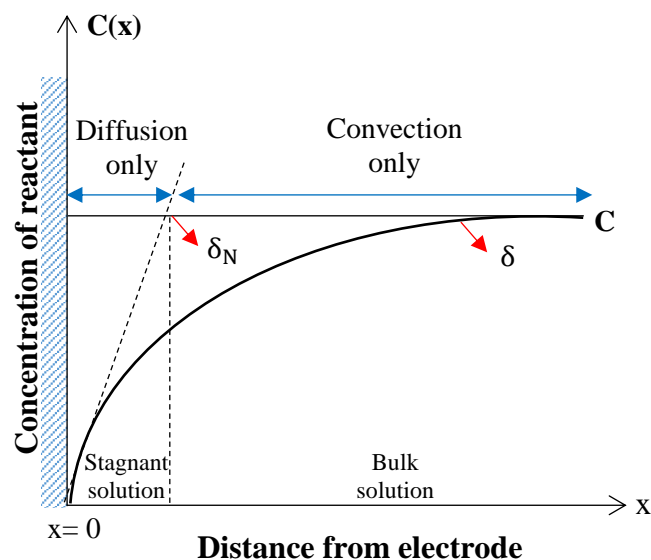


Figure 3.2 Nernst diffusion layer model for reactant species near to the vicinity of the electrode surface showing the actual boundary layer thickness ( $\delta$ ) and the Nernst diffusion layer thickness  $\delta_N$ . Adapted from [129].

For convenience, The Nernst diffusion boundary layer is often used for theoretical calculations and it can be estimated using equation 3.20.

$$\delta_N = 1.61\nu^{1/6}D^{1/3}\omega^{-1/2} \quad (3.20)$$

where  $\delta_N$  is the Nernst diffusion boundary layer,  $\nu$  is the kinematic viscosity,  $D$  is the diffusion coefficient, and  $\omega$  is the rotation rate of the electrode. If the overpotential is raised gradually, the reaction rate at the surface of the electrode keeps increasing [129], which means that the concentration of reactant in the vicinity of the electrode decreases as shown by the black curves in the concentration distance profile plot shown in Fig. 3.3. At some point, the replenishment of reactants is slower than that of the consumption which causes a depletion of the reactant species at the electrode surface [129]. When the supply of reactants from the bulk solution to the electrode surface is not enough, the surface concentration of reactant species is virtually zero [129] as indicated by the red curve in Fig. 3.3.

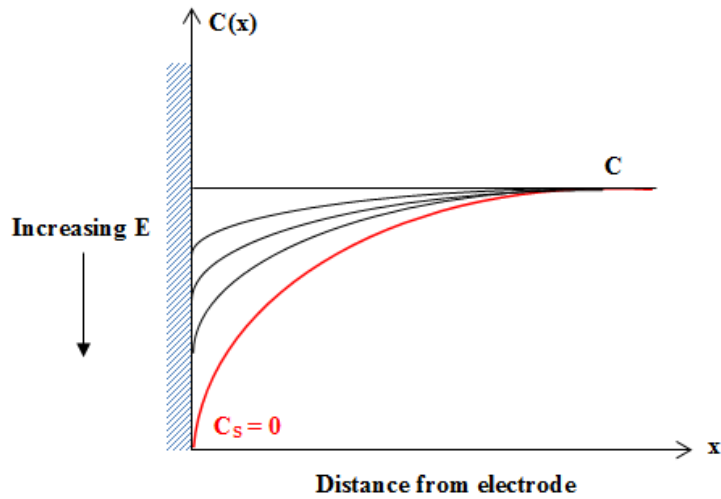


Figure 3.3 Concentration profile of reacting species as a function of the distance to the electrode surface. Adapted from [130].

At this point, when the surface concentration of the reactant species approximates to zero (cf. red curve in Fig. 3.3), the electrodeposition process is considered to be limited only by the mass transfer of reactant species since the maximum concentration gradient and maximum diffusion are achieved [129]. Under these conditions, the current density is known as the limiting current density ( $i_{lim}$ ) which in a polarization curve corresponds to the ‘flat’ or plateau region shown in Fig. 3.4. Despite an additional increase in overpotential, the limiting current density is not affected since the maximum rate of reduction has been attained. But at some point, the current density begins to increase again due to another reaction such as hydrogen evolution.

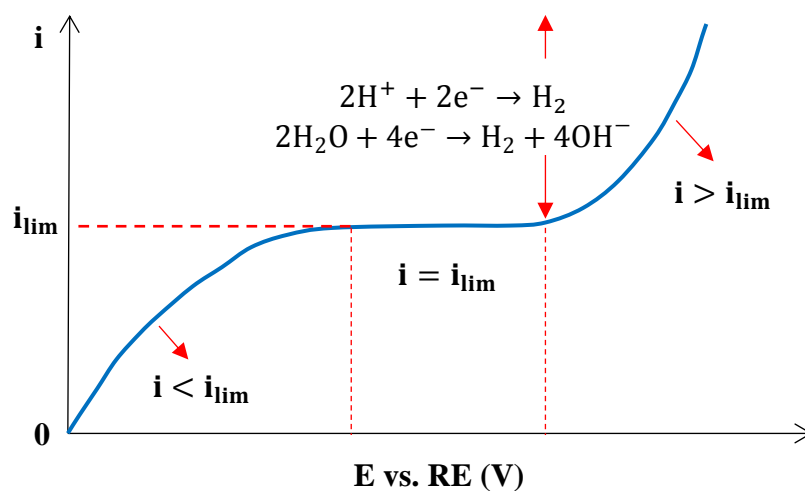


Figure 3.4 Schematic of the overpotential curve showing the limiting current density ( $i_{lim}$ ) as the plateau region of the curve. Adapted from [129].

Since this work has studied the electrochemical behavior of Cu using the rotating disk electrode, fundamental aspects of the RDE such as hydrodynamics, convective-diffusion and current distribution at the rotating disk electrode are discussed in the forth-coming sections.

### 3.5 Rotating disk electrode

The Rotating Disk Electrode (RDE) is a tool which allows one to impose force convection conditions [131]. The RDE is useful to study the mass transport and the electrode kinetics since both hydrodynamic equation and convective-diffusion equation have been solved for this type of electrode under steady-state conditions [131]. The working electrode is a disk electrode which is embedded in an insulator material. This non-conductive material generally is polytetrafluoroethylene (PTFE) or any other insulator. The function of the shaft is to electrically connect the working electrode to external connectors as well as to attach the disk electrode with a motor that imposes rotations to the electrolyte. In this fashion, the electrolyte is agitated at a certain frequency ( $f$ , Hz) from which an angular velocity can be obtained  $\omega = 2\pi f$ . Fig. 3.5 shows the basic components of the RDE (disk electrode, shaft and insulator) as well as the flow lines followed by the solution during agitation.

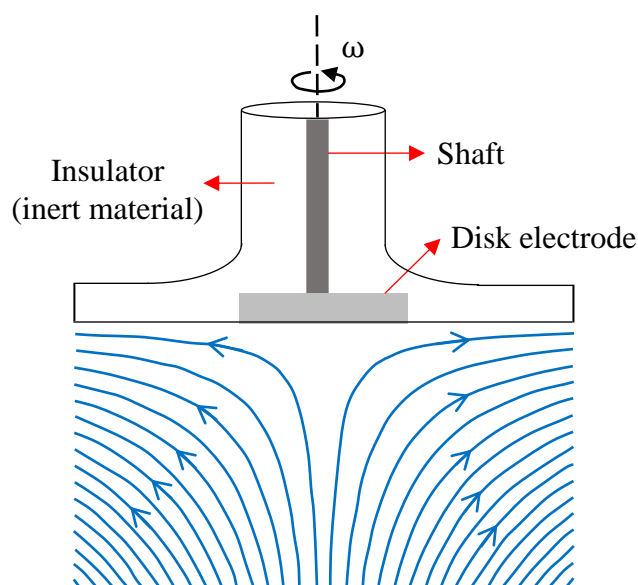


Figure 3.5 Schematic of the cross-section of the RDE showing its basic components and the flow lines followed by the liquid. Adapted from [131].

Karman [132] and Cochran [133] solved the hydrodynamic equation for the RDE under steady-state conditions by which the velocity profile at the RDE was defined. The authors defined that at the surface of the disk (e.g.  $y = 0$ ), the radial velocity ( $v_r$ ) and the disk velocity normal to the surface ( $v_y$ ) were zero as Fig. 3.6 (a) shows as well as equation 3.21.

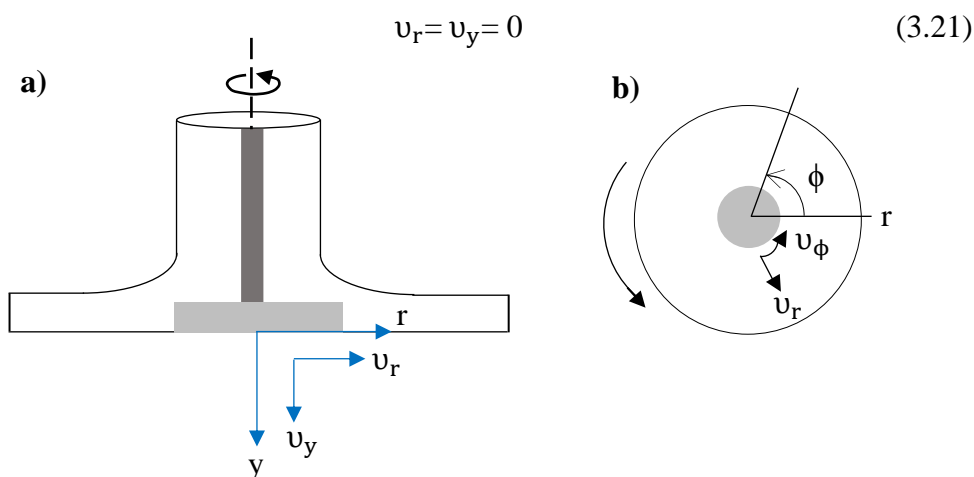


Figure 3.6 Coordinates useful to describe the solution velocity components in the  $y$ ,  $r$ , and  $\theta$  directions in the a) cross-section of the RDE and b) the bottom view of the RDE. Adapted from [131].

As the electrolyte was dragged along the electrode surface, the velocity depended on the rotation speed of the electrode and its radius (cf. Fig. 3.6 b) as equation 3.22 shows.

$$v_\phi = \omega r \tag{3.22}$$

Similar to the velocities nearby the electrode interface, the velocities have been established far from the disk electrode. For example, at the bulk solution ( $y \rightarrow \infty$ ), the radial and the angular velocities were negligible ( $v_r, v_\phi = 0$ ) but the disk velocity was related to a limiting velocity ( $v_y = -U_o$ ). Karman and Cochran [132, 133] determined that the relevant velocities near the surface ( $y \rightarrow 0$ ) of the RDE were the radial and the disk velocity, which relations are presented in equation 3.23 and 3.24.

$$v_r = 0.51\omega^{3/2}\nu^{-1/2}ry \tag{3.23}$$

$$v_y = -0.51\omega^{3/2}\nu^{-1/2}y^2 \tag{3.24}$$

The limiting velocity given by equation 3.25 holds when the disk electrode is placed far away, i.e. in the bulk solution ( $y \rightarrow \infty$ ).

$$U_o = \lim_{y \rightarrow \infty} v_y = -0.88447(\omega\nu)^{1/2} \quad (3.25)$$

Once the velocity profile at a RDE has been determined, the convective-diffusion equation can be solved by considering the appropriate boundary conditions [125]. Equation 3.26 shows the convective-diffusion relationship written in cylindrical coordinates.

$$v_r \left( \frac{\partial C_o}{\partial r} \right) + \frac{v_\phi}{r} \left( \frac{\partial C_o}{\partial \phi} \right) + v_y \left( \frac{\partial C_o}{\partial y} \right) = D \left[ \frac{\partial^2 C_o}{\partial y^2} + \frac{\partial^2 C_o}{\partial r^2} + \frac{1}{r} \frac{\partial C_o}{\partial r} + \left( \frac{1}{r^2} \frac{\partial^2 C_o}{\partial \phi^2} \right) \right] \quad (3.26)$$

Due to the complexity of this equation, a simplified expression was obtained considering that the concentration only depends on the normal distance from the disk [125], as shown in equation 3.27.

$$\underbrace{v_y \left( \frac{\partial C_o}{\partial y} \right)}_{\text{convection}} = D \underbrace{\frac{\partial^2 C_o}{\partial y^2}}_{\text{diffusion}} \quad (3.27)$$

Replacing equation 3.24 into equation 3.27 yields equation 3.28.

$$-0.51\omega^{3/2}\nu^{-1/2}y^2 \left( \frac{\partial C_o}{\partial y} \right) = D \frac{\partial^2 C_o}{\partial y^2} \quad (3.28)$$

Rearranging for  $\frac{\partial^2 C_o}{\partial y^2}$  and making  $B = \frac{(D\omega^{-3/2}\nu^{1/2})}{0.51}$  the following expression 3.29 is obtained.

$$\frac{\partial^2 C_o}{\partial y^2} = \frac{-y^2}{B} \frac{\partial C_o}{\partial y} \quad (3.29)$$

The integration of equation 3.29 yields equation 3.30.

$$C = \left( \frac{\partial C_o}{\partial y} \right)_{y=0} 0.8934 \left( \frac{3D\omega^{-3/2}\nu^{1/2}}{0.51} \right)^{1/3} \quad (3.30)$$

Since current represents the flux of reactant species to the electrode surface, equation 3.31 applies as follow.

$$i = nFAD \left( \frac{\partial Co}{\partial y} \right)_{y=0} \quad (3.31)$$

Under the limiting current conditions, where  $i = i_{lim}$ , the Levich equation was obtained as equation 3.32 shows.

$$i_{lim} = 0.620nFAD^{2/3}\nu^{-1/6}\omega^{1/2}C \quad (3.32)$$

where  $i_{lim}$  is the limiting current,  $n$  is the number of transferred electrons,  $F$  is Faraday's constant,  $A$  is the electrode area,  $D$  is the diffusion coefficient of electroactive species,  $\omega$  is the angular speed,  $\nu$  is the kinematic viscosity and  $C$  is the bulk concentration of the reactant. Levich equation applies to the mass transfer limited condition at the RDE and also predicts that  $i_{lim}$  of the system is proportional to the square root of the rotation speed and the bulk concentration of the reactant species [125].

After introducing the Levich equation, another useful expression was developed for the RDE that not only takes into account the transport of species but also the rate of the electrochemical half-cell reaction [125]. This relationship is known as the Koutecký-Levich equation [125], shown in expression 3.33.

$$\frac{1}{i} = \frac{1}{i_k} + \frac{1}{i_{lim}} \quad (3.33)$$

where  $i$  is the overall disk current,  $i_k$  is the current in the absence of any mass transfer effect or simply the kinetic current density and  $i_{lim}$  is the portion of the current limited by the convective diffusion process. Koutecký-Levich relationship allows one to obtain kinetic parameters such as the heterogeneous rate constant and charge transfer coefficient. A plot of  $i^{-1}$  vs.  $\omega^{-1/2}$  is expected to be linear and extrapolation to infinitely fast mass transport (e.g.  $\omega^{-1/2} = 0$ , where surface and bulk concentrations would be equal) yields  $i_k$  [125, 134]. The kinetic current density can be expressed as shown in equation 3.34.

$$i_k = nFk_f(E)C \quad (3.34)$$

where  $i_k$  is the kinetic current density,  $n$  is the number of transferred electrons,  $F$  is the Faradays' constant,  $k_f(E)$  is the potential-dependent rate constant and  $C$  is the concentration of species in the bulk electrolyte. Evaluating  $i_k$  at differing potentials allows one to determine  $k_f(E)$  [125], which logarithmic relation is shown in equation 3.35.

$$\ln k_f(E) = \ln k^0 - \frac{\alpha nF(E-E^{o'})}{RT} \quad (3.35)$$

where  $k^0$  is the standard heterogeneous rate constant,  $\alpha$  is the charge transfer coefficient,  $E$  is the electrode potential selected for analysis, and  $E^{o'}$  is the formal potential. An example of the plot corresponding to  $\ln k_f(E)$  vs.  $E-E^{o'}$  is shown in Fig. 3.7 from which  $\alpha$  and  $k^0$  can be computed from the slope ( $m$ ) and the intercept ( $b$ ), respectively.

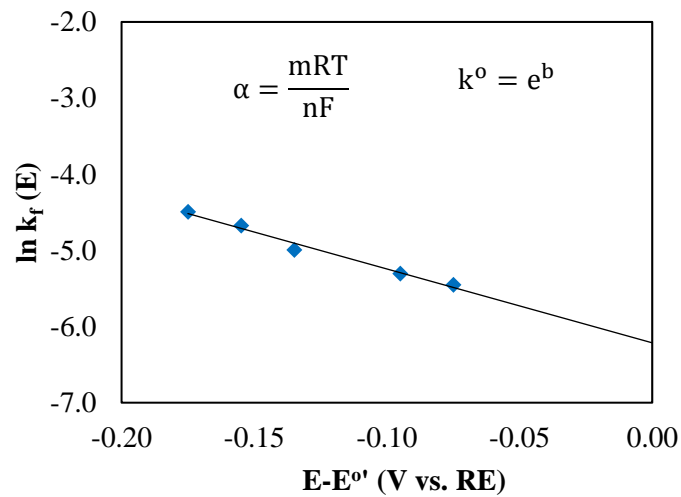


Figure 3.7 Plot of  $\ln k_f(E)$  against  $(E - E^{o'})$  from which heterogeneous rate constant and charge transfer coefficient can be calculated.



### *3.5.1 Current distribution at a Rotating Disk Electrode*

As per discussion in the above section, the RDE is popular to study the diffusivity and kinetics of electrode reactions because the hydrodynamics and the properties of mass transport have been extensively studied. However, one needs to understand the current distribution at the RDE. A uniform current distribution would mean that the current is evenly distributed at each point over the substrate length, which produces electrodeposits with almost the same thickness along the substrate. The current distribution at a RDE has been examined for two scenarios, when the applied current density was at the limiting current density and when the applied current density was set below the limiting current density [135].

Usually, in order to avoid powdery deposits and other issues, the applied current density is chosen as a fraction of the limiting current density. Once the applied current is lower than the limiting one, the lack of uniformity may arise due to ohmic drop potential in the electrolyte [135], which causes that the centre of the disk to be less accessible than the edge [136]. Thereby, the degree of uniformity of the current distribution is often governed by the non-uniform ohmic drop potential in the electrolyte [137].

The potential corresponding to ohmic drop depends on the conductivity of the electrolyte. Since the ionic conductivity of DESs have been measured to be much lower than the conductivity of aqueous solutions, this may be an issue for the eutectic systems. For instance, DES systems may exhibit a higher ohmic resistivity due to their low conductivity so that the ohmic drop potential becomes significant. The issues surrounding current distribution below the limiting current density at the RDE have been divided in two cases, e.g. the primary and the secondary current distribution [137].

### 3.5.2 Primary current distribution

The first case of the current distribution below the limiting current density is the primary current distribution, where kinetics and mass transport limitations are assumed to be negligible when compared to the ohmic resistance [137]. For instance, when the surface and concentration overpotential are insignificant compared to the potential corresponding to ohmic drop in the electrolyte, one can write equation 3.36.

$$\eta_{\Omega} \gg \eta_s + \eta_c \quad (3.36)$$

where  $\eta_{\Omega}$  is the overpotential due to ohmic drop,  $\eta_s$  corresponds to the surface overpotential, and  $\eta_c$  is the concentration overpotential. In this case, the current distribution is modelled based on geometric factors [137]. There several assumptions are considered: (i) the disc electrode is fixed within an infinite insulating material, (ii) the electrochemical cell is assumed to have no walls (iii) the counter electrode is placed far away from the working electrode, (iv) the solution is a diluted one and for this reason, (v) the diffusion coefficients, mobility and activity coefficients are assumed to be constant [137].

The solution for the primary current distribution has been proved to be complex even for the simplest geometry because it requires the solution of Laplace's equation [137]. For this reason, numerical calculation methods have been used to model only some geometries. For example, for a given configuration of two parallel electrodes within an insulating flow channel, the current distribution (red lines) and potential distribution (green lines) are represented in Fig. 3.8. It can be observed that the potential curves are getting closer to the edges of the electrode (point 1 and -1) and at these points "the current density is infinite" [137]. This phenomenon is ascribed to the capacity of the current to flow through the solution beyond the limits of the electrode [137]. Also, it is observed that the centre of the electrode (point 0) is the less reachable place so that at this point the electrode experiences a lower current density than that of the edge [137]. The primary current distribution of parallel electrodes along the length of the electrode is shown in Fig. 3.9, whereby infinite current develops at the edges of the electrode.

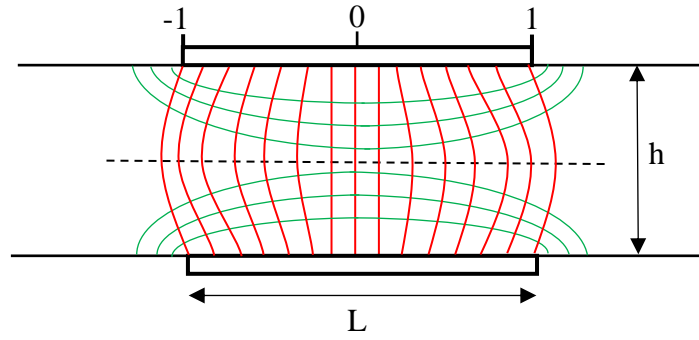


Figure 3.8 Potential distribution and current distribution at two parallel electrodes facing each other within an insulating flow channel. Equipotential surfaces (green) and current curves (red). The current distribution has been evaluated at the two edges of the substrate (e.g. points 1 and -1) whereby the current approaches infinite values. Adapted from [137].

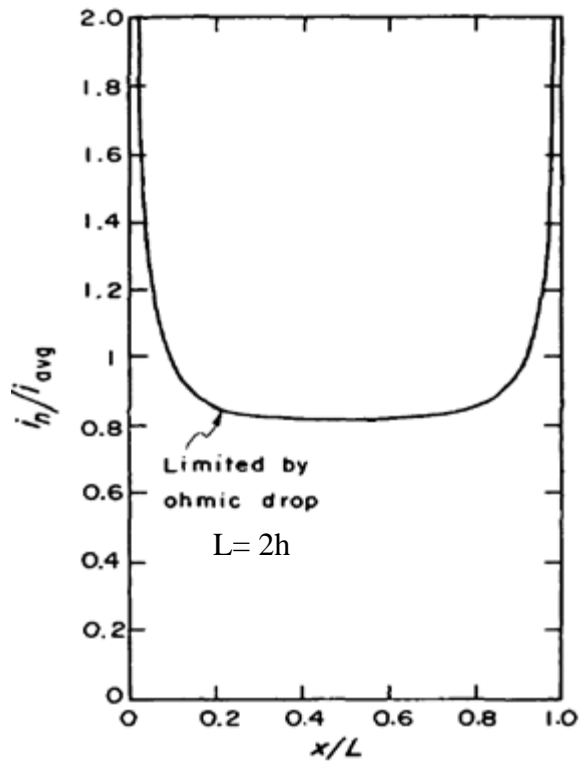


Figure 3.9 Primary current distribution for parallel planar electrodes. Adapted from [137].

The calculation of the primary current distribution for a rotating disk electrode was provided by Newman in 1966 [138]. The disk electrode was assumed to be embedded in an infinite insulating material and with the counter electrode placed far from the working electrode [138]. The equipotential lines (green) and the current distribution (red curves) are as shown in Fig. 3.10.

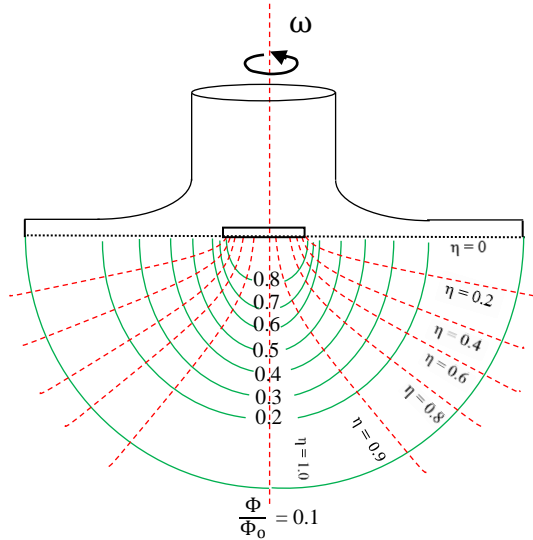


Figure 3.10 Equipotential lines and current distribution at a rotating disk electrode for the primary current distribution. Adapted from [138].

The equipotential curves are close together near to the edge of the electrode and at that point, the current density is infinite, being proportional to the square root of the distance from the edge near this point [138]. Likewise, the total current to the disk is as shown in equation 3.37.

$$I = 4\kappa r_0 \Phi_0 \quad (3.37)$$

where  $\kappa$  is the ionic conductivity,  $r_0$  the radius of the disk electrode and  $\Phi_0$  is the external potential extrapolated to the electrode surface. Since only geometric factors enter into the current distribution, the resistance to a hemispherical counter electrode at infinity can be expressed as equation 3.38 shows.

$$R = \frac{1}{4\kappa r_0} \quad (3.38)$$

where  $\kappa$  is the conductivity of the electrolyte and  $r_0$  is the radius of the electrode disk.

### 3.5.3 Secondary current distribution

Up to now, the analysis of the current distribution has not considered either kinetic or mass transfer limitations, which has resulted in the calculation of the primary current distribution. However, when the electrode reaction is sluggish, kinetics limitations cannot be ignored and the current distribution will be affected by the electrode polarisation [137, 139, 140]. This additional resistance has led to a lower current density at the edge of the electrode, i.e. the current at the edges are finite. As a result of this additional resistance at the electrode interface, the current distribution becomes more homogeneous and this type of distribution is known as the secondary current distribution. The analysis of the secondary current distribution still neglects mass transport limitations because the electrolyte is considered to be well-agitated.

In order to calculate the secondary current distribution, an expression that accounts for the surface overpotential as well as the potential derivative at the electrode interface had to be added to the mathematical analysis. Solutions for current distribution (below the limiting current density) use linear boundary conditions that translates to two limiting cases, e.g. linear polarisation and Tafel polarisation [135, 137].

#### 3.5.3.1 Secondary current distribution for linear polarisation

Linear polarisation occurs when the overpotential is small enough to produce a current density smaller than the exchange current density,  $|i| \ll i_0$ . Under this condition, the secondary current distribution ( $i/i_{avg}$ ) depends on geometric ratios ( $r_0/\kappa$ ) and the slope of the polarisation curve ( $d_i/d_{\eta_s}$ ) [135, 137], as relationship 3.39 shows.

$$\frac{d_i}{d_{\eta_s}} = (\alpha_a + \alpha_c) \frac{nF i_0 r_0}{RT\kappa} \quad (3.39)$$

where,  $r_0$  is the characteristic length of the system,  $\kappa$  is the conductivity of the electrolyte,  $\alpha_a$  and  $\alpha_c$  are anodic and cathodic charge transfer coefficients,  $n$  is the

number of transferred electrons,  $F$  is the Faraday's constant,  $i_o$  is the exchange current density,  $R$  is the gas constant,  $T$  is the absolute temperature. If one considers that the sum of the charge transfer coefficients is one, equation 3.39 can be expressed with the letter  $J$  known as the dimensionless exchange current density parameter [137], shown in equation 3.40.

$$J = \frac{nF i_o r_o}{RT\kappa} \quad (3.40)$$

This equation demonstrates that the current distribution is independent of the magnitude of the applied current but dependent on the exchange current density as long as the condition  $|i| \ll i_o$  holds.

The secondary current distribution for linear polarisation at an RDE has been solved by Newman [135]. Fig. 3.11 illustrates the family of curves that represents this type of current distribution on a disk electrode. One needs to remember that the electrolyte was assumed to be well-stirred so that the influence of the concentration overpotential was negligible, which is represented as  $N = \infty$  in Fig. 3.11.

If the dimensionless parameter  $J$  was small, (e.g. 0.1), the current distribution ( $i/i_{avg}$ ) appeared to be homogeneous exhibiting a flat profile from the centre to the edge of the deposit [137]. This phenomenon only occurs when electrodeposition is performed using the diffusion limiting current. However, as the magnitude of  $J$  increased, the current distribution between the centre and the edge become more significant, which meant that the distribution profile was less uniform [137]. Further, in the extreme case, when  $J$  approximates the infinite, the current distribution was comparable to the primary current distribution [137]. This profile is approached when the ohmic resistance dominates over the kinetic resistance at the electrode interface.

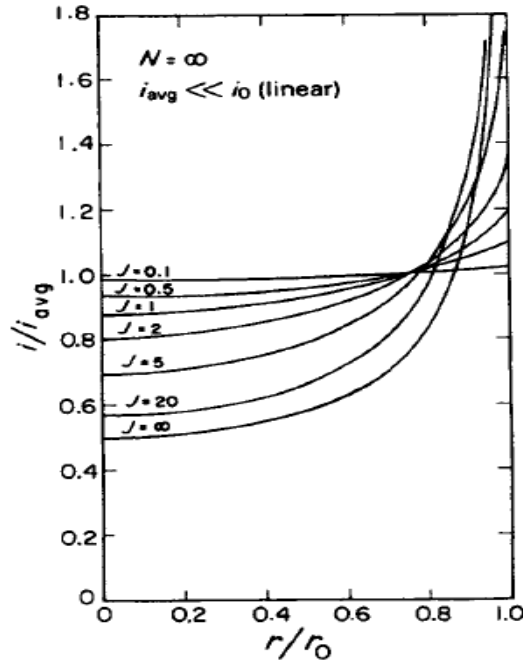


Figure 3.11 Secondary current distribution for linear polarisation at a disk electrode, where  $r/r_0 = 0$  is the centre of the electrode and  $r/r_0 = 1$  is the edge.  $N = \infty$  means that the variation of the concentration is not considered since the electrolyte was assumed to be well-agitated. Adapted from [135].

### 3.5.3.2 Secondary current distribution for Tafel polarisation

The other limiting case of the secondary distribution refers to Tafel polarisation. This type of polarisation dominates when the current density becomes higher than the exchange current density,  $|i| \gg i_0$  [137]. In this regard, when cathodic polarisation dominates, the anodic exponential term in the Butler-Volmer relation (equation 3.41) becomes negligible as equation 3.42 shows.

$$i = i_0 \left[ \exp \left\{ \frac{\alpha_a n F}{RT} \eta_s \right\} - \exp \left\{ -\frac{\alpha_c n F}{RT} \eta_s \right\} \right] \quad (3.41)$$

$$\exp \left\{ \frac{\alpha_a n F}{RT} \eta_s \right\} \ll -\exp \left\{ -\frac{\alpha_c n F}{RT} \eta_s \right\} \quad (3.42)$$

Thus, equation 3.41 (Butler-Volmer) can be written as equation 3.43.

$$i = -i_0 \exp \left( -\frac{\alpha n F}{RT} \eta_s \right) \quad (3.43)$$

Expressing equation 3.43 as the absolute value of the current and taking the natural logarithm (as equation 3.44 shows) one can obtain equation 3.45.

$$\ln|i| = \ln \left[ i_o \exp \left( - \frac{\alpha nF}{RT} \eta_S \right) \right] \quad (3.44)$$

$$\ln(i) = \ln(i_o) - \frac{\alpha nF}{RT} \eta_S \quad (3.45)$$

Rearranging equation 3.45 in terms of the overpotential yields equation 3.46

$$\eta_S = \frac{RT}{\alpha nF} [\ln(i_o) - \ln(i)] \quad (3.46)$$

The derivation of the overpotential with respect to the current density (equation 3.46) produces equation 3.47.

$$\frac{d\eta_S}{di} = - \frac{RT}{\alpha nFi} \quad (3.47)$$

Similar to the dimensionless current density parameter  $J$  ascribed to linear polarisation and discussed in section 3.5.3.1, the  $\delta$  letter has been assigned when Tafel polarisation proceeds and it is known as the dimensionless average current density [137]. The equation 3.47 is more conveniently expressed as equation 3.48.

$$\delta = \frac{d\eta_S}{di} = - \frac{RT}{\alpha nFi_{avg}} \quad (3.48)$$

where  $(d\eta_S/di)$  is the derivative of the overpotential to the current density,  $R$  is the gas constant,  $T$  is the absolute temperature,  $\alpha$  is the charge transfer coefficient,  $n$  is the number of transferred electrons,  $F$  is the Faraday's constant and  $i_{avg}$  is the average current density of the system.



### 3.5.4 Wagner number

The Wagner number ( $Wa$ ) is a useful dimensionless group in order to estimate the current distribution at the interface of an electrode [141]. This number has been defined as the ratio of the impedance of the reaction (activation resistance) over the electrical resistance of the solution (ohmic resistance) [141]. Equation 3.49 shows the relationship amongst these resistances.

$$Wa = \frac{d\eta_S}{di} / \frac{r_o}{\kappa} = \frac{d\eta_S}{di} \frac{\kappa}{r_o} \quad (3.49)$$

Replacing the activation resistance or  $\delta$  parameter defined in equation 3.48 in equation 3.49, the  $Wa$  can be written as equation 3.50.

$$Wa = - \frac{RT\kappa}{\alpha F i_{avg} r_o} \quad (3.50)$$

where most of the parameters have been detailed before in equation 3.48,  $r_o$  is the radius of the disk electrode and  $\kappa$  is the conductivity of the electrolyte. Fig. 3.12 shows a set of curves that corresponds to differing  $Wa$ . The y axis shows the corresponding current distribution expressed as a normalized local current density against the average current density, e.g.  $i/i_{avg}$  while the x axis correspond to the length of the substrate, i.e. number zero is the centre whereas number one is the edge of the substrate.

A large magnitude of  $Wa$  such as 9.9 is indicative of a uniform distribution of the current at the electrode interface [141]. This means the centre current density is approximately the same that the edge current density. However, as the value of  $Wa$  decreases, the density at the edge is higher than the one at the centre, which lead to a deterioration of the current distribution [141]. Moreover, when  $Wa \sim 0$  the primary current distribution is approached, wherein the current at the edge seems to be infinite. For a disk electrode, this phenomenon is plausible due to a reduced ohmic drop potential near to the edge of the electrode which induces a higher current density nearby this region of the electrode. Also,  $Wa$  can be susceptible to conductivity changes, in a fashion when the more conductive the solution, the more uniform the current distribution or deposit thickness is expected to be [137].

However,  $Wa$  is a function of other parameters such as the current density that play a significant role on the current distribution for Tafel polarisation. Thereby, the behaviour of each electrochemical system should be scrutinised individually.

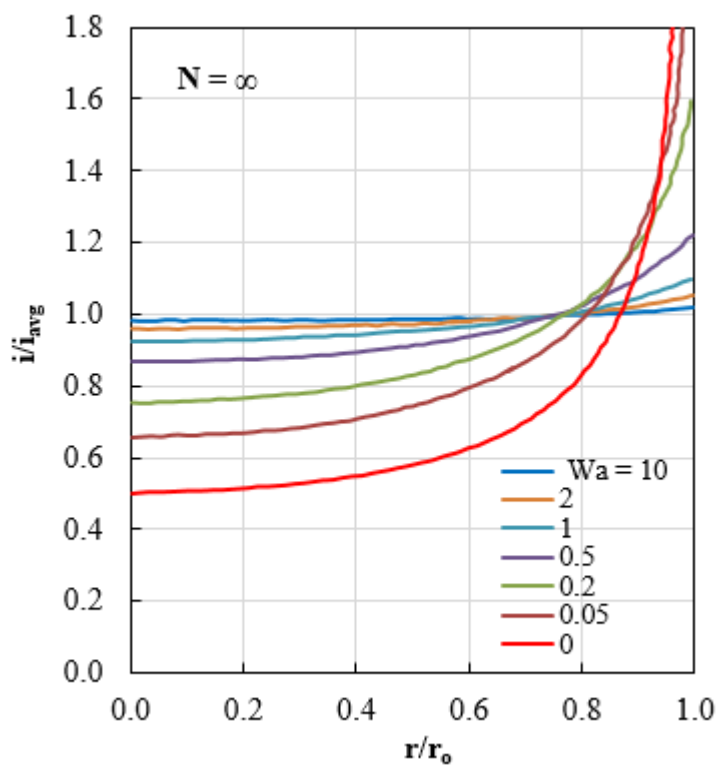


Figure 3.12 Secondary current distribution for Tafel polarisation at a disk electrode of radius  $r_0$ . The set of curves corresponds to various values of  $Wa$ .  $N = \infty$  means that mass transport limitations have been neglected since the electrolyte has been assumed to be well-agitated. Adapted from [135].

## **4. Chapter – Experimental**

## 4. Experimental

---

### 4.1 Measurement of water content

The deep eutectic solvent known as ethaline was prepared by mixing choline chloride ( $C_5H_{14}NOCl$ ) and ethylene glycol ( $C_2H_6O_2$ ) in a 1:2 molar ratio. Both choline chloride (ChCl) and ethylene glycol (EG) (Sigma Aldrich, purity >98%) were not dried in order to measure the initial concentration of water in ethaline was measured. The mixture was gently agitated using a stirring plate at 60 °C until a colourless and homogeneous liquid was obtained.

Thereafter, technical grade hydrated cupric chloride salt ( $CuCl_2 \cdot 2H_2O$ , Merck) was dissolved in ethaline to prepare 0.20 M solutions. This concentration was determined to be the optimal to yield reasonably dense deposits [89]. Two additional samples were prepared (0.05 and 0.10 M  $CuCl_2 \cdot 2H_2O$ ) in order to measure the water content with differing amounts of hydrated salt. For simplicity, the copper-containing solutions will be referred as “electrolyte” in the text.

Water content was measured using Karl Fischer (KF) chemical titration. To establish the adsorption of water with time, ethaline and the electrolyte (100 mL) were exposed to the air to be monitored over a month. Another beaker filled with ethaline was sealed with Parafilm paper to ascertain whether or not the ingress of water could be prevented by this provision. From these solutions, samples were collected each week to be analysed. During these experiments, no attempt was made to control humidity so results are approximated. Also, in order to determine the saturation point of the electrolyte, it was monitored for three additional months. Over this period, samples were withdrawn once a month. The level of humidity was not monitored as it remained relatively constant between 30-40% at room temperature.

#### 4.1.1 Karl Fischer titration principle

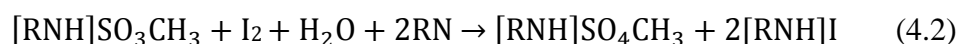
KF titration is an analytical technique which quantitatively determines the concentration of water in a variety of matrices [142]. There are two types of titration, the volumetric and coulometric one [143]. The coulometric titration has been suited

to detect small amounts of water from 0.01 mg [143, 144] whereas the volumetric titration can detect from 0.10 to 500 mg of water in a given sample volume [143]. Since the waters of hydration of 0.20 M  $\text{CuCl}_2 \cdot 2\text{H}_2\text{O}$  already accounted for  $\sim 7.2 \text{ mg mL}^{-1}$ , volumetric titration was most appropriate.

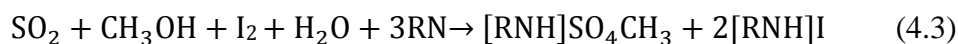
The fundamental principle of the KF reaction is based on the equimolar consumption of water in the presence of iodine ( $\text{I}_2$ ), sulphur dioxide ( $\text{SO}_2$ ), a base (RN) and an alcohol (usually methanol,  $\text{CH}_3\text{OH}$ ) [145, 146]. The KF reaction proceeds in two consecutive steps. Equation 4.1 shows the first reaction step, where  $\text{SO}_2$  reacts with  $\text{CH}_3\text{OH}$  and RN to form an intermediate compound known as the alkylsulfite salt, e.g.  $[\text{RNH}]\text{SO}_3\text{CH}_3$  [145].



The subsequent step is shown in equation 4.2 where the alkylsulfite intermediate is oxidised to alkylsulfate ( $[\text{RNH}]\text{SO}_4\text{CH}_3$ ) while water reacts with  $\text{I}_2$  [145].



The sum of equations 4.1 and 4.2 is the KF reaction as equation 4.3 indicates [145]. The KF reaction shows that one mole of  $\text{I}_2$  was consumed for each mole of water while the oxidation of  $\text{SO}_2$  to alkylsulfate occurred simultaneously [145].



The amount of water in a sample was determined by the relationship shown in equation 4.4a [145].

$$m_{\text{H}_2\text{O}} = w_{\text{E}} V \quad (4.4a)$$

where  $m_{\text{H}_2\text{O}}$  is the mass of water in the sample,  $w_{\text{E}}$  is the water equivalent that is a known value ( $5 \text{ mg H}_2\text{O mL}^{-1}$ ) and  $V$  is the consumed titrating reagent (in mL) which is regulated by the automatic burette.

Additionally, the water content can be expressed as weight percent based on the relation 4.4b.

$$\text{wt\% H}_2\text{O} = \frac{m_{\text{H}_2\text{O}}}{m} \times 100\% \quad (4.4b)$$

The endpoint of the titration was detected through bipotentiometric indication [145], which was possible due to an electrochemical reaction that occurred at the twin Pt electrode (Fig. 4.1). The principle of the bipotentiometric detection is to polarise the double Pt electrode with a small current while the potential difference between the electrodes is monitored [146, 147]. When water is exhausted, free I<sub>2</sub> molecules are available to be reduced to iodide ions (I<sup>-</sup>) and oxidised back to I<sub>2</sub> as equations 4.5 (a) and 4.5 (b) show [145, 146]. Those reactions generate a flow of electrons so that to maintain a constant polarisation current, the potential difference has to drop below the initial value, which is indicative of the titration endpoint [145].

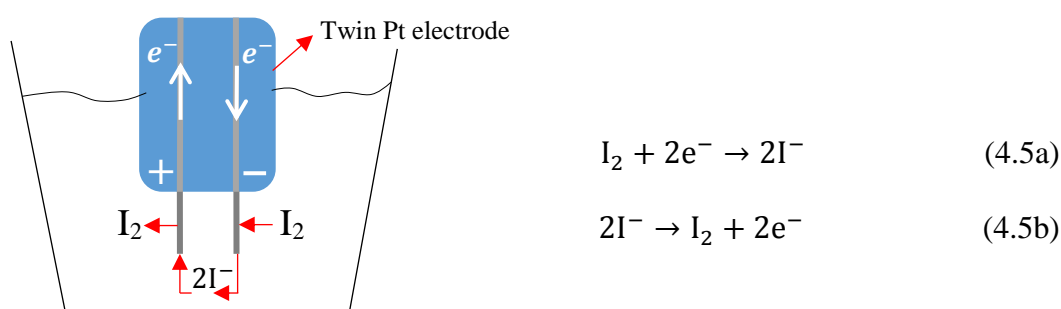


Figure 4.1 Schematic of the Karl Fischer titration vessel showing the twin Pt electrode for the detection of the end-point of the titration. Adapted from [145].

#### 4.1.2 Materials and apparatus of Karl Fischer titration

The titration experiments were performed at the Continuous Manufacturing and Crystallisation Centre (CMAC) of Strathclyde University using a Karl Fischer moisture titrator MKH-700 (Kem-Kyoto Electronics). Fig. 4.2 shows the schematic of the KF airtight titration vessel. The solvent medium was Methanol dry (100 mL) and the titrating reagent was Hydranal composite 5 (Fluka Analytical, >98%). Hydranal water standard 0.1 was used to verify the water equivalent of the titrating reagent (Fluka Analytical, > 98%). The samples were injected into the vessel using a

Hamilton syringe of 1 mL of volume and weighed using a Sartorius Quintix balance ( $\pm 0.1$  mg).

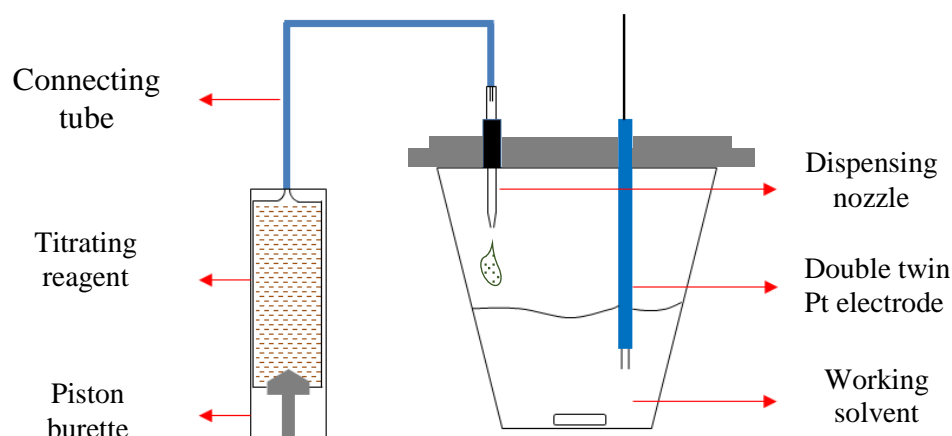


Figure 4.2 Schematic of the KF titration vessel and the automatic burette used to determine water content. Adapted from [145].

#### 4.1.3 Experimental procedure of Karl Fischer titration

Firstly, the burette was purged with the titrating reagent. A pre-titration was then performed to consume any remaining moisture from methanol. Later, the water equivalent of the titrant was verified using the Hydranal water standard. Afterwards, the testing samples were injected into the titration vessel. Due to the high viscosity of the samples, they had to be injected slowly to prevent the adhesion to the vessel walls, which would lead to erroneous results. The Hamilton syringe was weighed before and after injecting the sample so that the concentration of water was calculated using equation 4.4b. The experiments were repeated ten times to check for reproducibility.

An additional experiment was performed to construct a calibration curve (measured water by KF against added water). In that manner, the initial water content of the electrolyte would be calculated using the regression equation from the calibration line. In order to do that, a set of eight samples was prepared. As per the method of standard addition, known amounts of DI water were added to ethaline from 2 to 16 wt% (in 2 wt% intervals). A beaker was placed on the scale (Sartorius MC1,  $\pm 0.01$  g) and filled with blank ethaline, afterwards the scale was zeroed and DI

water was added using an automatic pipette. Thereafter,  $\text{CuCl}_2 \cdot 2\text{H}_2\text{O}$  salt was dissolved to obtain a concentration of 0.20 M. Those samples were analysed following the same titration procedure.

#### 4.1.4 Near-Infrared spectroscopy principle

Near-infrared (NIR) spectroscopy is an alternative non-destructive method to measure water content in a sample. Thereby, to cross-check the initial concentration of water (measured by KF titration) NIR spectroscopy was performed. Before discussing the experimental procedure, the principle of NIR spectroscopy will be summarised.

The NIR region ranges in wavelengths between 800 and 2500 nm in the electromagnetic spectrum, as Fig. 4.3 shows [148]. Infrared radiation stimulates the vibration of the molecules. Thereby, the NIR spectrum of a substance will be a reflection of its molecular composition [149, 150]. For instance, chemical substances possess distinctive functional groups such as O-H, C-H, N-H and S-H whose atoms are linked through chemical bonds [150]. The required energy to disturb a chemical bond from its equilibrium state will be different for each functional group. Thereby, the distinctive bands in the NIR region will be a reflection of that energy variation [148].

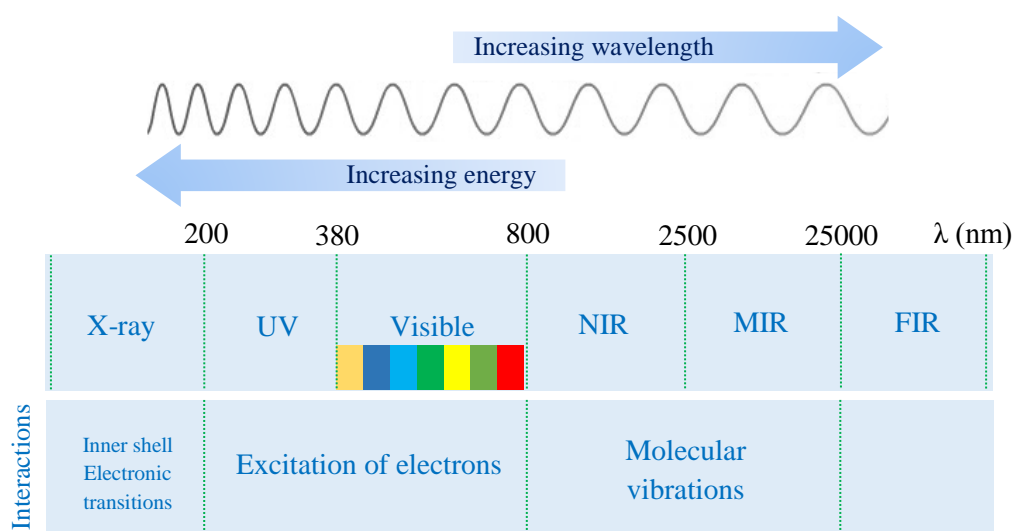


Figure 4.3 Electromagnetic spectrum showing the UV-Vis and NIR region from 800 to 2500 nm. Adapted from [151].



In practice, molecules that absorb NIR energy usually vibrate in two modes: stretching and bending [149]. In the stretching mode the distance between the atoms is constantly changing whereas in the bending mode the atoms vibrate in way that the bond angles change [149]. Fig. 4.4 illustrates stretching and bending vibration modes. NIR absorption bands arise when overtones and combinations of the vibration modes occur. For instance, the interaction between stretching and bending vibrations is known as a combination whereas a change of more than one level of energy is known as an overtone [149].

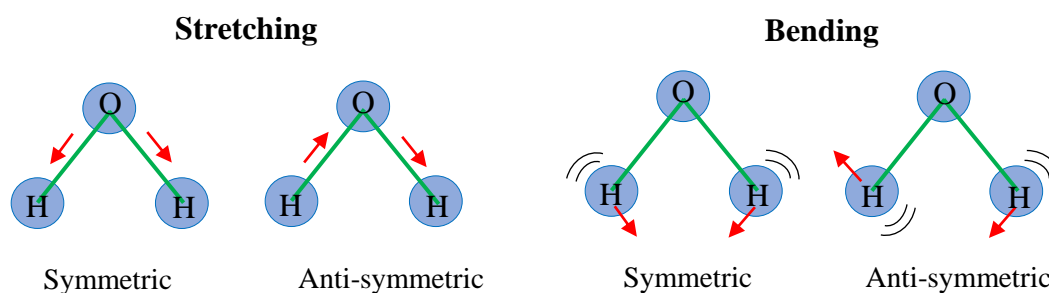


Figure 4.4 NIR vibrational modes of water: stretching and bending vibrations with symmetric and anti-symmetric modes [152].

Water possesses the O-H chemical bonds which are active in the NIR region and exhibit three fundamental vibrations, e.g. symmetric and anti-symmetric stretching and symmetric bending [152, 153]. The interactions amongst those vibrations give rise to three absorption bands of water in the NIR region [153]. Two of those bands are related to the first and second overtone of water while the third band arises due to the combination of the O-H stretching with the H-O-H bending of water [153]. The first overtone of water is observed nearby 1400 nm whereas a distinctive absorption peak around 1900 nm corresponds to its combination mode [153]. Since water exhibits a unique NIR spectrum, the content of water can be quantified analytically from Beer's law that establishes the absorbance of an analyte is proportional to its concentration (equation 4.6) [150]. Beer's law will be discussed in detail in the upcoming section.

$$A = C \varepsilon b \quad (4.6)$$

where A is the absorbance, C is the concentration of the analyte,  $\varepsilon$  is the molar absorptivity of the analyte and b is the path length of the cuvette.

Using the absorbance data against standard solutions (known amounts of added water), a calibration curve was constructed from which the initial concentration of water in the electrolyte was cross-checked. Due to the fact that a calibration curve could be derived, the NIR method may be a useful technique for process monitoring in a practical plating titration because water content can be monitored in-situ without pre-treatment, chemicals or consumables.

#### 4.1.5 Materials and apparatus of NIR spectroscopy

The same set of samples analysed by KF titration was used to measure the absorbance in the NIR region. This set of samples consisted of eight samples with known amounts of added water from 2 to 16 wt% (in intervals of 2 wt%). The concentration of Cu (II) species was adjusted to be 0.20 M. The NIR spectrum of each sample was acquired using a Cary Varian 5000 spectrophotometer between a wavelength of 600 and 2200 nm. The data interval corresponded to 1 nm and the integration time was set up to 0.1 s leading to a scan rate of 600 nm min<sup>-1</sup>. Each NIR spectrum was smoothed to improve the signal to noise ratio using the Cary WinUV Software.

The NIR measurements were carried out using a quartz magnetic cuvette of pathlength 125  $\mu\text{m}$  (Starna DMV Biocell) since water and Cu<sup>2+</sup> species are strongly absorbing. The cuvette was demountable and an internal magnetic mechanism held it together. The narrow compartment of the cuvette was filled up using an automatic pipette (range from 20 to 200  $\mu\text{L}$ ). Also, a magnifying glass (Starna DMV Biocell) was used to observe if bubbles were trapped in the solution compartment. Images of the magnetic cuvette and the magnifying glass are shown in Fig. 4.5.

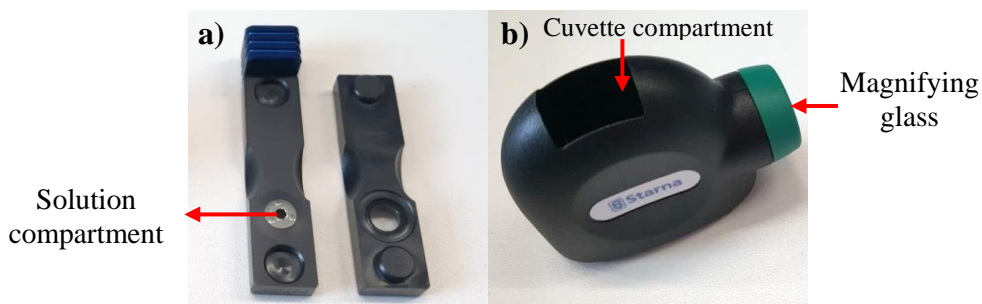


Figure 4.5 a) Demountable quartz magnetic cuvette (125  $\mu\text{m}$  pathlength) used for spectroscopy measurements and b) magnifying glass to check for bubbles.

#### *4.1.5.1 Experimental procedure of NIR spectroscopy*

The spectrophotometer was turned on two hours before carrying out the measurements so that the equipment had sufficient time to stabilise the NIR lamp source. Prior to running the measurement, a baseline correction with ethaline as the blank was performed. This step was necessary to correct for any absorption from the solvent. Notably, it was not necessary to repeat the baseline correction before each measurement because the Cary WinUV software stored and subtracted the baseline automatically.

Next, the cuvette was disassembled and thoroughly washed with DI water and thereafter dried with compressed air. Using the automatic pipette, a volume of 40  $\mu\text{L}$  of the test sample was transferred to the cuvette compartment. After, it was verified that bubbles were not trapped using the magnifying glass. This verification was important to avoid that bubbles interfered in the acquisition of the NIR spectra. The procedure was repeated to analyse each test sample.

## 4.2 Monitoring of Cu speciation on water-containing electrolyte

In order to determine if the inclusion of water in the electrolyte affected the speciation of the main electroactive species,  $[\text{CuCl}_4]^{2-}$ , the electronic spectrum was monitored using UV-Vis spectroscopy. To perform the analysis, a set of samples was prepared by adding known amounts of DI water to blank ethaline until reaching a total water content ranging from 1 to 40 wt%. Thereafter,  $\text{CuCl}_2 \cdot 2\text{H}_2\text{O}$  salt was dissolved to prepare 0.20 M solution. However, due to the out-of-range absorbance signal, e.g.  $A > 4$  (which is the maximum absorbance that Cary 5000 spectrophotometer can measure accurately); another solution had to be prepared with a lower metal loading, e.g. 0.05 M.

### 4.2.1 Ultraviolet Visible spectroscopy principle

Section 4.1.4 discussed that infrared radiation influenced the vibration of the molecules. On the contrary, UV-Vis radiation causes electronic excitation, which means that electrons are promoted to higher energy orbitals [154]. The fundamentals of UV-Vis spectroscopy relies on measuring the difference between the radiant power of the light before and after striking an absorbing solution [154]. Moreover, since light is absorbed by the species in the sample, the radiant power from the emerging beam will be smaller than the incident beam,  $P < P_0$  as Fig. 4.6 shows.

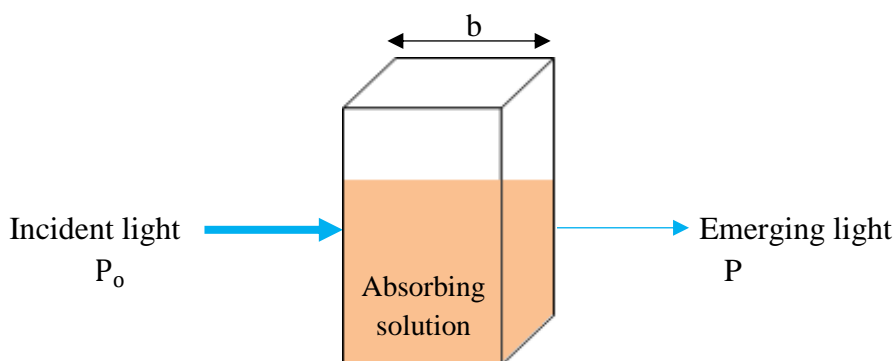


Figure 4.6 Schematic of the incident radiant power and the emerging radiant light after passing through an absorbing solution. Adapted from [154].

An illustration of a double-beam spectrophotometer is shown in Fig. 4.7 [154]. It can be observed that the monochromator chooses a narrow band from the beam light. Thereafter, the incident radiant power ( $P_0$ ) hits the cuvette that contains the blank solution while the emerging radiant power ( $P$ ) is detected after travelling across the testing solution. The source of ultraviolet light is usually a deuterium lamp whereas visible light is generated using a tungsten lamp. However, modern spectrophotometers such as CARY 5000 usually consist of a more complex instrumentation.

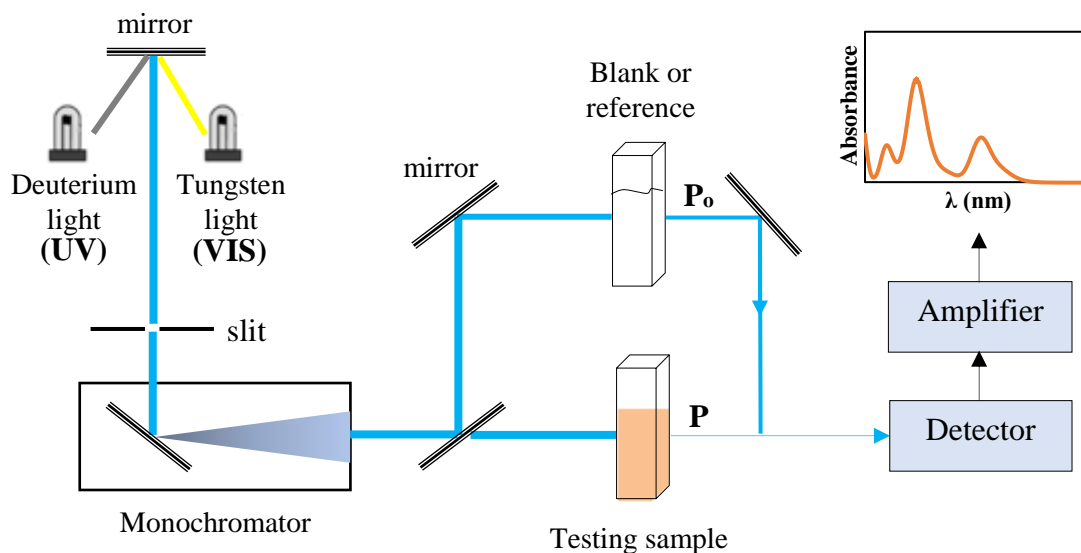


Figure 4.7 Diagram of a spectrophotometer showing its basic components and instrumentation. Adapted from [154].

The relationship between the incident and the emerging radiant power has been defined as the transmittance as indicated in equation 4.7.

$$T = \frac{P}{P_0} \quad (4.7)$$

where  $T$  is the transmittance,  $P_0$  radiant power of the incident light and  $P$  is the radiant power of the emerging light.

However, a more convenient expression can be written if the absorbance is the logarithmic function of the transmittance [154], as equation 4.8 shows.

$$A = -\log T = \log \left( \frac{P_o}{P} \right) \quad (4.8)$$

The fact that the absorbance is a logarithmic function can be explained by analysing Fig. 4.8. When the pathlength of an absorbing solution ( $b$ ) is divided in infinitesimal sections ( $dx$ ), a drop in power occurs ( $dP_o$ ) [154]. Consequently, in the following layers a decrease in power continues because the magnitude of the incident light has been already decreased ( $P_o - dP_o$ ) [154]. The drop in power is proportional to various parameters such as the incident power, the concentration of the absorbing species, the thickness of the infinitesimal section, and to a constant of proportionality [154]. That relationship is shown in equation 4.9, where the negative sign indicates a decreasing radiant power.

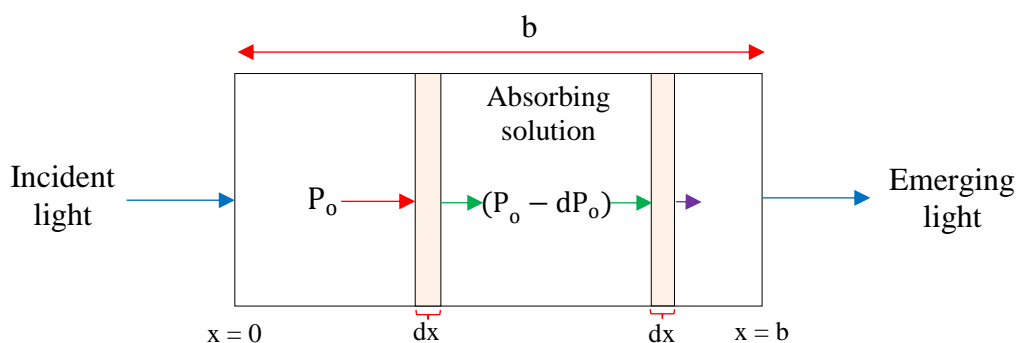


Figure 4.8 Schematic of the logarithmic relationship between transmittance and absorbance of a solution [154].

$$dP_o = -\beta P_o C dx \quad (4.9)$$

where  $dP_o$  is the radiant power drop,  $\beta$  is a constant of proportionality,  $P_o$  is the incident radiant power,  $C$  is the species concentration and  $dx$  is the infinitesimal section of the pathlength.

By rearranging and integrating both sides of the equation 4.9, equation 4.10 (d) can be obtained.

$$-\frac{dP_0}{P_0} = \beta C dx \quad (4.10a)$$

$$-\int_{P_0}^P \frac{dP_0}{P_0} = \beta C \int_0^b dx \quad (4.10b)$$

$$-[\ln P - \ln P_0] = \beta C b \quad (4.10c)$$

$$\ln\left(\frac{P_0}{P}\right) = \beta C b \quad (4.10d)$$

By applying the  $\ln x = (\ln 10)(\log x)$  in equation 4.10 (d), equation 4.11 is yielded.

$$\log\left(\frac{P_0}{P}\right) = \left(\frac{\beta}{\ln 10}\right) C b \quad (4.11)$$

Inserting equation 4.8 in equation 4.11 and since  $\frac{\beta}{\ln 10}$  is a constant, equation 4.12 can be derived which is Beer's law.

$$A = C \epsilon b \quad (4.12)$$

where  $\epsilon$  is the molar absorptivity of the absorbing species,  $b$  is the pathlength of the cuvette and  $C$  is the concentration of the absorbing species in the solution.

#### 4.2.2 Materials and apparatus of UV-Vis spectroscopy

The UV-Vis spectra wavelengths of the samples were recorded using a Cary Varian 5000 spectrophotometer between 200 to 600 nm. The step interval was adjusted to be 1 nm and the integration time to 0.2 s resulting in a scan rate of 300 nm min<sup>-1</sup>. A demountable quartz cuvette of 125  $\mu\text{m}$  pathlength was used due to the high absorption of the 0.20 M Cu (II) species. Despite this thin pathlength, the absorbance of the electrolyte was still high that the signal was distorted by background noise as Fig. 4.9 shows. Similar difficulties for measuring the spectrum of concentrated solutions have been encountered by other groups [105, 155]. Thereafter, a less concentrated solution, 0.05 M Cu (II), ensured a reproducible spectrum less distorted by the instrumental noise (cf. dashed curve in Fig 4.9).

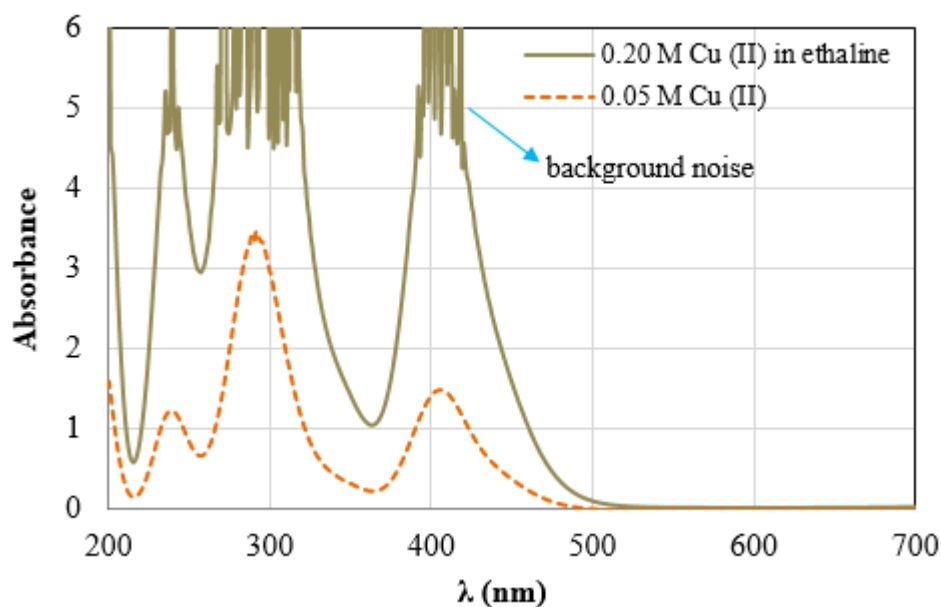


Figure 4.9 UV-Vis spectrum of 0.20 M Cu (II) species in ethaline acquired with the magnetic cuvette of 125  $\mu\text{m}$  pathlength.

The use of a quartz cuvette of lower pathlength (10  $\mu\text{m}$ ) has been recommended by Zhang's group in order to characterise the speciation of highly absorbing solutions [156]. The cuvette consisted of two quartz plates (Starna Scientific, type 20-C/Q/0.01) clamped together with a special holder (Starna Scientific, type CH/2049). Fig. 4.10 (a) shows the schematic of this type of cuvette in which sample was transferred and the plates were assembled. Although the UV-Vis



spectrum of the electrolyte was achievable, the absolute absorbance was not reproducible as Fig. 4.10 (b) shows due to the uncertainties in the pathlength. Thereby, this type of cuvette could not be used for quantitative analysis.

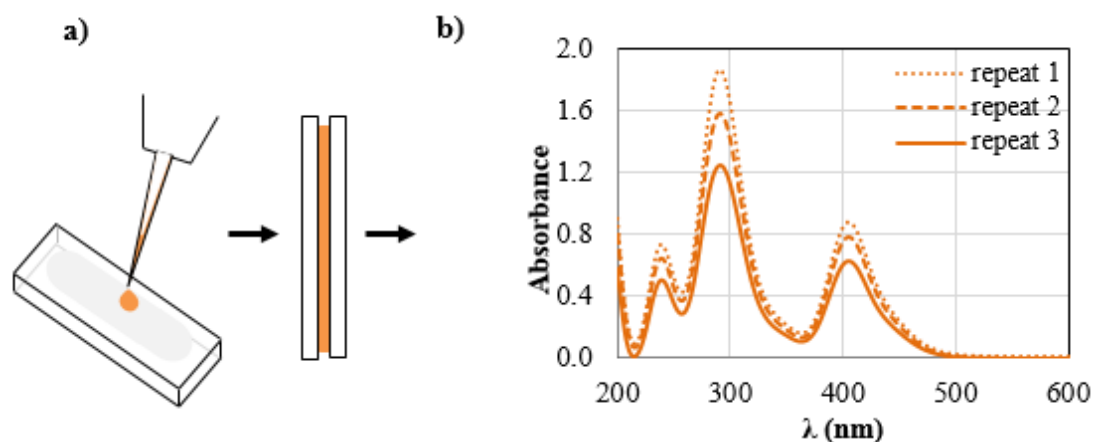


Figure 4.10 a) Schematic of the quartz cuvette with a narrow pathlength, e.g. 10  $\mu\text{m}$  and b) UV-Vis spectra of 0.20 M Cu (II) which were not reproducible due to the uncertainties in the thin pathlength of the cuvette.

#### 4.2.3 UV-Vis test procedure

Similar to the NIR experiment, the spectrophotometer was power on a couple of hours prior to conduct the measurements in order to warm up the UV-Vis lamps. The correction of the baseline was carried out using ethaline as the blank solution. Thereafter, a volume of 40  $\mu\text{L}$  of the sample (0.20 M  $\text{Cu}^{2+}$  in ethaline without added water) was placed in the magnetic cuvette of 125  $\mu\text{m}$  pathlength. Also, it was verified that no bubbles were trapped within the compartment with the magnifying glass. Before each measurement the cuvette was cleaned with DI water and dried with compressed air.

### **4.3 Physicochemical and electrochemical properties as a function of water content**

#### *4.3.1 Electrolyte preparation*

To examine the effect of water on physico-chemical and electrochemical properties such as density, viscosity, conductivity and electrochemical window, ethaline and copper-containing solutions (electrolytes) were prepared. At this point, the amount of moisture adsorbed by the electrolyte has been determined on a weekly basis over a period of a month. Thereafter, to prepare the solutions with the same total content of moisture, known amounts of DI water were added to ethaline and to the electrolyte to obtain 1, 3, 6, 10 and 15 wt%. Since the concentration of Cu (II) species decreased by the addition of H<sub>2</sub>O, cupric salt was dissolved to replenish the concentration back to 0.20 M of Cu (II) species.

#### *4.3.2 Density, viscosity and conductivity*

Sample density was determined using a specific gravity bottle of 50 mL (Fischer Scientific). Sample conductivity was measured using an InLab730 conductivity probe (Mettler Toledo) at room temperature. The probe was calibrated against a conductivity standard (12.85 mS cm<sup>-1</sup> at 25 °C). The viscosity of ethaline that contained different amounts of water (1 - 15 wt%) was measured using a calibrated DHR-2 Rheometer (TA Instruments) at 25 °C. The geometry was a flat stainless steel plate of 40 mm of diameter (TA instruments).

In between each measurement, the flat plate and the sample stage of the rheometer were cleaned with plenty DI water. Each sample was tested three times to account for reproducibility. A preliminary experiment to determine a suitable shear rate to perform the viscosity measurements was conducted using ethaline (without added water). In that test, the viscosity of ethaline was measured as a function of different shear rates. A shear rate of  $\dot{\gamma} = 20 \text{ s}^{-1}$  was chosen since at that point the viscosity of ethaline was stable.

Also, the viscosity of the copper-containing samples (0.20 M) was measured. However, for future work it is not advisable to measure it due to the corrosiveness nature of the Cu (II) solution which will be discussed in Chapter 7. Fig. 4.11 shows the DHR-2 Rheometer used for the viscosity measurements.

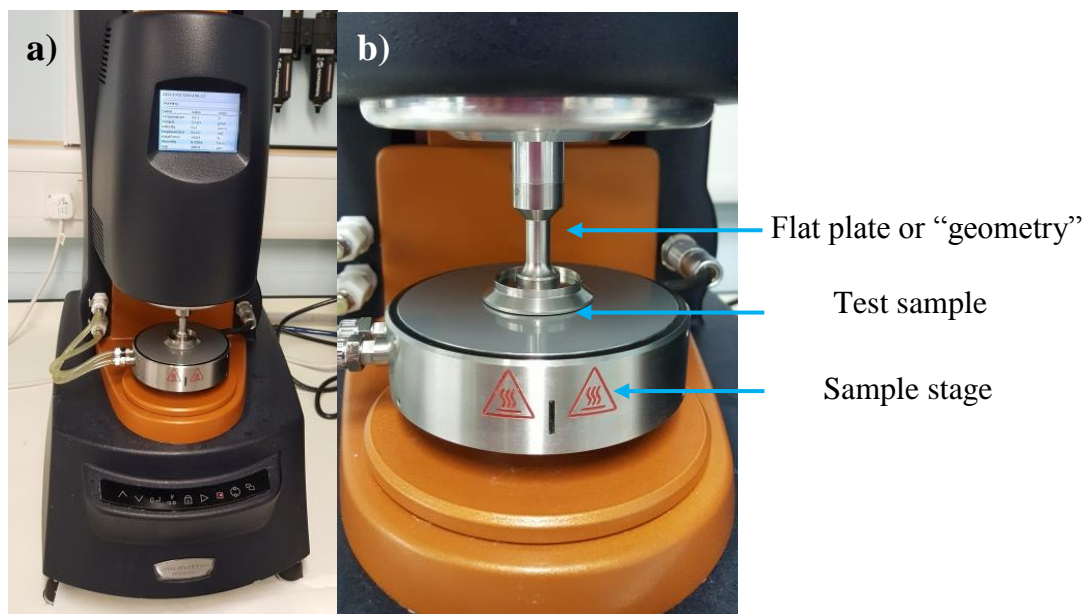


Figure 4.11 a) Picture of the DHR-2 rheometer and b) flat plate and sample stage of the rheometer.

#### 4.3.3 Electrochemical window

Water has been demonstrated to be detrimental to some ILs systems because it has the ability to reduce the anodic and the cathodic limit potentials (discussed in sections 1.3.3.1 and 1.4.6.1). Since water removes one of the most advantageous electrochemical properties of ILs as their wide electrochemical window, it was relevant to evaluate if the same occurred in DESs.

In order to measure the EW of ethaline with added water (1-15 wt%), one-compartment cell (0.40 L) with a three-electrode configuration was used. The working electrode was a rotating Pt disc ( $A = 0.031 \text{ cm}^2$ ,  $d = 0.2 \text{ cm}$ ) encased in an inert holder (Polytetrafluoroethylene -PTFE). The counter electrode was a Pt wire ( $A = 0.754 \text{ cm}^2$ ) and the reference electrode was a lab-made reference electrode (Ag wire,  $d = 0.1 \text{ cm}$ ). The arrangement of the RE will be described in the next section.

The potential was swept between +1.25 to -1.25 V vs. Ag RE at a rotation speed of 700 rpm using a scan rate of 5 mVs<sup>-1</sup> to assure steady-state conditions. The voltammetric scans were performed at 25 °C. The cathodic potential limit was determined when the current density exceeded -0.10 mA cm<sup>-2</sup> while the anodic limit was determined at +0.10 mA cm<sup>-2</sup>.

#### **4.4 Electrodeposition of Cu from water-containing electrolyte**

This section will discuss the materials, methods and experimental procedures used to perform the electrochemical measurements, electrodeposition experiments and material analysis of the fabricated deposits when the electrolyte contained different amounts of water (1 – 15 wt%). Also, a brief review of the fundamentals of the techniques will be presented.

##### *4.4.1 Divided electrochemical cell*

A divided electrochemical glass cell was used to carry out electrochemical measurements and electrodeposition experiments. The divided cell was designed to prevent the cathodic reaction to be affected by the products of the anodic reaction. The compartments were divided by a sintered porous frit (Schott Duran) of low porosity, e.g. 160 - 250 μm of nominal pore size. Both compartments were joined using two couplings (SVL coupling for butt joint, Fischer Scientific) sealed with O-rings to avoid leaking. Also, the volume capacity of each partition was of 0.75 L. The cell was jacketed to maintain the temperature of the solution at 25 °C using a water thermostatic bath (HAAKE B3, Thermo Scientific). The electrodes were inserted in the ports of the glass lids of the cell.

The source of the potential and current was a PGSTAT101 potentiostat (Metrohm Autolab) and the parameters of electrochemical measurements were controlled using NOVA software version 2.0 (Metrohm Autolab). The electrochemical measurements were performed using three techniques: linear sweep voltammetry, cyclic voltammetry and impedance. The schematic of the divided cell with the electrode configuration is shown in Fig. 4.12.

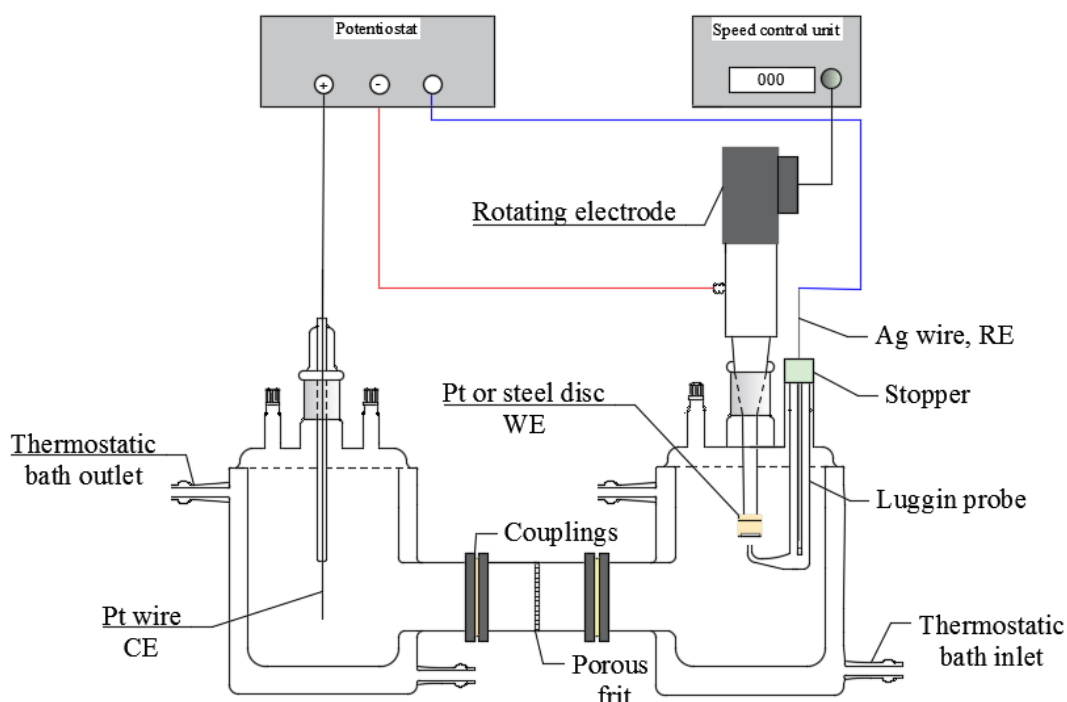


Figure 4.12 Schematic of the divided electrochemical cell used for the polarisation and electrodeposition experiments. The three-electrode configuration is also shown.

The working electrode (WE) was a rotating Pt disc electrode encased in an inert material (PTFE). The area of the WE was  $0.031 \text{ cm}^2$  ( $d = 0.2 \text{ cm}$ ) and the counter electrode was a Pt wire sealed within a glass tube. The OCP of the WE was measured using a multimeter IDM91E (IsoTech). Initially, Ag wire ( $d = 0.2 \text{ cm}$ ) was used as the quasi-reference electrode. However, in the course of the preliminary electrodeposition experiments, the Ag wire was etched while immersed in the copper-containing solution. The silver ions released into the solution then co-deposited with Cu on the WE.

To avoid this issue, a modified reference electrode was assembled. This consisted of a glass tube (length:  $15 \text{ cm}$ ,  $d = 0.5 \text{ cm}$ ) sealed with a porous glass frit using a PTFE heat-shrink tubing. Thereafter, the glass tube was filled with pure ethaline where the Ag wire was inserted -without pressing the porous glass frit. This ensured that the Ag wire was not in direct contact with  $\text{CuCl}_2$  solution. Also, in order to minimise the ohmic drop during the measurements, a Luggin probe with a U-shaped tip ( $d = 0.1 \text{ cm}$ ) was used.

Thereafter, the lab-made reference electrode was inserted in the Luggin probe that was designed to be movable within the cathodic compartment. Thereby, the distance between the WE and the tip of the Luggin probe was adjusted to be ~0.3 cm approximately. A diagram of the modified reference electrode is shown in Fig. 4.13.

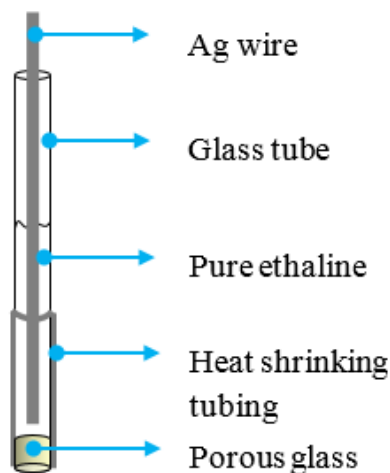


Figure 4.13 Schematic of the lab-made reference electrode.

The electrochemical measurements and electrodeposition experiments were performed using a rotating steel disk ( $A = 1.18 \text{ cm}^2$ ,  $d = 1.2 \text{ cm}$ , composition: 5 wt% of Ni, 13 wt% of Cr, and 74 wt% of Fe). The steel substrate was lodged in an electrode holder (Originalys) sealed with an O-ring to prevent leaking. The electrode was rotated using an EDI101 electrode rotator which was controlled by a speed unit CTV101 (Radiometer Analytical). The electrode holder and its components is shown in Fig. 4.14 (a-b).

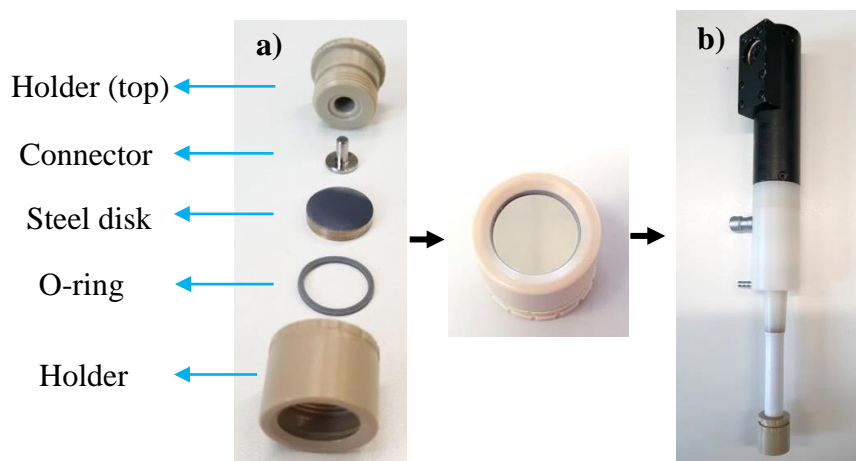


Figure 4.14 a) Electrode holder components and b) holder assembled to the RDE.

#### 4.4.2 Electrode preparation

Before each measurement, the Pt disc electrode was grinded manually using silicon carbide (SiC) paper, grit # 4000 on a polishing machine (Dap-7, Struers) until a mirror-like finish was obtained. In contrast, the steel disks were embedded in bakelite using a hot mounting press (ProntoPress-10, Struers). Thereafter, they were mechanically grinded on the Struers polishing machine, commencing with a coarser grit # 2400 and finishing with a finer one # 4000. Since bakelite was a brittle material, the holders were crushed using a vice so that the disks were extracted (Fig. 4.15). The disks were washed with Decon 90, DI water and dried with N<sub>2</sub> gas.

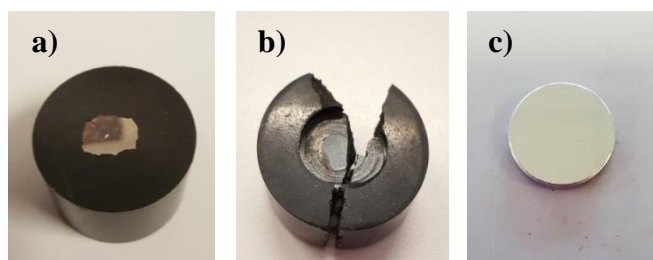


Figure 4.15 a) Images of the steel disk embedded in bakelite, b) holder after crushing and c) polished steel disk ( $A=1.18 \text{ cm}^2$ ,  $d = 1.20 \text{ cm}$ ).

#### 4.4.3 Experimental procedure to determine ohmic drop

Although the ohmic drop has been minimised by placing the Luggin probe close to the WE, the uncompensated resistance ( $R_u$ ) was measured in order to obtain reliable electro-kinetic data. This was measured using the same three-electrode configuration detailed in section 4.4.1 and a PalmSens4 impedance analyser. The AC signal amplitude was  $\pm 10 \text{ mV}$  and the applied frequency ranged from 10000 to 1 Hz controlled by PSTrace5 software. The measurements were performed three times and the  $R_u$  values were averaged. The ohmic drop was electronically compensated using the PGSTAT30-Methrom Autolab. The compensation corresponded to the 80% of the measured  $R_u$  since beyond this percentage the potentiostat started to oscillate.

The uncompensated resistance can be measured by impedance due to the fact that an electrochemical system is analogue to an electronic circuit as Fig. 4.16 (a) shows. The simplest electronic circuit possesses the double-layer capacitance ( $C_{dl}$ )

which is in parallel with the polarisation resistance ( $R_p$ ). It is known that at the highest frequency the  $C_{dl}$  acts as a short circuit (cable). Thereby, the current flows through the path that offers the lowest resistance as indicated by the red arrow in Fig. 4.16 (b).

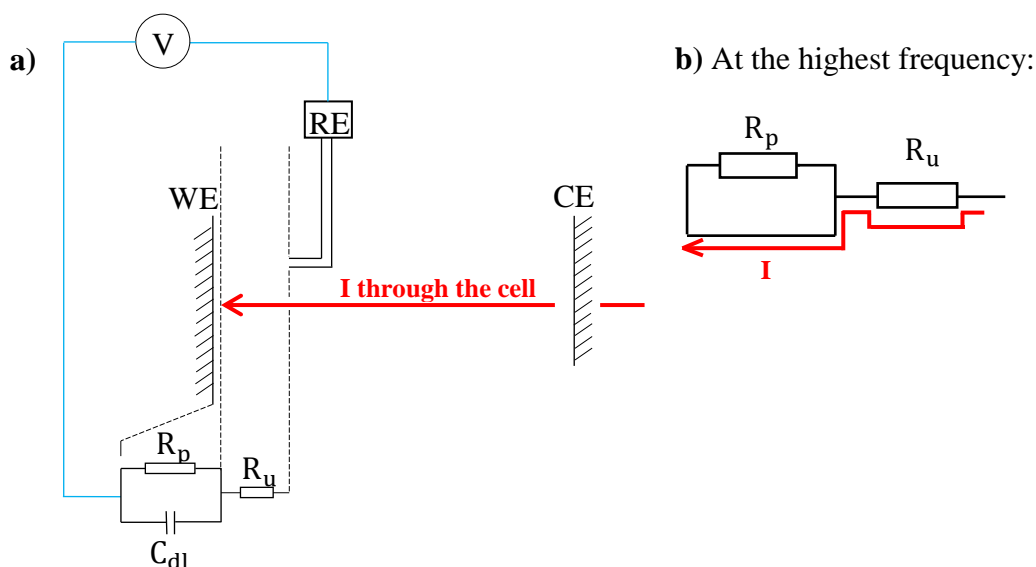


Figure 4.16 a) Schematic of an electrochemical cell showing the uncompensated resistance in an analogue mode to an electronic circuit, b) simplest circuit showing that at a high frequency, the  $C_{dl}$  acts a cable. Adapted from [2].

Fig. 4.17 shows that the  $R_u$  can be extracted from the intercept with the X-axis of a Nyquist plot since it is the point where the highest frequency was applied [2].

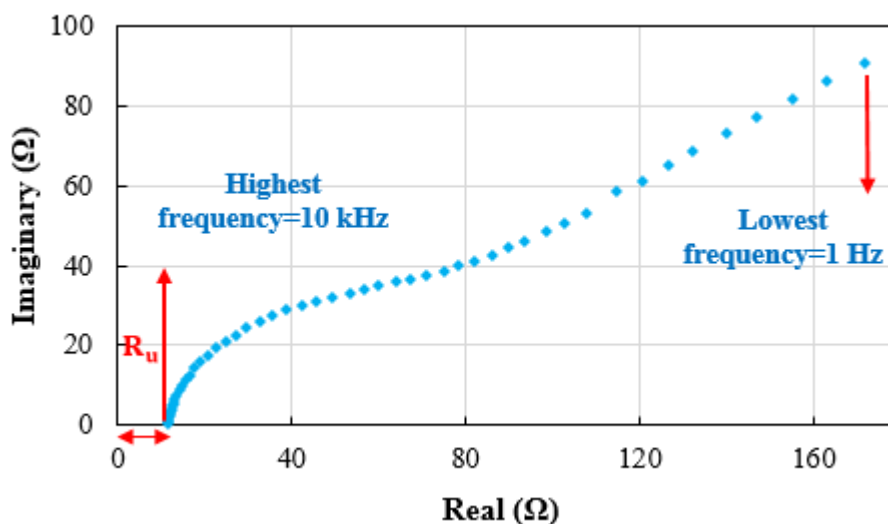


Figure 4.17 Example of a Nyquist plot where the  $R_u$  can be obtained from the intercept of the real component at the highest applied frequency.



Also,  $R_u$  was calculated using equation 4.13 [157]. This relation applies for a WE with a radius smaller than the gap between the WE and the tip of the Luggin probe.

$$R_u = \frac{z}{2\pi\kappa r^2} \quad (4.13)$$

where  $z$  is the electrode gap between the WE and the tip of the Luggin probe ( $\sim 0.3$  cm),  $r$  is the radius of the working electrode (0.1 cm for Pt dis)) and  $\kappa$  is the conductivity of the electrolyte ( $\Omega^{-1} \text{ cm}^{-1}$ ). Since the gap between the WE and the Luggin tip is only an estimation, it represents a source of error and discrepancies are likely to exist between the measured and the calculated  $R_u$ .

Table 4.1 shows that the measured  $R_u$  decreases from 248 to 130  $\Omega$  as the water content increased from 1 to 15 wt%. This decrease is due to the improved conductivity of the electrolyte which will be discussed in section 5.5.3. The relative error between the measured and the calculated  $R_u$  is within 17%. This error arises due to the distance between the Luggin tip and the working electrode which could not be measured accurately since it was adjusted manually each time.

Table 4.1 Measured and calculated  $R_u$  of the  $\text{CuCl}_2$ -ethaline system with increasing amounts of water from 1 to 15 wt%. The radius of the Pt electrode was 0.1 cm and the distance between the Luggin probe and the WE was  $\sim 0.3$  cm.

<b>Water content (wt%)</b>	<b><math>R_u</math> measured (<math>\Omega</math>)</b>	<b><math>R_u</math> from equation 4.13 (<math>\Omega</math>)</b>	<b>Error (%)</b>
1	248	221	12.2
3	209	189	10.6
6	166	167	0.6
10	124	142	12.7
15	130	111	17.1

#### *4.4.4 Experimental procedure to examine limiting currents*

Linear sweep voltammetry was carried out in order to investigate the influence of water on the diffusion limiting currents of Cu deposition. The Pt disc electrode was rotated at 700 rpm using a slow scan rate of 5 mV s<sup>-1</sup>. The potential commenced from the OCP (+0.63 V vs. Ag wire RE) and terminated at -0.85 V vs. Ag wire RE. The experiments were performed at 25 °C and the voltammetric scans of the remaining solutions were conducted in a similar fashion. The real-time plots (i versus E) were displayed in the interface of NOVA software.

#### *4.4.5 Experimental procedure to determine kinetic parameters*

In order to obtain the heterogeneous rate constants and charge transfer coefficient, linear sweep voltammetry at a rotating disk electrode was performed. The potential was swept from OCP and finished at -0.85 V vs. Ag wire RE. A slow scan rate of 5 mV s<sup>-1</sup> was applied to ensure steady-state conditions. The polarisation curves were recorded using different rotation speeds such as 700, 1400, 2100 and 2800 rpm. The experiments were performed at 25 °C.

#### *4.4.6 Experimental procedure of electrodeposition experiments*

The electrodeposition of Cu was performed in order to determine if the presence of water in the DES system improved or deteriorated the characteristics of the electrodeposits. The experiments were performed using the limiting currents derived from polarisation curves recorded as per procedure in section 4.4.4. Table 4.2 summarises the applied current density from which each electrodeposition process was performed. The applied current density was set to 78% of the  $i_{lim}$ . An earlier study determined that when using this fraction of the current, reasonable dense deposits could be produced [89]. All the electrodeposition processes were conducted with a rotation speed of 700 rpm and the plating time was set to 7200 s. Once the process finished, the substrate was immediately retrieved from the liquid, washed with DI water and dried with N<sub>2</sub> gas.

Table 4.2 Applied current density for each electrodeposition process according to the content of water in the electrolyte.

Water content (wt%)	Limiting current density, $i_{lim}$ (mA cm <sup>-2</sup> )	Applied current density (78% of $i_{lim}$ ) (mA cm <sup>-2</sup> )
1	6.0	4.68
3	8.0	6.24
6	8.5	6.67
10	12.5	9.75
15	18.1	14.12

#### 4.4.6.1 Experimental procedure to determine current efficiency by gravimetric method

The current efficiency of the electrodeposition process was determined gravimetrically and electrochemically. The gravimetric method consists on weighing the steel disks before and after each electrodeposition process using an analytical scale (KERN, ABJ-NM/ABS-N) with a precision of  $\pm 0.1$  mg. The current efficiency expressed as a percentage was calculated using equation 4.14.

$$\Phi = \frac{m_{actual}}{m_{expected}} \times 100\% \quad (4.14)$$

where  $m_{actual}$  is the mass measured experimentally and  $m_{expected}$  is the predicted mass by Faraday's law as equation 4.15 indicates.

$$m_{expected} = \frac{I t M}{nF} \quad (4.15)$$

where  $m_{expected}$  is the expected mass when no side-reactions occurred ( $\Phi=100\%$ ),  $I$  is the applied current,  $t$  is the plating time,  $M$  is the molecular mass of Cu,  $n$  is the number of transferred electrons and  $F$  is Faraday's constant.

#### 4.4.6.2 Experimental procedure to determine current efficiency by stripping method

Anodic stripping voltammetry was performed in order to cross-check the current efficiencies obtained gravimetrically. The stripping electrolyte was hydrochloric acid with a concentration of 0.5 M (Sigma-Aldrich, ACS reagent 37% wt%). HCl allows Cu to dissolve as Cu into Cu<sup>+</sup> due to the thermodynamic stabilisation of Cu<sup>+</sup> in chloride media [158]. The dissolution process occurred as per reactions 4.16 and 4.17 [159].



In order to establish the potential at which the dissolution of Cu was feasible in HCl, anodic sweep voltammetry was carried out using the three-electrode configuration mounted in an undivided electrochemical cell. Firstly, a thin layer of Cu had to be deposited to be subsequently dissolved in HCl. Cu was galvanostatically deposited using a Pt disk ( $A = 0.031 \text{ cm}^2$ ,  $d = 0.2 \text{ cm}$ ) from the electrolyte containing 1 wt% of H<sub>2</sub>O. The deposition time was set to 290 s to produce a film of thickness of 0.5  $\mu\text{m}$  so that the stripping time was short.

Secondly, the thin layer of Cu was immersed in HCl solution (0.5 M) where the counter electrode was a Pt wire and the reference electrode was a Saturated Calomel Electrode (SCE), whose potential is known to be +0.248 V vs. SHE. The potential was swept from -0.4 to +0.4 V vs. SCE using a scan rate of 10 mV s<sup>-1</sup> and a rotation speed of 700 rpm. Fig. 4.18 shows the anodic polarisation curve where two anodic peaks were observed. The first peak corresponds to the formation of CuCl<sub>(s)</sub> film (a<sub>1</sub>), as earlier shown in equation 4.16, which dissolved to CuCl<sub>2</sub><sup>-</sup> species (a<sub>2</sub>) as shown in equation 4.17 [159]. However, a more positive anodic overpotential led to further electrochemical oxidation of CuCl<sub>2</sub><sup>-</sup> species. Therefore, an appropriate oxidation potential was chosen to be 0.0 V vs. SCE where only the dissolution of Cu proceeded.

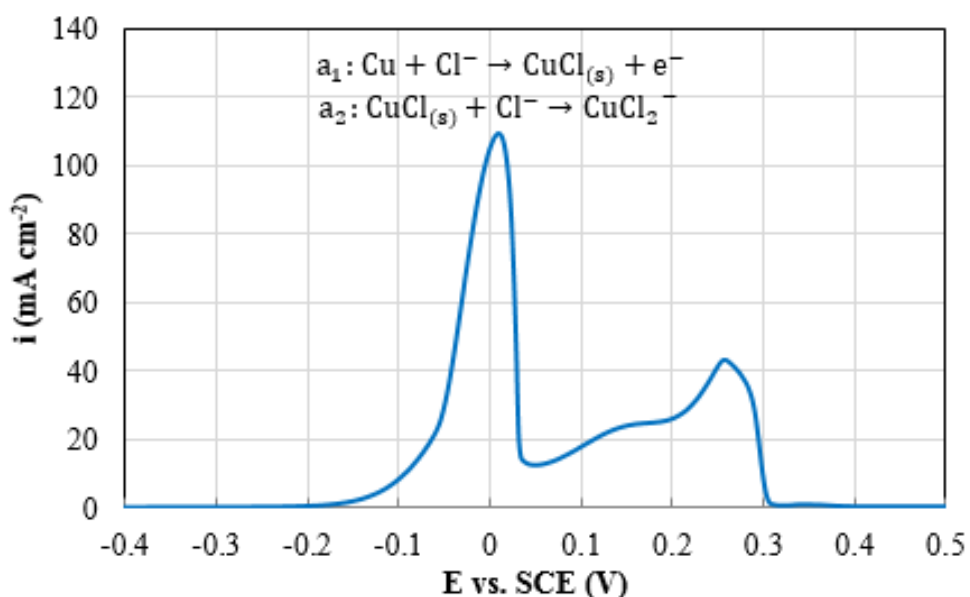


Figure 4.18 Anodic polarisation of Cu in 0.5 M HCl.

The same experimental procedure was deployed to strip off Cu deposits fabricated from the water-containing electrolytes (1-15 wt%). The Cu films were electrochemically dissolved from the substrate ( $A = 1.18 \text{ cm}^2$ ,  $d = 1.2 \text{ cm}$ ) applying 0.0 V vs. SCE. The total anodic charge was recorded in NOVA software, which was useful to quantify the current efficiency, as equation 4.18 shows.

$$\Phi = \frac{Q_a}{Q_c} \times 100\% \quad (4.18)$$

where  $Q_a$  is the anodic charge of the dissolution process and  $Q_c$  is the cathodic charge  $Q_c$  passed in the electrodeposition process. The cathodic charge was calculated from Faraday's law ( $Q_c = It$ ).

## 4.5 Material analysis

Some of the morphological and microstructural characteristics of the electrodeposits that were of interest to investigate included: grain shape, grain size, preferred orientation, and purity. These attributes were examined using various techniques such as optical microscopy, Scanning Electron Microscopy (SEM), X-ray Diffraction (XRD) and Electron Backscatter Diffraction (EBSD). Moreover, the chemical composition of the bulk specimens was determined by using Energy-Dispersive X-ray Spectroscopy (EDX). This section will briefly discuss the operating principle of each technique and the followed procedures to perform the analysis.

### *4.5.1 SEM, EDX and EBSD operating principle*

In order to examine the surface specimens, Scanning Electron Microscopy (SEM) was performed. SEM is a material characterisation technique that allows the inspection of a specimen topography [160, 161]. The versatility of this technique relies on its capability to image the surface morphology of samples regardless of their thicknesses or finishing [160]. For instance, specimens do not need to be polished or etched in order to be assessed. Also, rough surfaces and layers as thicker as 50  $\mu\text{m}$  can be analysed [160].

The SEM consists of a chamber wherein an electron beam is produced by heating up a tungsten filament. The beam is focused to collide with the surface of a specimen with the aid of an anode, a series of electromagnets and condensers [160]. Product of that interaction, various types of electrons can be released. Subsequently, the emitted electrons are acquired by specialised detectors to form an image with the collected information [160]. The basic instrumentation of an electron microscope is shown in Fig. 4.19.

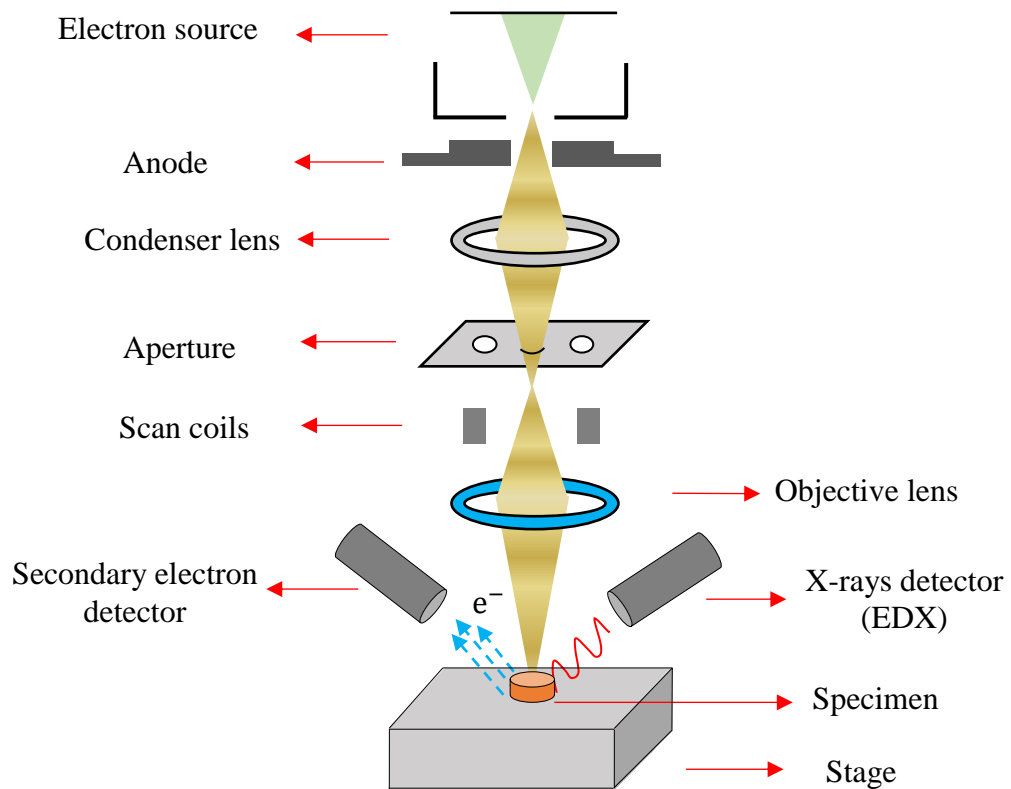


Figure 4.19 Basic operating principle of Scanning Electron Microscope. Adapted from [162].

The types of electrons that can be released are known as secondary electrons and backscattered electrons. When the incoming electrons (from the incident beam) collide with a specimen, some of the outer electrons of the atoms are released. Those ejected electrons are known as the secondary electrons (SE) which are useful to image the specimen surface [160]. On the contrary, backscattered electrons (BSE) are generated when the incoming electrons abandon the atom without striking any of its electrons. That type of interaction is known as elastic scattering of electrons [160]. When incoming electrons dislodge electrons from the inner shell of the atom, electrons from a higher energy level fill that vacancy and simultaneously release X-rays (photons). Thereafter, those X-rays are captured by an EDX detector to reveal the chemical composition of the specimen. Fig. 4.20 illustrates the various type of electrons emitted from a specimen and Fig. 4.21 shows the mechanism by which SE, BSE and X-rays are emitted.

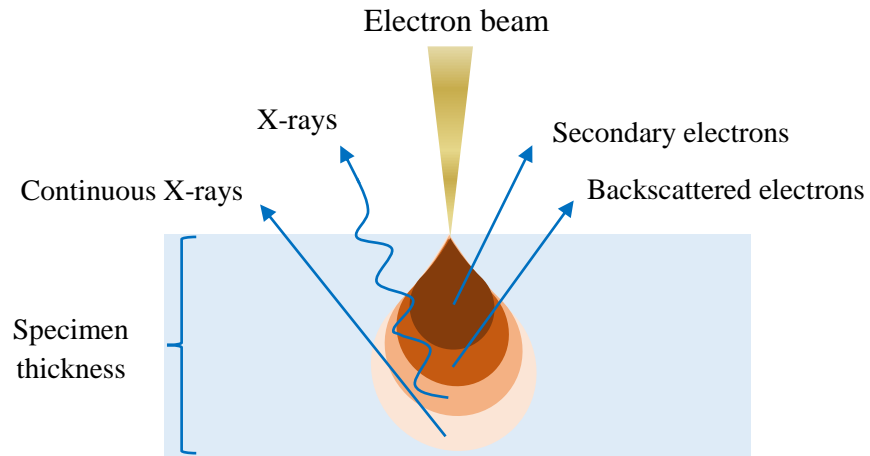


Figure 4.20 Type of emitted electrons depending on the interaction volume of the sample when the electron beam strikes the specimen. Adapted from [160].

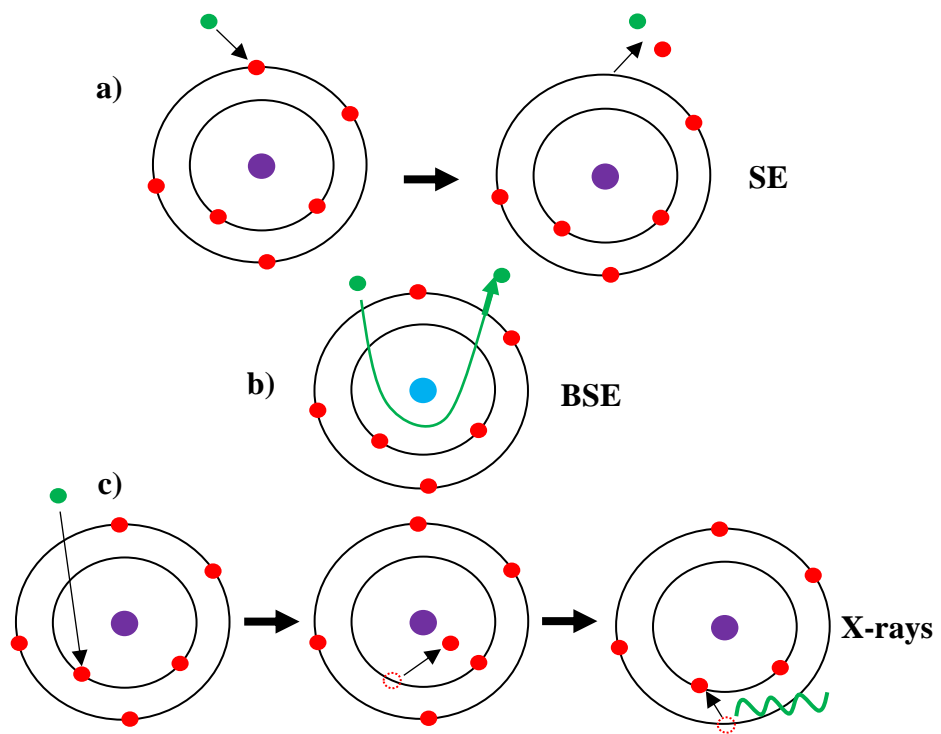


Figure 4.21 Mechanisms by which electrons are emitted such as a) secondary electrons, b) backscattered electrons and c) X-rays. Adapted from [160].



In order to examine the grain size, grain shape and crystallographic orientation of the electrodeposits, the cross-sections of the specimens were analysed using Backscattered Electron diffraction (EBSD). An EBSD system can be integrated into the SEM mechanism but its operating principle is somewhat different. To exemplify, the sample stage should be tilted  $70^\circ$  from the horizontal direction to obtain a sufficient backscattered intensity [160]. While the electron beam scans each fragment of the specimen surface, a cone of backscattered electrons is diffracted and collected by a detector, which is placed nearby the sample. The components of a detector are a phosphor screen and a charge coupled device (CCD) camera [160]. An illustration of the EBSD system is shown in Fig. 4.22.

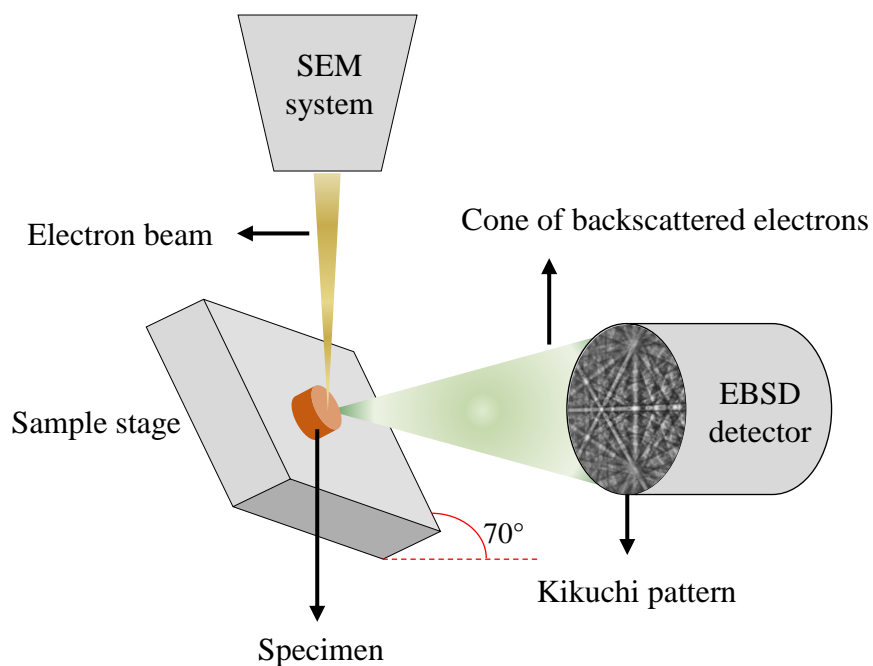


Figure 4.22 Diagram of the basic operating principle of EBSD analysis. Adapted from [160].

The interaction between the diffracted backscattered electrons and the phosphor screen creates a pattern known as the Kikuchi pattern [160]. The Kikuchi bands are acquired by a high speed and high sensitivity CCD camera placed behind the phosphor screen and thereafter the signal is transferred to a computer to be indexed [160]. The derived information is presented as an EBSD map whereby each crystallographic plane is assigned to a colour whose orientation is exhibited in the inverse pole figure [160]. An example of a generated EBSD map with the Inverse Pole Figure (IPF) can be observed in Fig. 4.23 (a-b).

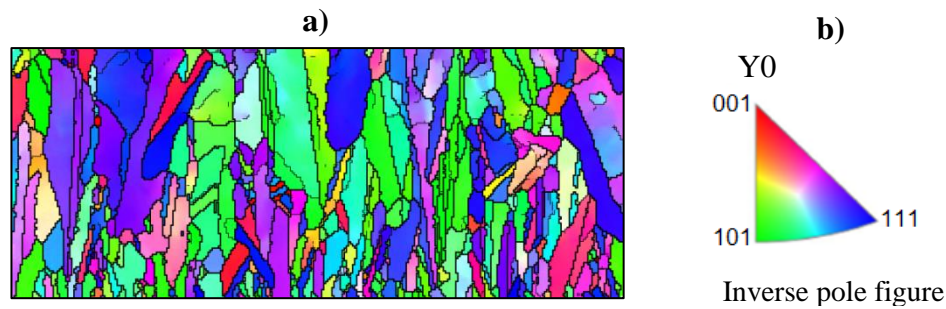


Figure 4.23 a) EBSD map with its corresponding b) inverse pole figure (IPF) in the growth direction (Y0).

#### 4.5.2 Experimental procedure for SEM, EDX and EBSD analysis

The specimens fabricated from each water-containing electrolyte, e.g. 1, 3, 6, 10 and 15 wt% were preliminary observed using a YenWay optical microscope. Afterwards, each specimen was lodged in the sample stage of a Hitachi SU6600 scanning electron microscope wherein an accelerating voltage of 15 kV was applied. The SEM was equipped with an Oxford Inca 350 20 mm X-Max detector that permitted the quantification of the chemical composition of the samples. The electron micrographs were imaged using two magnifications, e.g. x2500 and x5000.

The EBSD analysis was performed in the Department of Industrial and Materials Science of Chalmers of University of Technology (Sweden), whereby a Leo 1550 Gemini SEM was used to acquire the EBSD phase maps of the deposited samples. The EBSD measurements were performed on the cross-section of the coating using a HKL Channel 5 system and a Nordlys II detector. The samples were investigated in the ordinary EBSD setup (70 °C tilt of sample towards the EBSD detector). The EBSD maps were obtained by applying an accelerating voltage of 20 kV and a step size of 50 nm. The maps were afterwards stitched together by using Map Stitcher software.

All the acquired maps were processed. For example, wild spikes were removed and minor noise reduction (4 nearest neighbours) was performed. In the phase maps, high angle grain boundaries are shown by black lines (defined by misorientations larger than 10°).

#### 4.5.2.1 Metallographic preparation of specimens

The preparation of the specimens for EBSD analysis was performed in the Advanced Forming Research Centre (AFRC) at Strathclyde University. The samples were fabricated from electrolytes containing 1, 6 and 10 wt% of water. The plating time was corrected so that all the samples possess a similar thickness. Since Cu is known to be a soft material, it was sandwiched using a Ni layer of 20  $\mu\text{m}$ . This protected the deposits from damaging during the polishing process. The Ni film was deposited from sulfamate plating solution. The Cu electrodeposits were stored in a desiccator to prevent oxidation. The preparation process is summarised as following:

- a) Cu disks were cross-sectioned using a linear precision saw IsoMet 5000 (Buehler) as shown in Fig. 4.24 (a-b). The blade (101720 type HNF for ferrous materials) was chosen to section the steel disks. The blade speed was set to 4000 rpm and the cutting speed was 3.5 mm min<sup>-1</sup>. To avoid heating of the specimen, a continuous stream of water was supplied automatically.
- b) The specimens were embedded in conductive material using an automatic mounting press, SimpliMet 3000 (Buehler) at 150 °C for 2.5 minutes. The mounting material was Cu powder, as shown in Fig. 4.24 (c).
- c) The embedded specimens were grinded in a grinder-polisher machine, IsoMet 300 (Buehler) using SiC sandpaper of grits # 1200, 2400 and 4000 for 2 minutes each. The rotation was selected to be complimentary which meant that both the carrousel and the plate rotated in the same direction. The applied force was 25 N and the rotation of the platen was set to 240 rpm. In between each grinding step, the specimens were retrieved from the carrousel and washed with hot tap water. This process is shown in Fig. 4.24 (d-e).
- d) The specimens were polished using a 3  $\mu\text{m}$  Trident cloth (MetPrep) in the IsoMet 300 polishing machine for 4 minutes. The polishing substance was 3  $\mu\text{m}$  polycrystalline diamond suspension and the lubricant material was MetaDi lubricant. The force, rotation speed and type of rotation were the same detailed in c.

- e) Polishing a soft metal such as Cu sandwiched between two harder materials (Ni and steel) was a trial and error process. This step was crucial to minimise scratches. A 0.06  $\mu\text{m}$  MasterMet micro-cloth (MetPrep) and the 0.06  $\mu\text{m}$  colloidal silica polishing suspension (MetPrep) were used to polish the specimens in the IsoMet 300 machine. The polishing time was 4 minutes and the force and the rotation speed were reduced to 15 N and 80 rpm. Since the colloidal silica suspension recrystallized, the specimens had to be retrieved quickly and rinsed with cold tap water. Afterwards, they were swabbed with methanol, cleaned with cottons and dried with hot air.
- f) To improve the quality of the polishing surface, the specimens were placed in the vibratory polisher for 6 hours (VibroMet 2, Buehler), as shown in Fig. 4.24 (f). A mixture of 0.06 and 0.02  $\mu\text{m}$  silica suspensions diluted to 40% was prepared to be the polishing medium. The amplitude of vibration was set to 30% (recommended by the manufacturer).

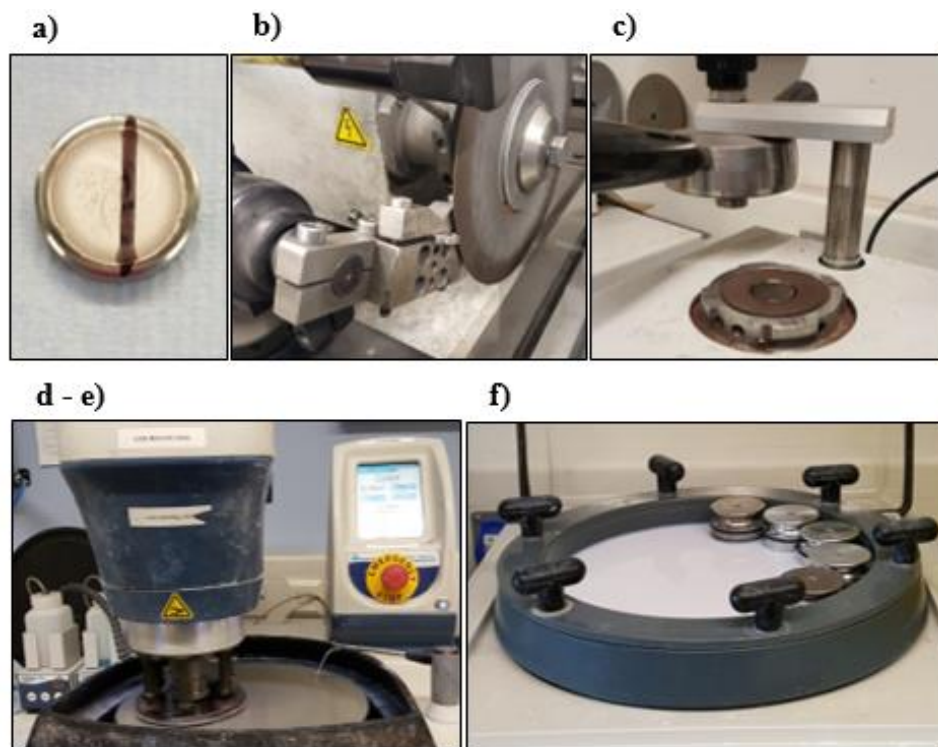


Figure 4.24 Process of the metallographic preparation of Cu deposits for EBSD analysis. The steps corresponded to: a) deposit before cross-sectioning, b) cutting, c) mounting, d-e) grinding/polishing and f) vibratory polishing.

Fig. 4.25 shows the prepared specimens which were embedded in the conductive material and placed in a desiccator to avoid oxidation.



Figure 4.25 Prepared specimens from the electrolyte containing 1, 6 and 10 wt% of water for EBSD analysis.

The crystallographic orientation of the grains was provided from the automatic index of the Kikuchi patterns [163]. The grain size information was obtained using the TANGO software. The software performed the calculation by applying the standard line intercept method [164], whereby a grid of five horizontal and vertical lines was fixed. An example of the line intercept technique is illustrated in Fig. 4.26. The average grain size was calculated dividing the length of the line by the number of intercepts or grains boundaries as equation 4.19 shows.

$$\text{Average grain size} = \frac{\text{line length}}{\text{number of intercepts}} \quad (4.19)$$

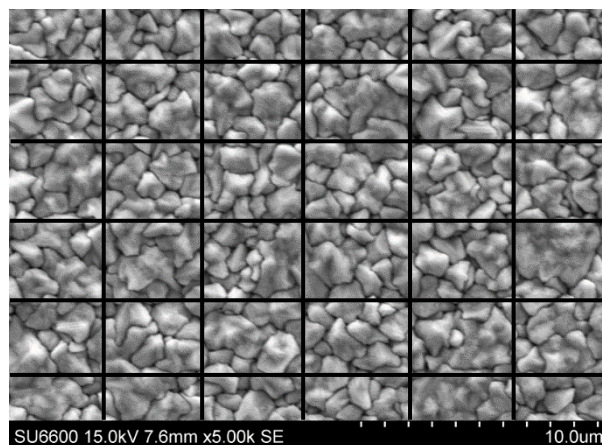


Figure 4.26 SEM image of Cu coating showing the grid of five horizontal and vertical lines in order to apply the line intercept method to calculate grain size [164].

### 4.5.3 XRD operating principle

XRD measurements were performed in order to determine if the electrodeposits exhibited texture. X-rays are a form of electromagnetic radiation generated by a cathode ray tube when a tungsten filament is heated [161]. When a targeted material is bombarded with a beam of X-rays, a fraction of these rays is scattered. The scattering phenomenon arises because X-rays encounter ‘obstacles’. Those obstacles are the electrons associated with the atoms that the material possesses [161].

Diffraction takes place solely when X-ray waves constructively interfere with one another as the beam of X-rays interacts with the electrons of a periodic arrangement of atoms [161]. For instance, Fig. 4.27 illustrates two waves (of amplitude  $A$  and wavelength  $\lambda$ ) that after the scattering process remain in the same phase. For this reason, the amplitudes of both waves sum up and the constructive interference occurs, which is known as diffraction [161]. The diffracted X-ray waves are sensed by an X-ray detector and processed as a diffractogram, which reflects the periodicity of the crystalline material [161].

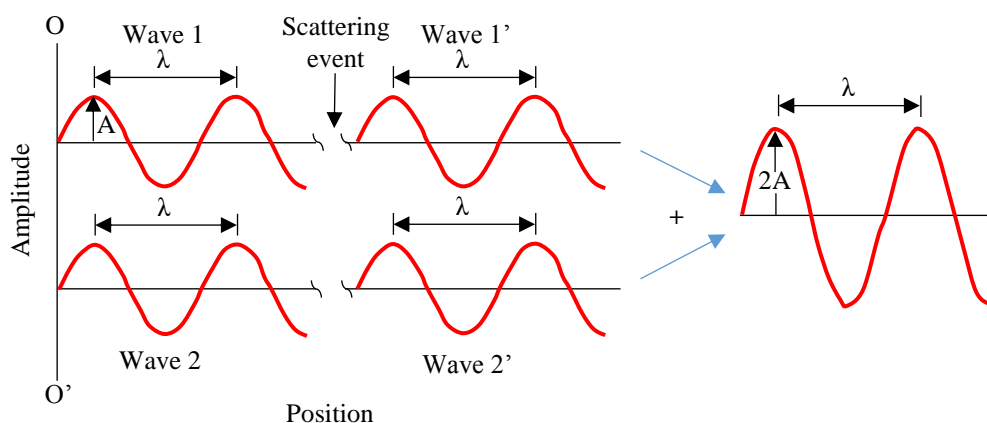


Figure 4.27 Schematic of the constructive interference when the beam of X-rays interacts with the electrons of a periodic arrangement of atoms. Adapted from [161].

Diffraction phenomenon is governed by Bragg's law [161], which is satisfied when constructive interference occurs as discussed beforehand. This law relates the wavelength of the X-rays to both the interplanar spacing and the angle of the diffracted X-rays beam [161]. Bragg's law is shown in equation 4.20.

$$n \lambda = 2d_{hkl} \sin\theta \quad (4.20)$$

where  $n$  is an integer number,  $\lambda$  is the X-rays wavelength,  $d_{hkl}$  is the interplanar spacing of crystal planes and  $\theta$  is the diffracted angle of the X-rays beam in degrees. Bragg's law can be understood by considering Fig. 4.28 that shows two planes (G-G' and H-H') separated by the interplanar space  $d_{hkl}$ . When the incident beam of two X-ray waves (1 and 2) impinges on the ordered crystalline structure at an angle  $\theta$ , these beams are scattered by the atoms P and Q which produces diffracted beams (1', 2'). When the difference of the pathlength amongst  $\overline{SQ}$  and  $\overline{QT}$  results into an integral number ( $e$ ), constructive interference proceeds that is known to be the main condition for diffraction [161].

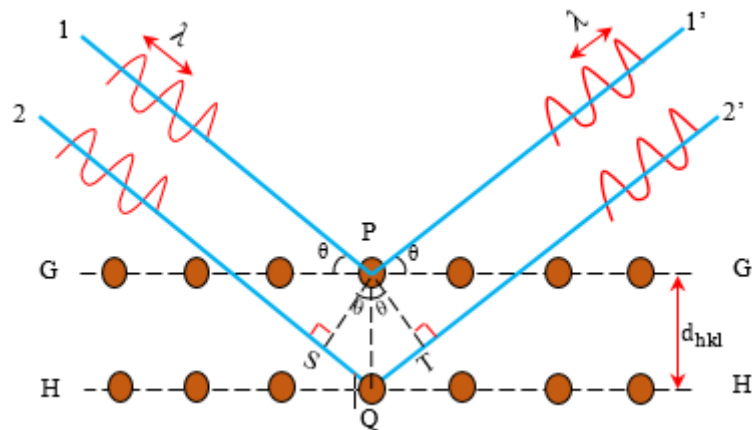


Figure 4.28 Schematic of Bragg's law. Incident X-ray waves with a  $\lambda$  wavelength impacts on atoms (P and Q) located at the crystal planes (G-G' and H-H'). The waves are scattered at a certain angle  $\theta$  and if the difference between of pathlength between  $\overline{SQ}$  and  $\overline{QT}$  is an integral number, diffraction ensues. Adapted from [161].

In practice, the angles at which diffraction occurs are determined by a diffractometer. This equipment consists on a tungsten filament that upon heating generates X-rays. There is a holder that supports the test specimen which is mechanically joined to an X-rays detector [161]. While the detector rotates on a  $2\theta$  angle so does the specimen at an angle  $\theta$ . In XRD theory  $2\theta$  is known as the diffraction angle. Since both the specimen holder and the detector are coupled, the incident and reflection angles remain equal to each other. A recorder plots the diffraction pattern that arises when constructive interference proceeds from the interaction of the X-rays beam with the arranged atoms at the crystal plane [161]. The diffractogram is plotted as relative intensity against the diffraction angle  $2\theta$ . An example of a diffractogram is shown in Fig. 4.29.

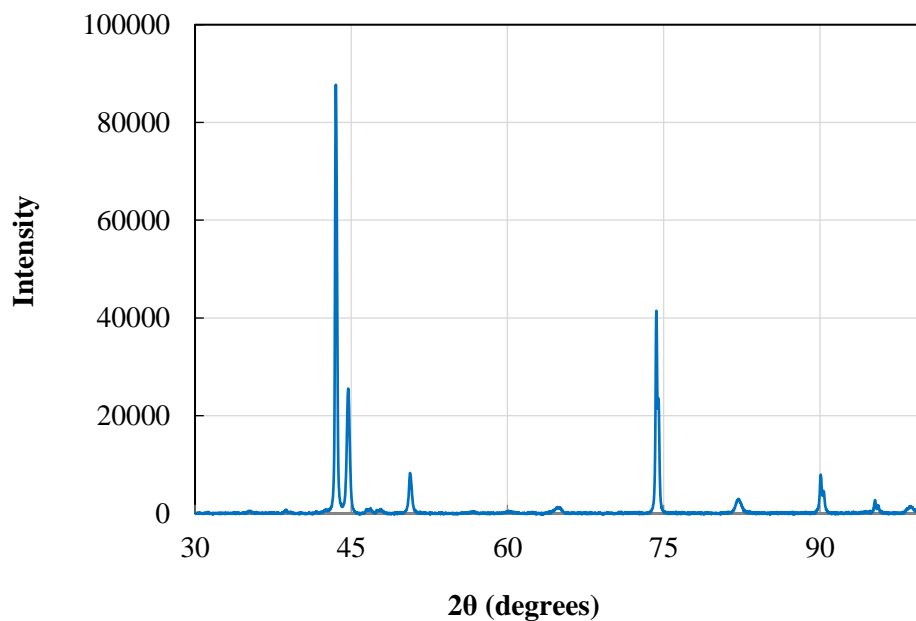


Figure 4.29 Example of a diffractogram of the crystalline structure of a metal.



#### 4.5.4 Experimental procedure of XRD analysis

The X-ray diffractograms of the electrodeposits fabricated from water-containing electrolytes were obtained using a Bruker diffractometer D8 Advance. To avoid the scattering of the light, a Göbel mirror with a slit of 0.06 cm was used. The scan parameters for the XRD experiment were controlled by the software Davinci 2010. The scanning commenced at a  $2\theta$  angle of  $30^\circ$  and finished at  $100^\circ$ . Also, the step time was set to  $0.5^\circ$  per second. Thereafter, each sample was placed in the sample stage to start the test.

The diffractograms were recorded and stored by the software Diffrac Eva Suite, whereby the subtraction of the background signal and the identification of the phases were possible. The crystallographic indexing was done with the ICDD Powder Diffraction File 2 database, which was available in the software Diffrac Eva Suite. In order to identify peaks arising from the substrate, an additional XRD scanning was performed using the steel substrate as the test specimen.

The relative texture coefficient (RTC) was computed in order to examine if the deposited grains exhibited texture, as equation 4.21 shows.

$$RTC_{(hkl)} = \frac{TC_{(hkl)}}{\sum_i^n TC_{(h_i k_i l_i)}} \quad (4.21)$$

where  $TC_{(hkl)}$  is the texture coefficient for the reflection (hkl) and  $\sum_i^n TC_{(h_i k_i l_i)}$  is the sum of all intensities. The texture coefficient was calculated from equation 4.22.

$$TC_{(hkl)} = \frac{I_{(hkl)m}/I_{(hkl)}^o}{\sum_i^n I_{(hkl)m}/I_{(hkl)}^o} \quad (4.22)$$

where  $I_{(hkl)m}$  is the measured intensity of the chosen (hkl) plane and the superscript in the term  $I_{(hkl)}^o$  refers to the reference powder sample (JCPDS database).

## 4.6 Anodic dissolution of copper

In order to implement a practical electrodeposition system where metal species is replenished by the anodic reaction, a full understanding of this reaction is crucial. However, there have been few investigations that characterised the anodic reaction from DES systems. This section thereby presents the experiments that were performed to comprehend the anodic dissolution process using a soluble anode during the electrodeposition of Cu from the ethaline-based DES system as well as from the water-containing DES systems.

### 4.6.1 Materials and apparatus

At this point of the study, the initial concentration of water in ethaline has been determined. Thereby, the concentration of water in ethaline was adjusted by adding known amounts of DI water to prepare solutions containing 1, 3, 6, 10 and 15 wt% of total H<sub>2</sub>O. In a similar fashion, the content of water in the electrolyte solutions was adjusted. The water content was measured using the moisture Karl Fischer titrator MKH-700 (Kem Kyoto Electronics).

The dissolution experiments were performed in the jacketed two-compartment cell described in section 4.4.1. The temperature during the experiments was maintained at 25 °C using a thermostatic bath to pump water through the jacket. For the anodic dissolution experiments, a three-electrode configuration was used. The anode was a Cu disk of area 1.18 cm<sup>2</sup> (Alfa-Aesar, 99.999% purity) inserted in a PEEK sample holder (Orignalys) and the reference electrode was the Ag lab-made electrode described in section 4.4.1. Before each dissolution process, the Cu disks were polished by following the procedure detailed in section 4.4.2. Both electrodes (i.e. CE and RE) were mounted in one compartment whereas a Cu rod acting as the working electrode was placed in the other cell compartment to avoid interferences from the cathodic process.

The source of current was a potentiostat PGSTAT101 (Metrohm Autolab). The rotation was applied using an electrode rotator EDI101 and the rotation rate was

controlled with a speed unit CTV101 (Radiometer analytical). In order to determine the dissolution valency, the Cu disk was weighed before and after every experiment using an analytical scale to an accuracy of  $\pm 0.1$  mg. The spectra of the complex species product of the dissolution of Cu were acquired using a Varian Cary 5000 UV-Vis spectrophotometer over a wavelength range of 200-600 nm. The spectra were corrected against ethaline as the blank reference. According to the concentration of Cu species, a cuvette of either 1 cm or 125  $\mu\text{m}$  of pathlength was employed.

#### 4.6.2 *Experimental procedure to ascertain the dissolution valency*

In order to determine the valency of the complex species product of the anodic reaction, the anodic dissolution of Cu was performed galvanostatically at 2.85 mA  $\text{cm}^{-2}$  over 3600 or 7200 s at stagnant conditions. The experiments were carried out from ethaline and electrolyte solutions containing 1-15 wt% of water. The Cu disks were weighed before and after each dissolution experiment in order to determine the valency state of the complex species. The dissolution valency was calculated from the rearranged Faraday's law as equation 4.24 shows.

$$n = \frac{I t_{\text{diss}} M}{\Delta m F} \quad (4.24)$$

where  $n$  is the dissolution valency,  $I$  is the applied current,  $t_{\text{diss}}$  is the dissolution time,  $M$  is the atomic mass of Cu,  $\Delta m$  is the experimental weight loss and  $F$  is the Faraday's constant. Also, the potential of the CE against the RE was monitored while the dissolution process proceeded.

In order to acquire the UV-Vis spectra of the generated complex species, a sample was withdrawn from the anodic compartment after the dissolution of Cu from ethaline solutions. However, due to the presence of the  $\text{CuCl}_4^{2-}$  complex, the absorption bands of the Cu (I) species were overlapped by the characteristic bands of the  $\text{CuCl}_4^{2-}$  species. Thereby, it was not feasible to ascertain the UV-Vis spectrum of the Cu (I) species when Cu (II) species were present in the electrolyte solutions.

#### *4.6.3 Dissolution valency as a function of current density, concentration of species and rotation speed*

In order to investigate the dependency of the dissolution valency on the applied current density, the dissolution experiments were carried out using two, three and four times the initial current density ( $2.85 \text{ mA cm}^{-2}$ ). At those current densities, the anodic process proceeds only from the active dissolution region since the active-passive transition region corresponded to an average current density of  $35 \text{ mA cm}^{-2}$ .

In those experiments, only the electrolyte solution containing  $0.20 \text{ M}$  of  $\text{Cu (II)}$  species was tested at different amounts of water (1-15 wt%). The electrochemical dissolution was carried out for  $7200 \text{ s}$  under agitated conditions, e.g.  $\omega = 700 \text{ rpm}$ . Experiments on solid copper electrodes indicated that active-passive transitions corresponding to the formation of a  $\text{CuCl}$  salt film [165] typically occurred at much higher current densities ( $> 35 \text{ mA cm}^{-2}$  in average) so that the present conditions corresponded to the active dissolution of copper.

To examine the dependency of the dissolution valency on the initial concentration of the  $\text{Cu (II)}$ , the dissolution experiments were performed from electrolyte solutions containing  $0, 0.05, 0.10$  and  $0.20 \text{ M Cu}^{2+}$ . The applied current density was fixed to  $2.85 \text{ mA cm}^{-2}$  and the dissolution time was  $7200 \text{ s}$ . In this case, the electrolyte solutions contained 1 and 15 wt% of water and the rotation regime was 700 and 1400 rpm.

The influence of the rotation speed upon the dissolution valency was studied from electrolyte solutions ( $0.20 \text{ M}$ ) containing 1 – 15 wt% of water. The applied current density was fixed to  $2.85 \text{ mA cm}^{-2}$  while the four regimes of rotation were applied, e.g. 300, 700, 1400 and 2100 rpm. In order to assess the effect of agitation on the dissolution valency from pure ethaline, the same rotation rates were applied.

#### 4.6.4 Experimental procedure to determine complex species as a function of anodic charge

A separate experiment was performed in order to identify the complex species formed when Cu was electrochemically dissolved in pure ethaline. In order to do that, Cu was galvanostatically dissolved in ethaline (with 1 wt% of water) as a function of the anodic charge. For example, the applied current density was fixed to  $2.85 \text{ mA cm}^{-2}$  while the dissolution time was increased from 3600, 7200, 14400 to 28800 s. Thereafter, the weight loss of the electrode was recorded and the concentration of the species was estimated using equation 4.25.

$$C = \frac{n_0}{V} \quad (4.25)$$

where C is the concentration of species,  $n_0$  is the number of moles and V is the volume of the solution. Also, the concentration of the species was estimated by spectroscopic means. Samples were collected from the anodic compartment after the dissolution process to be analysed by UV-Vis spectroscopy.

The concentration of the complex species was calculated using Beer's law as equation 4.26 indicates.

$$A = C \epsilon b \quad (4.26)$$

where A is the absorbance from the species, C is the concentration of the species,  $\epsilon$  is the molar absorptivity and b is the pathlength of the cuvette. After subtracting the background influence, the absorbance values were extrapolated at 273 nm and the concentration was calculated. However, the molar absorptivity of the species was unknown. Thereby, to obtain that coefficient, different amounts of CuCl salt (Sigma-Aldrich, > 97%) were dissolved in ethaline to prepare three standard solutions, e.g. 10, 20 and 30 mM of  $\text{Cu}^+$ . Thereafter, the molar absorptivity of the Cu (I) species was computed from the regression equation of the calibration curve.

**5. Chapter – Results and Discussion: Physico-chemical and electrochemical properties as a function of water content**

## 5. Results and Discussion

---

### 5.1 Measurement of water content

This section presents the results on the ability of the electrolyte to incorporate water over time. Some of the most important physico-chemical and electrochemical properties such as density, viscosity, conductivity and electrochemical window were investigated with increasing amounts of water in order to understand to what extent water content influenced these properties.

#### 5.1.1 Water content in ethaline and electrolyte by KF titration

To determine the initial concentration of water in ethaline and in the electrolyte, Karl Fischer titration was employed. As mentioned earlier, the electrolyte was  $\text{CuCl}_2 \cdot 2\text{H}_2\text{O}$  dissolved in ethaline and for simplicity it will be referred in the text as the “electrolyte”. Table 5.1 shows the concentration of water measured in ethaline and in the electrolyte with increasing amounts of metal salt (the dataset of KF titration can be found in Appendix A). The concentration of water in ethaline was measured to be 1.13 wt% while in the electrolyte (containing 0.20 M  $\text{CuCl}_2 \cdot 2\text{H}_2\text{O}$ ) was 1.80 wt%.

Table 5.1 Measurement of water content in ethaline and the electrolyte measured by Karl Fischer titration.

Sample	Water of hydration (wt%)	Experimental total H <sub>2</sub> O (wt%)
Ethaline	---	1.13 ± 0.07
0.05 M $\text{CuCl}_2 \cdot 2\text{H}_2\text{O}$	0.16	1.44 ± 0.03
0.10 M $\text{CuCl}_2 \cdot 2\text{H}_2\text{O}$	0.31	1.54 ± 0.07
0.20 M $\text{CuCl}_2 \cdot 2\text{H}_2\text{O}$	0.62	1.80 ± 0.02

Since water content in the electrolyte was somewhat higher than in ethaline, it seemed that the waters of hydration of the salt ( $\text{CuCl}_2 \cdot 2\text{H}_2\text{O}$ ) influenced the water content. For example, the waters of hydration of 0.20 M  $\text{CuCl}_2 \cdot 2\text{H}_2\text{O}$  were calculated to be 0.62 wt%, which reasonably accounted for the difference in water content

between ethaline and the electrolyte. Similar results were found for electrolyte containing 0.05 and 0.10 M of  $\text{CuCl}_2 \cdot 2\text{H}_2\text{O}$ . An earlier study explained that the water of hydration of the metal salt were replaced by  $\text{Cl}^-$  due to their high concentration in ethaline, e.g. 4.5 M [106]. Thereby, these waters of hydration could be available to be consumed during titration.

Karl Fischer titration was useful to construct a calibration curve to cross-check the initial content of water measured in the liquid. Fig. 5.1 shows the corresponding calibration line from which the initial water concentration was calculated to be 1.83 wt%, which was in good agreement with the measured one, e.g. 1.80 wt%.

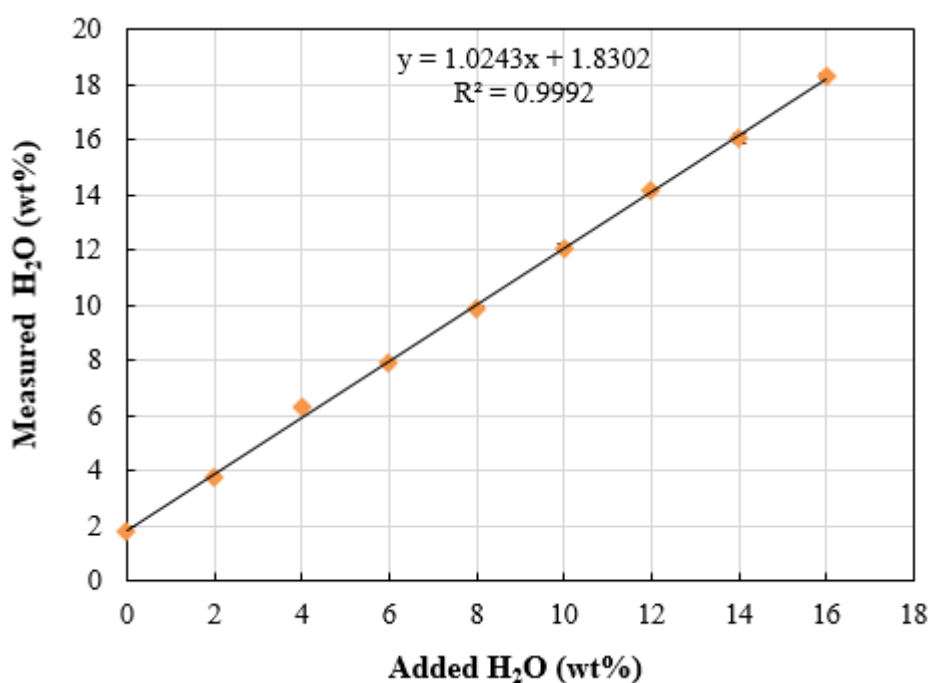


Figure 5.1 Calibration curve constructed using Karl Fischer titration data using 0.20 M  $\text{CuCl}_2 \cdot 2\text{H}_2\text{O}$  in ethaline. The error bars are smaller than the markers.

Although KF titration was a reliable technique to measure water content in ethaline and in the electrolyte, it may not be a sustainable method for practical applications since it is not an in-situ technique and it consumes reagents. Thereby, a non-destructive and reagentless method was examined such as Near Infrared (NIR) spectroscopy.



### 5.1.2 Water content in the electrolyte by NIR spectroscopy

Near Infrared (NIR) spectroscopy was performed to cross-check the initial concentration of water measured using KF titration earlier. NIR spectroscopy has been considered to be an alternative method to measure water concentration in room temperature ILs due to the fact that C-H, N-H and O-H functional groups can absorb energy in the NIR region [166]. However, it has been indicated that the spectra of both the solvent and water could overlap if their functional groups absorbed NIR light at the same wavelengths, thereby compromising the results [166].

Due to this concern, an experiment was performed to determine if overlapping absorption bands would confound the results. The NIR ethaline trace of a typical measurement is shown in Fig 5.2. It can be observed that the spectrum of ethaline shows a low absorbance near the wavelengths 1400 and 1900 nm that are the bands in which water absorbs NIR light. These results show that NIR spectroscopy may be a useful analytical method to measure water content in the electrolyte.

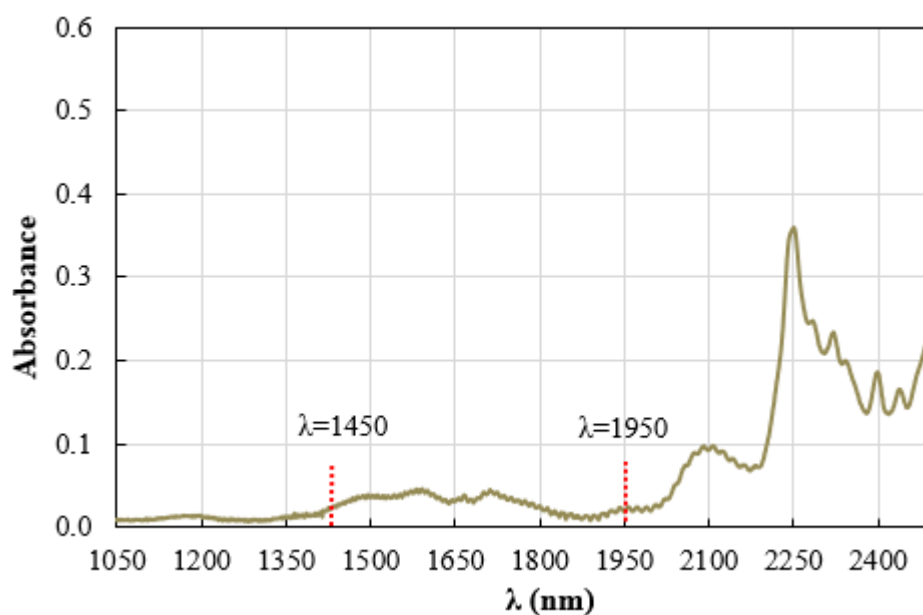


Figure 5.2 NIR spectrum of blank ethaline recorded between 1050 and 2040 nm.

Fig. 5.3 shows the NIR spectra of the electrolyte (0.20 M  $\text{CuCl}_2 \cdot 2\text{H}_2\text{O}$ ) with increasing amounts of added water (2-18 wt%). The NIR spectra exhibited two absorption bands that increased as a function of added water, e.g. 1450 and 1950 nm. Since the absorption band at 1950 nm was more quantifiable, the absorbance values were extracted from this band. The inset in Fig. 5.3 shows the absorption band at 1950 nm after being background subtracted and smoothed. These values were used to construct a calibration curve in order to determine the initial water content in the electrolyte.

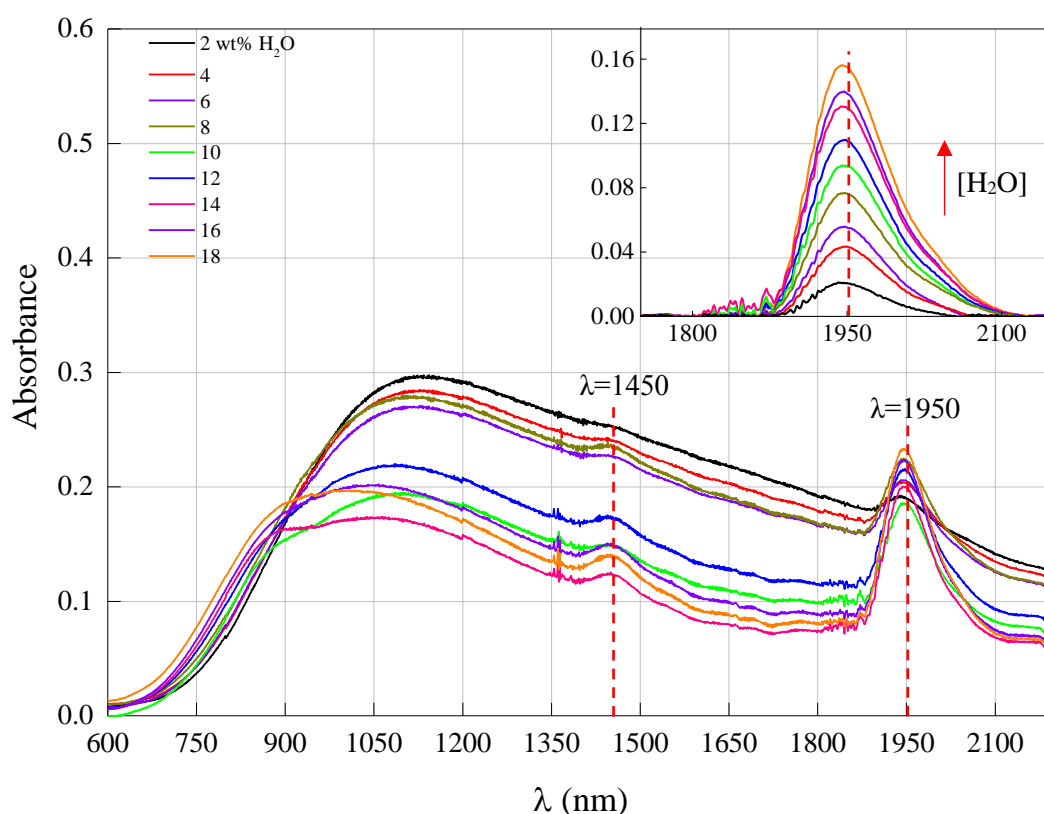


Figure 5.3 NIR spectra of the electrolyte (0.20 M  $\text{CuCl}_2 \cdot 2\text{H}_2\text{O}$ ) with added water (2 to 18 wt%). The inset graphic shows the absolute absorbance at 1950 nm after the contribution of the background was subtracted and the bands being smoothed.

Figure 5.4 shows the calibration line obtained from the NIR data at 1950 nm shown in Fig. 5.3. Assuming that the electrolyte –without added water– would exhibit negligible absorbance, the water content was calculated from the regression equation to be  $1.31 \pm 0.67$  wt%. The confidence interval, e.g.  $\pm 0.67$  was computed from an error analysis performed in commercial software (cf. Appendix B). Because

the initial concentration of water in the electrolyte could not be lower than the waters of hydration (e.g.  $\sim 0.62$  wt%), only the positive confidence interval was accounted. In this line, the initial content of water in the electrolyte varied from 1.31 to 1.98 wt%, which was in reasonable agreement with that determined by KF titration, e.g. 1.80 wt%.

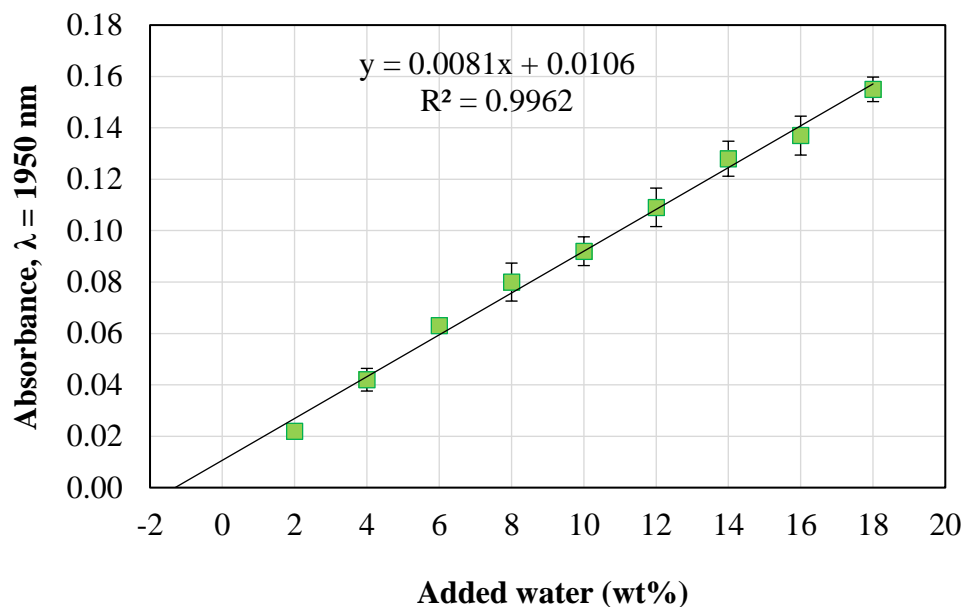


Figure 5.4 Calibration curve obtained using NIR data to cross-check the initial concentration of water in the electrolyte.

The good linearity between absorbance and water content in the electrolyte indicates that NIR could be a useful in-situ method for determining water content in DES systems.

### 5.1.3 Incorporation of water by ethaline and the electrolyte as a function of time

In order to determine the ability of the liquid to incorporate water from the atmosphere, ethaline and the electrolyte were exposed to the air and monitored. Before exposure, the water content in ethaline and the electrolyte were measured to be 0.26 and 1.05 wt%. The slight difference in the initial water content from the previous section was due to the fact that samples were prepared from other batch of reagents.

Fig. 5.5 shows that the electrolyte could incorporate water from 3 to 15 wt% within a month. Ethaline exhibited a similar behaviour but to a lesser extent. For instance, at the third week of monitoring ethaline adsorbed 7.98 wt% while the electrolyte did 10.6 wt%. Perhaps, the hygroscopic nature of the metal salt dissolved in the medium could have enhanced the incorporation of water by the electrolyte. Water content in ethaline remained constant, e.g. from 0.26 to 0.29 wt% when it was monitored from a sealed flask.

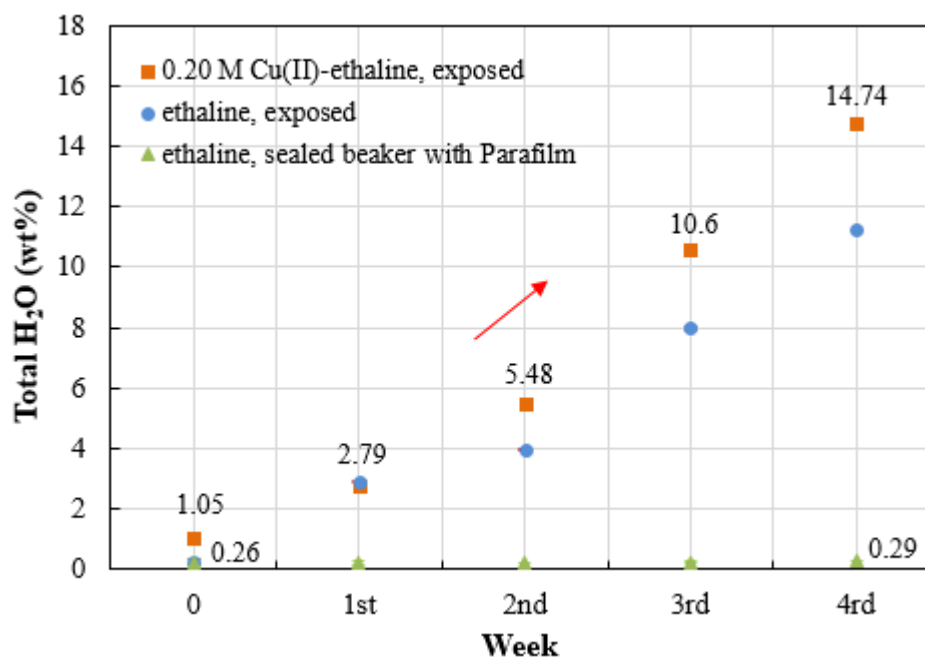


Figure 5.5 Ability of ethaline and the electrolyte to incorporate water with time. The error bars were smaller than the markers.

To evaluate the saturation point of the electrolyte, this was kept exposed to the air and monitored over three additional months. Fig. 5.6 shows that the saturation point of the electrolyte was 28.1 wt% since the variation of water content between the third and fourth month was considered to be negligible, e.g. 0.3 wt%. The saturation point of another DES such as reline was reported to be 40 wt% after 10 weeks of monitoring, where the humidity of the environment was monitored to be 60% [167]. Although the humidity was not registered in this study and thereby no comparisons can be drawn, our study is in broad agreement with that earlier result [167].

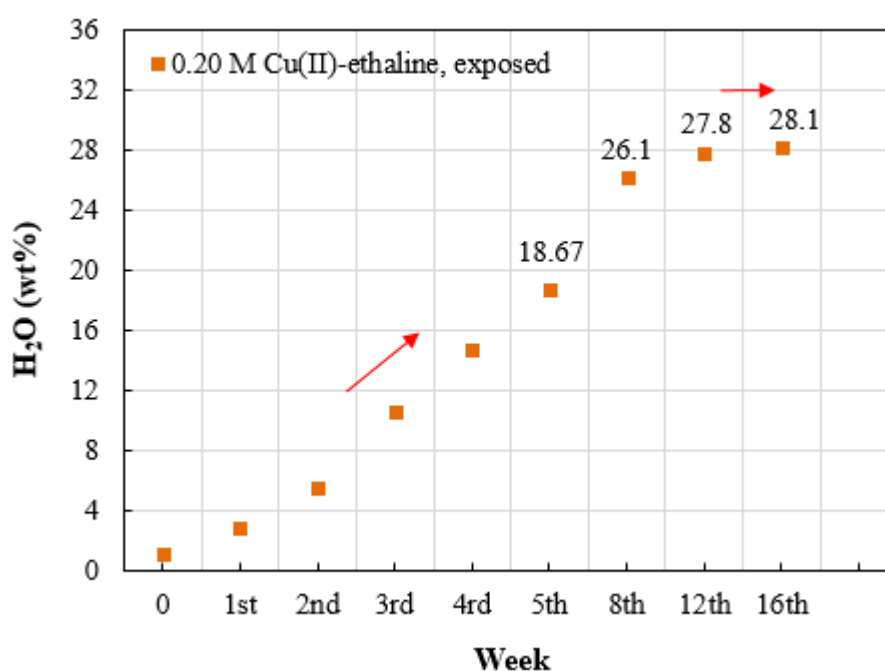


Figure 5.6 Monitoring of the electrolyte for water incorporation over four months to ascertain its approximated saturation point. The error bars were smaller than the markers.

The data shows that while significant amounts of water can be taken up by pure or metal-salt containing ethaline, it can be prevented by simple measures such as sealing the flask with plastic film (Parafilm paper). Processes based on DESs are therefore recommended to be performed from sealed containers.

## 5.2 Monitoring of Cu speciation as a function of water content in DESs

### 5.2.1 Speciation of Cu in aqueous systems

In order to understand the influence of water on the Cu-complex species formed in ethaline, it is essential to discuss some important aspects of Cu speciation in aqueous systems. Fig. 5.7 shows the Ultraviolet Visible (UV-Vis) spectrum of 0.05 M  $\text{CuCl}_2 \cdot 2\text{H}_2\text{O}$  dissolved in DI water. It can be observed that the maximum absorbance occurred at 286 nm which is characteristic of the fully hydrated hexa-aquacopper ion, e.g.  $[\text{Cu}(\text{H}_2\text{O})_6]^{2+}$ . Qualitatively, the colour of the solution tends to be bluish as shown in the inset image in Fig. 5.7 due to the existence of this ion in solution.

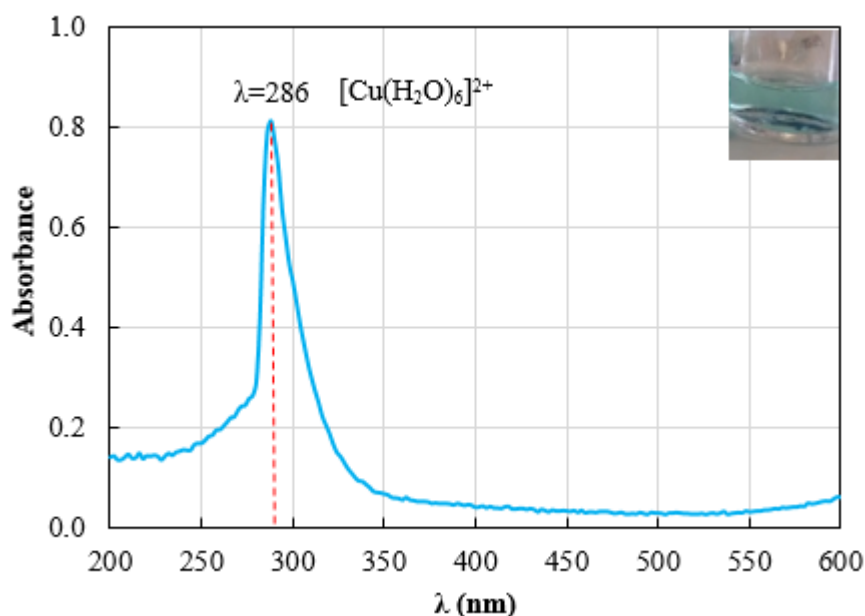
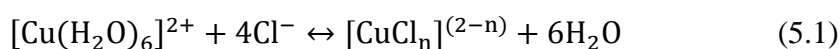


Figure 5.7 UV-Vis spectrum of 0.05 M  $\text{CuCl}_2 \cdot 2\text{H}_2\text{O}$  dissolved in DI water, cuvette pathlength = 1cm. The inset image shows the colour of this solution.

It is known that the inclusion of chloride yields a displacement reaction, where  $\text{H}_2\text{O}$  is replaced by  $\text{Cl}^-$  as shown in equation 5.1 [168].



Different types of Cu-Cl species can exist in chloride aqueous systems depending on the concentration of chloride [168]. These complexes can be of the form  $[\text{CuCl}_n]^{(2-n)}$ . Fig. 5.8 corresponds to the UV-Vis spectrum of 5.0 mM Cu (II) + 6 M HCl exhibiting electronic bands close to 290 and 400 nm. The occurrence of these bands has been attributed to the existence of a mixture of Cu-Cl species such as the  $[\text{CuCl}]^+$ ,  $[\text{CuCl}_3]^-$  and  $[\text{CuCl}_4]^{2-}$  [168]. Qualitatively, chloride aqueous systems containing  $\text{CuCl}_4^{2-}$  species tend to exhibit a greenish colour, as shown in the inset image in Fig. 5.8.

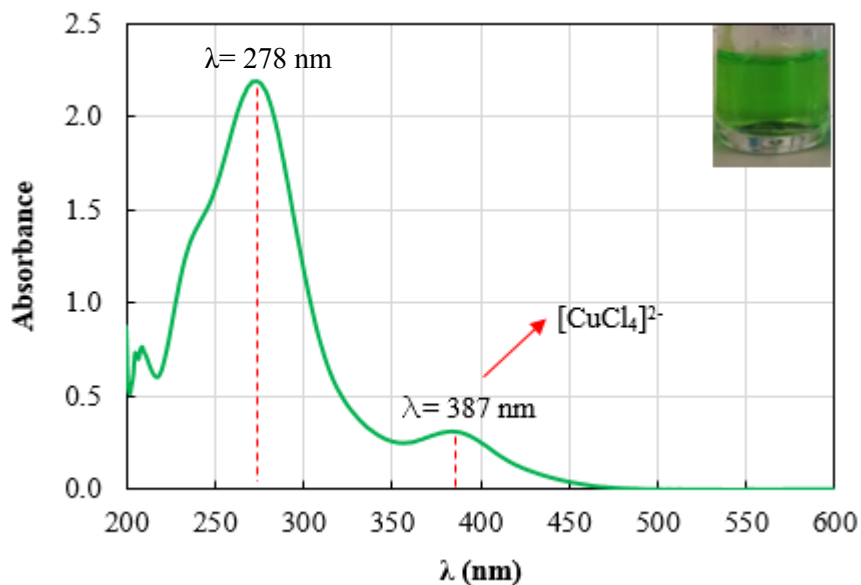


Figure 5.8 UV-Vis spectrum of 5.0 mM  $\text{CuCl}_2 \cdot 2\text{H}_2\text{O}$  dissolved in 6 M HCl, cuvette pathlength= 1 cm. The inset image shows the colour of this solution.

Having discussed that tetrachloro species can exist in high chloride-containing solutions, it is plausible that analogous speciation ensues in ethaline since this contains a high concentration of chloride, e.g.  $\sim 4.5$  M.

### 5.2.2 Speciation of Cu in DES systems

In order to determine the speciation of Cu (II) from ethaline, UV-Vis spectroscopy was performed. Fig. 5.9 shows the charge-transfer bands characteristics of Cu (II) in ethaline within the UV-Vis region. The bands were located from 200 to 600 nm. The first electronic band appeared between 200 and 260 nm with a maximum absorbance centred at 239 nm, followed by two bands whose maximum absorbance emerged at 290 and 404 nm. These bands have been attributed to the existence of the tetrachloro-cuprate complex, e.g.  $[\text{CuCl}_4]^{2-}$  [93]. Tetrachloro species has also been reported to form in imidazolium-based ILs such as such as 1-methyl-3-(3-trimethoxysilylpropyl) imidazolium chloride [169] and in Lewis-basic imidazolium ILs [170].

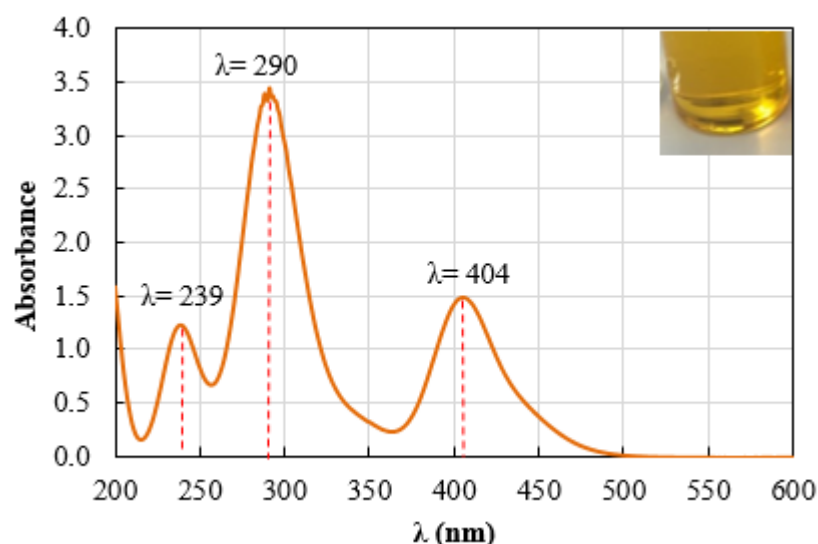


Figure 5.9 UV-Vis spectrum of 0.05 M Cu (II) in ethaline, cuvette pathlength = 125  $\mu\text{m}$ . The inset image shows the colour of this solution.

The existence of tetrachlorocuprate species has been crosschecked using X-ray absorption fine structure spectroscopy (EXAFS) by Hartley *et al.* [93]. This comprehensive study ascertained the speciation of transition metals in DESs. It was concluded that metals sharing the same oxidation number exhibit similar speciation. For example, metals bearing oxidation number of one can form complexes such as  $[\text{MCl}_2]^-$  or  $[\text{MCl}_3]^-$  [93]. In the case of metals with oxidation number of two, complexes such as  $[\text{MCl}_4]^{2-}$  can form and therefore  $[\text{CuCl}_4]^{2-}$  complex was corroborated to form in ethaline [93].



It has also been of interest to examine if waters of hydration can affect metal speciation since hydrated metal salts are preferred for practical applications. It was concluded that waters of hydration did not intervene in Cu (II) speciation for two reasons: (i) the UV-Vis spectra of both hydrated and non-hydrated metal salt exhibited no difference [106] and (ii) the coordination number between the cation and chloride was unchanged by the waters of hydration, as shown in the EXAFS analysis [93].

The influence of water upon Cu (II) speciation was studied within a concentration range of 1 - 40 wt%. Fig. 5.10 shows the UV-Vis spectra of 0.05 M Cu (II) in ethaline with increasing amounts of water. The absorbance of all charge-transfer bands gradually reduces as the red arrows indicate. This decrease has also been observed by De Vreese *et al.* [105] and it was attributed to a progressive reduction of the concentration of  $[\text{CuCl}_4]^{2-}$  species in the medium. This was believed to occur because water reduced the concentration of  $\text{Cl}^-$  in solution and thereby the amount of the  $[\text{CuCl}_4]^{2-}$  complexes [105].

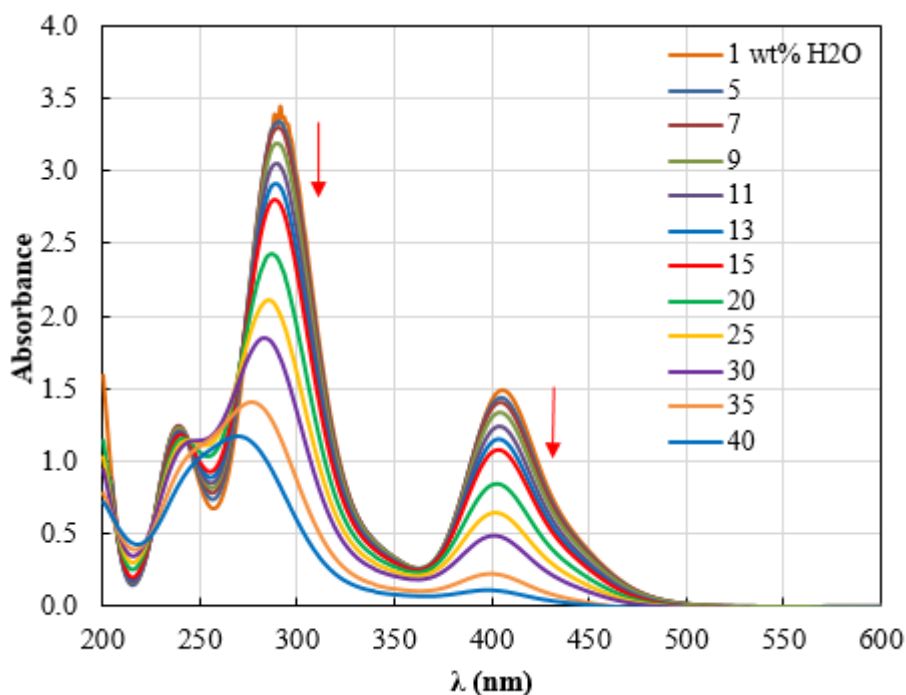


Figure 5.10 UV-Vis spectra of 0.05 M  $\text{CuCl}_2 \cdot 2\text{H}_2\text{O}$  in ethaline containing increasing amounts of water, cuvette pathlength = 125  $\mu\text{m}$ .

Fig. 5.11 shows a transition point beyond 35 wt% of water in the electrolyte, which is characterised by the appearance of a new band with a shoulder as shown by the green curve in Fig. 5.11. This spectrum resembles the UV-Vis trace of Cu (II) species in the chloride aqueous system [168] which for comparison has been included as the blue dashed curve in Fig. 5.11. Qualitatively, the spectrum of Cu (II) species in DES and chloride aqueous systems seem comparable pointing out that a mixture of chloro-aquo complexes might exist. This hypothesis agrees with earlier investigations where  $\text{Cl}^-$  has been reported to be replaced by  $\text{H}_2\text{O}$  when reaching concentrations beyond 40 and 49 wt% [105, 107]. These results suggest that the electrolyte containing water beyond 35 wt%, may behave rather as the chloride aqueous system.

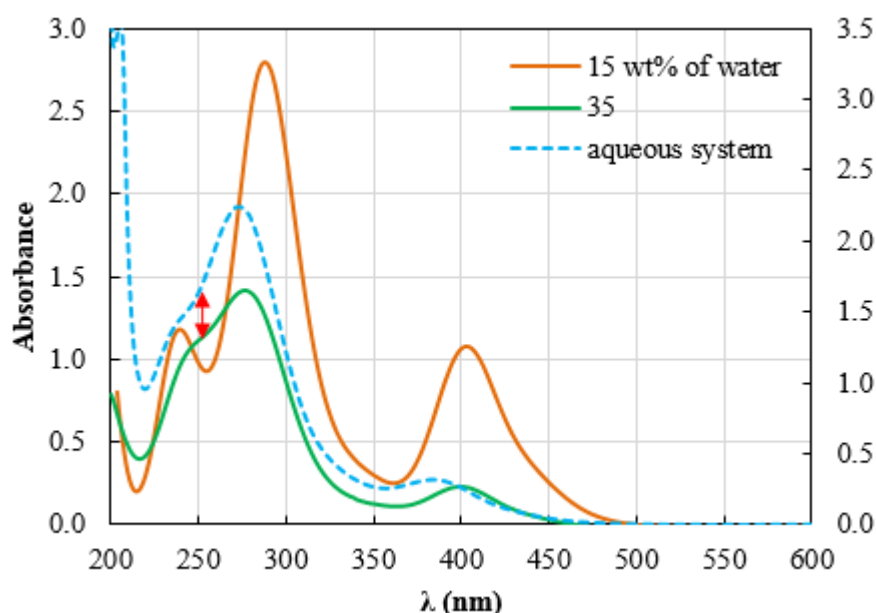


Figure 5.11 UV-Vis spectra of 0.05 M  $\text{CuCl}_2 \cdot 2\text{H}_2\text{O}$  in ethaline solution containing 15 and 35 wt% of  $\text{H}_2\text{O}$ , cuvette pathlength 125  $\mu\text{m}$ . The spectrum of Cu (II) species in aqueous solution corresponds to a concentration of 5 mM Cu (II) + 6 M HCl. This latter spectrum was measured in a cuvette of pathlength= 1 cm.

Since water content seems to affect the speciation of Cu (II) species only beyond 35 wt%, it can be concluded that at 15 wt% the  $[\text{CuCl}_4]^{2-}$  complexes was probably the dominant species. This implied that redox potentials, electro-kinetics, microstructure and other aspects should not be strongly influenced by the changes in speciation of copper complexes. The physico-chemical properties of the electrolyte as a function of water concentration were the next ones to be examined.

### 5.3 Physico-chemical properties as a function of water content

#### 5.3.1 Density as a function of water content

The examination of density as a function of water may provide some insights on structural changes of the molecular organisation. To shed some light on this, a set of water-containing samples were prepared. The samples were prepared to match the concentration of water incorporated over the monitored month, e.g. 3, 6, 10 and 15 wt% of total H<sub>2</sub>O.

Figure 5.12 shows the density of ethaline and the electrolyte as a function of water content. The density of ethaline and the electrolyte were found to decrease with increasing amounts of water. For example, ethaline density reduced from 1.127 g cm<sup>-3</sup> (at 1 wt%) to 1.098 g cm<sup>-3</sup> (at 15 wt%). Likewise, electrolyte density decreased from 1.145 g cm<sup>-3</sup> to 1.130 g cm<sup>-3</sup> in the same range of water concentration. These findings are consistent with earlier results where water-containing DESs were examined [171-176], reporting that water content decreased density.

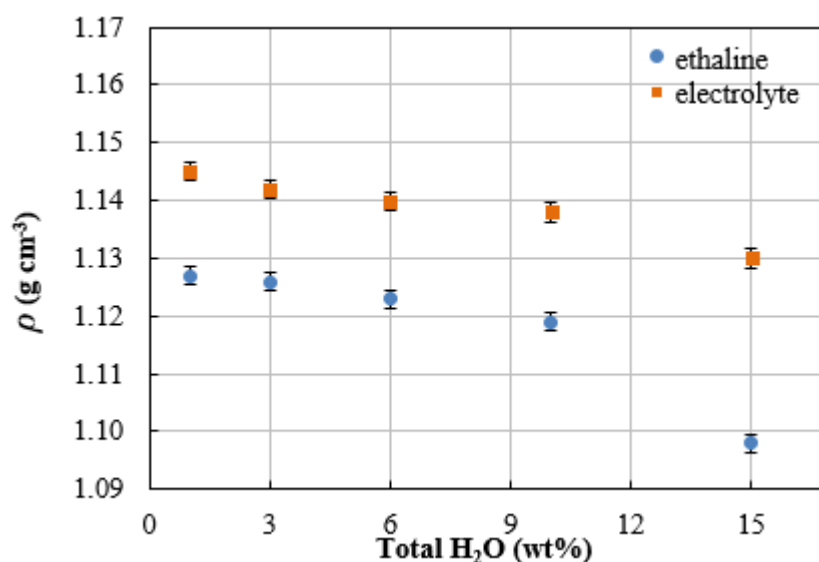


Figure 5.12 Density of ethaline and electrolyte measured with increasing amounts of water (1-15 wt%). The measurements were carried out at room temperature.

It is notable that the electrolyte is denser than pure ethaline which has been attributed to a more packed molecular structure [173, 177] caused by the formation of the tetrachloro-cuprate complex as shown in Fig. 5.13. Protsenko *et al.* [177] explained that denser structures in DESs are the result of increased surface tension. This occurs when additional H-bonding (product of the formation of metal-DES complex) increases the cohesive forces amongst the molecules which in turn increases the density of the electrolyte [177].

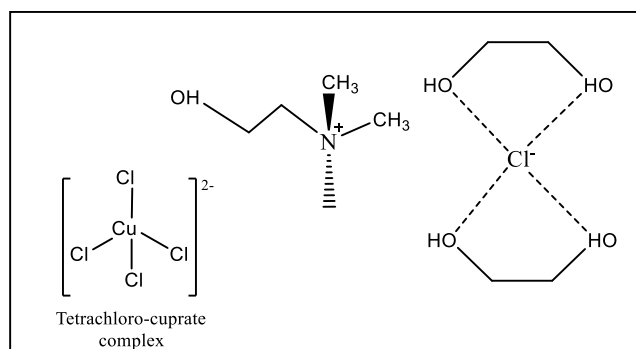


Figure 5.13 Schematic of the tetrachlorocuprate complex likely to form when  $\text{CuCl}_2$  dissolved in ethaline.

At the moment, the decrease on density of DESs with the inclusion of water has been justified via two different explanations. The first one refers to the conventional hole theory, which was proven to be applicable to DESs (cf. section 1.4.5.2) [80]. This theory conceptualises that interstitial voids of random size and positions emerge within the solvent [73, 76, 77]. Since DES density was believed to be governed by the size of these holes, they were dependent on water content [177]. To test this hypothesis, the surface tension of the liquid is measured and the average radii of the interstitial holes have been calculated using equation 5.2 [177].

$$4\pi r^2 = \frac{3.5kT}{\gamma} \quad (5.2)$$

where  $r$  is the average size of the interstitial hole,  $k$  is the Boltzman constant,  $T$  is the absolute temperature, and  $\gamma$  is the surface tension of the liquid. It was reported that the average dimensions of the interstitial voids consistently increased as water content increased in the system [177] as calculated from equation 5.2 and surface tension measurements. It was therefore concluded that water brought about larger

voids, which in turn modified the density of DESs, i.e. the inclusion of water decreased the density of DESs due to a more open structure.

An alternative explanation suggests that water disrupts the hydrogen bond network amongst DESs components [178]. To elucidate the mechanism, the average number of H-bonds (between 50 and 250) were estimated using molecular dynamic simulations [178]. The number of H-bonds in ethaline was calculated for the following pairs: HBD/H<sub>2</sub>O, Cl<sup>-</sup>/H<sub>2</sub>O, Ch<sup>+</sup>/H<sub>2</sub>O as well as for HBD-HBD, HBD-Ch<sup>+</sup> and HBD-Cl<sup>-</sup> interactions. For example, the largest number of H-bonds was found to form between HBD/H<sub>2</sub>O in ethaline increasing from 50 to 250 due to the high polarity of the HBD over the remaining constituents of a DES. By contrast, the inclusion of water decreased H-bonding amongst HBD-HBD, HBD-Ch<sup>+</sup> and HBD-Cl<sup>-</sup> half their initial value (from 200 to 100) [178]. It was therefore concluded that H-bonds between DES components and H<sub>2</sub>O began to form in expense of DES-DES interactions producing a disruption in the assembly of the molecules and causing the decrease in density. It is important to remark that although both explanations seem correct, the present data do not allow one to discriminate which one would be applicable to this work.

### 5.3.2 Viscosity as a function of water content

Ethaline viscosity has been measured to be 32.1 mPa s (at 1 wt% of H<sub>2</sub>O) exhibiting one of the lowest viscosities compared with other DESs such as glyceline and reline (225 and 552 mPa s respectively [176, 179]) both measured at 30 °C. Also, no significant difference in viscosity exists amongst ethaline and [EMIM]<sup>+</sup>[CF<sub>3</sub>SO<sub>3</sub>]<sup>-</sup> ( $\eta=35$  mPa s) which is one of the less viscous imidazolium-based ILs. Despite that, DESs remain substantially more viscous than aqueous systems (1-2 mPa s), which perhaps may be alleviated by the addition of water.

Figure 5.14 shows that ethaline viscosity decreases almost three times from 32.1 to 11.7 mPa s with increasing amounts of water, 1-15 wt%. Similarly, the electrolyte viscosity reduced from 47.3 to 15 mPa s in the same range of water concentration. Comparable trends have been reported in earlier studies when adding

water to the electrolyte [175, 179]. However, although the electrolyte viscosity decreased with the addition of water, it was still twelve times greater than that of the aqueous system comprising of 0.5 M CuCl<sub>2</sub> and 5 M HCl (1.21 mPa s) [180].

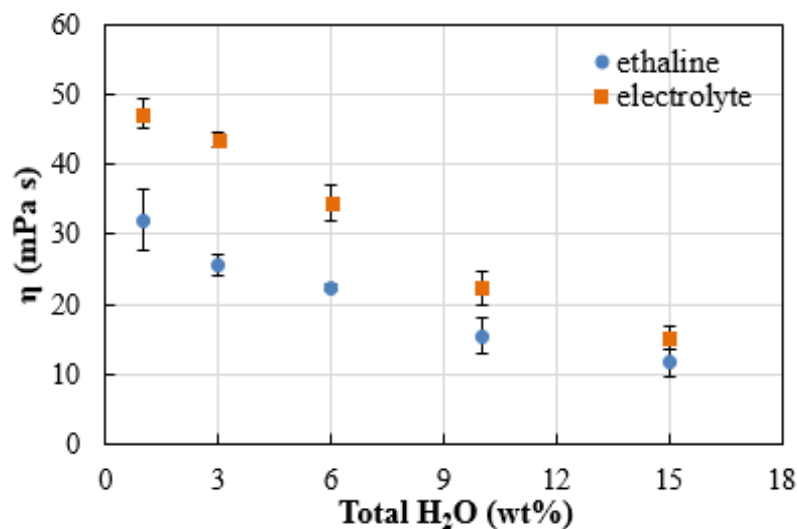


Figure 5.14 Ethaline and electrolyte viscosity with increasing amounts of water, 1-15 wt% at 25 °C.

Although most authors agree that water caused a decrease on viscosity [174-176, 179], the underlying reasons have not been fully elucidated due to the complexity of the system. In an endeavour to explain the viscosity reduction, two approaches have been explored.

The first one examined if the addition of water weakened the cohesive forces of the liquid so that the interstitial vacancies increased facilitating the movement of ionic species [173, 177]. For this purpose, two different eutectic systems containing Ni (II) and Cr (III) salts were assessed. These systems were reported to exhibit larger voids with increasing amounts of H<sub>2</sub>O resulting in less viscous melts and therefore assisting the mobility of species [173, 177].

The second approach assessed if the addition of water caused structural changes in DESs that consequently altered viscosity [181]. Hammond's group used neutron total scattering and empirical potential structure refinement (EPSR) to identify transition points where structural changes of reline occurred as water was added [181]. It was found that up to 3 wt% of water reline, proved to be tolerant to water since its original structure was not affected. However, a further increase to 42

wt% caused a decrease in the DES-DES interactions because water preferred to be around the  $\text{Ch}^+$  cation and triggered the formation of a nanostructure with ionic clusters. It can therefore be considered that a decrease in viscosity occurs as the strength of the intermolecular interactions reduces.

Low viscosity might be desirable for electrodeposition processes because the mass transport of diffusing species could be faster than that of low water-containing DES systems, which would be translated in higher plating rates.

### 5.3.3 Conductivity as a function of water content

Table 5.2 summarises the conductivity of the electrolyte with increasing amounts of water. The electrolyte conductivity exhibits a significant improvement from 0.795 to 1.530  $\text{S m}^{-1}$  as water increased from 1 to 15 wt%, which is nearly twice the initial value. This conductivity is comparable to one of the most conductive conventional ILs, e.g. 1.400  $\text{S m}^{-1}$  [182]. The improvement of conductivity with increasing moisture has been reported on DESs systems in earlier investigations [173, 177, 183]. For instance, the conductivity of the Ni (II) species in ethaline solution improved almost five times, e.g. from 0.764 to 3.42  $\text{S m}^{-1}$  as the mole fraction of water increased from 0.62 to 0.81 [177]. The enhancement of the electrical conductivity has been correlated to a lower activation energy brought about by water, which implied a facile ionic motion for the charge carriers [177, 183].

Table 5.2 Conductivity of the electrolyte as function of water concentration in the system. The measurements were performed at room temperature.

<b>Water content (wt%)</b>	<b>Conductivity (<math>\text{S m}^{-1}</math>)</b>
1	0.795
3	0.953
6	1.020
10	1.160
15	1.530

ILs and DESs have been often promoted as high-conductive reaction media; however, it should be noted that compared to aqueous systems they are resistive. For example, an aqueous system containing  $\sim 0.2 \text{ M}$  concentration of  $\text{CuCl}_2$  exhibits a

conductivity of  $4.2 \text{ S m}^{-1}$  [184] whilst the conductivity of our electrolyte is five times lower, e.g.  $0.795 \text{ S m}^{-1}$ . Contrary to molecular solvents, the structure of DESs is bulkier whereby interstitial holes of small sizes restrict ionic conduction. This has been reasonable to conceive due to the fact that high viscous DESs have been associated to sluggish ionic movement [79].

Abbott demonstrated that as a consequence of the formation of small interstitial voids as well as the low probability of finding them  $10^{-4}$  to  $10^{-7}$ , ionic conduction was limited by the density of voids instead of the concentration of the charge carriers as presented in equation 1.20 (cf. section 1.4.5.3).

In order to assess if the conductivity of the water-containing electrolyte was controlled by the mobility of the charge carriers in the medium, a graph of the conductivity against the fluidity ( $\eta^{-1}$ ) was plotted. Fig. 5.15 shows that almost a linear correspondence exists establishing the correlation between ionic motion and ionic conduction for each system. As discussed earlier, the movement of the electroactive species was limited by the availability of holes of suitable sizes to move whereas the ionic conduction was limited by the density of interstitial holes. Since the average size of the voids was calculated to increase as water was added to the system, the ionic conduction was facilitated which in turn was reflected in the improved ability of the material to conduct electricity [177, 183].

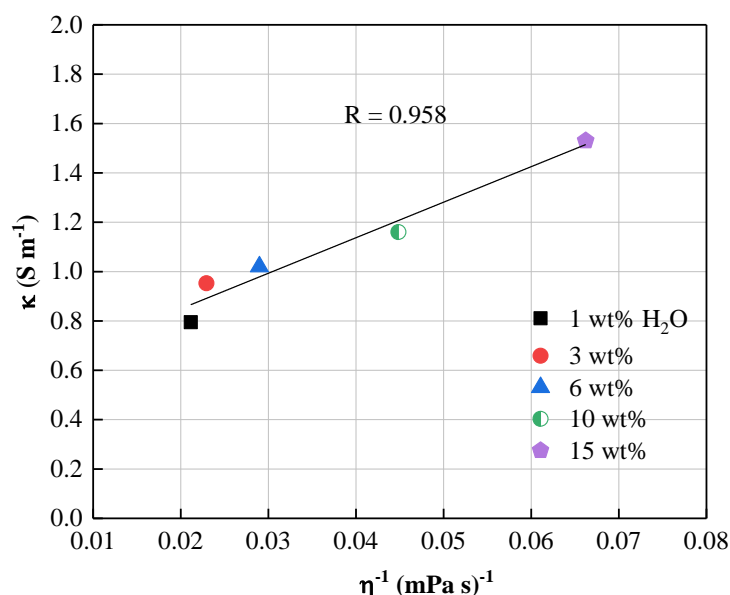


Figure 5.15 Conductivity of the electrolyte against the fluidity containing increasing amounts of water (1-15 wt%).



Overall, it has been identified that water can cause significant effects on density of a DES system such as: a) disruption of the DES-DES hydrogen bonds, b) weakening of the cohesive forces of the liquid with increase in the interstitial vacancies and c) alteration of the nanostructure of the solvent beyond a particular concentration of water. Hence, the decrease on the electrolyte density can be the result of a more open structure which in turn decreases electrolyte viscosity facilitating ionic transport. The increase of electrical conductivity also accounts as a beneficial effect of water content. But once again, it is important to remind that the data in this work do not allow one to distinguish which explanation is suitable to describe changes in viscosity and conductivity with the addition of water content in the DES system.

#### *5.3.4 Electrochemical window as function of water content*

The electrochemical window (EW) holds a relevant role in electrochemical deposition since it is the potential range wherein an electrochemical reaction can take place without involving the solvent, i.e. it is the region where the solvent is stable.

Traditional ILs based on chloroaluminate salts and water-air stable anions have been popular due to their wide EWs. For example, ILs based on chloroaluminate salts were characterised to offer up to 5.4 V of potential range under vacuum or dry conditions [185]. Likewise, water-air stable ILs exhibited EWs as large as 4.4 V. Nevertheless, the potential windows of DESs have been found to be smaller than conventional ILs. For instance, DESs such as ethaline possessed an EW of 1.5 V and reline exhibited a somewhat smaller window of 1.2 V. These electrochemical windows were almost threefold lower than the ones achieved with traditional ILs [185].

Interestingly, water has been proven to be detrimental to ILs systems since it could reduce both the anodic and the cathodic limit potentials [3, 43]. Due to the fact that chloroaluminate-based ILs were found to be unstable under wet conditions, i.e. they hydrolysed [3], water-air stable ILs were employed to assess the impact of water upon the potential window. For instance, after being exposed to an environment

saturated in water, ILs such as  $[\text{BMIM}]^+[\text{BF}_4]^-$  and  $[\text{MDIM}]^+[\text{BF}_4]^-$  showed a substantial reduction on their potential windows. They narrowed down to half of their initial value. To exemplify, the electrochemical window of  $[\text{BMIM}]^+[\text{BF}_4]^-$  decreased from 4.10 to 1.95 V.

Due to the fact that water was deleterious for the EW of ILs, the influence of water upon the anodic and cathodic potential limits of ethaline were examined. Fig. 5.16 shows the linear scan voltammogram of blank ethaline with various amounts of water. The potential window of ethaline at 1 wt% was measured to be 1.7 V, which was in reasonable agreement with the EW of ethaline reported to be 1.5 V in an earlier investigation [88].

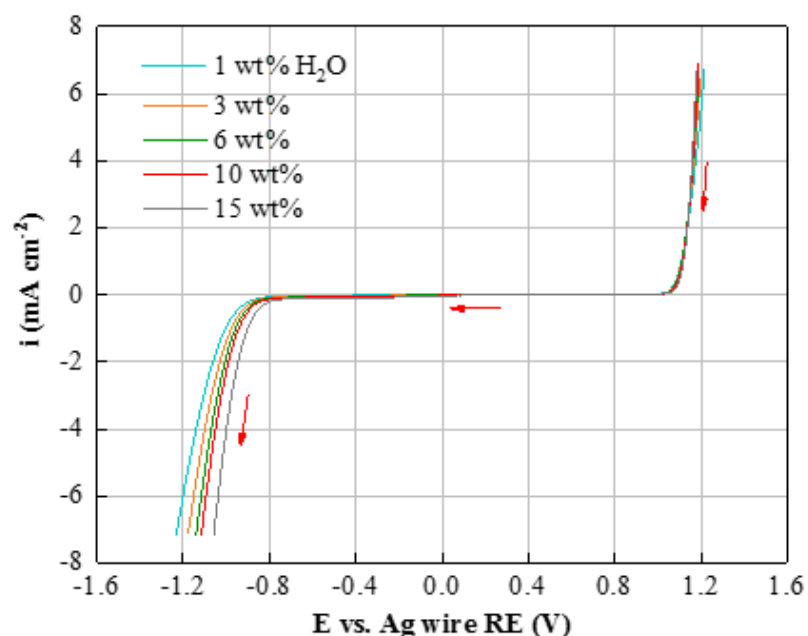


Figure 5.16 Voltammetry of ethaline containing water from 1 to 15 wt% of water. All the experiments were performed using a Pt electrode at a scan rate of  $5 \text{ mV s}^{-1}$ , rotation speed of  $\omega = 700 \text{ rpm}$  at  $25 \text{ }^\circ\text{C}$ .

The voltammogram of Fig. 5.16 also reveals that the addition of water hardly changed the anodic limit potential of ethaline, e.g.  $+0.95 \text{ V}$  vs. Ag wire RE. On the contrary, the cathodic process exhibited a more complex behaviour, i.e. the cathodic potentials shifted to less negative overpotentials. Table 5.3 summarises the cathodic potentials and thereby the change in the EW for each water-containing ethaline solution. It can be observed that increasing the water content from 1-15 wt% reduced

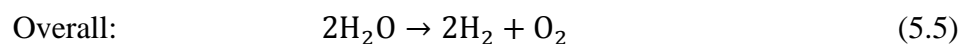
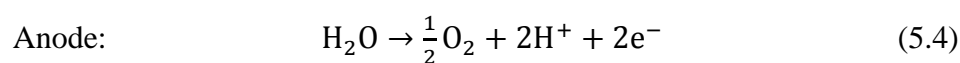
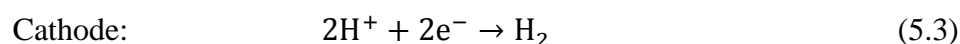
the overall potential window by approximately 0.068 V. It is notable that while the EW of conventional ILs were minimised substantially by the presence of water, the EW of ethaline exhibited a greater tolerance to hydration. Contrary results have been reported by Du *et al.* [167] when examining the EW of reline. For example, beyond 6 wt%, the EW narrowed from 2.54 to 1.45 V and a further increase to 12 wt% decreased the EW to 1.24 V [167]. This reduction was greater than the registered for ethaline in this study.

Table 5.3 EW of ethaline with increasing amounts of water. The anodic potential was +0.95 V vs. Ag wire RE that remained unchanged. The anodic and cathodic limits were defined at current densities such as +0.010 and -0.010 mA cm<sup>-2</sup>.

<b>Water content (wt%)</b>	<b>Cathodic potential (V vs. Ag wire)</b>	<b>EW (V)</b>
1	-0.755	1.705
3	-0.731	1.681
6	-0.726	1.676
10	-0.709	1.659
15	-0.687	1.637

So far the influence of water content on the positive and the negative potential limits of ethaline has been presented. However, in the absence of the analysis of the breakdown products, it is not possible to conclusively show which breakdown reactions correspond to the electrolysis of ethaline. For this reason, the anodic and cathodic decomposition products of some DESs such as reline and ethaline were reviewed.

Before discussing the decomposition products of DESs, it is essential to indicate the breakdown products that proceed from aqueous solutions. It is known that hydrogen and oxygen evolution ensued when the reduction and oxidation of water occurred. Assuming acidic medium, the reactions by which those gases were released are shown in equations 5.3 and 5.4. and relation 5.5 shows the overall reaction.



The decomposition of DESs, however, occurred in a more complex mode due to the involvement of organic compounds. Until now, there are few investigations that have elucidated which by-products were formed and their mechanisms of reaction. The most comprehensive study has been performed by Haerens' group when ethaline electrolysis was examined in both a divided and undivided electrochemical cell [115]. The separation of the compartments facilitated to discern the reaction mechanisms for the formation of the by-products. The samples were analysed using Gas Chromatography-Mass Spectrometry (GC-MS) technique and chemical analysis. Ethaline electrolysis was performed over 190 h using a stainless steel cathode, RuO<sub>2</sub>/IrO<sub>2</sub> as the anode and applying a current density of 5 mA cm<sup>-2</sup>.

By-products such as trimethylamine, acetaldehyde and 2-methyl-1,3-dioxolane were identified to form at the cathode whereas chloroform was found at the anodic compartment [115]. The reaction pathways for the formation of acetaldehyde and 2-methyl-1,3-dioxolane were explained to occur by the dehydration of ethylene glycol as Fig. 5.17 shows [115].

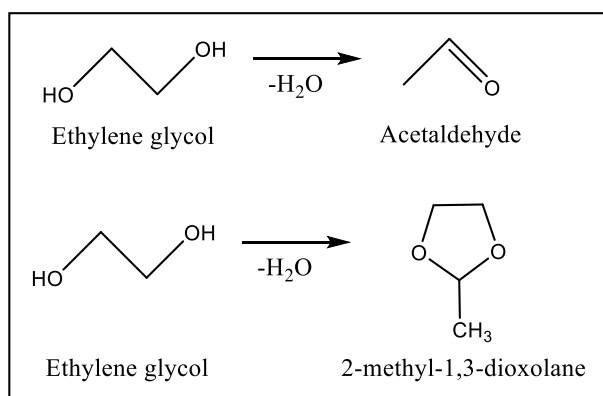


Figure 5.17 Reaction mechanisms for the formation of acetaldehyde and 2-methyl-1,3-dioxolane via dehydration of ethylene glycol. Adapted from [115].

Although DESs formulated based on choline chloride possessed a high concentration of Cl<sup>-</sup>, e.g. 4.5 M, the evolution of chlorine gas, Cl<sub>2</sub>, was not detected neither visually nor quantitatively [115]. By contrast, it was proposed that Cl<sub>3</sub><sup>-</sup> species was the dominant form of the oxidised Cl<sup>-</sup> [115]. It was therefore stated that the reaction between Cl<sub>3</sub><sup>-</sup> and other species in the liquid gave rise to the formation of some chlorinated by-products such as chloroform [115].

Contrary findings were reported by Ru group during the electro-reduction of lead oxide (PbO) from ethaline. They reported the evolution of O<sub>2</sub> and Cl<sub>2</sub> to occur using a Pt anode [186]. Chlorine evolution is known to proceed as per the following reaction:  $2\text{Cl}^- \rightarrow \text{Cl}_2 + 2\text{e}^-$ . In addition, Yue group analysed the stability of reline (ChCl:2 urea) using a divided cell, whereby Cl<sub>2</sub> was characterised to evolve at the anode [187] while the decomposition product at the cathode was found to be trimethylamine which was in agreement with the findings of Haerens' group [115, 187].

The subsequent electrolysis of ethaline in the undivided cell demonstrated that products formed individually either at the cathode or at the anode further reacted amongst them to yield additional compounds [115]. More than eight chemicals were identified after electrolysis such as trimethylamine, acetaldehyde, 2-methyl-1,3-dioxolane, chloroform, chloromethane and dichloromethane. Trimethylamine was proposed to arise from Hoffman elimination reaction as Fig. 5.18 shows. Choline hydroxide was described to form at the cathode due to the presence of OH<sup>-</sup> due to the reduction of water, e.g.  $4\text{H}_2\text{O} + 4\text{e}^- \rightarrow 4\text{OH}^- + 2\text{H}_2$  [115]. The presence of OH<sup>-</sup> was justified as the incorporation of water by ethaline which thereafter yielded the release of H<sub>2</sub>.

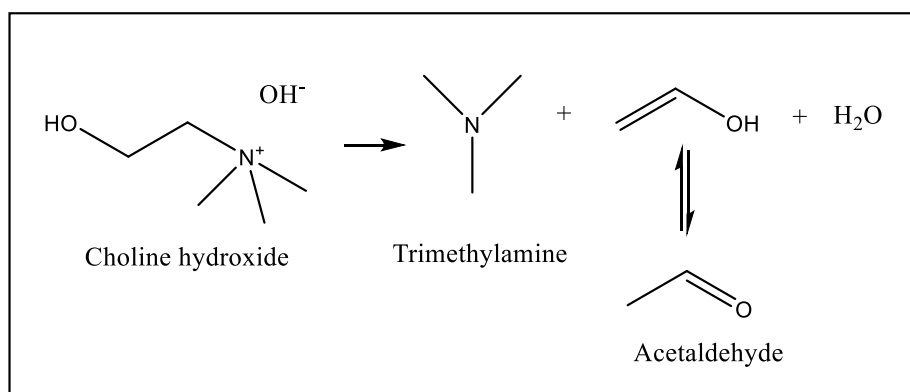


Figure 5.18 Reaction mechanism for the formation of trimethylamine via Hoffman elimination of choline hydroxide in the undivided cell. Adapted from [115].

Alternatively, choline cation was proposed to undergo an electrochemical reduction reaction at the cathode that gave rise to the choline radical as Fig. 5.19 illustrates. Subsequently, the formation of trimethylamine and methyl radical proceeded. The occurrence of chloromethane and dichloromethane was attributed to the further reaction between methyl radical and  $\text{Cl}_3^-$  ions [115].

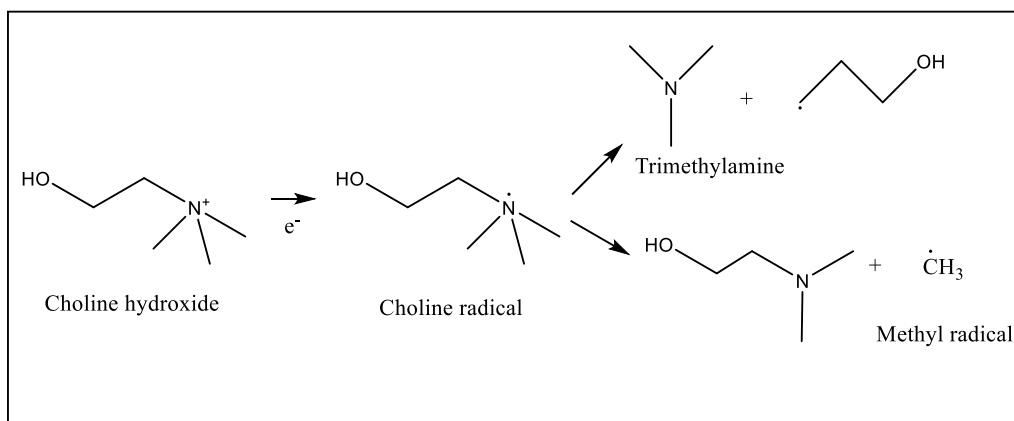


Figure 5.19 Reaction mechanism of trimethylamine via electrochemical reduction of choline hydroxide in the undivided cell. Adapted from [115].

Now that the influence of water content on some of the most important physico-chemical properties of DESs and the electrochemical window of ethaline has been evaluated, the electrochemical behaviour of the water-containing electrolyte is next examined.

## **6. Chapter – Results and Discussion: Electrodeposition of Cu from water-containing electrolyte**

## 6. Results and Discussion

---

### 6.1 Polarisation experiments

This chapter presents the most important results of the electrochemical properties of Cu (II) reduction from the ethaline-based DES system and it is divided in two sections: (i) the first one describes the electrochemical behaviour of the electroactive species from the water-containing electrolytes; including mass transport and electro-kinetic of Cu electrodeposition, and the next one presents (ii) the characteristics of the electrodeposits obtained from the water-containing electrolytes.

#### 6.1.1 Electrochemical behaviour of Cu in DES system

Firstly, the electrochemical behaviour of Cu (II) reduction from ethaline containing 1 wt% of water is presented prior to discussing the influence of increasing amounts of water in the DES system. Fig. 6.1 shows the voltammogram obtained for 0.20 M CuCl<sub>2</sub> in ethaline at a stationary Pt electrode using a scan rate of 5 mV s<sup>-1</sup> at 25°C. The cathodic process shows two cathodic peak potentials, e.g. E<sub>pc1</sub> and E<sub>pc2</sub>, which are indicative of reduction of the electroactive species (Cu<sup>2+</sup> and Cu<sup>+</sup>) at the electrode surface. The first peak corresponds to the electron-transfer, whereby the reduction of Cu (II) to Cu (I) species proceeded and it commenced at +0.48 V vs. Ag RE. It has been reported that the oxidation state of Cu (I) species was thermodynamically stable in aqueous systems containing a high concentration of chloride, e.g. ~3-6 M [109, 110]. Since Cu-DES system exhibits a similar content of Cl<sup>-</sup> (4.5 M), the stabilisation of Cu (I) complexes is plausible.



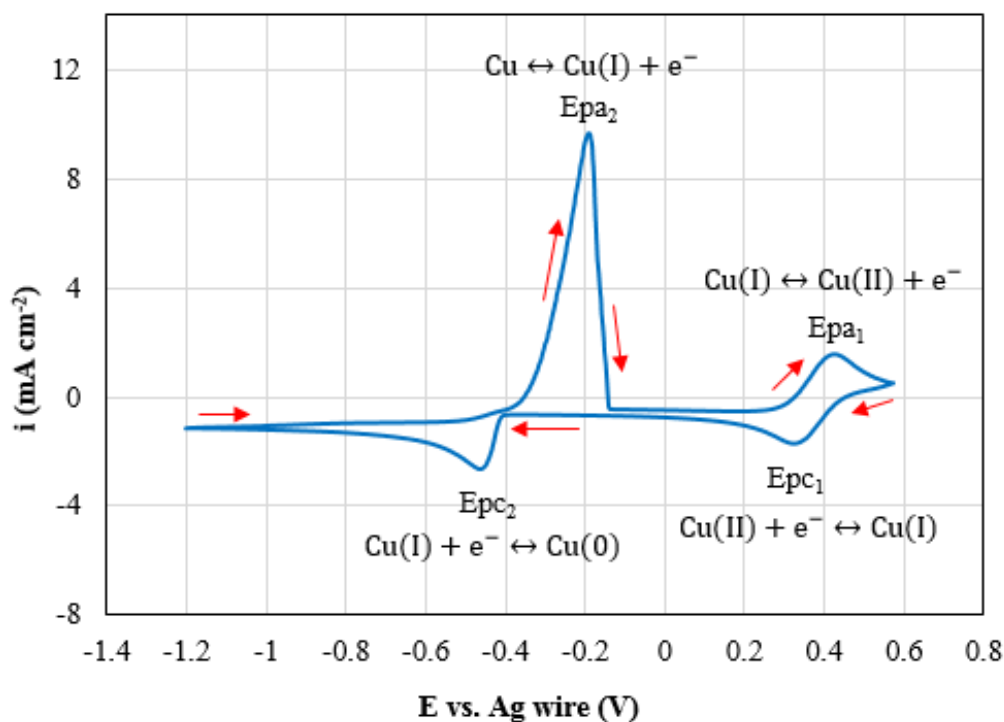
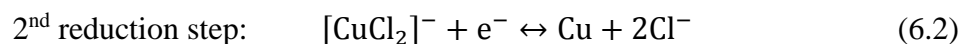
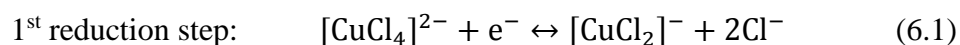


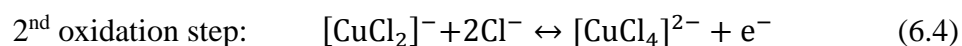
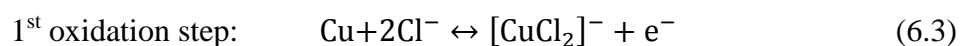
Figure 6.1 Cyclic voltammogram of 0.20 M  $\text{CuCl}_2 \cdot 2\text{H}_2\text{O}$  in ethaline (1 wt%  $\text{H}_2\text{O}$ ) using a stationary Pt electrode ( $A = 0.031 \text{ cm}^2$ ) at 25 °C. The CE was a Pt wire and the RE was a Ag wire. The scan rate was  $5 \text{ mV s}^{-1}$ . The red arrows show the direction of the scan that commenced at the rest potential, +0.55 V vs. Ag wire RE.

As the overpotential becomes more negative, a subsequent wave was observed which corresponded to the reduction of Cu (I) species to Cu (0). This second electron-transfer started at -0.41 V vs. Ag RE. The reduction potentials observed in this study were in agreement with earlier investigations that reported the first and second reduction potentials to proceed at +0.50 V and -0.40 V vs. Ag wire RE [89, 106]. The subsequent voltammograms show that the reduction potentials are shifted by approximately 0.10 V (e.g. to +0.60 and -0.30 V vs. RE) due to the junction potential of the RE. This junction potential arises because the Ag wire was inserted in a glass tube filled with ethaline and sealed with a glass porous frit in order to avoid etching of the wire as explained in section 4.4.1. The junction potential between the Ag wire and the modified RE was measured to be +0.095 V, which reasonably accounted for the shift on the reduction potentials. This junction potential was measured as the potential difference between the lab-made RE and the bare Ag wire when both were immersed in the electrolyte.

The dominant electroactive species formed in CuCl<sub>2</sub>-ethaline system has been identified as the tetra-chlorocuprate complex, e.g. [CuCl<sub>4</sub>]<sup>2-</sup> [93, 105] so that the reduction reactions were likely to proceed as equations 6.1 and 6.2 show.



During the anodic process a stripping peak, e.g. Epa<sub>2</sub> emerged between -0.45 and -0.14 V vs. Ag RE which was associated to the oxidation of the deposited Cu to Cu (I) species. As the scan was swept to more positive overpotentials, a second oxidation step proceeded at +0.26 V vs. Ag RE which was due to the oxidation of Cu (I) back to Cu (II) species. The anodic reactions occurring are show in equations 6.3 and 6.4.



It is useful to compare the plating current attained with 0.2 M CuCl<sub>2</sub> in ethaline containing 1 wt% of water against that in an aqueous system. In order to do so, steady-state linear scans were performed using both our electrolyte and a solution of 0.20 M CuCl<sub>2</sub> containing 5.0 M of NaCl as the supporting electrolyte, using the same experimental parameters ( $v = 5 \text{ mV s}^{-1}$ ,  $\omega = 700 \text{ rpm}$ ,  $T = 25 \text{ }^\circ\text{C}$ ). The data are not corrected for ohmic drop because limiting current values are not affected. This is shown in Fig. 6.2 where the limiting current for our electrolyte ( $i_{\text{lim}} = i_{\text{lim1}} + i_{\text{lim2}}$ ) extracted from the second plateau is  $6.0 \text{ mA cm}^{-2}$ , which is in agreement with an earlier study under identical conditions [89]. The limiting current for the aqueous system is calculated as  $i_{\text{lim}} = 96.7 \text{ mA cm}^{-2}$  which is almost 15 times greater than the plating rate of the DES system at the same CuCl<sub>2</sub> concentration. These results show that much lower plating currents are achievable from DES systems representing a distinct disadvantage.

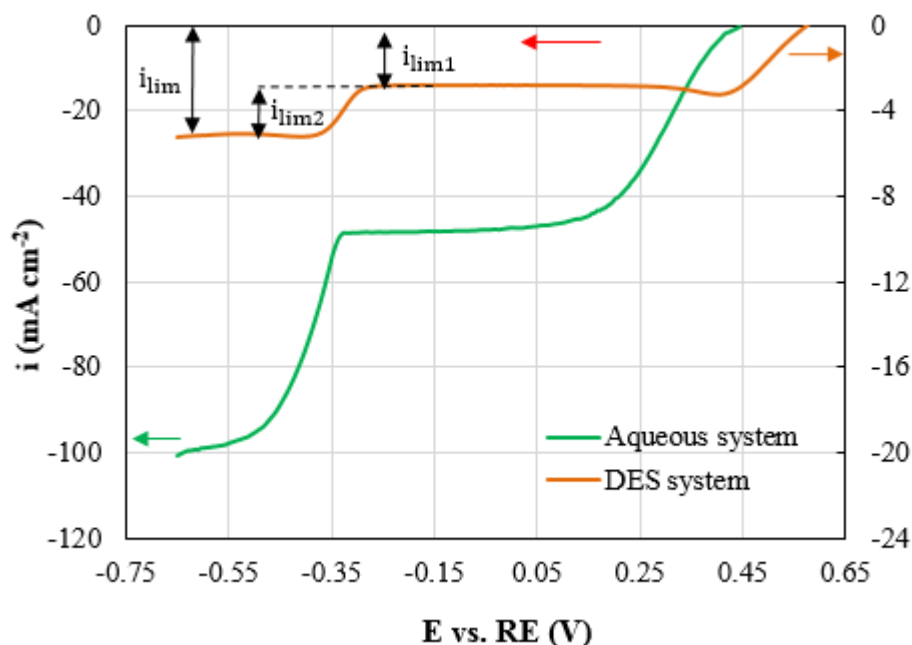


Figure 6.2 Linear potential scans of 0.20 M CuCl<sub>2</sub> + 0.5 M NaCl (—) and 0.20 M CuCl<sub>2</sub> in ethaline (—) using a Pt electrode ( $A = 0.031 \text{ cm}^2$ ) at a scan rate of  $5 \text{ mV s}^{-1}$  and  $\omega = 700 \text{ rpm}$  at  $25^\circ\text{C}$ . For the aqueous system the RE was SCE and Ag wire for the DES system. The red arrow shows the direction of both scans that started from the rest potential. Data are not corrected for ohmic drop.

In order to check if the electrochemical reduction of Cu from ethaline is governed by the rate of mass-transport, voltammetric data were obtained at a Pt RDE electrode using a scan rate of  $5 \text{ mV s}^{-1}$  and increasing rotation speeds from 700 to 3500 rpm. Fig. 6.3 shows that both current plateaux increase as the rotation speed increases. This shows that electrodeposition of Cu from ethaline is controlled by mass transfer. The values of the stripping peak currents at faster rotation speeds also exhibit an increase from 16 to  $20 \text{ mA cm}^{-2}$ , which is due to the greater amount of electrodeposited material. The limiting current density of an electrochemical reaction at a RDE is given by the Levich equation.

$$i_{\text{lim}} = 0.62nFAD^{2/3}\nu^{-1/6}\omega^{1/2}C \quad (6.5)$$

where  $n$  is the number of transferred electrons,  $F$  is the Faraday constant,  $A$  is the area of electrode,  $D$  is the diffusion coefficient,  $\nu$  is the kinematic viscosity,  $\omega$  is the rotation speed and  $C$  is the bulk concentration of species.

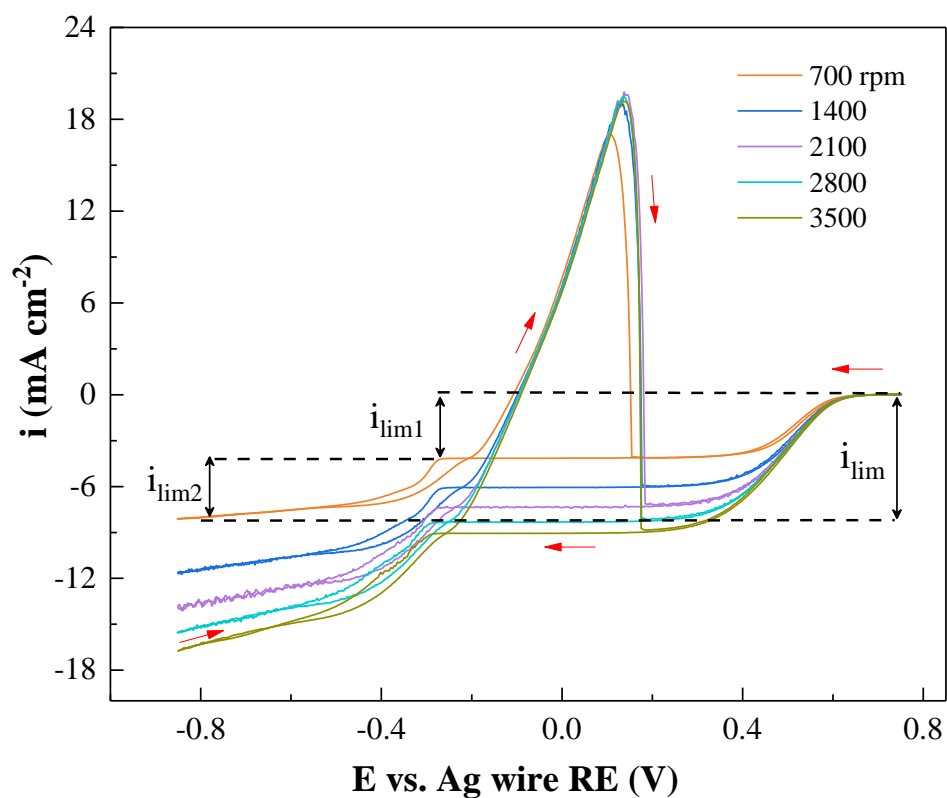


Figure 6.3 Cyclic voltammogram of 0.20 M  $\text{CuCl}_2$  in ethaline (1 wt%  $\text{H}_2\text{O}$ ) using a Pt electrode ( $A=0.031 \text{ cm}^2$ ). The scan rate was  $\nu = 5 \text{ mV s}^{-1}$  using different rotation speeds of  $\omega = 300\text{-}3500 \text{ rpm}$ . The experiments were performed at  $25 \text{ }^\circ\text{C}$ .

### 6.1.2 Effect of water on limiting current

Now that the electrochemical behaviour of Cu (II) reduction from ethaline has been discussed, this section will examine the effect of increasing amounts of water on the limiting currents of the Cu-DES system. Fig. 6.4 shows that the addition of water increases the two limiting current plateaux for the reduction of Cu (II) to Cu (I) species and Cu (I) to Cu (0) species. The values of  $i_{lim1}$  and  $i_{lim2}$  are shown in Table 6.1 as water content increased in the electrolyte from 1 to 15 wt%. Since at these concentrations,  $[CuCl_4]^{2-}$  and  $[CuCl_2]^-$  complexes are the dominant diffusing species, these results show that the addition of water facilitates their transport.

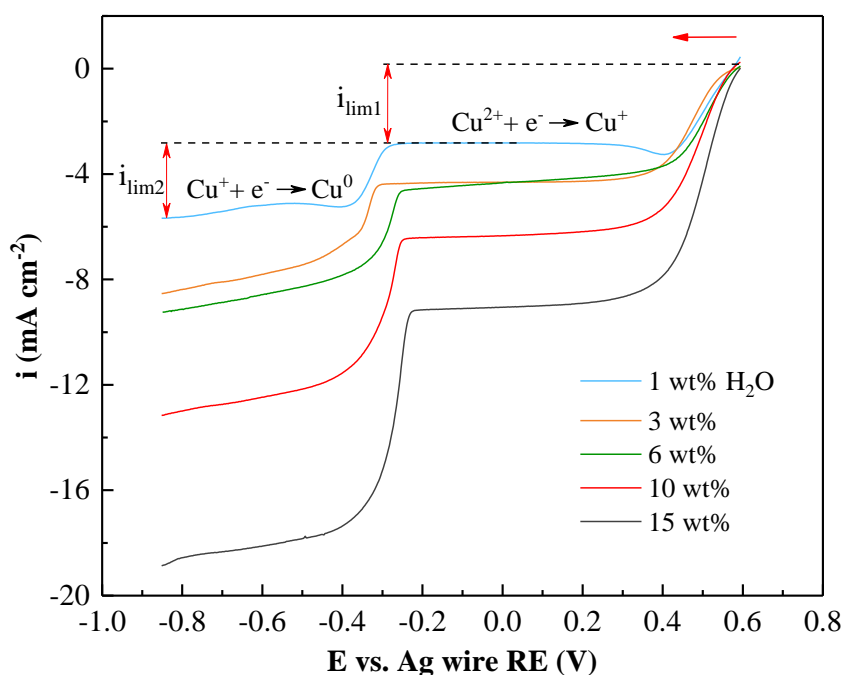


Figure 6.4 Linear potential scan of 0.20 M  $CuCl_2 \cdot 2H_2O$  in ethaline using a Pt electrode ( $A = 0.031 \text{ cm}^2$ ) at 25 °C. The scan rate was  $5 \text{ mV s}^{-1}$  and  $\omega = 700 \text{ rpm}$ . The red arrow shows the direction of scan that commenced (OCP), around +0.60 V vs. Ag wire RE.

Examining the Levich equation one finds that in this study the concentration of reacting species and the rotation speed are constant and since viscosity is independently measured, the diffusion coefficient is likely to be a more influential factor. Thereafter, the diffusion coefficients of  $[CuCl_4]^{2-}$  and  $[CuCl_2]^-$  species were calculated from the experimental data given in Table 6.1 using Levich equation. The values for diffusivity of both cuprous and cupric species with increasing amounts of water are presented in Table 6.1.

The simplest explanation for the observed increase in diffusivity relates to the corresponding decrease in viscosity at higher water content. Applying the Stokes-Einstein relationship to the data in Table 6.1, it can be seen that approximately 80% of the observed enhancement in diffusivity could be attributed to viscosity changes. Normally, at constant temperature and constant ionic radii:

$$D \eta = \text{constant} \quad (6.6)$$

where  $D$  is the diffusion coefficient of the Cu(II) and Cu(I) species and  $\eta$  is dynamic viscosity. The product of  $D$  and  $\eta$  is not constant over the range of water contents studies, suggesting some deviations. These might arise if the ionic radii of the diffusing species were also varying. However, as discussed in section 5.2.2 the speciation of copper in the melt was not strongly affected until water content reached ~35 wt%.

Table 6.1 Dynamic viscosity and limiting currents to calculate diffusion coefficients of Cu (II) and Cu (I) species and the Stokes-Einstein product at each water content.

H <sub>2</sub> O (wt%)	$\nu$ (cm <sup>2</sup> s <sup>-1</sup> )	$\eta$ (Pa s)	Limiting currents (mA cm <sup>-2</sup> )		Diff. coefficients From Eq. 6.5 (x 10 <sup>-7</sup> cm <sup>2</sup> s <sup>-1</sup> )		D $\eta$ = constant From Eq. 6.6 (x 10 <sup>-13</sup> )	
			$i_{lim1}$	$i_{lim2}$	$D_{Cu^{2+}}$	$D_{Cu^+}$	$D_{Cu^{2+}} \eta$	$D_{Cu^+} \eta$
<b>1</b>	0.419	0.0473	3.0	2.8	1.29	1.16	6.10	5.49
<b>3</b>	0.387	0.0436	4.3	3.7	2.14	1.71	9.33	7.46
<b>6</b>	0.307	0.0345	4.3	4.2	2.02	1.95	6.97	6.72
<b>10</b>	0.199	0.0223	6.3	6.2	3.22	3.14	7.18	7.00
<b>15</b>	0.137	0.0151	9.0	9.1	5.07	5.09	7.66	7.69

Table 6.1 shows that the diffusion coefficient corresponding to the Cu (II) complex  $1.29 \times 10^{-7} \text{ cm}^2 \text{ s}^{-1}$  (at 1 wt% of H<sub>2</sub>O) reasonably agrees with the values reported in earlier investigations [54, 106, 188, 189]. It is observed that diffusion coefficients corresponding to Cu (II) and Cu (I) complexes are somewhat different, perhaps due to their geometrical structure that enables them to be either more or less mobile [188, 190]. It is also important to evaluate the difference in the diffusivity values reported for the Cu (II) and Cu (I) species in aqueous and DES systems. Table 6.2 presents that diffusion coefficients for Cu (II) and Cu (I) species are in the order

of  $10^{-5}$  and  $10^{-6}$   $\text{cm}^2 \text{s}^{-1}$  from aqueous systems [110, 190, 191] whereas in DES systems are an order of magnitude smaller (cf. Table 6.2). This highlights the sluggish diffusivity in DES media, which can be attributed to the viscosity of the DES system that is almost 46 times greater than that of aqueous systems, e.g.  $\sim 1\text{-}2$  mPa s.

Table 6.2 Diffusion coefficients for Cu (I) and Cu (II) species in aqueous systems versus DES systems at 25 °C.

Electrolyte	Electrode	$D_{\text{Cu}^{2+}}$ ( $\text{cm}^2 \text{s}^{-1}$ )	$D_{\text{Cu}^+}$ ( $\text{cm}^2 \text{s}^{-1}$ )	Ref.
0.53 mM Cu (II) in 0.50 M KCl + 0.10 M HCl	GC	$0.60 \times 10^{-5}$	$1.20 \times 10^{-5}$	[190]
0.05 M Cu (II) without supporting electrolyte	Pt	$1.12 \times 10^{-5}$	---	[191]
0.05 M $\text{CuCl}_2$ + 1.5 M NaCl	Pt	$4.10 \times 10^{-6}$	$4.20 \times 10^{-6}$	[110]
15 mM $\text{CuCl}_2$ in ethaline	Pt	$2.28 \times 10^{-7}$	$1.86 \times 10^{-7}$	[188]
20 mM $\text{CuCl}_2$ in ethaline	Pt	$1.32 \times 10^{-7}$	---	[189]
20 mM $\text{CuCl}_2$ in ethaline	Pt	$1.45 \times 10^{-7}$	$2.70 \times 10^{-7}$	[54]
0.10 M $\text{CuCl}_2$ in ethaline	Pt	$2.42 \times 10^{-7}$	---	[106]
0.20 M $\text{CuCl}_2$ in ethaline (containing 1 wt% of water)	Pt	$1.29 \times 10^{-7}$	$1.16 \times 10^{-7}$	This work

A closer examination to the second electron-transfer step in Fig. 6.5 shows that the second reduction potential shifts to less negative overpotentials with increasing amounts of water (1-15 wt%). From thermodynamics, it is possible that the formal potential for the second reduction reaction changes with water content leading to shifting of the electrode potential. This ‘apparent’ shifting of the reduction potential has been recorded in the cyclic voltammetric data in an earlier study [105]. It is also possible that water content influences the electro-kinetics of Cu deposition since the mixed control region of the steady-state curves in Fig. 6.4 seems to be somewhat different. In other words, as water increases in the electrolyte, the mixed control region of the steady-state curves (deposition step) appears to be steeper compared to the ones recorded with low water content. The next section summarises the set of experiments performed in order to study if water content influences the electro-kinetics of Cu deposition from the  $\text{CuCl}_2$ -ethaline system.

## 6.2 Effect of water on kinetics of Cu electrodeposition

### 6.2.1 Reduction potential and standard heterogeneous rate constant

Since the potential drop due to ohmic resistance can distort the steady-state curves, the experiments were repeated with ohmic correction (80% of measured  $R_u$ ). The voltammograms in Fig. 6.5 corroborate the occurrence of a systematic shift of the reduction potentials to less negative overpotentials (cf. black arrow in Fig. 6.5). For example, the second reduction potential shifted from -0.222 V (1 wt%) to -0.088 V vs. Ag RE (15 wt%). The remaining reduction potentials are given in Table 6.3. As mentioned earlier, these lower overpotentials can reflect a decrease in activation overpotential indicating a faster reaction rate. If this is the case, the standard heterogeneous rate constant should increase as a function of water in the electrolyte.

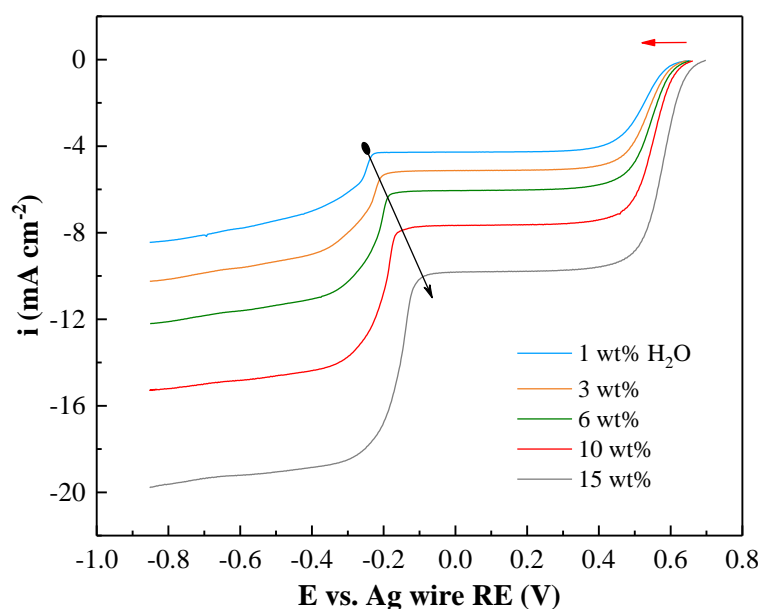


Figure 6.5 Steady-state curves of 0.20 M  $\text{CuCl}_2 \cdot 2\text{H}_2\text{O}$  in ethaline as a function of water using a Pt electrode ( $A = 0.031 \text{ cm}^2$ ) at 25 °C. The scan rate was  $5 \text{ mV s}^{-1}$  and  $\omega = 700 \text{ rpm}$ . The black arrow shows the shift of the reduction potentials. The experiments were performed with ohmic drop correction (80% of measured  $R_u$ ).

Table 6.3 Second reduction potentials for the  $\text{CuCl}_2$ -ethaline system with increasing amounts of water from 1 to 15 wt%.

Water content (wt%)	2 <sup>nd</sup> reduction potential (V vs. Ag RE)
3	-0.185
6	-0.167
10	-0.146



The standard rate constant for the first and second reduction reactions was calculated according to the Koutecký-Levich method described in section 3.5. Cathodic scans were performed using a Pt RDE at a scan rate of  $5 \text{ mV s}^{-1}$  with increasing rotation speeds from 700 to 2800 rpm. The experiments were carried out by correcting 80% of the measured  $R_u$  since the potentiostat started to oscillate beyond this percentage. The remaining  $R_u$  that could not be compensated ranged from  $49.6 \text{ } \Omega$  (1 wt%) to  $26 \text{ } \Omega$  (15 wt%). Fig. 6.6 shows the cathodic linear scans at increasing rotation speeds for the electrolyte containing 1 and 10 wt% of water. The polarisation scans corresponding to the electrolyte containing 3, 6 and 15 wt%  $\text{H}_2\text{O}$  can be found in Appendix C.

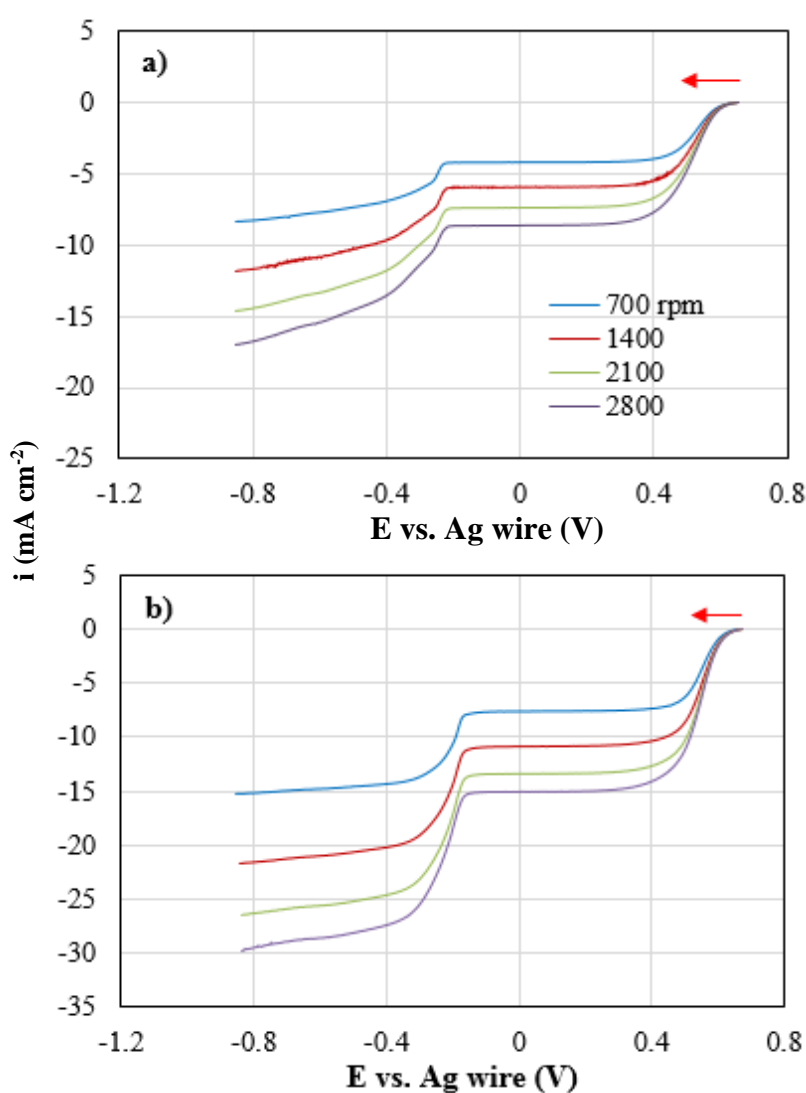


Figure 6.6 Cathodic linear scans of  $0.2 \text{ M CuCl}_2$ -ethaline system using a Pt electrode ( $A = 0.031 \text{ cm}^2$ ) with increasing  $\omega$  from 700 to 2800 rpm for a) 1 wt% and b) 10 wt% of water. The experiments were performed with ohmic drop correction (80% of  $R_u$ ).

The Koutecký-Levich plots ( $i^{-1}$  versus  $\omega^{-1/2}$ ) were constructed by selecting overpotentials above the first and second reduction steps. The chosen fraction corresponds from 35 up to 60% of the ascending region of the polarisation curves as highlighted by the green curves in Fig. 6.7.

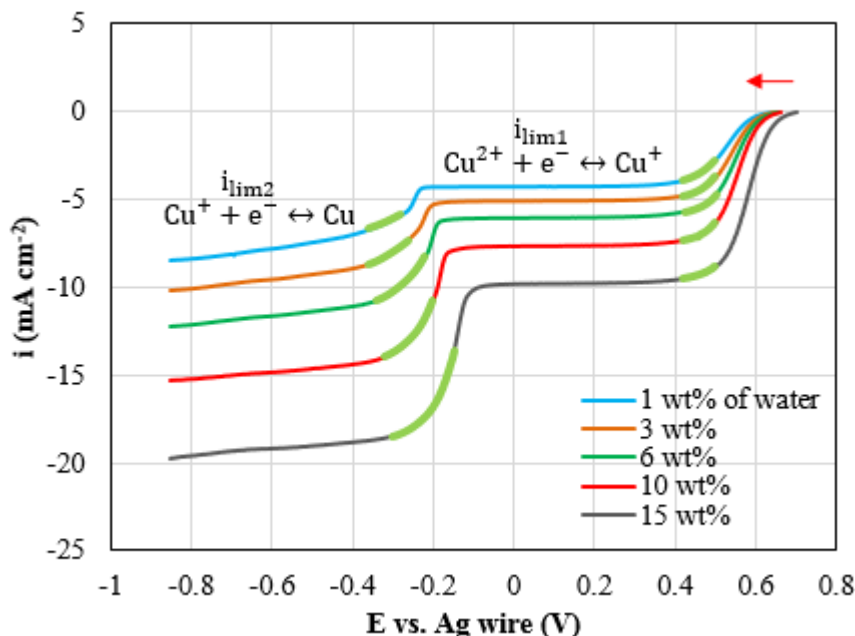


Figure 6.7 Cathodic potential scans of 0.20 M  $\text{CuCl}_2 \cdot 2\text{H}_2\text{O}$  in ethaline using a Pt electrode ( $A = 0.031 \text{ cm}^2$ ) at 25 °C. The scan rate was  $5 \text{ mV s}^{-1}$  and  $\omega = 700 \text{ rpm}$ . The highlighted region corresponds from 35 up to 60% of the ascending part of the polarisation curve. The red arrow shows the direction of scan. The experiments were performed with ohmic correction (80% of measured  $R_u$ ).

From the extrapolations of the Koutecký-Levich plots, the kinetic current densities ( $i_k$ ) were obtained. The Koutecký-Levich plots shown in Fig. 6.8 (a-b) corresponds to the  $\text{Cu(II)} \leftrightarrow \text{Cu(I)}$  reduction reaction while Fig. 6.9 (a-b) refers to the  $\text{Cu(I)} \leftrightarrow \text{Cu(0)}$  reduction step. The insets in Fig. 6.8 and Fig. 6.9 show more clearly the intercepts of each plot. The remaining Koutecký-Levich plots can be found in Appendix D.

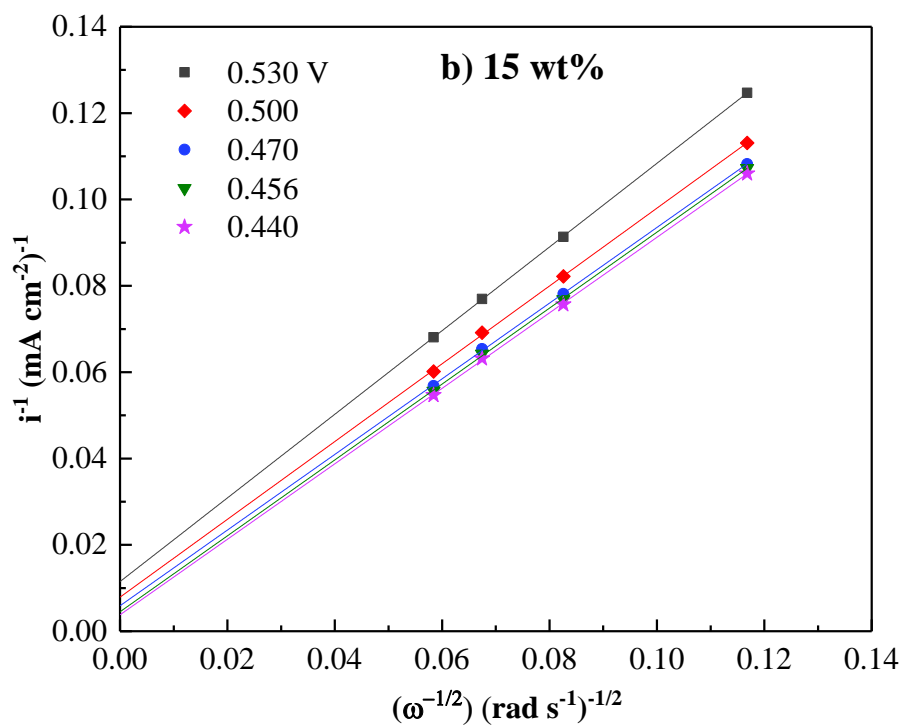
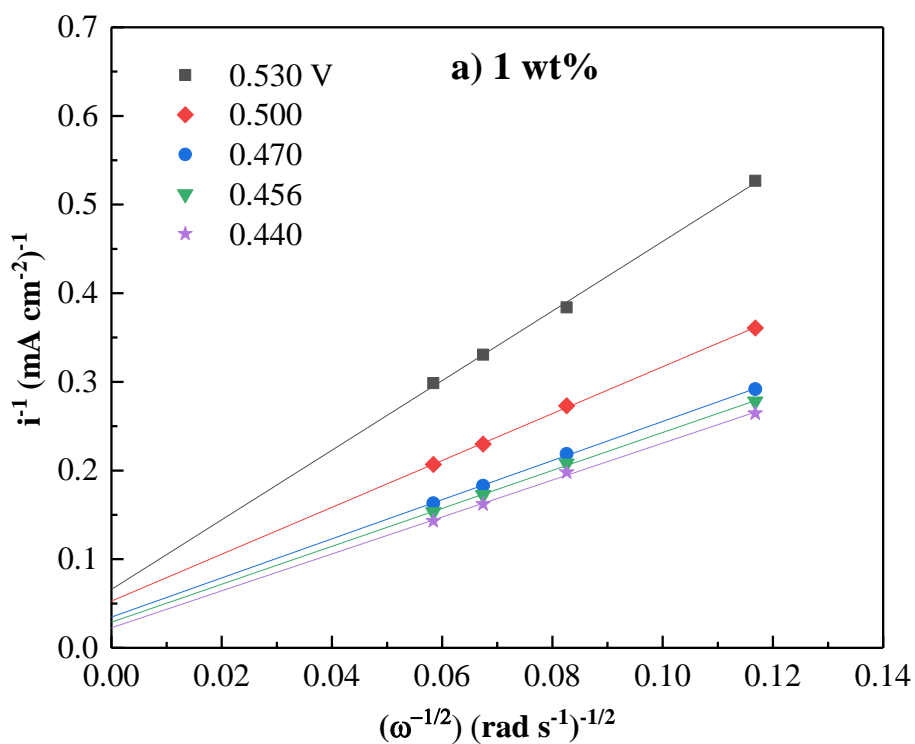


Figure 6.8 Plot of  $i^{-1}$  vs.  $\omega^{-1/2}$  for Cu(II)/Cu(I) step for electrolyte containing a) 1 wt% and b) 15 wt% of water. The scans were performed using a Pt WE ( $A = 0.031 \text{ cm}^2$ ) at differing rotation speed as  $\omega = 700, 1400, 2100$  and  $2800 \text{ rpm}$ . The experiments were performed with ohmic correction (80% of  $R_u$ ).

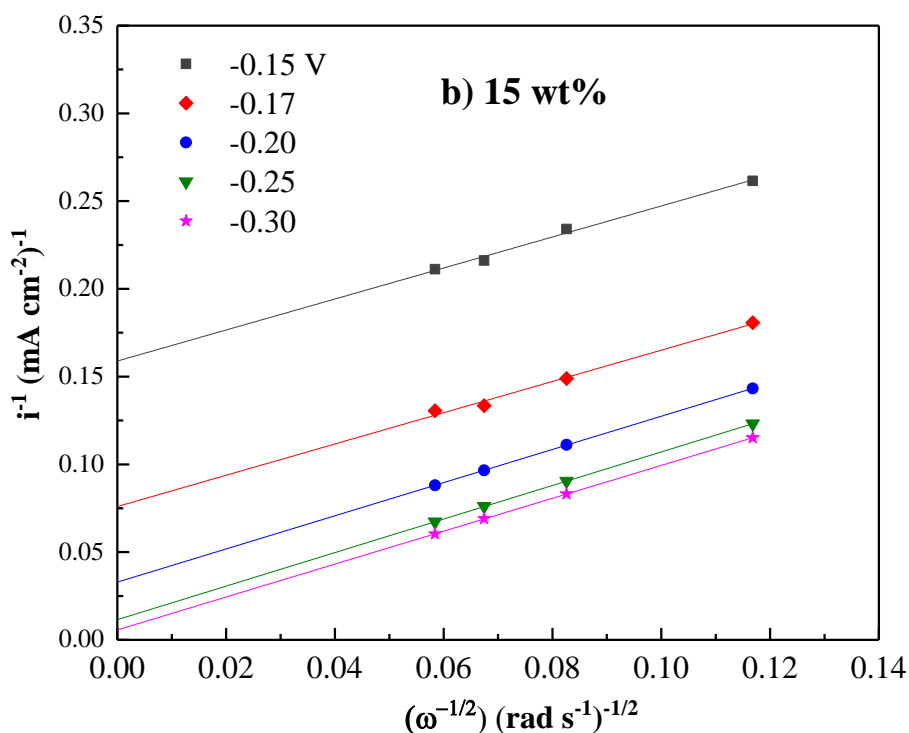
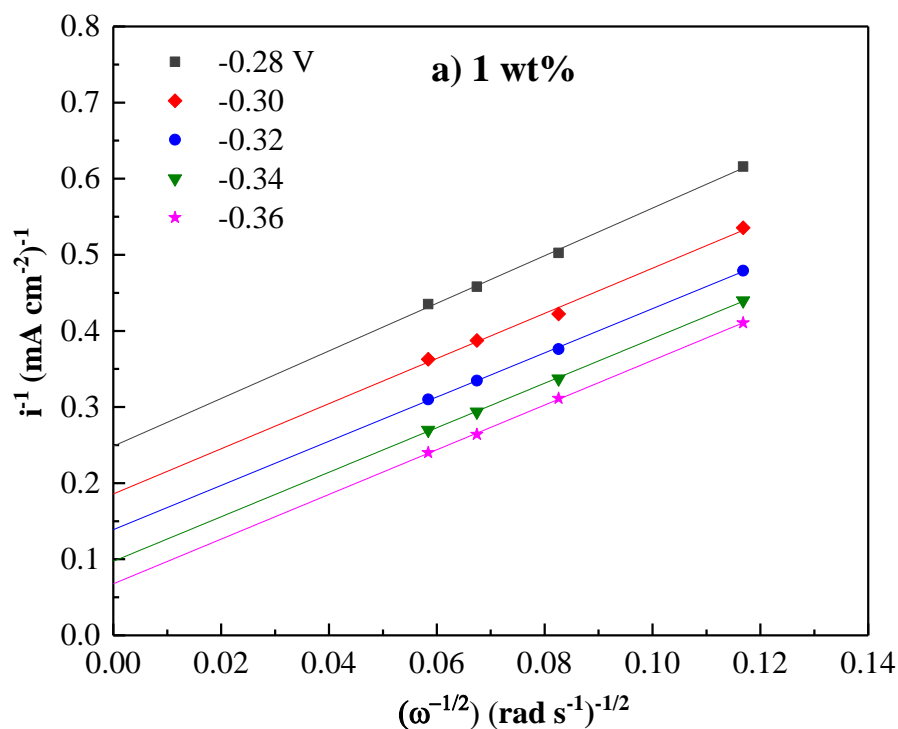


Figure 6.9 Plot of  $i^{-1}$  vs.  $\omega^{-1/2}$  for Cu(I)/Cu(0) step for electrolyte containing a) 1 wt% and b) 15 wt% of water. The scans were performed using a Pt WE ( $A = 0.031 \text{ cm}^2$ ) at differing rotation speeds such as  $\omega = 700, 1400, 2100$  and  $2800 \text{ rpm}$ . The experiments were performed with ohmic correction (80% of  $R_u$ ).

The potential-dependent rate constant  $k_f(E)$  was calculated by rearranging equation 3.34 (introduced in section 3.4). Thereafter, the standard rate constant and the charge transfer coefficient were computed from the slope and intercept of the graph  $\ln k_f(E)$  vs.  $E-E^{o'}$ , as shown in equation 6.7.

$$\ln k_f(E) = \ln k^o - \frac{\alpha n F(E-E^{o'})}{RT} \quad (6.7)$$

where  $k_f(E)$  is the potential-dependent rate constant,  $k^o$  is the standard heterogeneous rate constant,  $\alpha$  is the charge transfer coefficient,  $E$  is the electrode potential selected for analysis,  $R$  is the gas constant,  $T$  is the absolute temperature and  $E^{o'}$  is the formal potential. The plot corresponding to  $\ln k_f(E)$  vs.  $E-E^{o'}$  is shown in Appendix E.

The formal potential for the first reduction reaction was determined from  $E^{o'} = (E_{pa} + E_{pc})/2$  using the cyclic voltammetry data shown in Appendix F. An alternative method proposed by Abbott *et al.* [192] uses the onset potential ( $E_{onset}$ ) as an approximation of  $E^{o'}$ . The onset potentials were calculated as shown in Table 6.4 and these were similar to the values of  $E_{1st}^{o'}$ , as expected for quasi-reversible reactions.

Table 6.4 Formal potential and rate constant for the first and second reduction reactions with increasing amounts of water.

H <sub>2</sub> O (wt%)	Cu(II)↔Cu(I)			Cu(I)↔Cu(0)	
	$E_{1st}^{o'} \approx$ ( $E_{pa} + E_{pc}$ )/2	$E_{onset}$	$k_{1st}^o$ ( $cm\ s^{-1}$ )	$E_{2nd}^{o'} \approx$ ( $E_{pa} + E_{pc}$ )/2	$E_{onset}$
	(V vs. Ag RE)			(V vs. Ag RE)	
1	0.530	0.539	$0.00073 \pm 0.00001$	-0.150	-0.192
3	0.536	0.545	$0.00131 \pm 0.00002$	-0.136	-0.185
6	0.544	0.549	$0.00142 \pm 0.00051$	-0.102	-0.179
10	0.548	0.545	$0.00190 \pm 0.00009$	-0.112	-0.152
15	0.574	0.557	$0.00264 \pm 0.00033$	-0.073	-0.120

For the first reduction reaction, the rate constant was found to increase almost four times with the addition of water from  $7.30 \times 10^{-4}$  (1 wt%) to  $2.64 \times 10^{-3} \text{ cm s}^{-1}$  (15 wt%) as presented in Table 6.4. Our rate constant at 1 wt% reasonably agrees with earlier investigations in which  $k^0$  for the first reduction reaction has been reported to range from  $2.66 \times 10^{-4}$  to  $9.9 \times 10^{-4} \text{ cm s}^{-1}$  as given in Table 6.5 [112, 188]. The  $k^0$  for an aqueous system comprising 5 mM of Cu (II) + 8 molal HCl has been reported to be  $4.1 \times 10^{-3} \text{ cm s}^{-1}$  using a Pt electrode [193]. This result shows that a faster reaction rate is obtained from aqueous systems than that of DES systems.

Table 6.5 The heterogeneous rate constant,  $k^0$ , for Cu deposition calculated in earlier studies from DES and aqueous systems.

Electrolyte	Electrode	$k^0 \text{ (cm s}^{-1}\text{)}$		
		1 <sup>st</sup> step	2 <sup>nd</sup> step	Ref.
5 Mm Cu (II) +8 molal HCl	Pt	$4.10 \times 10^{-3}$	---	[193]
20 mM CuCl <sub>2</sub> in reline	Pt	$9.90 \times 10^{-4}$	---	[112]
15 mM CuCl <sub>2</sub> in ethaline	Pt	$2.66 \times 10^{-4}$	$1.29 \times 10^{-3}$	[188]
20 mM CuCl <sub>2</sub> in ethaline	Pt	$9.50 \times 10^{-4}$	---	[54]
0.20 M CuCl <sub>2</sub> in ethaline (containing 1 wt% of water)	Pt	$7.30 \times 10^{-4}$	$2.61 \times 10^{-6}$	This work

Various publications have often examined the first step due to its ease of analysis [54, 112, 189]. However, the second reduction reaction is more crucial since the deposition process occurs at this point. In this case,  $E_{2\text{nd}}^{0'} \neq E_{\text{onset}}$  (cf. Table 6.4) which may reflect high irreversibility of the second reduction reaction. We have measured  $E_{2\text{nd}}^{0'}$  to be in average  $-0.012 \pm 0.018 \text{ V}$  vs. Ag wire RE; the calculation of  $E_{2\text{nd}}^{0'}$  can be found in Appendix G. The rate constant was found to increase from  $2.61 \times 10^{-6}$  to  $2.05 \times 10^{-5} \text{ cm s}^{-1}$  when water content raises from 1 to 15 wt%, as presented in Fig. 6.10. Comparing the standard rate constant amongst the first ( $7.30 \times 10^{-4} \text{ cm s}^{-1}$ ) and the second reduction reaction ( $2.61 \times 10^{-6} \text{ cm s}^{-1}$ ), one observes that the Cu(I)↔Cu(0) deposition step is the slowest one, corresponding to the rate-determining step.

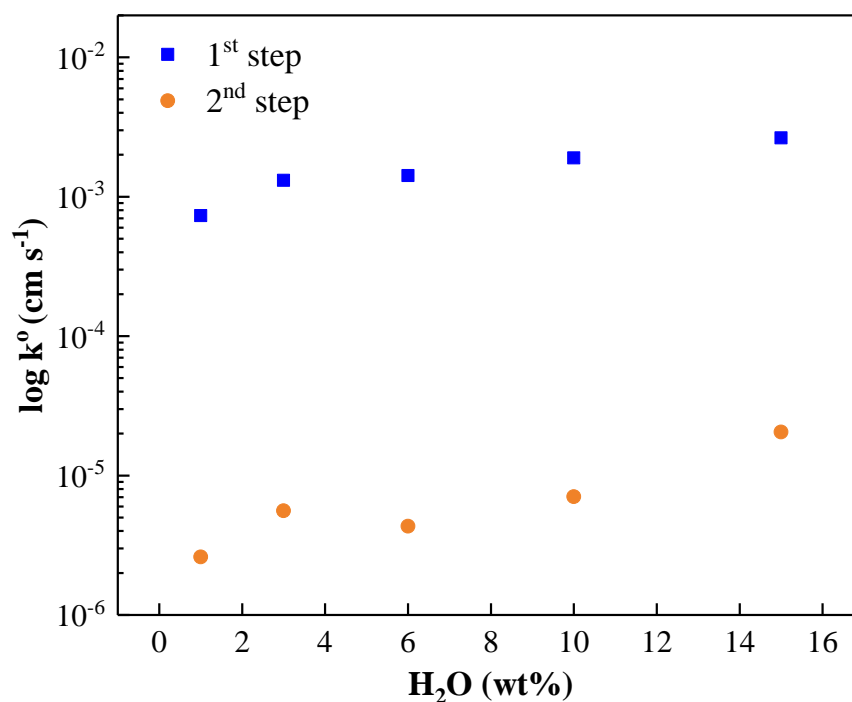
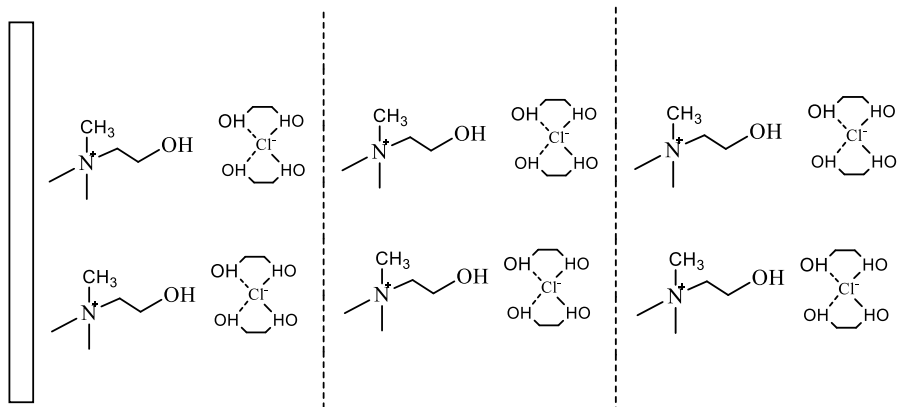


Figure 6.10 Standard heterogeneous rate constant  $k^\circ$  for the first and second reduction reaction with increasing amounts of water in the electrolyte, e.g. 1-15 wt%.

Currently, there is no available information in the literature to compare against, but our results show that when water is added to the electrolyte, a somewhat faster reaction rate occurs. The reason of this phenomenon is unclear but it might arise due to differences in the DES/electrode interface [88, 194]. A recent study has reported that the interfacial arrangement of the liquid components can be modified by water content [195]. For example, under the simplest condition (e.g. OCP), the structure of dry DES/electrode interface has been proposed to be as Fig. 6.11 (a) illustrates whereby a layer of  $\text{Ch}^+$  exists [195]. It was stated that as water content increases from 10 up to 40 wt%, the structure of the DES is gradually 'swollen' (cf. Fig. 6.11 b). This is thought to be due to the H-bond network that water forms with the components of the DES [195], where the largest number of H-bonds were formed between  $\text{H}_2\text{O}$  and the HBD (e.g. ethylene glycol for ethaline) [178].

**a) Low water-containing DES**



**b) Wet DES**

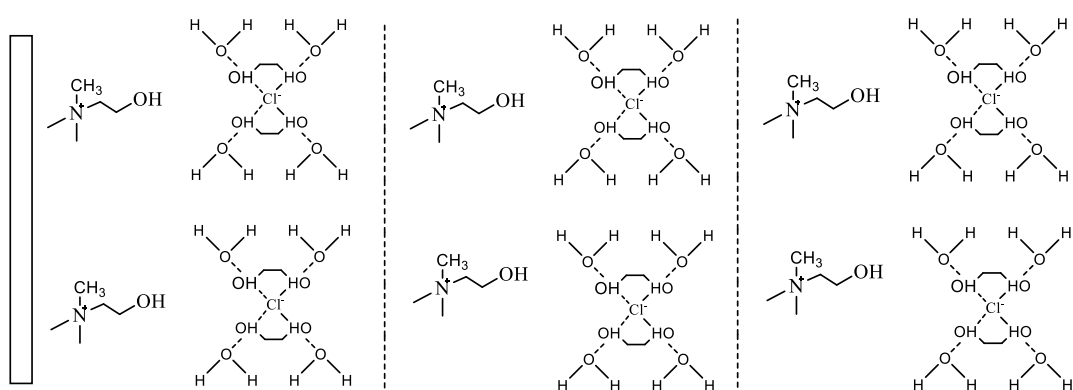


Figure 6.11 Proposed DES/electrode interface structure for a) low and b) high water content under OCP conditions [195], assuming that the more intense H-bonding occurs between H<sub>2</sub>O and the HBD [178]. Adapted from [195].



Regarding the charge transfer coefficients, no trends were observed neither for the first nor the second reduction reaction in this kinetic parameter as adding water to the electrolyte. The charge transfer coefficients for both reduction steps are shown in Fig. 6.12. Although no data are available for the  $\text{Cu(I)} \leftrightarrow \text{Cu(0)}$  reaction to compare against,  $\alpha$  for the  $\text{Cu(II)} \leftrightarrow \text{Cu(I)}$  reaction has been reported to range from 0.25 to 0.41 in earlier investigations [54, 112, 189].

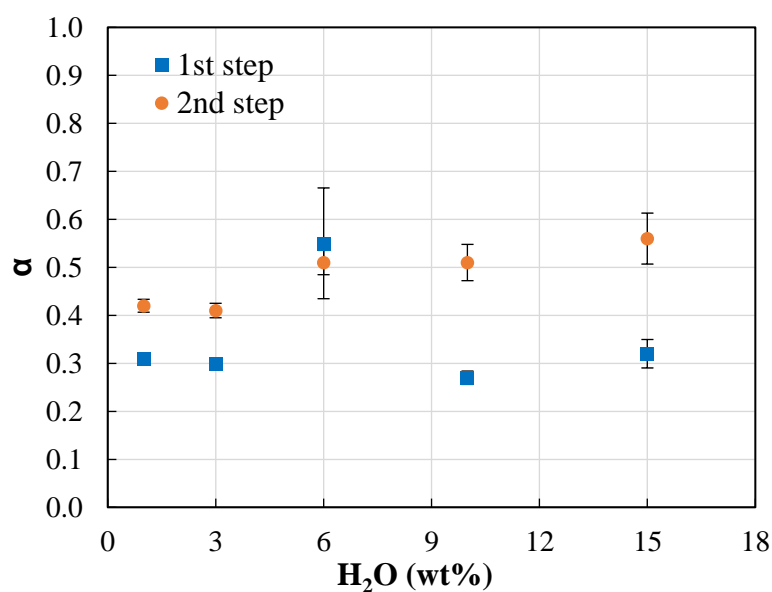


Figure 6.12 Charge transfer coefficients for the first and second reduction step from 0.2 M  $\text{CuCl}_2$  in ethaline with increasing amounts of water (1-15 wt%).

Overall, it can be restated that water content changes but not drastically the electro-kinetics of Cu electrodeposition since the  $k^0$  of the process changed by approximately a factor of ten. One explanation can be related to changes in speciation of Cu (II) species in the electrolyte. However, as presented in section 5.2.2 only a high concentration of water (e.g. beyond 35 wt%) can alter the speciation of Cu (II) complexes in the liquid. The second reason corresponds to the EDL of the DES system which has been proposed to be modified by water content beyond 40 wt% [195], but at the moment no absolute explanation has been identified. The EDL could be measured using high speed chronopotentiometry.

### 6.2.2 Prediction of deposit uniformity from the water-containing electrolytes

Physico-chemical and electrochemical properties of DESs systems have been investigated intensively. However, the overall influence of these properties has not been evaluated on the ability of the electrolyte to fabricate electrodeposits with uniform thicknesses. Due to the fact that practical electrochemical systems should produce homogeneous deposits, this section discusses if uniform electrodeposits can be fabricated from the water-containing electrolytes based on the analysis of the Wagner number.

The uniformity of the current distribution can be predicted in terms of the dimensionless Wagner number [135, 139, 196], which relates the ratio of the polarisation resistance to the ohmic resistance [141]. In this case, the secondary current distribution for Tafel polarisation is given by Wagner number in equation 6.8.

$$Wa = \frac{RT\kappa}{\alpha nF|i_{avg}|r_o} \quad (6.8)$$

where  $Wa$  is the Wagner number,  $R$  is the gas constant,  $T$  is the absolute temperature,  $\kappa$  is the conductivity of the electrolyte,  $\alpha$  is the charge transfer coefficient for reduction reaction,  $n$  is the number of transferred electrons,  $F$  is the Faraday's constant,  $i_{avg}$  is the average current density of the system and  $r_o$  is the radius of the disk electrode.

Wagner numbers were calculated for each water-containing electrolyte using the electrical conductivity measurements as well as  $i_{avg}$  derived from the linear polarisation scans and the charge transfer coefficients from the Koutecký-Levich analysis corresponding to the second step. Table 6.6 shows that the  $Wa$  for the water-containing electrolytes range from 0.17 (1 wt%) to 0.08 (15 wt%). The  $Wa < 1$  implies an uneven current distribution affecting the homogeneity of the deposits, i.e. the current density at the electrode centre tends to be lower than at the edge leading to a thin layer at this region.

Table 6.6 Wagner number as a function of water content in the electrolyte, e.g. 1-15 wt%. The characteristic length  $r_0$  of the working electrode was 0.6 cm.

Water content (wt%)	$\kappa$ ( $\times 10^{-2} \Omega^{-1} \text{cm}^{-1}$ )	$i_{\text{avg}}$ ( $\text{mA cm}^{-2}$ )	$\alpha_{\text{Cu}^+/\text{Cu}}$	Wa
1	0.00795	4.68	0.42	0.17
3	0.00953	5.62	0.41	0.18
6	0.1020	6.63	0.51	0.13
10	0.1160	9.75	0.51	0.10
15	0.1530	14.12	0.56	0.08
Aqueous syst.	0.4400	24.20	0.50	1.56

By contrast, the Wagner number computed from the aqueous sulphate system was  $Wa \sim 1.56$ . The aqueous system comprises of 0.2 M  $\text{Cu}^{2+}$  + 1.0 M  $\text{H}_2\text{SO}_4$  from which the  $i_{\text{avg}}$  (e.g.  $i_{\text{avg}} = 80\%$  of  $i_{\text{lim}}$ ), the measured conductivity and charge transfer coefficient are given in Table 6.6. This  $Wa$  is indicative of electrodeposits with even thicknesses. To clarify this point, a set of current distribution curves ( $i/i_{\text{avg}}$ ) is shown in Fig. 6.13. The green dashed curve ( $Wa = 0.2$ ) represents the scenario where  $i_{\text{centre}} = 0.75 i_{\text{avg}}$  likely to arise in deposits produced from DES systems. By contrast, the blue dotted line ( $Wa > 1.0$ ) shows a highly uniform distribution, i.e. when  $i_{\text{centre}} = 0.92 i_{\text{avg}}$ . These findings suggest that electrodeposits with less uniform thickness distribution may be obtained from DES systems when compared to aqueous systems.

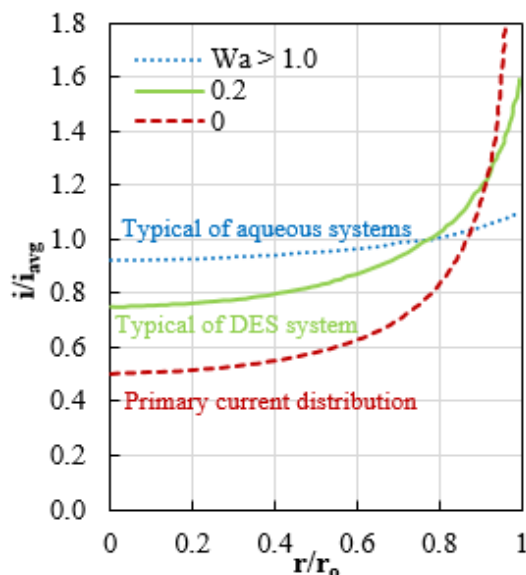


Figure 6.13 Secondary current distribution for Tafel polarisation at a disk electrode of radius  $r_0$ . The distribution profile corresponds to  $Wa = 0.2$ . Mass transport limitations are neglected due to the agitation of the electrolyte. Adapted from [135].

From the Wagner number relationship (e.g.  $Wa = c \kappa / i_{avg}$ ) it is notable that the current distribution depends on the ratio of the conductivity to the average current density provided that the remaining terms are constant. Although water content increases the conductivity of the electrolyte, it seems that it is not enough to compensate the increase on the average current density also brought about by water content. For example, conductivity was increased by water content almost twofold (i.e. from 0.795 at 1 wt% to 1.530 at 15 wt%), whereas the average current density increased three times (i.e. from 4.68 to 14.12 mA cm<sup>-2</sup>). In order to test if this less uniform Cu electrodeposits may be produced from the DES systems, Cu electrodeposition from the water-containing electrolytes were subsequently performed. The next section presents the findings of these experiments.

## 6.3 Material analysis

### 6.3.1 Electrodeposition of Cu from water-containing electrolyte

Since Cu electrodeposition is achieved only beyond the Cu (I)→Cu (0) mass-transport controlled step, the current has to be set between the first and the second current plateaux shown in Fig. 6.14 to perform galvanostatic electrodeposition. The current was fixed to 78% of  $i_{lim}$  since an earlier study by this group found reasonably dense Cu deposits using this operational current [89]. Besides, it is well-known that mass transfer limiting current should not be exceeded during formation of the solid phase since it provides poor microstructure as dendrites and high roughness [197, 198]. The applied current density for electrodeposition using different water content is given in Table 6.7. Since increasing amounts of water increase both current plateaux, it was not possible to perform the experiments at a single current. However, depositing at different fractions of limiting currents is a valid point of reference, as this has been used in prior work for microstructural interpretation [199-203].

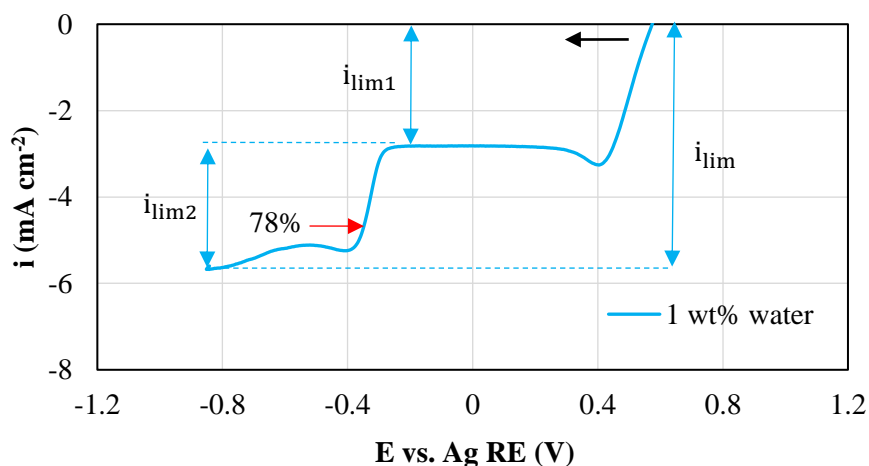


Figure 6.14 Linear scan of 0.20 M  $\text{CuCl}_2 \cdot 2\text{H}_2\text{O}$  in ethaline using a Pt electrode ( $A=0.031 \text{ cm}^2$ ) at 25 °C. The scan rate was  $5 \text{ mV s}^{-1}$  and  $\omega= 700 \text{ rpm}$ . The black arrow shows the direction of scan that started at OCP conditions, around +0.60 V.

Table 6.7 Applied current density for each water-containing electrolyte, 1-15 wt%.

Water content (wt%)	Mass-transfer-limited current ( $\text{mA cm}^{-2}$ )	Applied current density 78% of $i_{lim}$ ( $\text{mA cm}^{-2}$ )
1	6.0	4.68
3	8.0	6.24
6	8.6	6.67
10	12.5	9.75
15	18.1	14.12

Images of Cu deposits fabricated from 0.2 M CuCl<sub>2</sub>-ethaline with increasing amounts of water are shown in Figure 6.15 (a). The first notable feature is the colour difference between the edge and centre of the disk. An “annulus” close to the edge exhibits a darker colour whilst the centre of the deposit is light. Although efforts were made to measure thickness variations across the disk using optical profilometry, this was not possible due to the poor reflectance of the electrodeposits. Similarly, the deposit thickness was attempted using a Stylus Profilometer but due to the roughness of the samples no sensible results were obtained. A more accurate measurement would be X-ray fluorescence; however, it was not available in this study. An estimate of the thickness of the deposits close to the centre were made using Wagner numbers 0.20 and 0.05, which are close to the actual ones for our water-containing electrolyte, i.e. 0.18 (1 wt%) and 0.08 (15 wt%). The currents at the centre of the electrode can be obtained from the following relationships [135]:

$$\frac{i_{\text{centre}}}{i_{\text{avg}}} = 0.75 \text{ when } Wa \sim 0.20 \quad (6.9)$$

$$\frac{i_{\text{centre}}}{i_{\text{avg}}} = 0.66 \text{ when } Wa \sim 0.05 \quad (6.10)$$

where  $i_{\text{avg}} = 78\%$  of  $i_{\text{lim}}$ , since deposition occurs at the second reduction step,  $i_{\text{lim}1}$  was subtracted from  $i_{\text{centre}}$  prior thickness calculation using equation 6.11.

$$T = \frac{m \ 10000}{\rho A} \quad (6.11)$$

where T is the thickness of the deposit in  $\mu\text{m}$ , m is the mass of the deposit,  $\rho$  is the density of bulk Cu ( $8.96 \text{ g cm}^{-3}$ ) and A is the area of the electrode.

Table 6.8 shows that thicknesses close to the centre of the deposit varied from 1.83 to 0.77  $\mu\text{m}$  when the electrolyte contains water between 1 to 15 wt%. Less plating was observed at the centre of the deposit as water content increased from 1 to 15 wt% as the white arrows in Fig. 6.15 (a) shows. In fact, at 15 wt% water content the coating is translucent (cf. Fig. 6.15 b). A similar non-homogeneous colour distribution has been reported by Xing *et al.* [118] from ethaline containing 1.0 M CuCl<sub>2</sub>·H<sub>2</sub>O, although no causes were proposed.

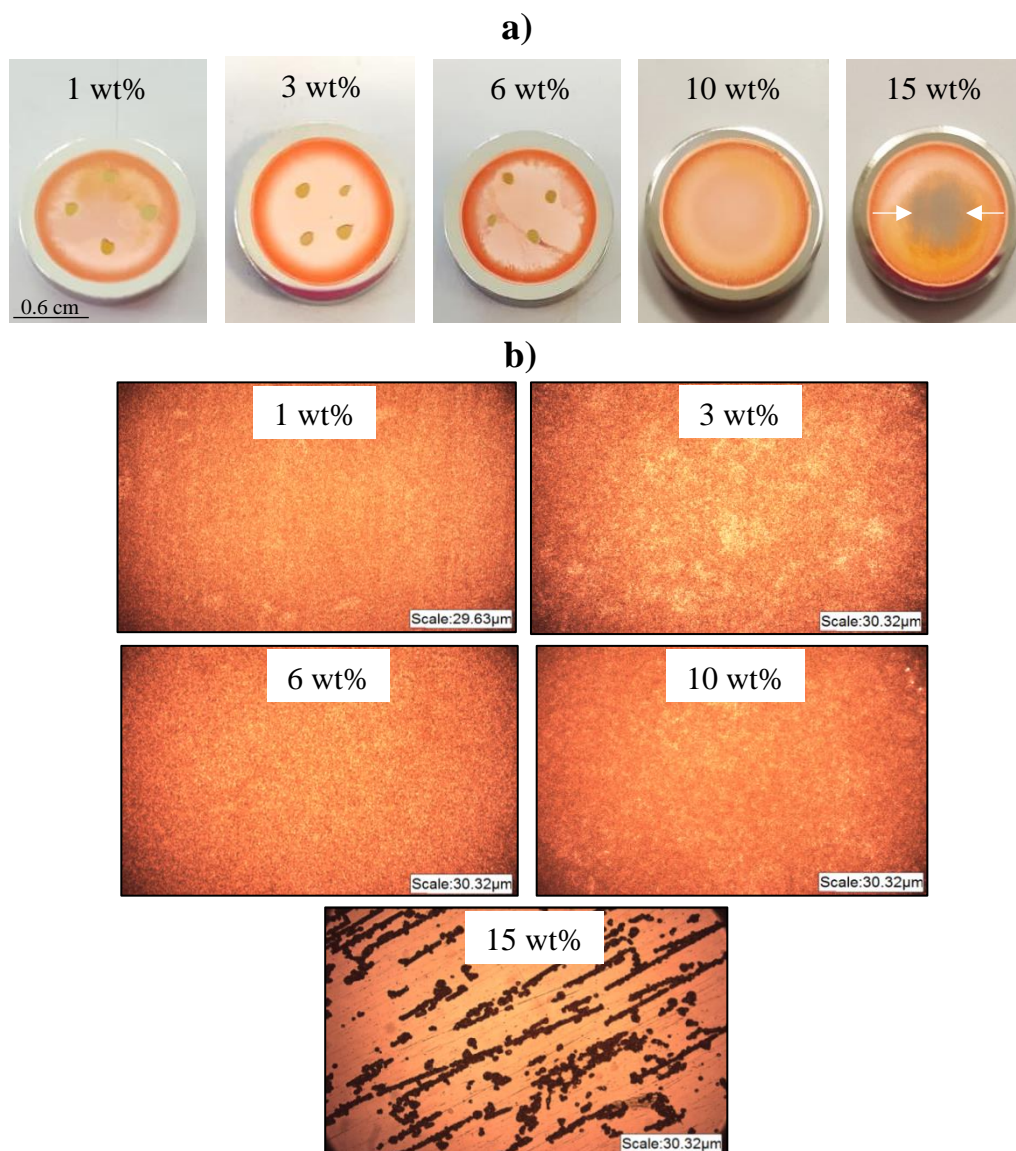


Figure 6.15 a) Images of Cu coatings deposited at steel substrate ( $A=1.18 \text{ cm}^2$ ) from  $0.20 \text{ M CuCl}_2$  in ethaline with increasing amounts of water, 1-15 wt%. The experiments were performed at 78% of  $i_{lim}$  at  $\omega = 700 \text{ rpm}$  at  $25 \text{ }^\circ\text{C}$ . b) Optical images of the deposit centre, magnification x200.

Table 6.8 Estimated thickness at the electrode centre for electrodeposits obtained when water content ranged from 1-15 wt% in the electrolyte.

$\text{H}_2\text{O}$ (wt%)	$i_{avg}=78\%$ of $i_{lim}$ ( $\text{mA cm}^{-2}$ )	$Wa$	$\frac{i_{centre}}{i_{avg}}$ , $r_o=0$	$(\text{mA cm}^{-2})$			Estimated thickness near centre ( $\mu\text{m}$ )
				$i_{centre}$	$i_{lim1}$	$i_{centre}-i_{lim1}$	
1	4.68	0.17	0.75	3.51	2.82	0.69	1.83
3	6.24	0.18		4.68	4.29	0.39	1.03
6	6.67	0.13		5.00	4.31	0.69	1.83
10	9.75	0.10	0.66	6.44	6.30	0.14	0.37
15	14.12	0.08		9.32	9.03	0.29	0.77

In order to test if the homogeneity of the deposit could be improved by changing the current, an additional experiment was performed in which the current was increased to 95% of  $i_{lim}$ . The deposit fabricated using the electrolyte with 15 wt% of water looked dark and rough both at the edges and the centre as Fig. 6.16 (a-b) shows. This is an expected occurrence for plating rates close to the mass-transfer limiting current [198]. Although the centre of the deposit appeared denser, the optical image revealed a thin and poor deposit (cf. Fig. 6.16 b). This finding showed that changing current could not improve homogeneity, but also that homogeneity issues could be the result of a non-uniform current distribution. It is well-known that current at the centre of a rotating disk is lower than at the edge [135, 139, 140], leading to a thicker layer at the edge than that of the deposit centre [140]. This would be consistent with our prediction of less homogeneous deposits anticipated to be produced from water-containing electrolyte since their Wagner numbers were  $<1.0$  (cf. discussed in section 6.2.2).

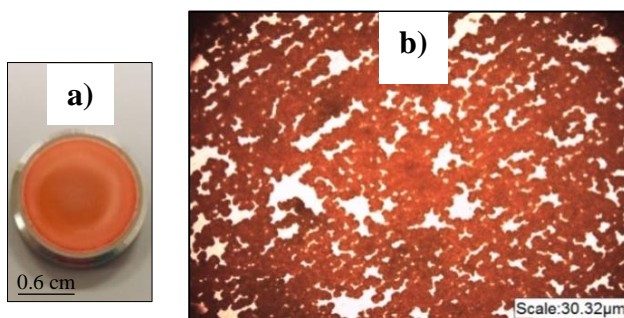


Figure 6.16 a) Image of Cu coating deposited at steel substrate ( $A= 1.18 \text{ cm}^2$ ) from 0.2 M  $\text{CuCl}_2$  in ethaline system with 15 wt%. The experiment was performed at 95% of  $i_{lim}$  with  $\omega = 700 \text{ rpm}$  at  $25 \text{ }^\circ\text{C}$ . b) Optical image close to the deposit centre, magnification x200.

A second point to note is the current efficiency of the electrodeposition process which was consistently low ranging from 48.3 to 58.8 % (cf. Table 6.9). In order to crosscheck the efficiency results, a set of experiments using anodic stripping voltammetry was performed. The efficiency was computed as the ratio of the anodic to the cathodic charge yielding comparable results given in Table 6.9. The average difference between gravimetry and voltammetric methods is  $\pm 3.4\%$  showing that efficiency measurements from the two independent techniques are in agreement. Efficiencies such as 50-59% have also been reported from  $\text{CuCl}_2$ -ethaline electrolyte by other researchers [118, 204, 205].



Table 6.9 Current efficiency for each electrodeposition experiment performed from the water-containing electrolytes.

Water content (wt%)	$\Phi$ (%) Gravimetric method	Stripping method		
		$Q_C$ (C)	$Q_A$ (C)	$\Phi$ (%)
1	$48.3 \pm 3.6$	16.56	37.44	44.2
3	$58.8 \pm 2.4$	22.25	43.20	51.5
6	$57.9 \pm 1.9$	31.98	54.72	58.4
10	$57.2 \pm 1.3$	46.32	78.48	59.0
15	$52.3 \pm 1.8$	50.80	104.40	48.7

To evaluate if the current efficiency was affected by the non-uniform current distribution, the current at the electrode centre was estimated. This analysis was done using the current distribution curves corresponding to the Wagner numbers of 0.20 and 0.05 (cf. Figure 6.17) because they were reasonably similar to the ones calculated for our electrolyte, e.g. 0.17 (1 wt%) and 0.08 (15 wt%) presented in Table 6.8 earlier. It was found that the current at the electrode centre ( $i_{\text{centre}}$ ), where Cu (II) is reduced to Cu (I), was low and just exceeded the first plateau current ( $i_{\text{lim1}}$ ) as previously shown in Table 6.8. For instance, the system containing 1 wt% of water exhibits  $i_{\text{centre}} \sim 3.51 \text{ mA cm}^{-2}$  while  $i_{\text{lim1}} = 2.82 \text{ mA cm}^{-2}$ ,  $i_{\text{centre}}$  has been estimated using equation 6.9. Consequently, the current consumed for Cu (I)→Cu (0) is only  $0.69 \text{ mA cm}^{-2}$  and much of the Cu (I) remains unconverted.

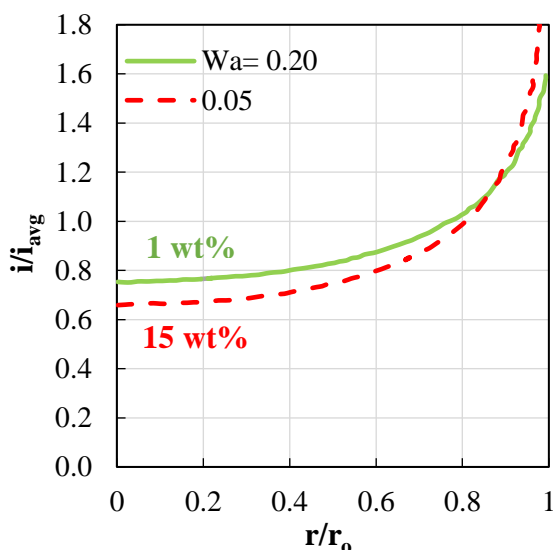


Figure 6.17 Secondary current distribution for Tafel polarisation at a disk electrode of radius  $r_0$ . The distribution profile corresponds to  $Wa = 0.2$  and  $0.05$ . Mass transport limitations are neglected since the electrolyte is assumed to be well-agitated.

Adapted from [135].

Using the current distribution based on  $Wa$  numbers, one can also compute the copper plated during electrodeposition. This is done by computing the copper deposited by integrating the volume of revolution formed by the current corresponding to  $Wa = 0.20$  and  $0.05$ . This volume, as shown in Fig. 6.18 corresponds to the region bound between the polynomial equation and the abscissa. In order to obtain the net current used in the fabrication of the deposit, the current consumed in the first reduction step ( $I_2$ ) (cf. dotted cylinder in Fig. 6.18) had to be subtracted from the total current ( $I_1$ ) (cf. inset in Fig. 6.18). The difference between  $I_1$  and  $I_2$  corresponds to the net current utilised in the process to fabricate the deposit, which relation is shown in equation 6.12.

$$I = I_1 - I_2 \quad (6.12)$$

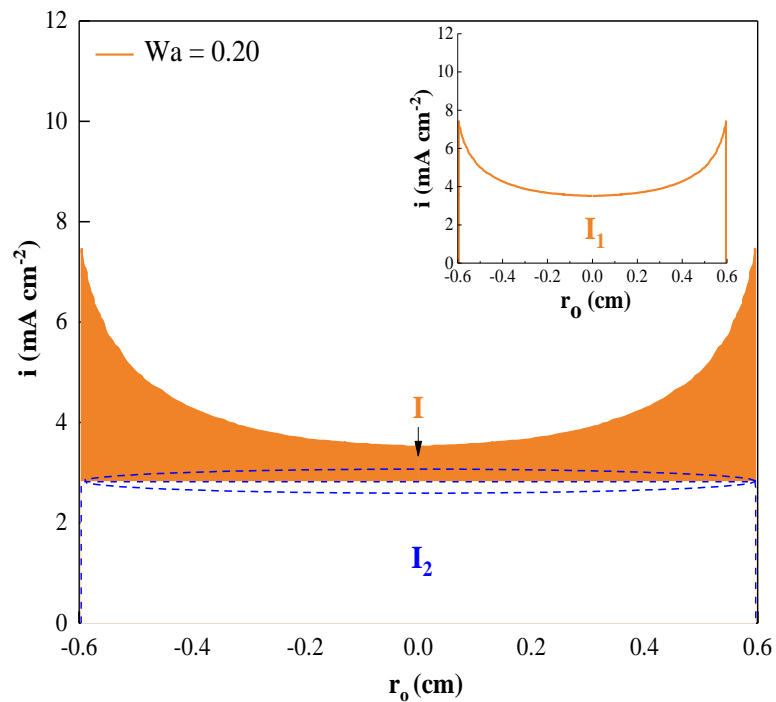


Figure 6.18 Secondary current distribution for Tafel polarisation at a disk of electrode of radius  $r_0 = 0.6$  cm. The distribution profile corresponds to  $Wa = 0.2$ . Adapted from [135].

Using the net currents summarised in Table 6.10 the mass of the deposit was calculated. Mass from the Wa number analysis and their computation is shown in Appendix H. The efficiencies calculated were broadly similar to the ones obtained from the experimental methods as given in Table 6.10. One can conclude that the non-uniform current distribution not only affects the homogeneity of the deposit it also decreases the efficiency of the process.

Table 6.10 Comparison of current efficiency yielded by the Wagner number analysis and gravimetric measurements.

Water content (wt%)	I (A)	Mass (g) from Wa analysis	Experimental mass (g)	$\Phi$ (%)	
				Wa analysis	Gravimetry method
1	0.0019	0.0045	0.0110	40.9	48.3 ± 3.6
3	0.0026	0.0062	0.0140	44.3	58.8 ± 2.4
6	0.0033	0.0078	0.0158	49.4	57.9 ± 1.9
10	0.0039	0.0092	0.0230	40.0	57.2 ± 1.3
15	0.0058	0.0138	0.0330	41.8	52.3 ± 1.8

Due to the poor homogeneity of the current distribution along the electrode, it is probable that morphological differences arise at differing areas on Cu electrodeposits. In order to observe if indeed differences in the morphology occur, SEM examination was thereafter performed.

### 6.3.2 Morphology of electrodeposits produced from water-containing electrolyte

SEM images (planar view) of Cu deposits fabricated from 0.20 M CuCl<sub>2</sub>-ethaline with increasing amounts of water (1-15 wt%) are presented in Fig. 6.19 (a-j). The deposit morphology was examined in the proximity of the centre and edge of the samples. The micrographs at the left-hand side of Fig. 6.19 (a-e) correspond to the images acquired close to the deposit centre while the other images show the morphology of the grains deposited at the edge. Overall, it is observed that the grain morphology of Cu coatings fabricated from water-containing electrolyte somewhat changes with applied current and water content. Besides, the shape of the grains deposited close to the centre differs from the form of the grains at the edge.

The sample deposited using the electrolyte with 1 wt% of water is characterised with rounded or equiaxed grains (Fig. 6.19 a) whereas the deposits fabricated with higher amounts of water as 3 and 6 wt% exhibit fibre-like grains with hardly discernible boundaries (Fig. 6.19 b-c). As water increased in the electrolyte to 10 and 15 wt%, the deposited grains appear to be an assembly of smaller crystals (Fig. 6.19 d-e). It is important to clarify that the SEM micrograph of the sample fabricated with the electrolyte containing 15 wt% of H<sub>2</sub>O (cf. Fig. 6.19 e) corresponds to an area far from the centre of the deposit since plating close to this area was scarce.

On the other hand, the deposited grains close to the edge exhibit a needle-like shape as Fig. 6.19 (f-j) shows. Furthermore, the Cu coatings obtained from the electrolyte containing 15 wt% of water exhibit star-shaped grains. The difference in grain morphology may be related to the higher current density at the edge of the deposit compared with the current density at the centre. These differing nominal currents are shown in Fig. 6.19 (a-j) that have been estimated using the current distribution curves corresponding to the Wagner numbers of 0.2 and 0.05.

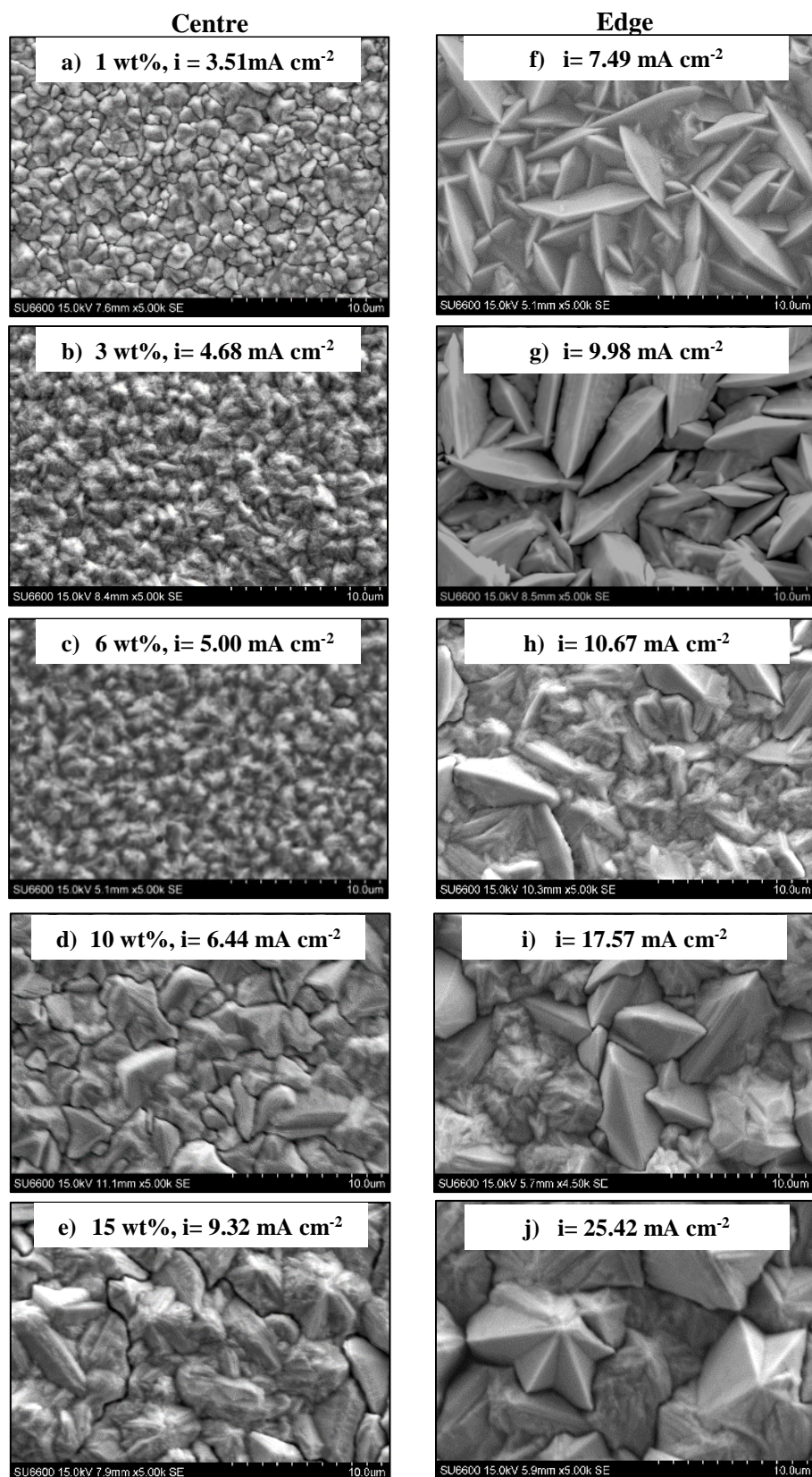


Figure 6.19 SEM micrographs of Cu deposits obtained from  $\text{CuCl}_2$  in ethaline with increasing amounts of water (1-15 wt%). The experiments were performed using steel disks ( $A = 1.18 \text{ cm}^2$ ), 78% of  $i_{\text{lim}}$ ,  $\omega = 700 \text{ rpm}$  at  $25 \text{ }^\circ\text{C}$ . Magnification x5000.

Although electrocrystallisation is a complex subject due to numerous factors that influence this process, Winand's diagram is a useful guide for practitioners to qualitatively associate morphological features with electrolysis parameters [206, 207]. According to this well-known diagram, our Cu deposits would fall in the boundaries of un-oriented dispersion (UD) type deposits and field-oriented texture (FT) deposits (cf. red arrow within the dotted area in Fig. 6.20). There is the possibility that electrodeposits obtained with high amounts of water exhibit twins as predicted in Winand's diagram, i.e. Z type deposits are likely to exhibit twins. According to Fischer's classification, UD grain growth may be characterised with rounded crystals while FT polycrystalline deposits may consist of elongated grains growing perpendicular to the substrate, which are morphological features consistent with the SEM examination of our Cu electrodeposits.

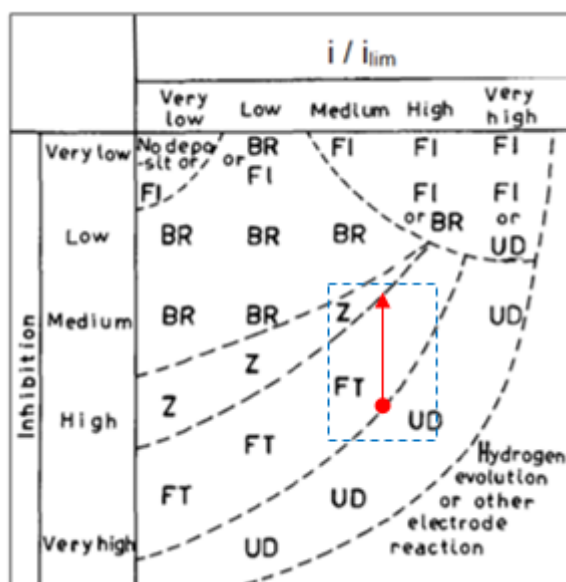


Figure 6.20 Winand's diagram illustrating types of electrodeposits that can be produced according to electrolysis conditions such as the ratio of the operational current to the diffusion limiting current density  $i/i_{lim}$  and inhibition intensity. Adapted from [208].

Winand predicted the occurrence of possible types of polycrystalline deposits according to two factors: (i) the ratio of the current density to the diffusion limiting current density ( $i/i_{lim}$ ) and (ii) inhibition intensity [206, 207]. Due to the non-uniform current distribution in the DES system, two ratios need to be considered, e.g.  $i_{centre}/i_{lim} \approx 0.56$  and  $i_{edge}/i_{lim} \approx 0.78$ . We have assigned them as medium and high

ratios at the horizontal coordinate of Winand's diagram (Figure 6.20). The remaining coordinate corresponds to the inhibition factor which arises due to the presence of molecules, atoms, or ions differing from the cations of interest at the surface of the electrode [206]. These foreign ions can affect the cathodic overvoltage and thereafter the metallographic structure of the deposits [206].

Although inhibition is a complex factor, in practice it has been simplified in terms of the exchange current density [206]. For example, if  $i_0$  of the electrodic reaction is known, it can be related to low or high inhibition, i.e. the higher  $i_0$  the lower inhibition [206]. Since the standard rate constant of Cu reduction in water-containing electrolyte (1-15 wt%) has been obtained in section 6.2.1, we used the data to calculate the exchange current density from equation 6.13.

$$i_0 = nFk^0C \quad (6.13)$$

where  $i_0$  is the exchange current density,  $n$  is the number of transferred electrons,  $F$  is Faradays' constant,  $k^0$  is the standard rate constant and  $C$  is the bulk concentration of species. It was found that that increasing amounts of water in the electrolyte increase almost eight times the exchange current density from 0.05 (1 wt%) to 0.39 mA cm<sup>-2</sup> (15 wt%), as summarised in Table 6.11. This may correspond to an inhibition factor that fluctuates between high to medium as the concentration of water increases in the electrolyte. It can be therefore concluded that the observed morphological features match the shape of the deposits shown by the dashed rectangle in Fig. 6.20. If one compares morphology of Cu deposits between DES systems and chloride aqueous systems, it is notable that Cu grains tend to grow as elongated grains from the aqueous systems [208].

Table 6.11 Exchange current density calculated for each electrodeposition process from the water-containing electrolytes.

Water content (wt%)	$i_0$ (mA cm <sup>-2</sup> )
1	0.050 ± 0.008
3	0.108 ± 0.020
6	0.084 ± 0.020
10	0.136 ± 0.050
15	0.396 ± 0.200

Prediction of electrodeposit morphology from Winand’s diagram suggests that deposits produced from electrolyte with increasing content of water may exhibit texture since they transition from the boundary of the un-oriented to the boundary of the field-oriented textured deposits (cf. arrow in Fig. 6.20). In order to test this probability, XRD measurements were performed. Fig. 6.21 shows the XRD diffractogram with corresponding (hkl) planes for each of the peak obtained from the electrodeposits fabricated with increasing amounts of water. Four distinctive planes are observed as shown by the red peaks in Fig. 6.21: (111), (200), (220) and (311) and the remaining ones (green peaks) correspond to the substrate, e.g. steel disks. It is important to remark that these results may be interpreted with caution due to the non-uniform thickness distribution of the samples.

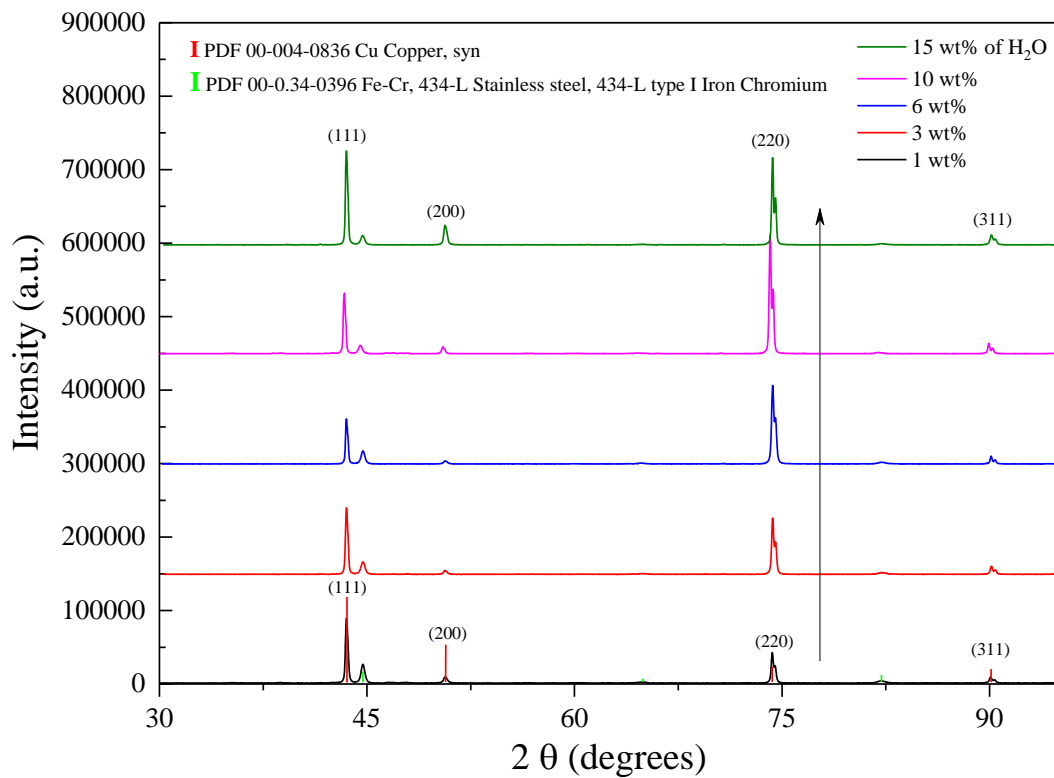


Figure 6.21 XRD diffractogram of Cu electrodeposits at steel substrate. The  $i_{avg} = 78\%$  of  $i_{lim}$ . RTCs were calculated using relative intensities of peaks corresponding to (111), (200), (220) and (311) planes.

Relative intensities of (hkl) planes were used to calculate the Relative Texture Coefficient (RTC) using equation 6.14 [209].

$$RTC_{(hkl)} = \frac{TC_{(hkl)}}{\sum_i^n TC_{(h_i k_i l_i)}} \quad (6.14)$$



where  $TC_{(hkl)}$  is the texture coefficient for the reflection (hkl) and  $\sum_i^n TC_{(h_i k_i l_i)}$  is the sum of all intensities. The electrodeposit obtained from 1 wt% water-containing electrolyte does not exhibit a preferred orientation since no predominance of RTC is observed, i.e. RTC of (111) and (220) are 0.24 and 0.58 respectively. This finding is in good agreement with other studies in which a similar crystalline microstructure of Cu electrodeposits has been reported [89, 113].

As water increases in the electrolyte from 3 up to 10 wt%,, a textured deposit with mostly (220) orientation appears. For instance, deposits obtained with 6 and 10 wt% of water show a predominant orientation in the (220) direction compared to the (111) plane, as presented in Fig. 6.22 (a). It can be concluded that the transition from un-oriented to oriented deposits arises due to the effect of current density. An illustration of the planes in which Cu electrodeposits grow is shown in Fig. 6.22 (b).

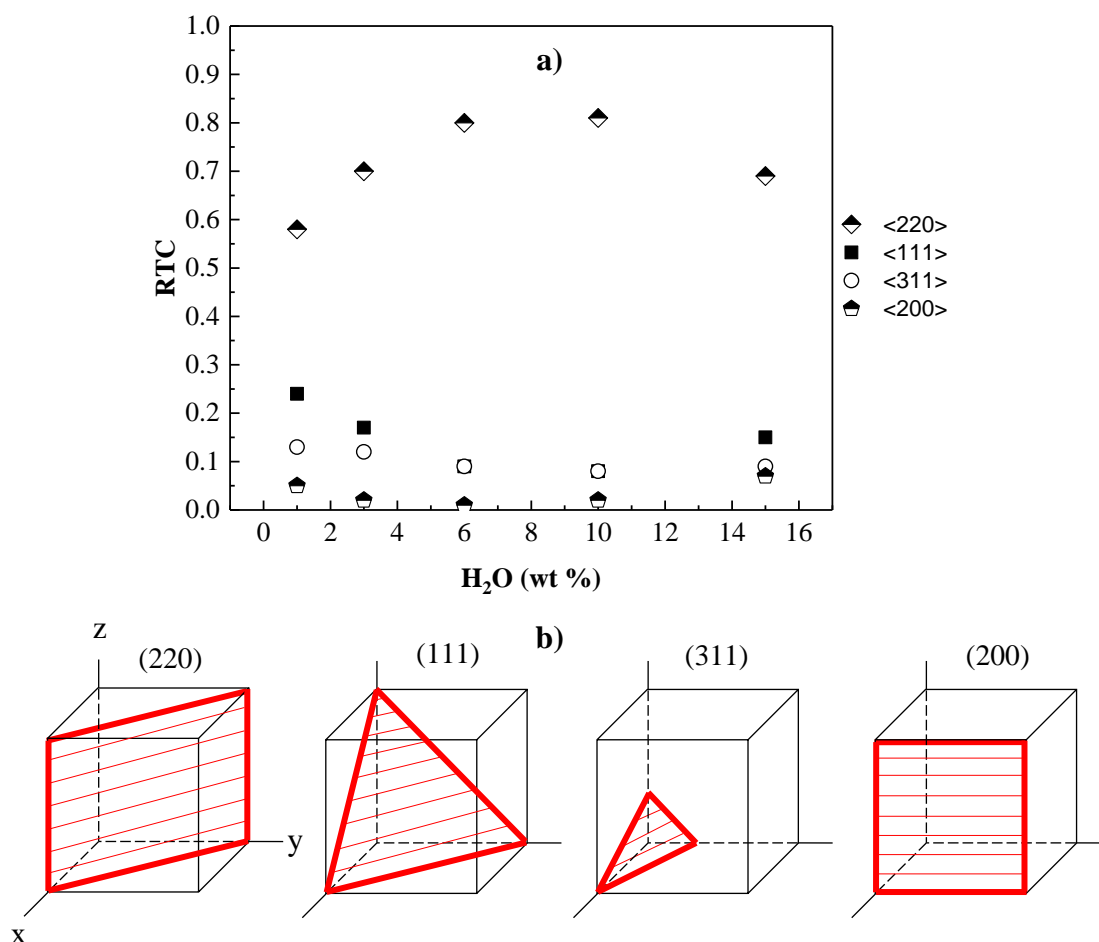


Figure 6.22 a) RTC of electrodeposits fabricated from water-containing electrolyte (1-15 wt%) and b) main crystallographic planes of Cu electrodeposits obtained from the water-containing DES system.

### 6.3.3 Chemical composition of Cu electrodeposits

The chemical composition of the deposits was analysed using Energy-Dispersive X-ray spectroscopy (EDX). The deposits fabricated with the electrolyte containing 1, 3 and 6 wt% contained mostly Cu as the purity ranged from 93.2 to 100% as presented in Table 6.12. The remaining percentage corresponded to C and Fe. In order to test whether or not C was included in our electrodeposits, the chemical composition of a Cu coating fabricated from the aqueous sulphate system was examined (0.6 M Cu<sup>2+</sup> with 2.0 M H<sub>2</sub>SO<sub>4</sub>). Due to the fact that a carbon content of 3.8 wt% was detected, which is very unlikely to occur in Cu deposits obtained from an aqueous system without additives, it was concluded that the presence of C was due to carbon contamination within or outside the SEM chamber.

Fe content may arise from the detection of the substrate (steel). For instance, the expected thicknesses of the deposits ranged from ~5 to 15 µm. However, due to the non-uniform current distribution, thicknesses were estimated to be < 2.0 µm (cf. Table 6.8) allowing the electron beam to somewhat penetrate the thin deposited layer.

Table 6.12 Chemical composition (EDX results) of Cu deposits fabricated from water-containing electrolyte, 1-15 wt%. The EDX analysis shows the chemical composition in wt%.

Water content (wt%)	Centre			Edge			
	Cu	Fe	C	Cu	Fe	C	O
	(wt%)			(wt%)			
1	100.0	---	---	100.0	---	---	---
3	95.7	1.3	3.0	100.0	---	---	---
6	100.0	---	---	100.0	---	---	---
10	100.0	---	---	94.9	---	5.1	---
15	93.2	2.9	3.9	94.4	---	4.5	1.1

If the above argument is correct, Fe should not be detectable at the edge because the deposits tend to be thicker at this area. The EDX analysis showed that the deposits consisted of 100% of Cu at this region demonstrating that Fe signal

arises from the substrate. Also, a small inclusion of O, e.g. 1.1 wt% was detected in the deposit edge fabricated from 15 wt% water-containing electrolyte (cf. Table 6.12). We speculate that this might be associated with the formation of oxides as high amounts of water existing in the electrolyte or alternatively to partial oxidation of the deposit. Other publications have reported the inclusion of chlorine in the deposits (2 wt%) which was thought to occur due to either a degree of DES breakdown or interfering anodic reactions (when using inert anode) [89, 210]. This study used a two-compartment cell resulting in electrodeposited Cu that did not contain Cl. It is possible that Cl incorporation, detected earlier, was affected by anodic reactions in the undivided cell.

Attempts to calculate grain size of the deposits using the SEM micrographs proved difficult due to either ill-defined boundaries or elongated shape (cf. Fig. 6.19). Thereby, in order to determine grain size of the electrodeposits, Electron Backscatter Diffraction (EBSD) was performed. These results are presented in the next section.

#### 6.3.4 Grain size of deposits obtained from the water-containing electrolytes

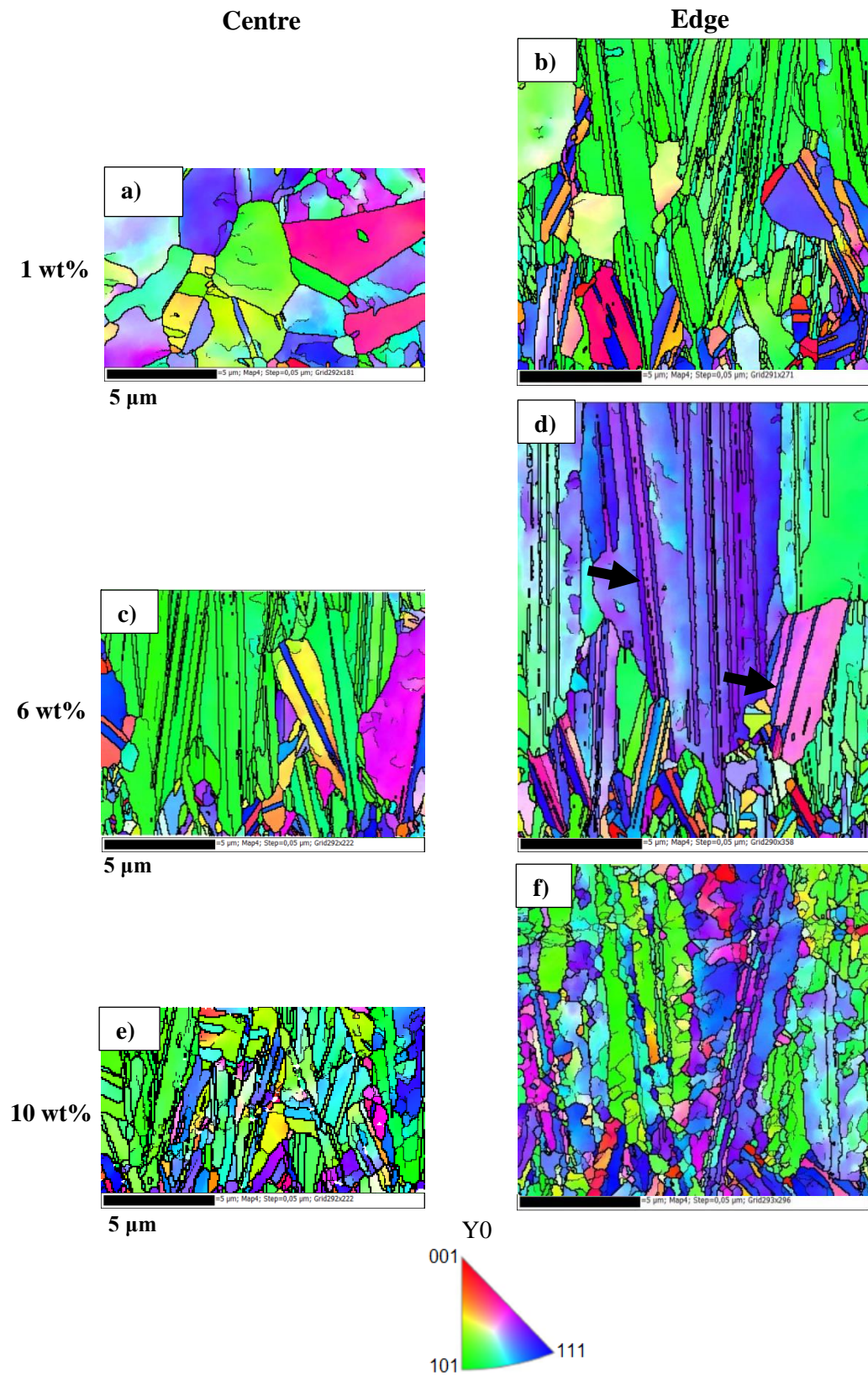
Fig. 6.23 (a-f) shows the EBSD maps acquired from the cross-sections of the electrodeposits with the electrolyte containing 1, 6 and 10 wt% of water. All EBSD maps are presented as inverse pole figures (IPF) in the Y-direction (cf. Fig. 6.23 g). The studied area was in the proximity of the centre and the edge of each sample. It is observed that most of the deposits are characterised with a columnar grain structure with elongated grains that extend along the film thickness. The EBSD map corresponding to the deposit obtained with 1 wt% of H<sub>2</sub>O (Fig. 6.23 a) exhibits mainly equiaxed grains similar to the SEM micrograph earlier shown in Fig. 6.19 (a).

The grain size calculation was performed using the EBSD post-processing software by means of the line intercept method, setting five equidistant horizontal and vertical lines per map. This method, described in section 4.5.1.1, was selected to analyse the columnar structure of the grains.

The average grain size of the electrodeposit fabricated from the DES system (1 wt% of water) close to the deposit centre was calculated to be  $1.25 \pm 0.94 \mu\text{m}$ . This average grain size is almost 10 times smaller than that of an acidic aqueous system without additives,  $11.5 \pm 4.26 \mu\text{m}$ , containing 0.6 M Cu<sup>2+</sup> and 2.0 M H<sub>2</sub>SO<sub>4</sub> without additives [114]. The grain size of the remaining deposits is reported in terms of their average column thickness due to the elongated shape of the grains (cf. Fig 6.23 b-f). Table 6.13 shows that the average column thickness is within the micrometre scale ranging between  $0.33 \pm 0.19$  and  $0.50 \pm 0.31 \mu\text{m}$ . Since the difference in the reported values is within the statistical variance, it can be concluded that the average column thickness of the grains was not strongly influenced by the presence of water content.

Table 6.13 Average column thickness of electrodeposits fabricated from the electrolyte containing 1, 6 and 10 wt% of water. Cu was deposited at steel disks ( $A=1.18 \text{ cm}^2$ ), using 78% of  $i_{\text{lim}}$ ,  $\omega = 700 \text{ rpm}$  at  $25 \text{ }^\circ\text{C}$ .

Water content (wt%)	Average column thickness ( $\mu\text{m}$ )			
	Centre	SD	Edge	SD
1	---	---	0.39	0.32
6	0.44	0.32	0.37	0.22
10	0.33	0.19	0.50	0.31



g) Inverse Pole Figure (IPF) colouring

Figure 6.23 EBSD maps of cross-sections of Cu deposits fabricated from electrolyte containing 1, 6 and 10 wt% of H<sub>2</sub>O. Maps are presented as IPFs in the Y0-direction.

In an attempt to observe how the grain size evolves through the film thickness, i.e. from the bottom to the top of the deposit, a nominal thickness for each electrodeposit was chosen to be 20  $\mu\text{m}$ . However, as observed in Fig 6.23 (a, c and e) cross-sections close to the deposit centre show thicknesses between 9 and 11  $\mu\text{m}$ . This may be due to surface roughening, which is a process known to increase the surface area leading to a low current density [198]. In our system the current at the electrode centre is already low and just exceed  $i_{lim1}$  due to the non-uniform current distribution. Therefore, only current density sitting above  $i_{lim1}$  would lead to conversion of Cu (I) into Cu. On the other hand, deposit thickness close to the deposit edge ranged from 14 to 18  $\mu\text{m}$  (cf. Fig. 6.23 b, d, f). These results show that despite surface roughening, the deposit continue to grow close to the edge. This is due to the higher current that arises at the edge of the deposit than that of the centre, i.e.  $i_{edge} = 1.6 i_{avg}$ .

EBSM maps also reveal the presence of twins as the black arrows in Fig. 6.23(d) point out. Twinning is a recognised phenomenon likely to occur in face centred cubic structures such as Cu [211, 212] due to the lower energy of the twin boundary than that of the high-angle boundary [213-216]. Also, the electrodeposit fabricated with 10 wt% of water exhibits subdivided grains as Fig. 6.23 (f) illustrates. Grain subdivision is known to arise due to dislocation boundaries induced by plastic deformation [217].

EBSM maps also provide information regarding the orientation of the grains. Fig. 6.24 shows that most of the grains are randomly orientated within the studied area, e.g. 135-250  $\mu\text{m}^2$ . However, there are some regions such as the centre and the edge of the deposits fabricated with 1 and 6 wt% of H<sub>2</sub>O that exhibit a texture in the direction of the (101) plane. This is shown by the inverse pole legend in Fig. 6.24 (a-b). The predominance of this orientation can be distinguished by the green colour in the EBSM maps. Since the analysed areas are relatively small, the grain orientation can be regarded as local texture and therefore the information yielded by the XRD examination is considered to be more representative.

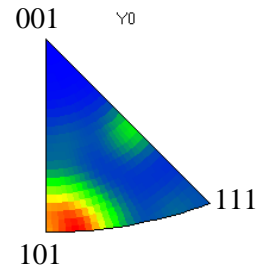
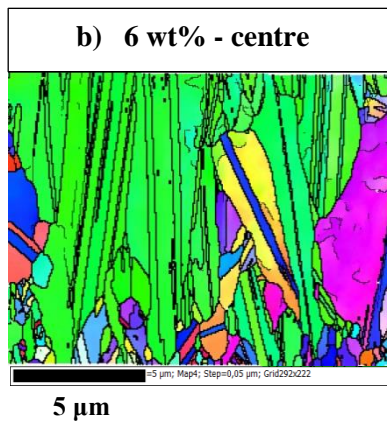
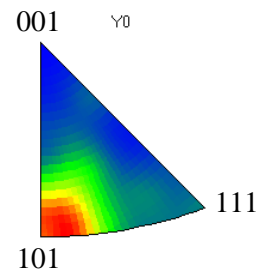
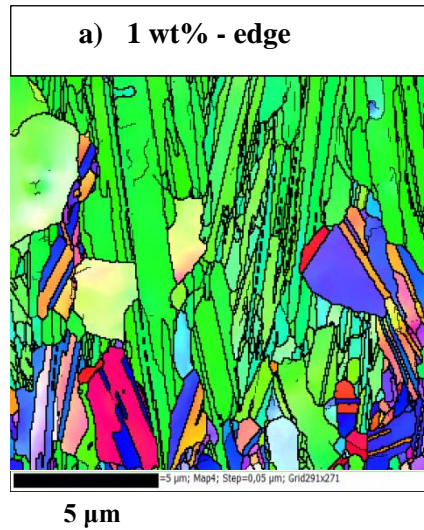


Figure 6.24 EBSD orientation maps showing the preferred orientation of the grains in the direction of the (101) plane for the deposits obtained with 1 and 6 wt% of H<sub>2</sub>O in the electrolyte. The remaining EBSD maps and IPFs are not shown because the grains are randomly orientated.

**7. Chapter – Results and Discussion: Anodic reactions and  
Cu corrosion from water-containing electrolyte**



## 7. Results and Discussion

---

Up to now, chapters 5 and 6 have concentrated on the physico-chemical and electrochemical properties of the electrolyte as well as current distribution, homogeneity and microstructure of the electrodeposits. This chapter presents the results of the anodic reaction using a Cu soluble anode during the electrodeposition of Cu from the DES system. The discussion commences with the investigation of the anodic species formed during the electro-dissolution process, moves to the analysis of the dissolution valency proposing a mechanism occurring in parallel to the anodic dissolution, and finishes with an explanation of the influence of water content on the dissolution process.

### 7.1.1 Anodic species product of the electro-dissolution process in DES system

Initially, in order to examine which species arise as products of the electrochemical dissolution of Cu in ethaline, galvanostatic dissolution of Cu was performed in neat ethaline containing 1 wt% of H<sub>2</sub>O. The current density was fixed to 2.84 mA cm<sup>-2</sup> and the dissolution time varied from 1 to 4 h. Fig. 7.1 shows the UV-Vis spectra with an absorption peak emerging at 270 nm and another one at ~200 nm but it is less quantifiable since it is close to the UV transmission range of the cuvette (190 nm).

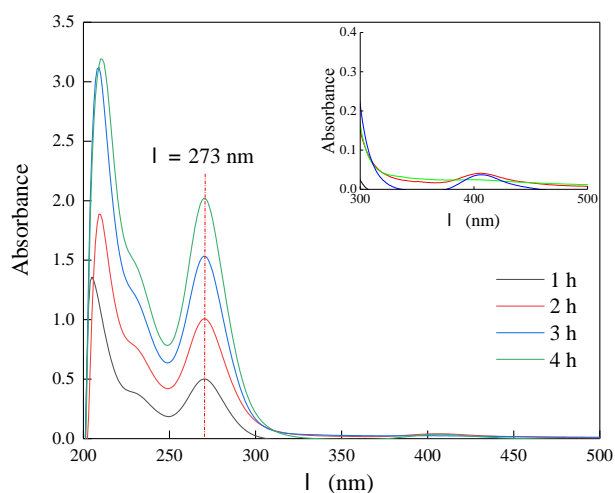


Figure 7.1 UV-Vis spectrum obtained from the anode compartment solution after galvanostatic dissolution of Cu in neat ethaline containing 1 wt% of water. The current density was 2.84 mA cm<sup>-2</sup> and the rotation speed was 700 rpm at 25 °C. The dissolution time varied from 1 to 4 h. The cuvette pathlength was 1 cm.

In order to determine which complexes are likely to correspond to the above spectrum, two metal salts such as CuCl and CuCl<sub>2</sub>·2H<sub>2</sub>O with differing oxidation states of I and II were dissolved in ethaline. Fig. 7.2 (a) shows the UV-Vis spectrum of CuCl in ethaline exhibiting a single peak at 273 nm that has been attributed to the existence of either CuCl<sub>2</sub><sup>-</sup> or CuCl<sub>3</sub><sup>-</sup> species in DES systems [188, 218]. The UV-Vis spectrum in Fig. 7.2 (b) reflects three electronic bands which are generally ascribed to the presence of the tetra-chlorocuprate complex, e.g. CuCl<sub>4</sub><sup>2-</sup> [93, 105, 106, 188, 218], as per discussion in section 5.2.2.

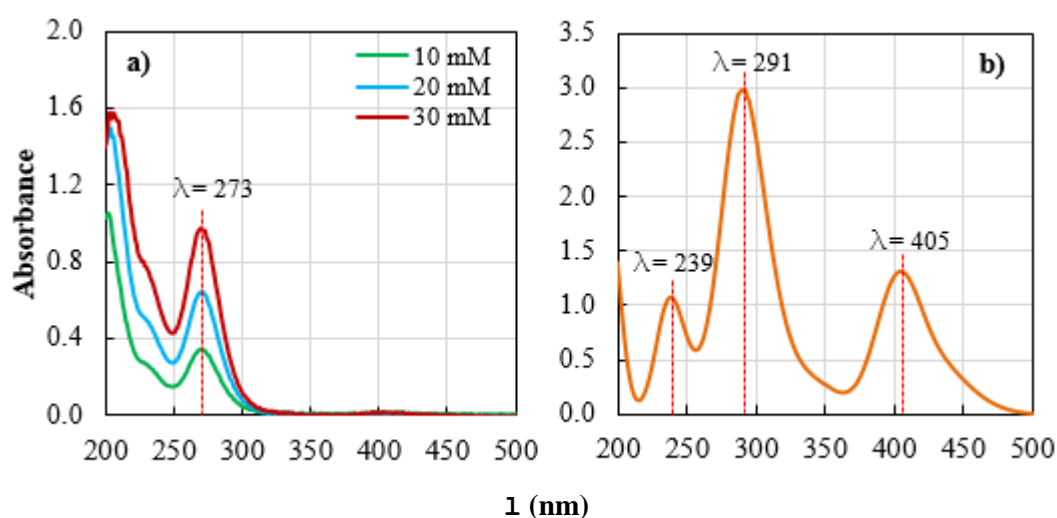


Figure 7.2 UV-Vis spectra of two metal salts dissolved in ethaline containing 1 wt% of H<sub>2</sub>O using a) CuCl (10, 20 and 30 mM) and b) CuCl<sub>2</sub>·2H<sub>2</sub>O (50 mM). The cuvette pathlength was 125  $\mu$ m.

If one correlates Fig. 7.1 and Fig. 7.2 (a-b), it is observed that the product of the anodic dissolution is possibly the CuCl<sub>2</sub><sup>-</sup> species, indicating that the charge transfer occurs as a single electron transfer reaction. The inset in Fig. 7.1 shows a weak absorption band between 350 and 450 nm which may be due to traces of the CuCl<sub>4</sub><sup>2-</sup> complex. Such species however may have formed either by disproportionation or oxidation of CuCl<sub>2</sub><sup>-</sup> species instead of electro-dissolution of Cu [188].

Cu was anodically dissolved in ethaline by applying increasing amounts of charge and thereafter the UV-Vis spectrum was recorded. The results revealed that

the highest absorbance peak at 270 nm increased as a function of the passed charge. This relationship is presented in a more quantitative way in Fig. 7.3. The red symbols represent the expected concentration of Cu (I) species based on measured weight loss of the anode, i.e. assuming that the only complex formed is Cu (I) and dissolution efficiency of 100 %. The blue markers correspond to the concentration of Cu (I) species based on the measured absorbance (using  $\epsilon = 3600 \text{ M}^{-1} \text{ cm}^{-1}$  for the band at  $\lambda = 270 \text{ nm}$ ). Since the concentration of Cu (I) species based on the measured absorbance reasonably agreed with the expected concentration predicted by the weight loss of the anode, the  $\text{CuCl}_2^-$  species were the most likely products to form during the electro-dissolution process.

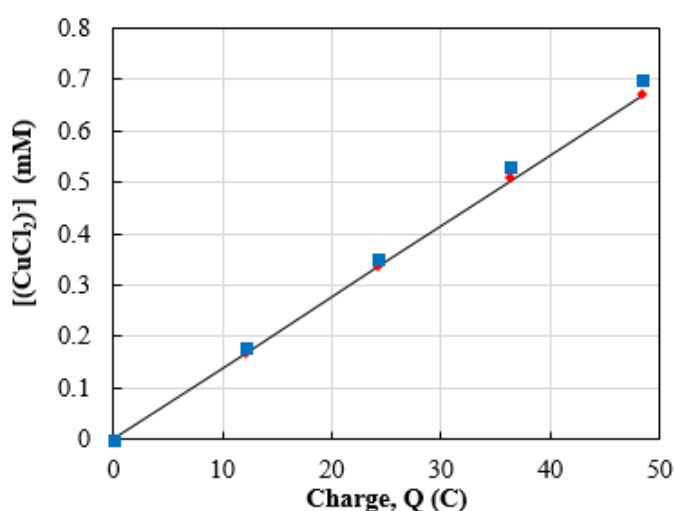


Figure 7.3 Plot of  $[\text{CuCl}_2^-]$  concentration versus anodic charge, Q in neat ethaline. (■) symbol shows the concentration inferred from the absorbance data and (♦) symbol shows the concentration based on the mass loss of the anode. The solid line indicates the expected value from Faraday's law with  $n = 1$ .

The electrode potential of Cu was monitored while it was electrochemically dissolved in ethaline containing differing amounts of water (1-15 wt%). The electrode potential was found to range from 0.010 to 0.082 V versus Ag wire RE (Fig. 7.4). The red dots in the voltammetric data in Fig. 7.5 correspond to the points at which these electrode potentials sit while the electrochemical dissolution occurs. As observed, these electrode potentials are sufficient to allow the formation of  $\text{CuCl}_2^-$  but not  $\text{CuCl}_4^{2-}$  species. For instance, for the electrolyte containing 10 wt% of  $\text{H}_2\text{O}$ ,  $\text{CuCl}_4^{2-}$  species may form only beyond 0.20 V vs. RE, which is about 0.12 V greater

than that of the measured electrode potential. These results further support the occurrence of  $\text{CuCl}_2^-$  species as products of the anodic dissolution of Cu in ethaline. It is important to mention that due to strong overlapping of absorption bands, UV-Vis measurements could not be done when Cu was electrochemically dissolved in the electrolyte (e.g. containing 0.2 M of  $\text{CuCl}_2$ ).

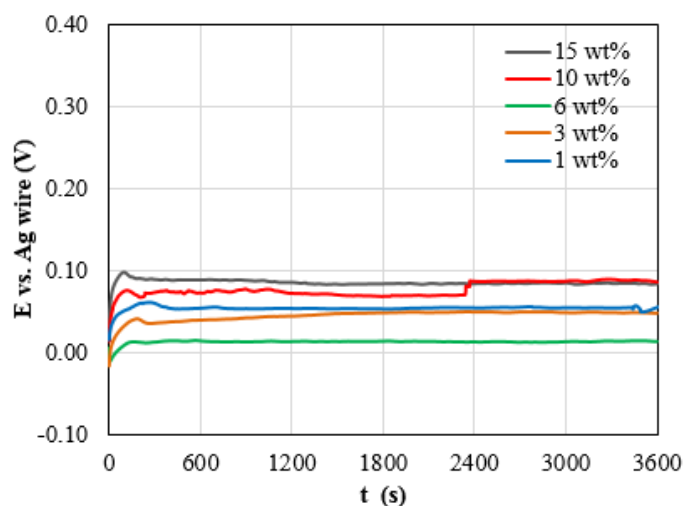


Figure 7.4 Monitoring of the electrode potential of Cu vs. Ag wire RE during its anodic dissolution in ethaline containing increasing amounts of water (1-15 wt%). The area of the Cu electrode was  $1.18 \text{ cm}^2$ . The current density was set to  $2.84 \text{ mA cm}^{-2}$  and the rotation speed was 700 rpm at  $25^\circ \text{C}$ .

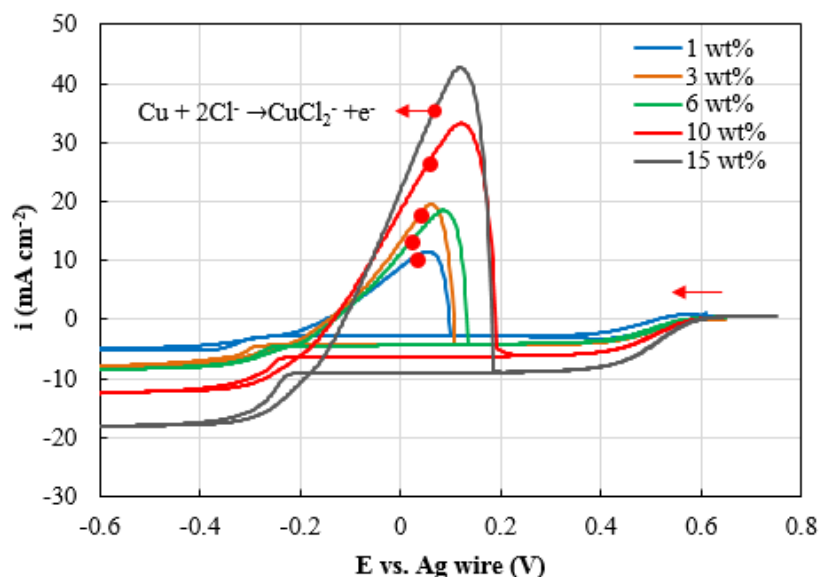


Figure 7.5 Voltammetric data of  $0.20 \text{ M CuCl}_2 \cdot 2\text{H}_2\text{O}$  in ethaline containing increasing amounts of water using a Pt WE ( $A=0.031 \text{ cm}^2$ ) with a rotation speed of 700 rpm at  $25^\circ \text{C}$ . The red arrow shows the direction of the scans. The red dots represent the electrode potentials while anodic dissolution of Cu in ethaline occurred.

### 7.1.2 Dissolution valency and apparent dissolution valency in DES system

Faraday's law is a useful relationship to study the characteristics of an electro-dissolution process since it correlates the charge with the mass loss of the electrode as written in equation 7.1.

$$n = \frac{QM}{\Delta m F \Phi} \quad (7.1)$$

where  $n$  is the number of transferred electrons or dissolution valency in the case of anodic studies,  $Q$  is the charge,  $M$  is the molecular mass of the metal,  $\Delta m$  is the mass loss of the electrode,  $F$  is the Faraday's constant and  $\Phi$  is the efficiency of the dissolution process.

Current efficiencies close to 100% are typical in metal dissolution. However, the faradaic efficiency of a dissolution process can be lowered due to side reactions such as  $O_2$  evolution. Efficiencies higher than 100% are unusual in anodic dissolution processes but when these occur, it can be related to a mass loss greater than the calculated using Faraday's law [219, 220]. Thereby, it is appropriate to write the dissolution valency ( $n$ ) in terms of the 'apparent' dissolution valency, e.g.  $n'$  [219, 220]. When a dissolution process exhibits  $\Phi = 100\%$ , then  $n = n'$ . For the remaining cases, it is suitable to discuss the data in terms of  $n'$ .

In order to determine the dissolution valency of the anodic process, dissolution experiments were performed from water-containing ethaline applying a constant current density ( $2.84 \text{ mA cm}^{-2}$ ) and using a stationary Cu electrode. Table 7.1 summarises the mass loss of the Cu electrode quantified gravimetrically. Since the measured mass loss is similar to the predicted one from Faraday's law, the dissolution valency is virtually the unity for all water-containing ethaline (1-15 wt%). Doche *et. al* [221] has recently reported  $n = 0.97$  when leaching Cu from pure ethaline, which is in good agreement with our dissolution valency, e.g.  $n = 0.99$  (computed as the average  $n$  values in Table 7.1). Overall, these findings are supportive of the anodic dissolution process from neat ethaline to occur as per reaction:  $\text{Cu} + 2\text{Cl}^- \rightarrow \text{CuCl}_2^- + e^-$  where  $\Phi = 100\%$  and  $n = n' = 1$ .

Table 7.1 Dissolution valency in water-containing ethaline (1-15 wt%) with constant current density without rotation at 25 °C. The area of the Cu electrode was 1.18 cm<sup>2</sup>.

Water content (wt%)	Applied anodic current density (mA cm <sup>-2</sup> )	t <sub>diss</sub> (s)	Δm <sub>expected</sub> (g)	Δm <sub>exp</sub> (g)	n
1	2.84	10800	0.0240	0.0242	1.008
3		3600	0.0080	0.0081	1.012
6				0.0079	0.975
10				0.0080	1.000
15				0.0080	1.000

The electrochemical oxidation of Cu was thereafter evaluated from the electrolyte (0.20 M CuCl<sub>2</sub>·2H<sub>2</sub>O in ethaline with 1 wt%) using both stationary and rotating electrode ( $\omega = 700$  rpm). Fig. 7.6 shows the apparent dissolution valency ( $n'$ ) according to the applied current density. Contrary to the dissolution valency  $n=0.99$  from pure ethaline, the apparent dissolution valency from the electrolyte was found to be  $n' < 1$ . This is indicative of a mismatch between the expected and experimental mass loss of the anode since the measured mass loss is greater than the calculated from the passed charge. The smallest  $n'$  arises when the applied anodic current density was low and when the electrode was rotated (cf. red curve in Fig. 7.6). The apparent dissolution valency approaches the unity only when the electrode was stationary and with high applied anodic current density ( $> 10$  mA cm<sup>-2</sup>).

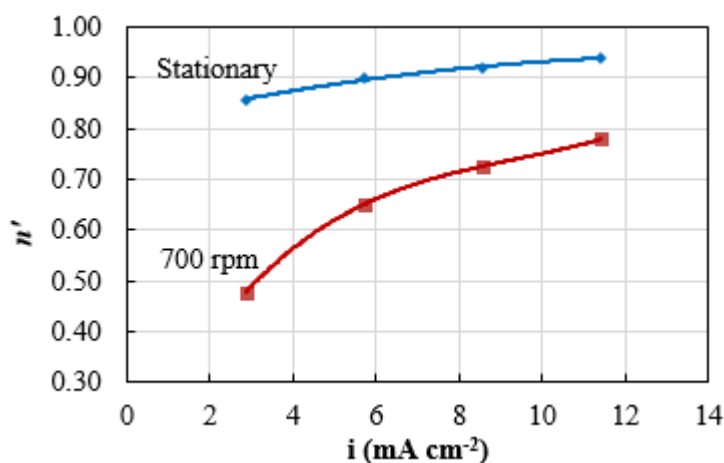


Figure 7.6 The apparent dissolution valency,  $n'$ , of the Cu electrode in 0.20 M CuCl<sub>2</sub>·2H<sub>2</sub>O in ethaline containing 1 wt% H<sub>2</sub>O as a function of the applied current density and electrode rotation rate. ( $\blacklozenge$ )  $\omega = 0$  rpm ( $\blacksquare$ )  $\omega = 700$  rpm.

The present results open up discussion about the role that Cu (II) species play in the electrochemical dissolution process since the main difference between pure ethaline and the electrolyte is the presence of these species. Besides, mass transfer effects may be relevant due to the fact that  $n'$  was much lower for the rotating electrode than for the stationary one.

In order to assess possible mass transfer effects on the anodic dissolution process, the concentration of Cu (II) species was increased from 0 to 0.2 M in ethaline (containing 1 wt% of H<sub>2</sub>O). In these experiments, the applied anodic current density was maintained constant at 2.85 mA cm<sup>-2</sup> and the electrode was either stationary or rotated ( $\omega = 700$  rpm). The  $n'$  in solutions of differing concentration of Cu (II) is shown in Fig. 7.7. It is notable that increasing amounts of Cu (II) species reduce  $n'$  in both scenarios, e.g. with and without agitation. For example, when the electrolyte was stirred, the apparent dissolution valency reduces from  $n \sim 1$  to  $n' = 0.514$  (cf. red curve in Fig. 7.7). This is equivalent for the efficiency of the dissolution process to range from 100% (absence of Cu<sup>2+</sup> species) to 148% (0.2 M Cu<sup>2+</sup> species).

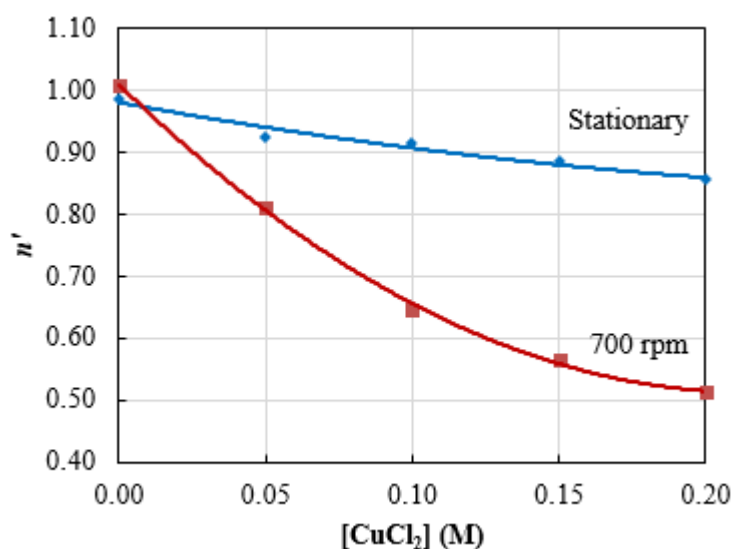


Figure 7.7 The apparent dissolution valency,  $n'$ , of the Cu electrode at 2.85 mA cm<sup>-2</sup> as a function of the Cu(II) concentration and electrode rotation rate in an ethaline solution containing 1 wt% H<sub>2</sub>O. ( $\blacklozenge$ )  $\omega = 0$  rpm ( $\blacksquare$ )  $\omega = 700$  rpm.

An additional test was conducted to further study mass transfer effects. The dissolution valency was recorded as a function of increasing rotation speeds (0-2100 rpm). The experiments were performed from pure ethaline and the electrolyte containing 0.2 M of Cu (II) species and fixing the applied anodic current density at  $2.85 \text{ mA cm}^{-2}$ . Fig. 7.8 shows that the anodic process from pure ethaline is not influenced by the rotation rate since the dissolution valency is always the unity. On the other hand,  $n'$  decreases with faster rotation rates when the dissolution proceeds from the electrolyte (0.2 M of  $\text{CuCl}_2$ ). It is therefore thought that the electro-dissolution process is affected by the mass transport of species.

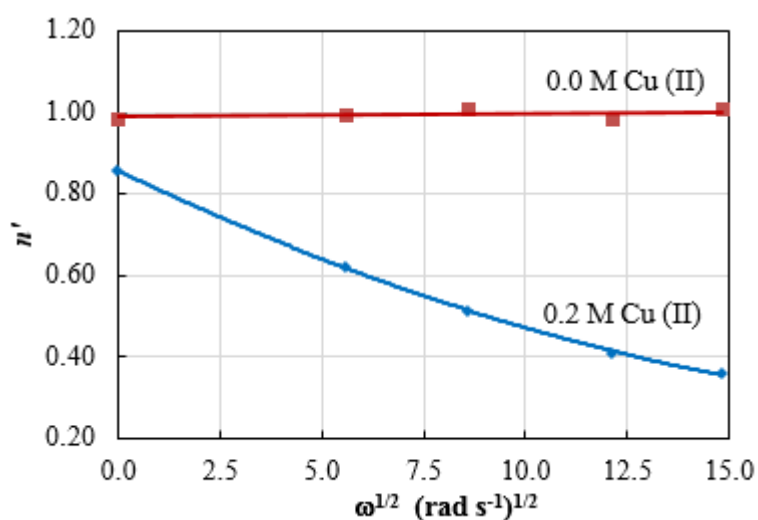


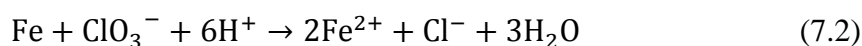
Figure 7.8 The apparent dissolution valency,  $n'$ , of the Cu electrode at  $2.85 \text{ mA cm}^{-2}$  with a rotation speed of  $\omega = 700 \text{ rpm}$ . Symbol ( $\blacklozenge$ ) corresponds to 0.20 M Cu (II) and ( $\blacksquare$ ) 0.0 M (neat ethaline).

As discussed earlier, the existence of competing reaction may lower the efficiency of the anodic dissolution process resulting in an apparent dissolution valency  $n' > 1$ . Alternatively, if a mixture of species such as Cu (I) and Cu (II) complexes arises, then  $1 < n' < 2$  may be anticipated. However, none of these interpretations are adequate to elucidate our findings, e.g.  $n' < 1$ . Hence, other explanations related to either a non-electrochemical process or a corrosion reaction, which can proceed simultaneously with the anodic dissolution process, are conceivable.



An apparent dissolution valency  $n' < 1$  has been reported to occur in DES systems earlier [204]. Nonetheless, the exact reason has not been documented. In the corrosion literature, dissolution processes labelled as ‘anomalous’ have been attributed if the measured mass loss and the corrosion rate exhibit significant differences. One possible explanation for this effect refers to a non-electrochemical process occurring when individual grains detach from the electrode surface due to inter-granular corrosion [220]. This phenomenon can lead to a mass loss greater than the expected one from the actual anodic charge. In this line, metallic residues have been reported in some corroding systems earlier [219]. However, as metallic debris likely to arise from electrode disintegration was not detected in our electrolyte, this effect has been discounted as an explanation for our observed results.

The following interpretation relates to a corrosion reaction that occurs at the anode surface [222]. This reaction, which is superimposed on the dissolution process, accounts for the additional mass loss of the anode and it is independent of the externally measured anodic charge. Anodic dissolution of metals such as Fe and Ni from aqueous systems are examples of processes whereby  $\Phi > 100\%$  and  $n' < 1$  have been encountered [223-225]. In these scenarios, corrosion reactions have been proposed to proceed during anodic dissolution. To exemplify, the reaction in which Fe is corroded from chlorate solutions has been reported to occur as equation 7.2 shows.



In that investigation metallic residues were not observed. Instead, a mass balance using the  $\text{Cl}^-$  ions accumulated in the system accounted for the efficiency of the dissolution process to be  $\Phi > 100\%$ .

Having discussed that corrosion reactions can plausibly couple with an anodic dissolution processes, now it is necessary to identify the corrosion reaction that might occur in our DES system.

### 7.1.3 Mechanism of corrosion reaction of Cu in DES system

By examining the steady-state voltammogram of 0.2 M Cu (II) from ethaline shown in Fig. 7.9, it is observed that the anodic process for the oxidation of Cu (0) to Cu (I) commences while the current is still cathodic involving the reduction of Cu (II) to Cu (I) species (cf. dashed area in Fig. 7.9).

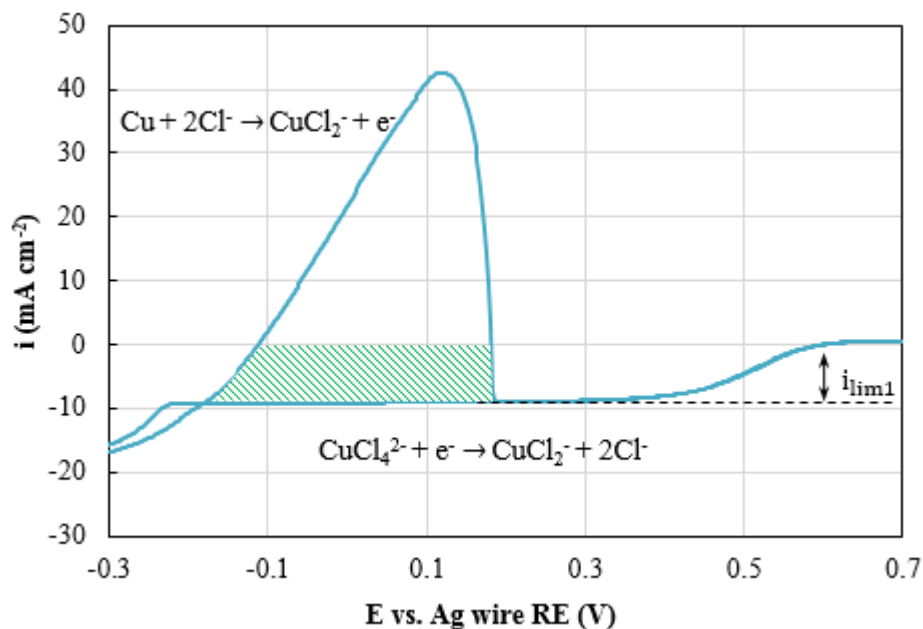
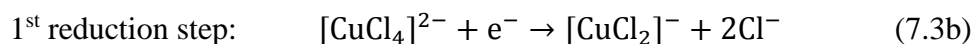
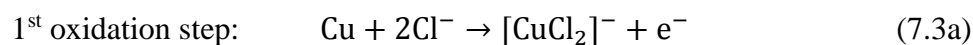


Figure 7.9 Polarisation data of 0.2 M  $\text{CuCl}_2 \cdot 2\text{H}_2\text{O}$  in ethaline containing 15 wt%  $\text{H}_2\text{O}$  at a rotation speed of 700 rpm, showing coupling of the anodic and cathodic processes.

Thus, the following reactions (equations 7.3 (a) and 7.3 (b)) can occur in parallel:



If one adds the equation 7.3 (a) to equation 7.3 (b), the overall reaction can be written in equation 7.4.



This equation represents a comproportionation reaction in which Cu (II) species reacts with the Cu anode producing Cu (I) complexes. In order to test the thermodynamic feasibility of this reaction, the Gibbs free energy was computed. The calculation was performed using standard potential values estimated from ethaline-based DES systems, i.e.  $E^0(\text{Cu}^{2+}/\text{Cu}^+) = +0.58 \text{ V}$  and  $E^0(\text{Cu}^+/\text{Cu}) = -0.22 \text{ V}$  [5, 188]. The resulting  $\Delta G^0 = -77 \text{ kJ mol}^{-1}$  shows that the comproportionation reaction is spontaneous under standard conditions.

The proposed mechanism by which the comproportionation reaction proceeds is illustrated in Fig. 7.10, whereby Cu (II) species react with the Cu anode producing  $\text{CuCl}_2^-$  species in solution. As discussed earlier in section 6.1.1, the cathodic reaction  $\text{Cu (II)} + e^- \rightarrow \text{Cu (I)}$  is under mass transport control thereby is it likely that the corrosion rate will be dictated by the cathodic limiting current, e.g.  $i_{\text{corr}} = i_{\text{lim}1}$ . Assuming that the corrosion reaction is the dominant process and it is coupling with the anodic dissolution reaction, one can write equation 7.5.

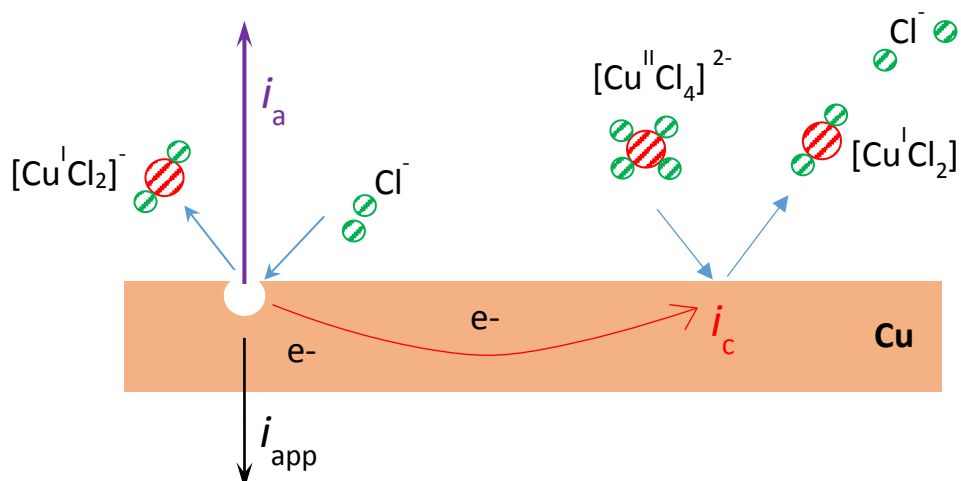


Figure 7.10 Schematic of the overall dissolution processes showing contributions from anodic dissolution and the corrosion reaction.

$$i_a = i_{\text{app}} + i_{\text{corr}} \quad (7.5)$$

where  $i_a$  is the anodic current density,  $i_{\text{app}}$  is the anodic applied current density and  $i_{\text{corr}}$  is the corrosion current density.

If one replaces Faraday's law to the anodic current density, the following expression applies:

$$i_a = \frac{n'F\Delta m}{t_{\text{diss}}MA} \quad (7.6)$$

where  $n'$  is the apparent dissolution valency,  $F$  is the Faraday's constant,  $\Delta m$  is the mass loss of the anode,  $t_{\text{diss}}$  is the dissolution time,  $M$  is the molecular weight of the metal and  $A$  is the area of the electrode. By replacing equation 7.6 in 7.5 and rearranging for  $n'$ , an expression that correlates the apparent dissolution valency with the corrosion current density is obtained as equation 7.7.

$$n' = \frac{(i_{\text{corr}} + i_{\text{app}})t_{\text{diss}}MA}{\Delta mF} \quad (7.7)$$

This equation predicts that in the absence of corrosion, a dissolution valency of  $n' = n$  is obtained. By contrast, if corrosion occurs,  $n' < n$  would be expected. Moreover, if the corrosion reaction is assumed to be mass transport controlled, one can write equation 7.8

$$i_{\text{corr}} = i_{\text{lim}} = \frac{nFDC}{\delta} \quad (7.8)$$

where  $n$  is the number of electrons transferred in the cathodic process,  $\delta$  is the diffusion layer thickness, and  $D$  and  $C$  are the diffusion coefficient and bulk concentration of the  $\text{CuCl}_4^{2-}$  species. This relationship suggests that if  $i_{\text{lim}}$  is raised by increasing  $C$  or  $D$  (or by reducing  $\delta$ ) then  $i_{\text{corr}}$  is increased and this results in a lower apparent dissolution valency.

In order to test the assumption that the corrosion rate is mass-transport limited, the corrosion current ( $i_{\text{corr}}$ ) was extracted by applying equation 7.7 to the data given in Appendix I (cf. Table I.1). Fig. 7.11 presents the extracted  $i_{\text{corr}}$  versus the square root of the rotation rate, exhibiting a Levich-like response as predicted in equation 7.8. A similar dependence on  $\omega^{1/2}$  was observed for all water-containing electrolytes confirming that the corrosion rate is dictated by the mass transport of corroding species towards the anode.

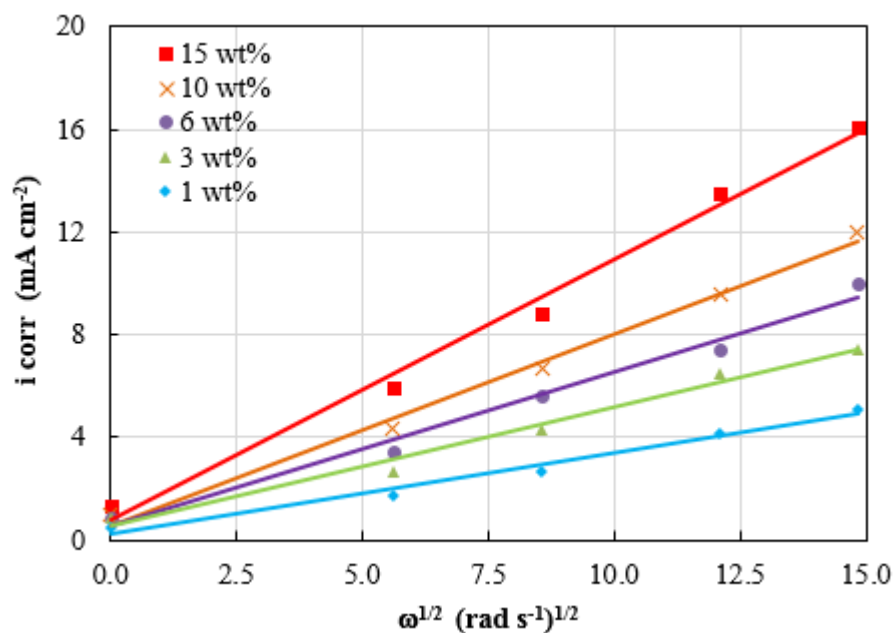


Figure 7.11 Corrosion current density,  $i_{\text{corr}}$ , extracted from the dissolution valency data plotted as a function of rotation rate and water content (1 – 15 wt% H<sub>2</sub>O).

In a similar fashion,  $i_{\text{corr}}$  can be obtained from the data in Appendix J (cf. Table J.1) where the apparent dissolution valency was recorded according to the concentration of Cu (II) species in the electrolyte. The first point to note is the high linearity of the plots in Fig. 7.12 (a-b) for the electrolyte containing 1 and 15 wt% of water. It is observed that the addition of water raises the corrosion currents. These findings are interpreted as the improved diffusivity of  $\text{CuCl}_4^{2-}$  species (cf. discussion in section 6.1.2). A recent study has also attributed a high corrosion rate to the enhanced transport of species brought about by water [218].

It is also important to mention that the electrode disintegration effect is not applicable to our system. Otherwise, the corrosion currents would not be linear-dependent on the rotation rate and concentration of Cu (II) species. In addition, the corrosion rate of Cu in oxygen-containing pure ethaline under similar hydrodynamic conditions (e.g.  $\omega = 700$  rpm) has been measured in a recent study to be  $0.02 \text{ mA cm}^{-2}$  [221]. This corrosion rate is much lower than the calculated one in our system. It is therefore thought that the amount of dissolved O<sub>2</sub> that may exist in ethaline cannot explain the obtained corrosion rates in this work.

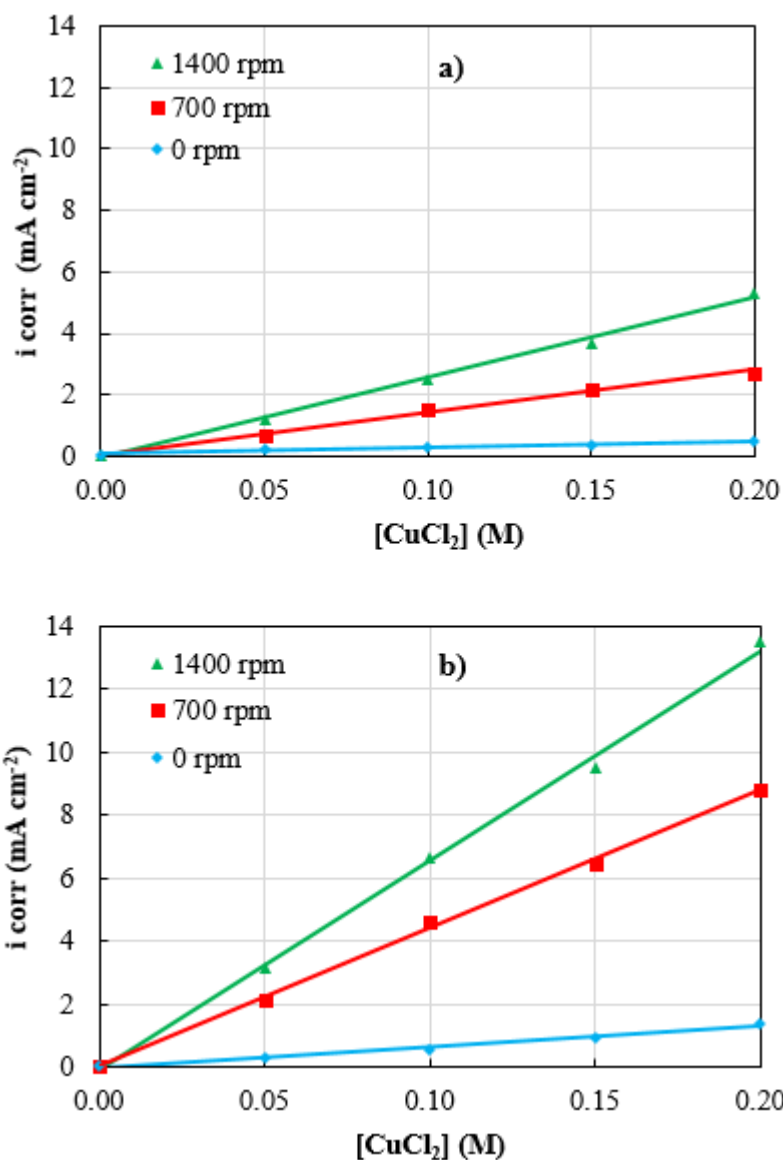


Figure 7.12 Corrosion current density,  $i_{\text{corr}}$ , extracted from dissolution valency data as a function of  $\text{CuCl}_2 \cdot 2\text{H}_2\text{O}$  concentration and rotation rate in an ethaline containing a) 1 wt% and b) 15 wt% of  $\text{H}_2\text{O}$ .

Up to now, it has been discussed the corrosion reaction to be under mass-transport control. Thus, if the corrosion model is acceptable, the corrosion currents should be similar to the first limiting current measured for the reduction of  $\text{CuCl}_4^{2-}$  species. In order to perform this comparison,  $i_{\text{corr}}$  and  $i_{\text{lim1}}$  were assessed under identical conditions, i.e. applied anodic current density =  $2.85 \text{ mA cm}^{-2}$ , concentration of 0.2 M Cu (II) and rotation rate of  $\omega = 700 \text{ rpm}$ . Table 7.2 shows that both  $i_{\text{corr}}$  and  $i_{\text{lim1}}$  are in good agreement (within 5% of experimental error),

showing that the corrosion model quantitatively accounts for the electro-dissolution of Cu from the DES system.

Table 7.2 Comparison amongst  $i_{\text{corr}}$  extracted from the dissolution valency data and  $i_{\text{lim}}$  measured for the reduction of  $\text{CuCl}_4^{2-}$  species at various water amounts. The applied anodic current density was  $2.85 \text{ mA cm}^{-2}$ ,  $0.2 \text{ M}$  of Cu (II) species and  $\omega = 700 \text{ rpm}$ .

Water content (wt%)	$i_{\text{corr}}$ ( $\text{mA cm}^{-2}$ )	$i_{\text{lim1}}$ ( $\text{mA cm}^{-2}$ )
1	2.69	2.82
3	4.30	4.32
6	5.66	4.44
10	6.70	6.39
15	8.81	9.11

The results reinforce the importance of mass transport effects on the corrosion reaction by comproportionation. For instance, by adjusting controlling factors such as electrode rotation rate, concentration of Cu (II) species and water content, corrosion can be minimised but will always be present to some extent in the  $\text{CuCl}_2$ -ethaline system.

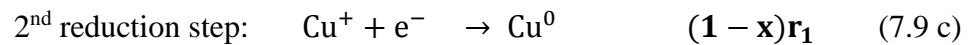
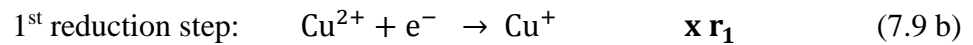
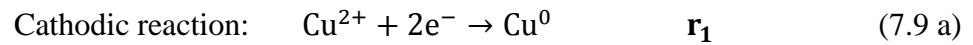
It is essential to reflect that other ILs and DES systems can also exhibit corrosion effects. For example, a comproportionation reaction has been identified to occur while Cu was pulse plated from the  $\text{CuCl}_2$ -ethaline electrolyte during the off-time, etching the deposited Cu and therefore reducing the efficiency of the electroplating process [226]. Moreover, it has been reported that under open circuit conditions, a soluble Cr anode encountered corrosion from the Cr (III)-DES system based on choline chloride and Cr (III) salts [227, 228].

Fe electrodeposition from a  $\text{FeCl}_3$ -DES system has been performed utilising insoluble anodes [229]. However, a soluble Fe anode would be corroded by the comproportionation reaction:  $2\text{FeCl}_4^- + \text{Fe} + 4\text{Cl}^- \rightarrow 3\text{FeCl}_4^{2-}$  [230]. This corroding behaviour has been seen during the discharge of iron redox-batteries using DESs, whereby Fe (III) species travelled to the anodic compartment and etched the Fe anode [231].

These previous experiences suggest that corrosion effects can not only influence the anodic reaction process but also affect the stability of the electrolyte. For instance, the overall dissolution rate may not be readily predictable since the corrosion rate depends on various experimental conditions such as concentration of species, agitation and applied current density. More importantly, the comproportionation reaction will introduce species into the plating solution in a different (e.g. lower) oxidation state such as Cu (I), Cr (II) or Fe (II) while depleting the solution of the higher-valency species that normally deposit at the cathode. Due to this fact, the prediction of the production rate of Cu (I) species in the DES-system during electrodeposition is needed.

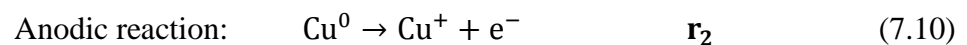
#### 7.1.4 Prediction of the production rate of Cu (I) species in the electrolyte

In order to estimate the rate of Cu (I) production in our DES-system, only the heterogeneous solution has been considered while the equilibrium between Cu (II) and Cu (I) species in the bulk electrolyte is neglected for simplicity. Cu (I) species are generated during the cathodic reaction, which is electrochemically driven, as equations 7.9 (a-c) show.



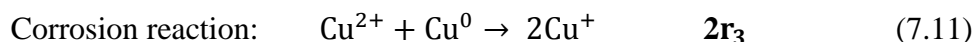
where  $\mathbf{r}$  is the rate of mass production of Cu (I) while  $\mathbf{x}$  refers to the fractional reactant conversion. Due to the fact that the current efficiency of the electrodeposition process has been measured in section 6.3.1, the difference corresponds to the amount of Cu (I) species that are converted to metallic Cu.

The generation of Cu (I) species product of the anodic reaction can be expressed as shown in equation 7.10.





The comproportionation reaction, not driven by the applied current, also contributes to produce Cu (I) species as described in equation 7.11.



The total moles of Cu (I) species can then be described in equation 7.12.

$$N_{\text{TCu}^+} = N_{1\text{Cu}^+} + N_{2\text{Cu}^+} + N_{3\text{Cu}^+} \quad (7.12)$$

where  $N_{\text{TCu}^+}$  is the total moles of Cu (I) species produced from the individual heterogeneous reactions. If  $N_{i\text{Cu}^+}$  in equation 7.12 is substituted by the rate of the electrochemical reaction shown in equation 7.13, a more convenient expression for the total moles of Cu (I) species can be written in equation 7.14.

$$N_{\text{TCu}^+} = rt = \frac{i}{nF} t \quad (7.13)$$

$$N_{\text{TCu}^+} = (xr_1 + r_2 + 2r_3) t = \frac{t}{nF} (x \vec{i}_{\text{app}} + \vec{i}_{\text{app}} + 2 i_{\text{corr}}) \quad (7.14)$$

where  $r$  is the reaction rate,  $t$  is the time of the reaction,  $i$  is the applied current,  $n$  is the number of transferred electrons,  $F$  is the Faraday's constant. The resultant expression in equation 7.14 can be used to predict the production rate of Cu (I) species in an electrochemical cell in the presence of agitation.

Fig. 7.13 illustrates the production and depletion rate of  $\text{CuCl}_2^-$  and  $\text{CuCl}_4^{2-}$  species respectively when the electrolyte contains increasing amounts of water. For the electrolyte containing 1 wt% of  $\text{H}_2\text{O}$ , Cu (I) and Cu (II) complexes exhibit a similar concentration after 10 days of electrodeposition (e.g.  $\sim 0.15$  M). However, at 10 wt% of  $\text{H}_2\text{O}$ , the concentration of Cu (I) species rapidly increases to a relatively high concentration (e.g.  $\sim 0.17$  M) in a shorter time, 6 days. These results can be rationalised by the following reasons:

- i) The poor uniformity of the current distribution causes that nearly half of the generated Cu (I) species in the first reduction step are not converted to the solid phase. These Cu (I) species therefore remain unconverted in the bulk electrolyte.

- ii) The product of the anodic dissolution has been established to be the  $\text{CuCl}_2^-$  complex, which may accumulate in the solution over time.
- iii) The corrosion model shows that the comproportionation reaction is under mass-transport controlled. Thus, as  $i_{\text{lim}1}$  is increased by water content so does  $i_{\text{corr}}$  due to the improved transport of the corroding species  $\text{CuCl}_4^{2-}$  towards the Cu anode. Therefore, a faster formation of Cu (I) species proceeds from the water-containing electrolytes.

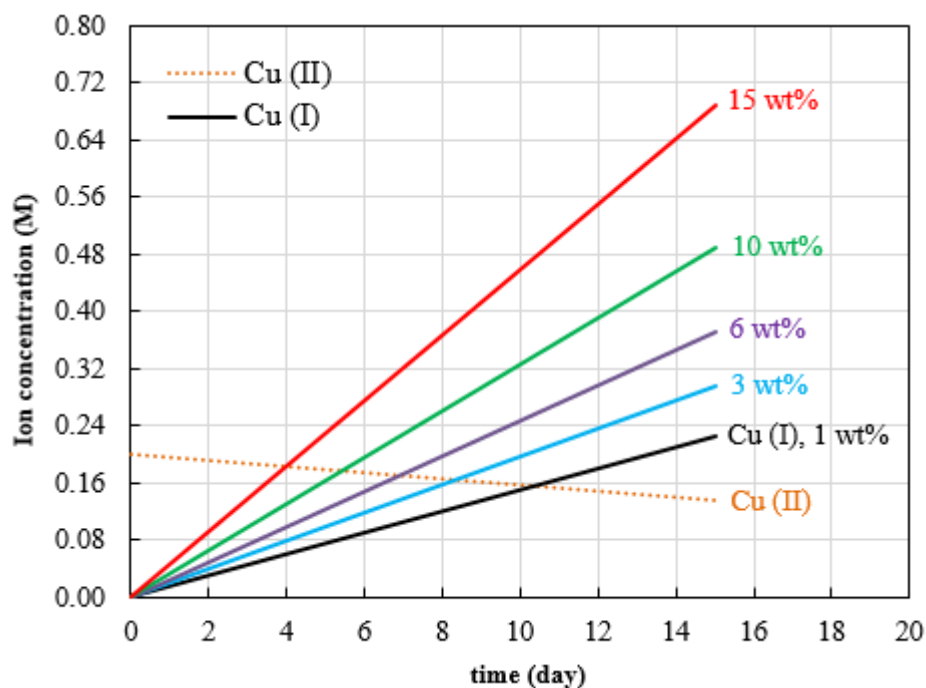


Figure 7.13 Production rate of Cu (I) species in the electrolyte (1-15 wt%  $\text{H}_2\text{O}$ ) as a function of time. For comparison, the depletion of Cu (II) ions is shown as the dotted orange curve.

Lower-valency species as in this case (e.g.  $\text{Cu}^+$ ) may introduce stability issues for the electrodeposition process since they may undergo further reactions at the cathode or in solution. For instance, there is the possibility that Cu (I) species, anodically generated, may discharge at the cathode changing the current efficiency of the process. Moreover, a colour change was observed from light yellow to greenish in the samples used to construct Fig. 7.3 (a) suggesting an alteration in speciation. Thereby, in order to detect if changes in speciation occurred, the UV-Vis spectra of these samples were monitored over three weeks. The UV-Vis results show that after

one week of monitoring, the absorption band at 405 nm appeared and steadily increased as shown in Fig. 7.15 (a-c). Since this electronic band is indicative of the presence of  $\text{CuCl}_4^{2-}$  species, it is possible that Cu (I) species further disproportionate in solution as per the following reaction:  $2\text{Cu}^+ \leftrightarrow \text{Cu}^{2+} + \text{Cu}^0$ . This therefore indicates that the electrolyte may present stability issues in the long-term.

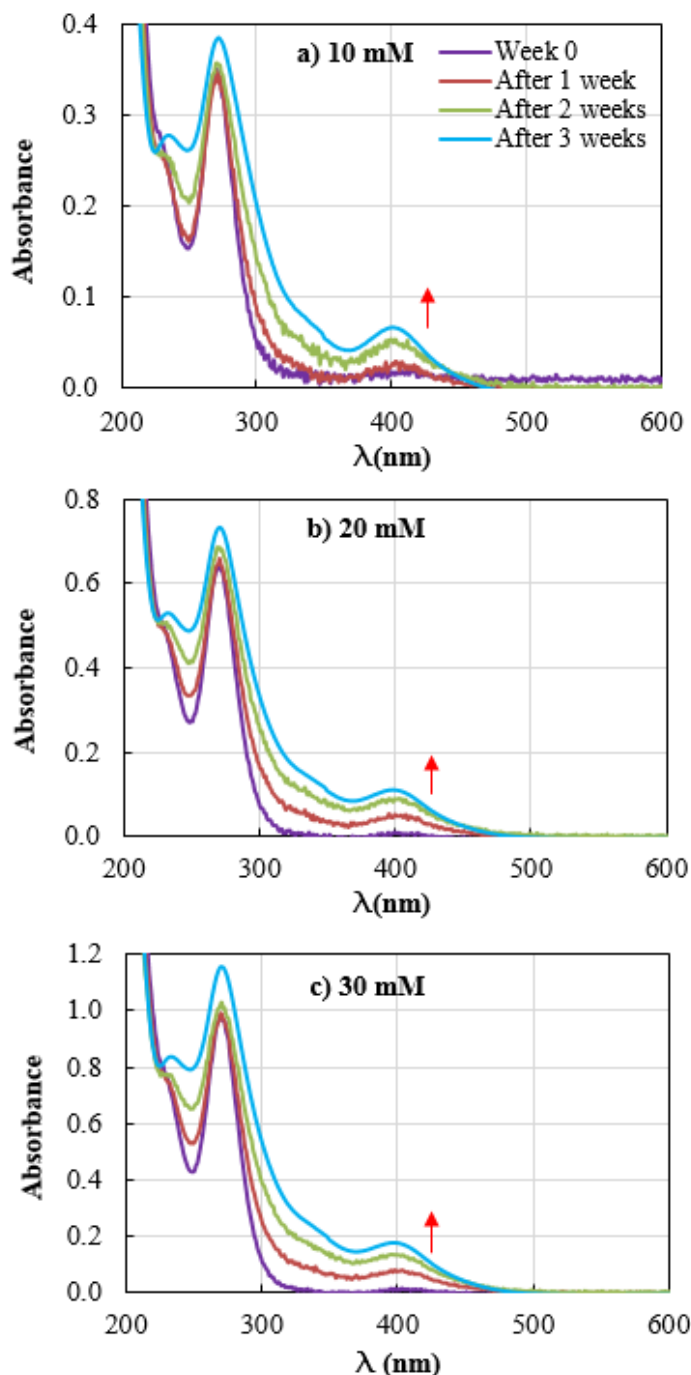


Figure 7.14 UV-Vis monitoring of the stability of  $[\text{CuCl}_2]^-$  species in ethaline over time. The samples were prepared by dissolving CuCl salt in ethaline using concentrations of a) 10 mM, b) 20 mM, and c) 30 mM.

## **8. Chapter - Conclusions and Future Work**

## 8. Conclusions and Future Work

---

### 8.1 Conclusions

DESs are generally more viscous than aqueous solutions which may be translated in poor mass transport properties for electrodeposition processes. Since the addition of water may mitigate this problem, the present study concentrated on investigating the effect of water content on the electrochemical properties of Cu electrodeposition from hydrated DES systems and examined if the addition of water affected the characteristics of the electrodeposits. Some of the most important physico-chemical properties, in terms of electrodeposition, were measured as a function of water content. This showed to what extent the addition of water influenced them. To evaluate the effect of water on the mass transport and electrokinetics properties of Cu electrodeposition, the diffusion limiting currents and heterogeneous rate constants were obtained. Characteristics such as purity, uniformity, morphology and microstructure of Cu deposits obtained from the water-containing DES systems were examined in order to assess if the addition of water improved or deteriorated these properties.

Due to the fact that ethaline is hygroscopic substance, the electrolyte (0.2 M  $\text{CuCl}_2$  in ethaline) was monitored for four weeks in order to determine its ability to incorporate water from the atmosphere. It was found that the concentration of water in the electrolyte increased from 3, 6, 10 to 15 wt% in this period.

The water-containing electrolytes were prepared using the above amounts of water from which physico-chemical properties such as density, viscosity and conductivity were measured as a function of water. The effect of water content on these properties was considered to be beneficial due to the following reasons:

- The density of the electrolyte decreased which may be the result of a disrupted hydrogen bonding network brought about by water content leading to a more open structure.

- The viscosity of the electrolyte significantly decreased from 47.3 (1 wt%) to 15.1 mPa s (15 wt%) which may be the result of a molecular structure with large interstitial voids which in turn can facilitate the movement of diffusing species.
- The conductivity of the electrolyte increased twofold from 0.795 (1 wt%) to 1.530 S m<sup>-1</sup> (15 wt%) which may be attributable to the ease of ionic conduction of the charge carriers.

The effect of water on the mass transfer behaviour of the Cu electrodeposition from ethaline was assessed by measuring both limiting currents,  $i_{lim1}$  and  $i_{lim2}$ , corresponding to the electron-transfer reactions Cu(II)→Cu(I) and Cu(I)→Cu(0). It was found that the both limiting currents increased which was attributed to the enhanced transport of diffusing species (e.g. CuCl<sub>2</sub><sup>-</sup> and CuCl<sub>4</sub><sup>2-</sup>) towards the interface. Due to the fact that mass transfer rates were increased significantly, the issue with DES systems of low plating rates has been partially solved.

No adverse effect was observed on the electrochemical window of ethaline, speciation of Cu complexes, and electro-kinetics of Cu electrodeposition when the concentration of water increased in the electrolyte. The reasons of these were as follows:

- Ethaline was found to be relatively insensitive to hydration since the anodic and cathodic limits were not strongly reduced as water content increased from 3 to 15 wt% in the electrolyte.
- The monitoring of the speciation of Cu (II) complexes showed that the dominant species [CuCl<sub>4</sub>]<sup>2-</sup> continues up to 35 wt% of H<sub>2</sub>O. Only beyond this concentration, a mixture of chloro-aquo complexes might exist since the UV-Vis trace exhibited similar characteristics than that of the aqueous chloride system.
- The water content does not drastically influence the charge transfer reaction since the rate of electron transfer for the second reduction step was found to increase about eight times when water content increased from 1 to 15 wt% in the electrolyte.

Findings from this stage were thereafter useful to predict how uniform the Cu electrodeposits would be. Using the Wagner number relationship, the electrodeposits were anticipated to exhibit a non-uniform current distribution leading to a poor homogeneity. However, analysis of the Wagner number showed that this was not directly related to the water content but to the conductivity of the electrolyte, as explained below:

- The Wagner number was calculated to be  $W_a \sim 0.20$  for all water-containing electrolytes indicating that the deposits would tend to be thin near the centre of the electrode and thicker at the edges. If one expresses this dimensionless parameter as  $W_a = c \kappa / i_{\text{avg}}$  where  $c$  represents the constant terms, it can be observed that the ratio of the conductivity to the average current density plays a significant role. For instance, deposits fabricated from aqueous systems containing supporting electrolyte usually exhibit a homogeneous thickness due to the high conductivity of the medium. In the case of DES systems, although the conductivity of the electrolyte increased with water content, it was not enough to compensate the increase on the average current density also brought about by water. Therefore, poor uniformity of the electrodeposits could be related to low conductivity of the DES system.
- The uneven current distribution also affected the efficiency of the electrodeposition process, which was found to be 48.3% for the electrolyte containing 1 wt% of water. However, the results showed that increasing amounts of water do not further reduce the efficiency of the process as it was found to be 58.8% for the DES system containing 15 wt% of water.

Cu electrodeposits obtained from the water-containing electrolytes were examined in order to evaluate their morphology and microstructural features. The following conclusions were derived from these experiments:

- Due to the uneven current distribution along the electrode, morphological differences occurred between the centre and the edge of the deposits. SEM and EBSD analysis revealed that two types of morphology developed;

equiaxed and columnar structures. From Winand's diagram, these morphological features were associated to exist due to differences in current density between the centre and the edge of the deposits.

- EDX results showed that the purity of Cu electrodeposits was not affected by increasing amounts of water in the DES system as it varied from 100 to 97.1 wt% of Cu for the electrolytes containing 1 and 15 wt% of water, respectively.
- The average grain size of the electrodeposit obtained from the electrolyte containing 1 wt% of water was computed to be  $1.25 \pm 0.94 \mu\text{m}$  representing crystals almost ten times smaller than the ones obtained from the aqueous sulphate system without additives,  $11.52 \pm 0.43 \mu\text{m}$  (0.6 M  $\text{Cu}^{2+}$  + 2.0 M  $\text{H}_2\text{SO}_4$ ). This represents an advantage of DES systems since no additional substances were required to produce finer grains.

Therefore, the effect of water content on Cu electrodeposition from the DES system was considered to be beneficial for various reasons: (i) the conductivity of the electrolyte improved which would be reflected in a reduced energy consumption, (ii) faster deposition rates were achieved without a drastic change in electrochemical window, speciation of complexes and electro-kinetics, (iii) the efficiency of the electrodeposition process was not reduced, (iv) the electrodeposits were highly pure without the presence of hydroxides, and (v) the morphological and microstructural features of the deposits were not deteriorated since there was no evidence of formation of either dendritic or porous materials. The addition of water therefore was a simple way to improve the electrodeposition of Cu from ethaline-based DES system with no real disadvantage apart from uniformity.

While water addition had minimal influence on deposit characteristics and beneficial effect on electrolyte properties, the effect of water on the characteristics of the anodic process was unknown. Therefore, the feasibility of using a soluble copper anode during the electrodeposition of Cu from the DES system was investigated and the influence of water incorporation on the performance of anodic process was quantified. The results showed that:



- In pure ethaline, the current efficiency of the anodic process was 100% and the dissolution valency was one. However, in the presence of Cu (II) species the apparent dissolution valency measured gravimetrically was typically less than unity ( $n' < 1$ ), corresponding to an observed mass loss greater than that expected from Faraday's law.
- The anodic species product of the electro-dissolution of the Cu anode were the  $[\text{CuCl}_2]^-$  complex.
- The apparent dissolution valence,  $n'$ , was found to be depended on three variables: (i) concentration of Cu (II) in the electrolyte, (ii) rotation rate of the electrode, and (iii) concentration of water in the electrolyte. This phenomenon was rationalised in terms of a corrosion process involving a comproportionation reaction that occurred in parallel to the anodic process.
- The comproportionation reaction was:  $[\text{CuCl}_4]^{2-} + \text{Cu} \rightarrow 2[\text{CuCl}_2]^-$ .  
 Voltammetric data indicated that the rate of the comproportionation reaction was controlled by the mass transport of the  $[\text{CuCl}_4]^{2-}$  complex to the surface of the anode and readily explained the observed dissolution valency dependencies.

It was noted that the electro-dissolution of Cu anodes in ethaline-based DES system was complex due to the fact that the electrolyte was replenished with anodic species of lower oxidation state than that of the species from which electrodeposition occurred. This would therefore affect not only the stability of the electrolyte but also the electrodeposition process in the long-term. Therefore, the implementation of soluble anodes may be difficult and further research would be a requirement prior to deploying practical systems based on DESs.

## 8.2 Future work

The anodic process during Cu electrodeposition was investigated using a soluble anode. Due to the fact that the electrolyte is replenished by species with a different oxidation state than that of the ones deposited at the cathode, the electrodeposition process would not be stable. The electroplating process using a soluble anode should therefore be investigated to examine if cuprous species affect the current efficiency as well the morphological characteristics of the deposits. The influence of disproportionation of cuprous species on the electrodeposits is another aspect that could be looked at in the future.

It has been reported that the addition of water was beneficial for the anodic process using an inert anode [115]. Indeed, it was reported that the addition of water hindered the formation of chlorinated substances during Zn electrodeposition from ethaline-based DES system since the oxidation of water prevented the formation of these by-products. It would be therefore important to elucidate the optimal concentration of water to minimise the formation of hazardous substances.

Since the effect of water on Cu electrodeposition was considered to be beneficial due to the explained reasons, it would be instructive to examine the influence of the addition of water in ethaline-based DES systems for the electrodeposition of metals such as Ni, Cr, Fe, Sn and others. Moreover, the assessment of the anodic reactions using soluble anodes during their electrodeposition from DES systems would establish if comproportionation reactions occur, their mechanism, and implications.

Although the complexity of the chemistry of the electrolyte would increase with the use of additives, the influence of additives on Wagner number should be investigated since this improvement would be translated in more uniform thickness distribution. Since the presence of additives may induce changes in electrochemical characteristics and microstructural properties of the electrodeposits, these should also be assessed in future.

Water content brought about a greater activity of the electrode, which might arise due to differences in the electrical double layer (EDL) of the DES system. Since scarce experimental evidence on the EDL of water-containing DESs is available, it would be ideal to determine the effect of water content on the double layer characteristics by capacitance measurements. This would allow one to improve the understanding of electro-kinetics in hydrated DES systems.

## Appendices

### *Appendix A: Uptake of water with time by ethaline and the electrolyte.*

The data obtained from Karl Fischer titration are summarised in the following tables.

Table A.1 Data to calculate the initial concentration of water in blank ethaline. Data obtained from Karl Fischer titration. Titration factor = 5 mg mL<sup>-1</sup>. Sample volume = 0.5 mL.

w <sub>1</sub> (g)	w <sub>2</sub> (g)	Moisture (mg)	[H <sub>2</sub> O] wt%
24.3551	23.8049	6.3750	1.1587
24.3672	23.8096	5.7500	1.0312
24.3670	23.8063	6.6000	1.1771
24.3698	23.8045	6.5000	1.1498
		Average water content	1.1292
		Standard deviation	± 0.0663

$$w_1 = \text{syringe} + \text{sample} \quad (\text{A.1})$$

$$w_1 = \text{empty syringe} \quad (\text{A.2})$$

Table A.2 Data to calculate the initial concentration of water in the electrolyte (0.20 M CuCl<sub>2</sub>·2H<sub>2</sub>O dissolved in ethaline). Data obtained from Karl Fischer titration.

Titration factor = 5 mg mL<sup>-1</sup>. Sample volume = 0.5 mL.

w <sub>1</sub> (g)	w <sub>2</sub> (g)	Moisture (mg)	[H <sub>2</sub> O] wt%
24.3755	23.8062	10.1750	1.7873
24.3786	23.8085	10.1500	1.7804
24.3688	23.8064	10.0500	1.7870
24.3743	23.8076	10.1750	1.7955
24.3662	23.8074	10.0000	1.7595
24.3570	23.8081	9.9000	1.8036
24.2563	23.8071	8.2750	1.8422
24.3669	23.8052	10.2720	1.8293
24.3738	23.8066	10.250	1.8115
		Average water content	1.8006
		Standard deviation	± 0.0254

Table A.3 Data to calculate the initial concentration of water in the electrolyte (0.10 M  $\text{CuCl}_2 \cdot 2\text{H}_2\text{O}$  dissolved in ethaline). Data obtained from Karl Fischer titration.

Titration factor = 5 mg  $\text{mL}^{-1}$ . Sample volume = 0.5 mL.

<b>w<sub>1</sub> (g)</b>	<b>w<sub>2</sub> (g)</b>	<b>Moisture (mg)</b>	<b>[H<sub>2</sub>O] wt%</b>
24.3617	23.8044	8.600	1.5432
24.3663	23.8063	8.600	1.5357
24.3689	23.8067	8.6500	1.5386
24.3663	23.8062	8.6000	1.5354
24.3598	23.8037	8.6500	1.5555
24.3650	23.8064	8.6250	1.5440
24.3711	23.8062	8.6750	1.5357
24.3617	23.8067	8.5250	1.5358
24.3703	23.8061	8.6500	1.5331
24.3615	23.8081	8.6000	1.5484
		Average water content	1.5405
		Standard deviation	± 0.0071

Table A.4 Data to calculate the initial concentration of water in the electrolyte (0.05 M  $\text{CuCl}_2 \cdot 2\text{H}_2\text{O}$  dissolved in ethaline). Data obtained from Karl Fischer titration.

Titration factor = 5 mg  $\text{mL}^{-1}$ . Sample volume = 0.5 mL.

<b>w<sub>1</sub> (g)</b>	<b>w<sub>2</sub> (g)</b>	<b>Moisture (mg)</b>	<b>[H<sub>2</sub>O] wt%</b>
24.3659	23.8101	8.0250	1.4439
24.3674	23.8065	8.1500	1.4530
24.3671	23.8067	8.1250	1.4490
24.3631	23.8074	8.0500	1.4486
24.3543	23.8046	7.9500	1.4462
21.3649	23.8050	8.0250	1.4333
24.3627	23.8051	8.1500	1.4616
24.3644	23.8035	8.4250	1.4991
24.3626	23.8052	7.6500	1.3724
24.3635	23.8055	8.0500	1.4427
		Average water content	1.4449
		Standard deviation	± 0.0311

Table A.5 Data for calibration curve. Karl Fischer titration experiments.

Added H <sub>2</sub> O (wt%)	Sample volume (mL)	w <sub>1</sub> (g)	w <sub>2</sub> (g)	Moisture (mg)	[H <sub>2</sub> O] wt%
2	0.5	24.3750	23.8061	21.3250	3.7485
		24.3686	23.8063	21.0000	3.7347
		24.3693	23.8055	20.9750	3.7170
4	0.2	24.0387	23.8080	14.4750	6.2744
	0.5	24.3715	23.8054	35.7250	6.3107
		24.3728	23.8072	35.4750	6.2721
6	0.3	24.1457	23.8051	26.9750	7.9198
		24.1391	23.8050	26.5250	7.9392
		24.1379	23.8034	26.3000	7.8625
8	0.3	24.1560	23.8130	33.6250	9.8032
		24.1484	23.8137	33.3750	9.9716
		24.1522	23.8142	33.4750	9.9038
10	0.3	24.1539	23.8177	40.0000	11.8977
		24.1480	23.8165	40.4000	12.1870
		24.1526	23.8159	40.7500	12.1028
12	0.2	24.0141	23.8013	30.2000	14.1917
		24.0242	23.8020	31.5500	14.1989
		24.0245	23.8034	31.2750	14.1452
14	0.2	24.0327	23.8116	35.1750	15.9091
		24.0305	23.8101	35.2500	15.9936
		24.0318	23.8118	35.8000	16.2727
16	0.2	24.0352	23.8077	41.8000	18.3736
		24.0293	23.8128	39.3250	18.1640
		24.0307	23.8070	41.0750	18.3610

**Appendix B: Error analysis – NIR calibration curve.**

The error analysis was performed in EXCEL and started with the calculation of the slope and the intercept values using equations B.1 and B.2.

$$m = \frac{\sum_{i=1}^n (x_i - \bar{x})(y_i - \bar{y})}{\sum_{i=1}^n (x_i - \bar{x})^2} \quad (\text{B.1})$$

$$b = \bar{y} - m\bar{x} \quad (\text{B.2})$$

where  $m$  is the slope of the curve,  $n$  is the number of calibration points (samples),  $x_i$  is the water concentration,  $\bar{x}$  is the average of the water concentration,  $y_i$  is the absorbance,  $\bar{y}$  is the average of the absorbance and  $b$  is the intercept of the curve. The slope was computed to be 0.0081 and the intercept was 0.0106. Table B.1 summarises the treatise of the values used to calculate both parameters.

Table B.1 Values used to calculate the slope and intercept using the regression method.

$x_i$	$y_i$	$(x_i - \bar{x})$	$(x_i - \bar{x})^2$	$(y_i - \bar{y})$	$(x_i - \bar{x})(y_i - \bar{y})$	$\frac{(y_i - y')^2}{10^{-3}}$
18	0.155	8	64	0.063	0.504	0.004
16	0.137	6	36	0.045	0.270	0.014
14	0.128	4	16	0.036	0.144	0.012
12	0.109	2	4	0.017	0.034	0.001
10	0.092	0	0	0.000	0.000	0.000
8	0.080	-2	4	-0.012	0.024	0.019
6	0.063	-4	16	-0.029	0.116	0.013
4	0.042	-6	36	-0.050	0.300	0.001
2	0.022	-8	64	-0.070	0.561	0.025
$\bar{x} = 10$	$\bar{y} = 0.092$		Sum = 240		Sum = 1.953	Sum = $0.089 \times 10^{-3}$

To calculate the uncertainty of a predicted value ( $y'$ ), it is necessary to estimate the standard error of regression and the variance. The standard error of the regression was computed to be 0.0036 using equation B.3.

$$SE_{\text{REG}} = \sqrt{\frac{\sum_{i=1}^n (y_i - y')^2}{n-2}} \quad (\text{B.3})$$

where  $SE_{REG}$  is the standard error of the regression for  $y'$  and  $y'$  is the predicted value using the calculated slope and intercept. Once that  $SE_{REG}$  and the variance have been estimated, the uncertainty can be obtained from relationship B.4.

$$U = \frac{SE_{REG}}{m} \sqrt{\frac{1}{N} + \frac{1}{n} + \frac{(\bar{y}_0 - \bar{y})^2}{m^2 \sum_{i=1}^n (x_i - \bar{x})^2}} \quad (B.4)$$

where  $U$  is the uncertainty of the predicted value,  $N$  is the number of repeated measurements made on the unknown solution (it was assumed to be 3),  $n$  is number of calibration points and  $\bar{y}_0$  is the mean of measurements for the test solution (it was assumed that absorbance of the solution was negligible  $\approx 0$ ). The uncertainty was estimated to be 0.3512 and using the 2-tailed Student's  $t$  value for 90% of confidence, the confidence deviation was obtained as shown in equation B.5.

$$C_i = Ut \quad (B.5)$$

where  $C_i$  is the confidence interval,  $U$  is the uncertainty of the predicted value and  $t$  is the 2-tailed Student's  $t$  value. The  $C_i$  was estimated to be  $\pm 0.67$ . To sum up, Table B.2 lists the parameters calculated in the error analysis of the regression curve.

Table B.2 Summary of analysis of error of the calibration line constructed from Near Infrared spectroscopy measurements.

<b>Predicted water content (wt%)</b>	<b><math>SE_{REG}</math></b>	<b>U</b>	<b><math>C_i</math> for 90% of confidence</b>
1.31	0.0036	0.3512	$\pm 0.67$



*Appendix C: Electro-kinetics of Cu electrodeposition from DES system.*

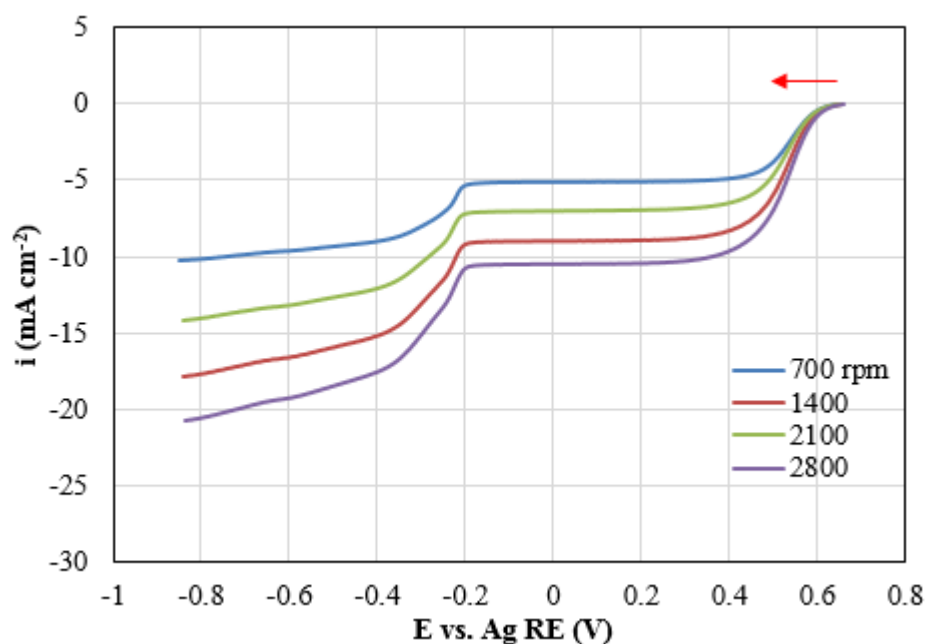


Figure C.1 Cathodic linear scans of 0.2 M CuCl<sub>2</sub>-ethaline systems onto Pt electrode (A=0.031 cm<sup>2</sup>) with increasing rotation speeds, e.g. 700, 1400, 2100 and 2800 for 3 wt% water-containing system.

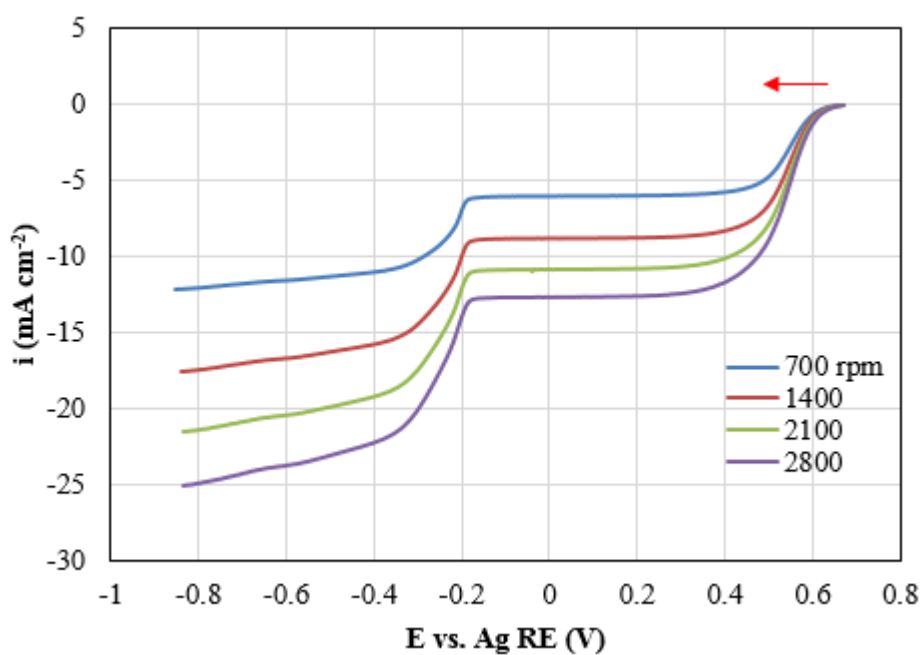


Figure C.2 Cathodic linear scans of 0.2 M CuCl<sub>2</sub>-ethaline systems onto Pt electrode (A=0.031 cm<sup>2</sup>) with increasing rotation speeds, e.g. 700, 1400, 2100 and 2800 for 6 wt% water-containing system.

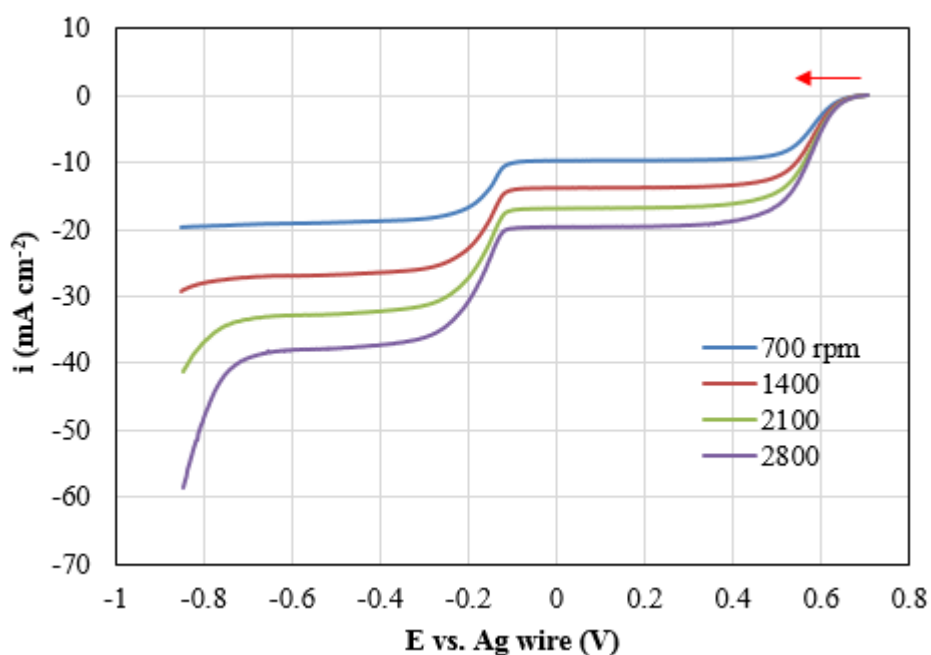


Figure C.3 Cathodic linear scans of 0.2 M  $\text{CuCl}_2$ -ethaline systems onto Pt electrode ( $A=0.031 \text{ cm}^2$ ) with increasing rotation speeds, e.g. 700, 1400, 2100 and 2800 for 15 wt% water-containing system.

Interestingly, the polarisation curve obtained with the electrolyte containing 15 wt% of  $\text{H}_2\text{O}$  at 2800 rpm shows a sharp increase of the cathodic current beyond -0.8 V vs. Ag wire RE. If one revises section 5.3.4 where the electrochemical window of ethaline was measured as a function of water, it is observed that at potentials  $> -0.8$  V vs. Ag wire RE, the solvent breaks down. It has been reported that gaseous components can evolve such as trimethylamine [115]. Alternatively,  $\text{H}_2$  gas might be another breakdown product due to the high content of water. However, the present work did not attempt to measure gaseous products.

**Appendix D: Koutecký-Levich plots for electrolyte containing 3, 6 and 10 wt% of water.**

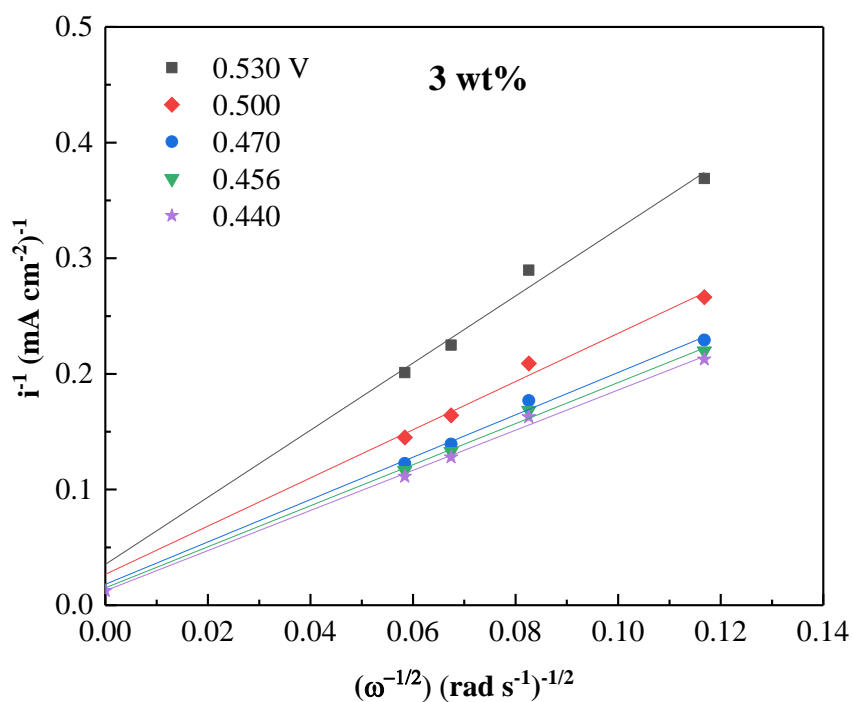


Figure D.1  $i^{-1}$  vs.  $\omega^{-1/2}$  for Cu(II)/Cu(I) step for 3 wt% water-containing electrolyte constructed from the indicated overpotential data. Pt WE ( $A = 0.031 \text{ cm}^2$ ).

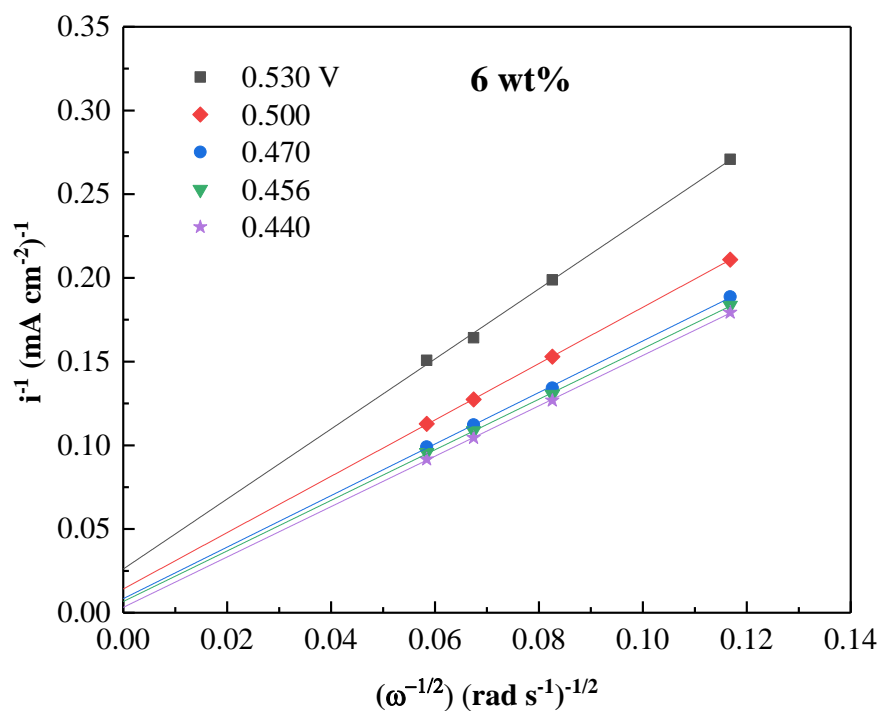


Figure D.2  $i^{-1}$  vs.  $\omega^{-1/2}$  for Cu(II)/Cu(I) step for 6 wt% water-containing electrolyte constructed from the indicated overpotential data. Pt WE ( $A = 0.031 \text{ cm}^2$ ).

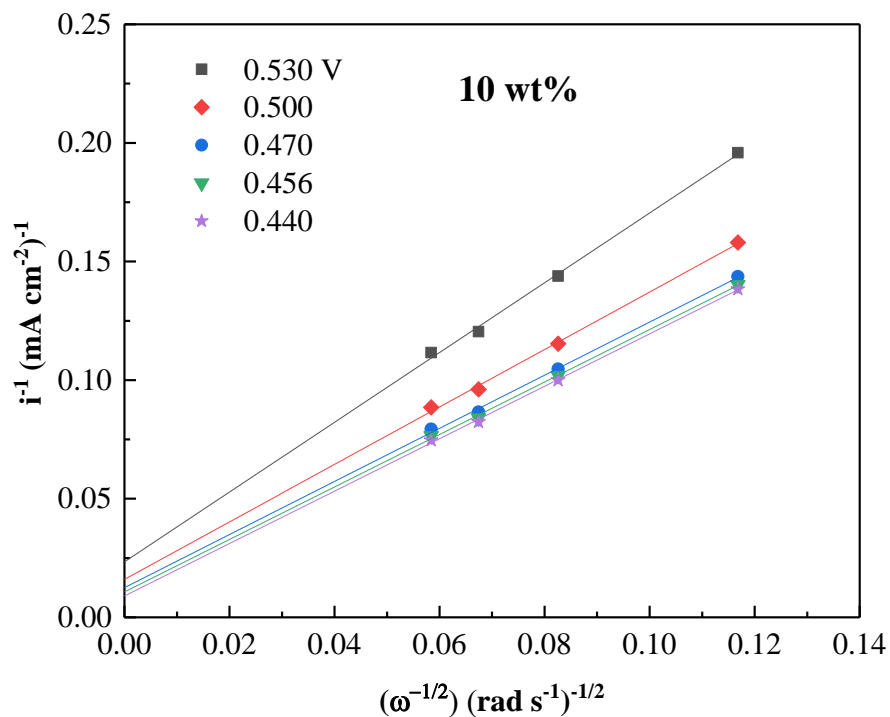


Figure D.3  $i^{-1}$  vs.  $\omega^{-1/2}$  for Cu(II)/Cu(I) step for 10 wt% water-containing electrolyte constructed from the indicated overpotential data. Pt WE ( $A = 0.031 \text{ cm}^2$ ).

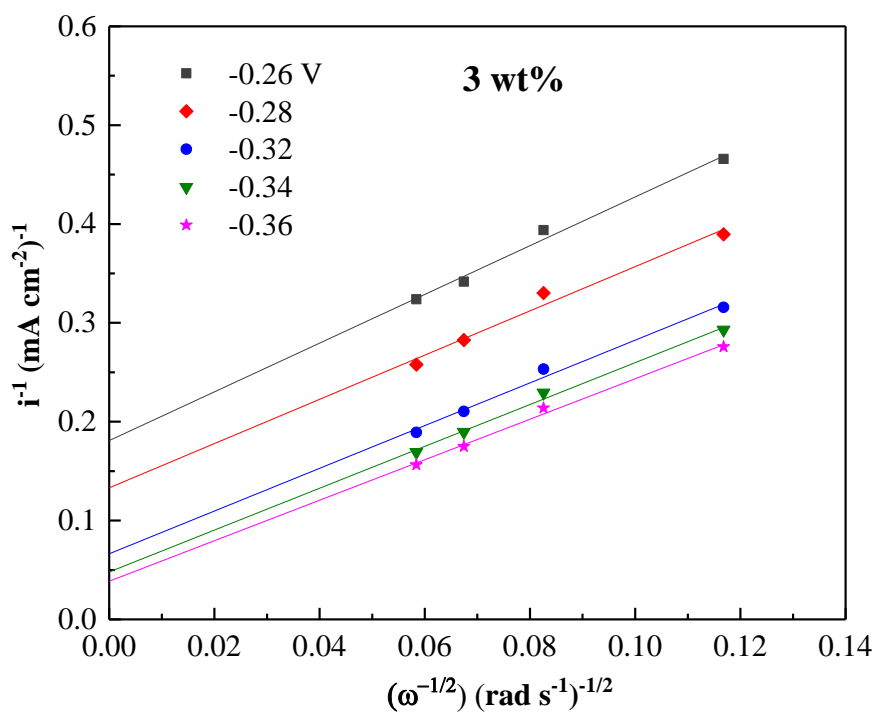


Figure D.4  $i^{-1}$  vs.  $\omega^{-1/2}$  for Cu(I)/Cu step for 3 wt% water-containing electrolyte constructed from the indicated overpotential data. Pt WE ( $A = 0.031 \text{ cm}^2$ ).

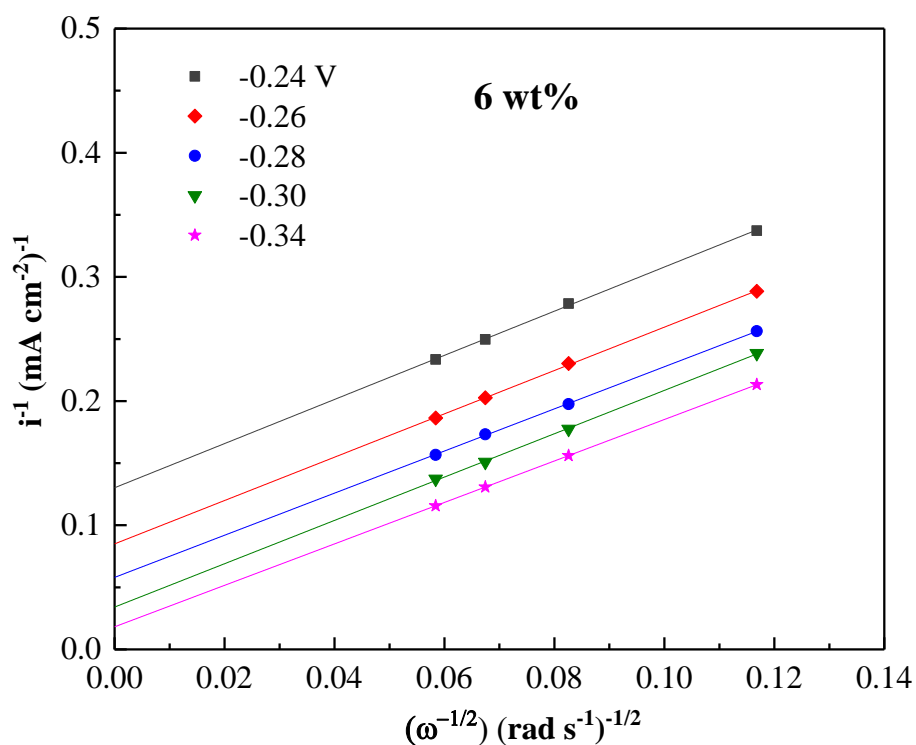


Figure D.5  $i^{-1}$  vs.  $\omega^{-1/2}$  for Cu(I)/Cu step for 6 wt% water-containing electrolyte constructed from the indicated overpotential data. Pt WE ( $A = 0.031 \text{ cm}^2$ ).

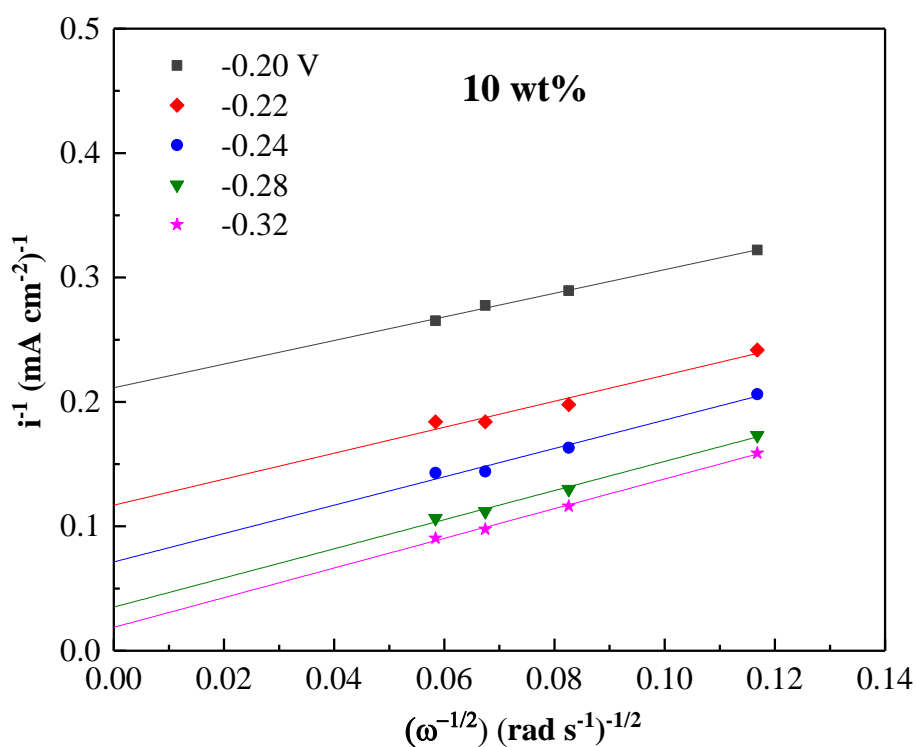


Figure D.6  $i^{-1}$  vs.  $\omega^{-1/2}$  for Cu(I)/Cu step for 10 wt% water-containing electrolyte constructed from the indicated overpotential data. Pt WE ( $A = 0.031 \text{ cm}^2$ ).

**Appendix E:** Plot of  $\ln k_f(E)$  versus overpotential from which kinetic parameters such as  $k^0$  and  $\alpha$  were calculated.

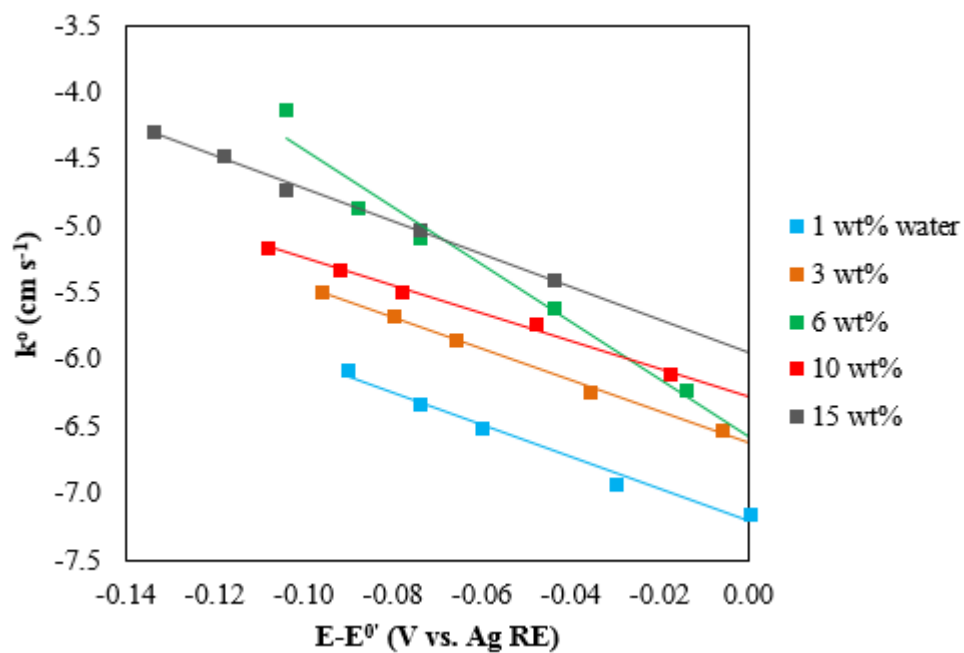


Figure E.1  $\ln k_f(E)$  vs.  $E - E^0$  for all water-containing electrolytes from which  $k^0$  and  $\alpha$  were calculated.

**Appendix F: Calculation of formal potential for the first reduction reaction in DES system.**

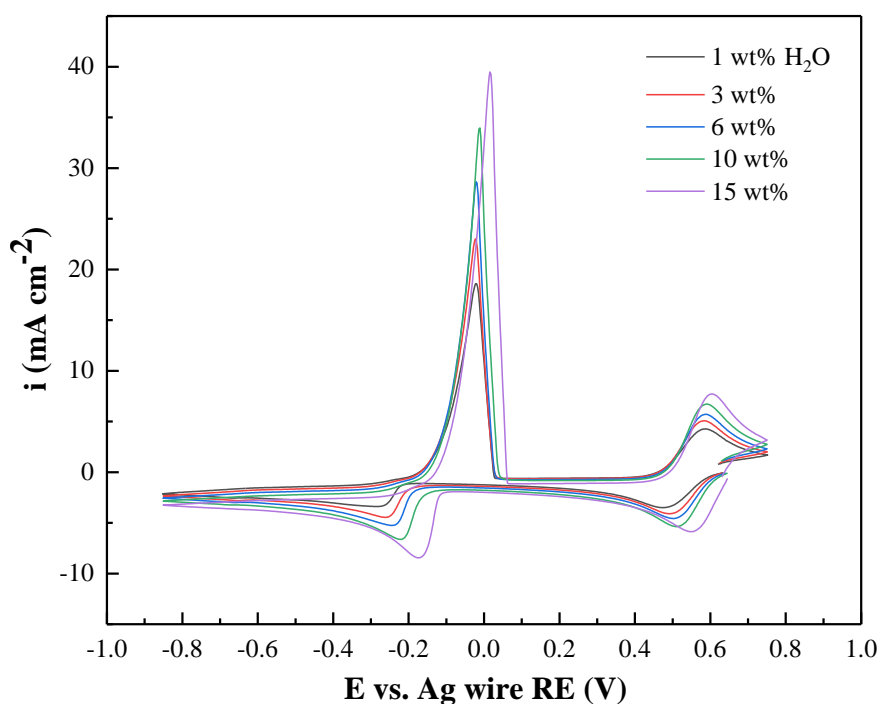


Figure F.1 Cyclic voltammetry of 0.2 M CuCl<sub>2</sub>-ethaline using a Pt WE (A= 0.031 cm<sup>2</sup>) at a scan rate of 30 mV s<sup>-1</sup> at 25 °C. The data was useful to extract the formal potential of the first reduction reaction Cu(II)/Cu(I).

Table F.1 Formal potential for the first reduction reaction extracted from Fig. F.1.

Water content (wt%)	E <sub>pa</sub> (V)	E <sub>pc</sub> (V)	E <sup>o'</sup> =(E <sub>pa</sub> +E <sub>pc</sub> )/2 (V vs. Ag wire RE)
1	0.490	0.569	0.530
3	0.499	0.573	0.536
6	0.516	0.572	0.544
10	0.518	0.577	0.548
15	0.547	0.601	0.574

Table F.2 Formal potential for the first reduction reaction extracted from Fig. F.1.

Water content (wt%)	Anodic <sub>onset</sub> (V)	Cathodic <sub>onset</sub> (V)	E <sup>o'</sup> = E <sub>onset</sub> (V vs. Ag wire RE)
1	0.607	0.470	0.539
3	0.605	0.485	0.545
6	0.618	0.48	0.549
10	0.614	0.475	0.545
15	0.620	0.493	0.557

**Appendix G: Measurement of formal potential for the second reduction reaction in the DES system.**

As discussed in section 6.2.1 the second reduction potential was measured in the electrolyte containing increasing amounts of water. In order to do so, CuCl salt was dissolved in water-containing ethaline until no particles were visible (cf. Table G.1). This salt was chosen in order to obtain species involved in the second reduction reaction:  $\text{CuCl}_2^- + e^- \leftrightarrow \text{Cu} + 2\text{Cl}^-$ . The experiments were performed in the divided electrochemical cell using a Cu WE ( $A = 1.18 \text{ cm}^2$ ), the lab-made RE (Ag wire in ethaline), and a Pt wire as the CE. The experiments were performed at 20 °C. The equilibrium potential ( $E_{\text{eq}}$ ) was measured for 30 minutes for each point which results are shown in Table G.1.

The Nernst relationship was used to calculate the formal potential ( $E^{0'}$ ) as shown in equation G.1.

$$E_{\text{eq}} = E^{0'} - \frac{2.3RT}{nF} \log \frac{[\text{Cl}^-]^2}{[\text{CuCl}_2^-]} \quad (\text{G.1})$$

Table G.1  $E_{\text{eq}}$  for the second reduction reaction measured at different concentration of Cu (I) species in water-containing ethaline using a Cu WE ( $A = 1.18 \text{ cm}^2$ ) at 20 °C.

[CuCl] $\times 10^{-3}$ (M)	$\log \frac{[\text{Cl}^-]^2}{[\text{CuCl}_2^-]}$	$E_{\text{eq}}$ (V vs. RE)				Intercept
		1 wt%	6 wt%	10 wt%	15 wt%	
100	2.306	-0.144	-0.113	-0.104	-0.147	+0.0010
30	2.829	-0.169	-0.141	-0.143	-0.181	+0.0043
10	3.306	-0.193	-0.174	-0.159	-0.206	-0.0347
1	4.306	-0.239	-0.216	-0.204	-0.259	-0.0192
<b>Average <math>E^{0'}</math> (V vs. Ag wire RE)</b>						-0.01215



Fig. G.1 shows the plot of  $E_{\text{eq}}$  against  $\log \frac{[\text{Cl}^-]^2}{[\text{CuCl}_2^-]}$  which extrapolation yields  $E^{0'}$ . Since the difference in the  $E^{0'}$  between the electrolyte containing 1 and 15 wt% of water was 0.018 V, which may be within the drift of the quasi-reference electrode,  $E^{0'}$  was averaged, e.g.  $-0.012 \pm 0.018$  V vs. Ag wire RE as Table G.1 shows.

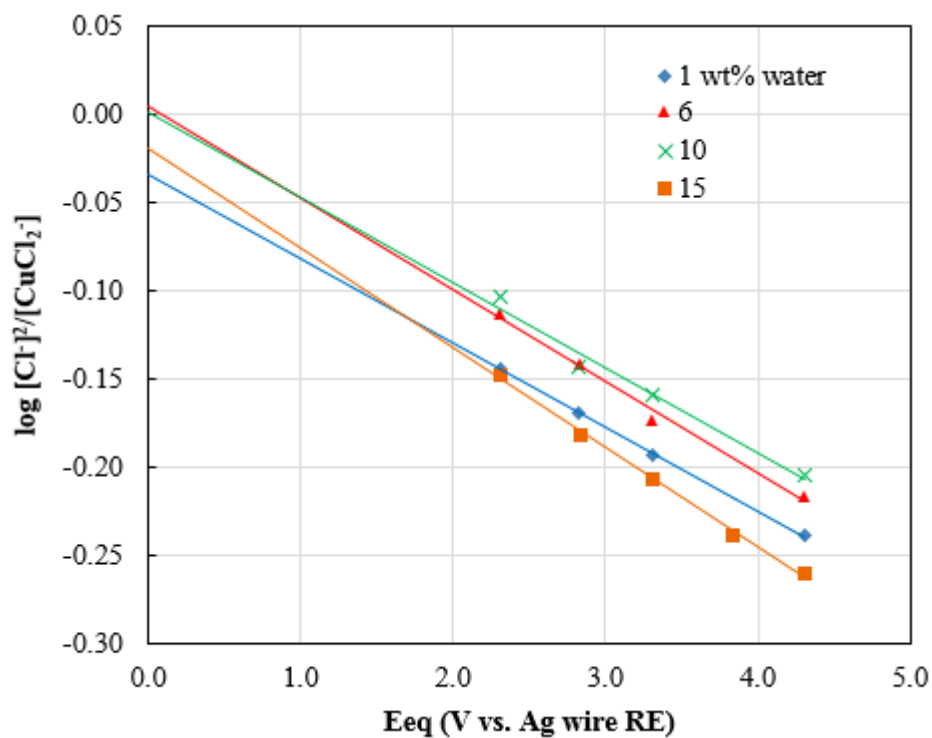


Figure G.1. Plot of  $\log [\text{Cl}^-]^2/[\text{CuCl}_2^-]$  vs.  $E_{\text{eq}}$  of Cu (I) species using a Cu WE ( $A=1.18 \text{ cm}^2$ ) for electrolytes containing 1, 6, 10 and 15 wt% of water. The formal potential for the second reduction reaction was obtained by averaging  $E^{0'}$  of each system.

**Appendix H:** Calculation of current efficiency using Wagner number by integration of the solids of revolution for each water-containing electrolyte.

In order to calculate the current used to fabricate the deposit, the current distribution curve was solved as a volume of revolution and thereafter the current efficiency was computed. Fig. H.1 shows the current distribution curve corresponding to Wagner number of 0.20 which was rotated in the y axis forming a solid of revolution. This volume corresponds to the region bounded between a polynomial relationship (solid curve) and the abscissa (x-axis). The limits of integration ranged from 0 to 0.6 corresponding to the radius of the steel disk used in the electrodeposition process. First,  $I_1$  is calculated by integrating equation H.1 using the cylindrical shell method.

$$I_1 = V = 2\pi \int_0^{0.6} f(x)x \, dx \quad (\text{H.1})$$

For the electrolyte containing 1 wt% of  $\text{H}_2\text{O}$ , equation H.1 was solved as follows:

$$I_1 = 2\pi \left[ \int_0^{0.6} 2506.8x^7 \, dx - \int_0^{0.6} 3900.6x^6 \, dx + \int_0^{0.6} 2307.1x^5 \, dx - \int_0^{0.6} 629.3x^4 \, dx + \int_0^{0.6} 81.8x^3 \, dx - \int_0^{0.6} 3.6x^2 \, dx + \int_0^{0.6} 3.6x \, dx \right]$$

$$I_1 = 2\pi [313.4x^8 - 557.2x^7 + 384.5x^6 - 125.9x^5 + 20.4x^4 - 1.2x^3 + 1.8x^2] \Big|_0^{0.6}$$

$$I_1 = 0.0053 \text{ A}$$

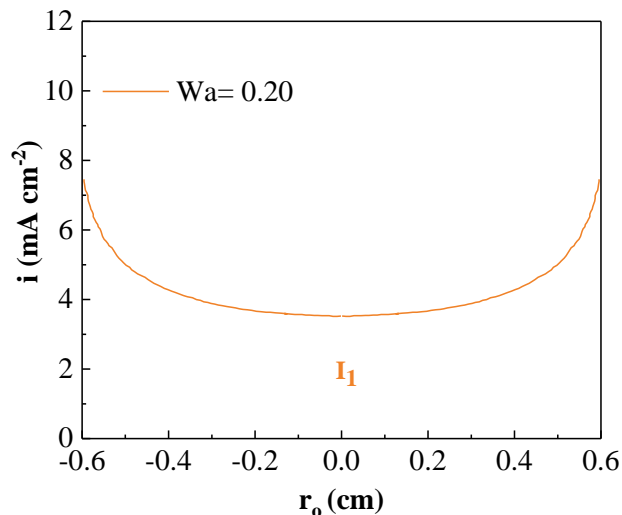


Figure H.1. Secondary current distribution for Tafel polarisation at a disk electrode of radius  $r_0$ . The distribution profile corresponds to  $Wa= 0.20$ .

Second, to obtain the net current used in the fabrication of the deposit, the current used in the first reduction step had to be removed. This was done by subtracting the volume of the cylinder from the total volume. The volume of the cylinder is shown as the dotted region in Fig. H.2 (a).  $I_2$  was obtained using equation H.2.

$$I_2 = V_{cyl} = \pi r^2 i_{lim1} \quad (H.2)$$

$$I_2 = \pi (0.6)^2 (2.82 \text{ mA cm}^{-2})$$

$$I_2 = 0.0032 \text{ A}$$

The difference between  $I_1$  and  $I_2$  corresponds to the net current utilised in the process (cf. Fig. H.2 b) to fabricate the deposit, which relation is shown in equation H.3.

$$I = I_1 - I_2 \quad (H.3)$$

$$I = 0.0021 \text{ A}$$

The mass was calculated using Faraday's law of electrolysis as equation H.4 shows:

$$m = \frac{ItM}{nF} = \frac{0.0021 \cdot 7200 \cdot 63.54}{2 \cdot 96485} = 0.00498 \text{ g} \quad (H.4)$$

The current efficiency was computed as equation H.5 shows:

$$\Phi = \frac{\text{calculated mass}}{\text{experimental mass}} = \frac{0.00498 \text{ g}}{0.0110 \text{ g}} = 40.9\% \quad (H.5)$$

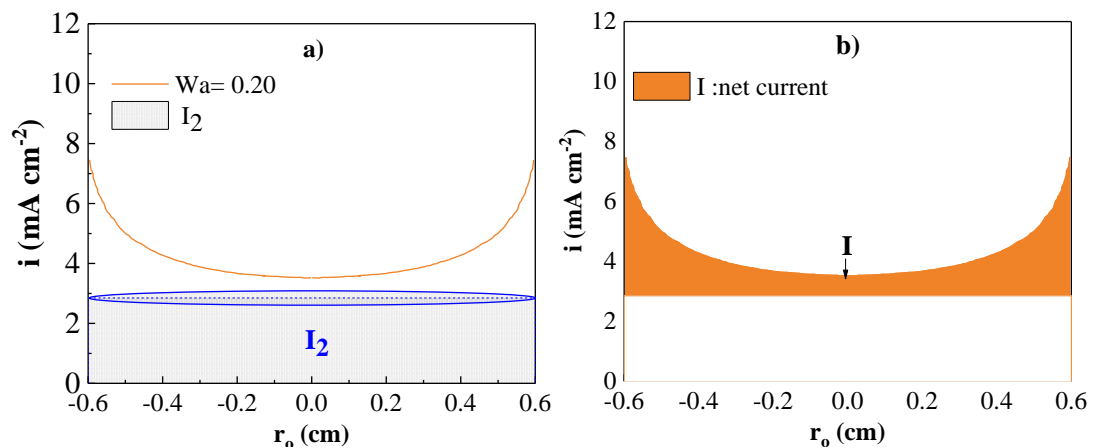


Figure H.2 Secondary current distribution for Tafel polarisation at a disk electrode of radius  $r_0$ . The distribution profile corresponds to  $Wa=0.20$ .

The remaining solids of revolution for each water-containing electrolyte were solved in a similar fashion. Table H.1 summarises  $I_1$ ,  $I_2$  and the net current ( $I$ ) used to fabricate the deposits as well as the calculated mass yielded by the analysis of the Wagner number.

Electrolyte containing 3 wt% of water:

$$I_1 = 2\pi[417.8x^8 - 743.0x^7 + 512.7x^6 - 167.8x^5 + 27.5x^4 - 1.6x^3 + 2.4x^2] \Big|_0^{0.6}$$

Electrolyte containing 6 wt% of water:

$$I_1 = 2\pi[700.6x^8 - 1255.3x^7 + 875.0x^6 - 291.0x^5 + 47.9x^4 - 3.1x^3 + 2.6x^2] \Big|_0^{0.6}$$

Electrolyte containing 10 wt% of water:

$$I_1 = 2\pi[1468.2x^8 - 2636.1x^7 + 1834.3x^6 - 610.1x^5 + 99.7x^4 - 6.5x^3 + 3.3x^2] \Big|_0^{0.6}$$

Electrolyte containing 15 wt% of water:

$$I_1 = 2\pi[2141.4x^8 - 3844.7x^7 + 2675.3x^6 - 889.8x^5 + 145.4x^4 - 9.5x^3 + 4.9x^2] \Big|_0^{0.6}$$

Table H.1. Calculated mass of plated electrodeposits from Wagner number analysis.

<b>H<sub>2</sub>O (wt%)</b>	<b>Wa</b>	<b>Wa used in the analysis</b>	<b>I<sub>1</sub> (A)</b>	<b>I<sub>2</sub> (A)</b>	<b>I (A)</b>	<b>Calculated mass (mg)</b>	<b>Experimental mass (mg)</b>
1	0.17	0.2	0.0051	0.0032	0.0019	4.50	11.0
3	0.18		0.0074	0.0048	0.0026	6.20	14.0
6	0.13		0.0081	0.0048	0.0033	7.82	15.8
10	0.10	0.05	0.0110	0.0071	0.0039	9.24	23.0
15	0.08		0.0160	0.0102	0.0058	13.8	33.0

**Appendix I: Dissolution valency of electro-dissolution of Cu from the DES system as a function of rotation speed and water content.**

Table I.1 Dissolution valency in water-containing electrolyte with constant current density ( $2.85 \text{ mA cm}^{-2}$ ) with increasing rotation speeds at  $25 \text{ }^{\circ}\text{C}$ . The area of the Cu electrode was  $1.18 \text{ cm}^2$ . The dissolution time was 3600 s and the expected mass loss based on the passed charge was 0.0080 g. The deviation of the scale was  $\pm 0.0001 \text{ g}$ .

Water content (wt%)	Rotation speed (rpm)									
	0*		300		700		1400		2100	
	$\Delta m_{\text{exp}}$ (g)	$n'$	$\Delta m_{\text{exp}}$ (g)	$n'$	$\Delta m_{\text{exp}}$ (g)	$n'$	$\Delta m_{\text{exp}}$ (g)	$n'$	$\Delta m_{\text{exp}}$ (g)	$n'$
1	0.0186	0.857	0.0128	0.622	0.0155	0.514	0.0195	0.409	0.0222	0.359
3	0.0206	0.773	0.015	0.517	0.020	0.398	0.026	0.306	0.029	0.278
6	0.0210	0.759	0.018	0.453	0.024	0.335	0.029	0.278	0.036	0.222
10	0.0214	0.744	0.0200	0.398	0.0267	0.298	0.0348	0.229	0.0415	0.192
15	0.0118	0.675	0.0245	0.325	0.0326	0.244	0.0457	0.174	0.0530	0.150

\*The dissolution time for 0 rpm and all water-containing electrolyte was 7200 s so the expected mass loss based on Faraday's law was 0.0159 g. In the case of the electrolyte containing 15 wt% with 0 rpm the dissolution time was 3600 s.

**Appendix J:** Dissolution valency of electro-dissolution of Cu from the DES system as a function of concentration of Cu (II) species, rotation speed and water content.

Table J.1 Dissolution valency in water-containing electrolyte with constant current density ( $i = 2.85 \text{ mA cm}^{-2}$ ) as a function of concentration of  $\text{CuCl}_2$  and rotation speed. The area of the Cu electrode was  $1.18 \text{ cm}^2$ . The dissolution time was 3600 s and the expected mass loss based on the passed charge was 0.0080 g. The deviation of the scale was  $\pm 0.0001 \text{ g}$ .

[CuCl <sub>2</sub> ] (M)	Rotation speed (rpm)	Water content			
		1 wt%		15 wt%	
		$\Delta m_{\text{exp}}$ (g)	$n'$	$\Delta m_{\text{exp}}$ (g)	$n'$
0.05	0	0.0086	0.926	0.0088	0.905
	700	0.0098	0.813	0.0140	0.569
	1400	0.0114	0.699	0.0168	0.474
0.10	0	0.0087	0.916	0.0096	0.830
	700	0.0123	0.648	0.0209	0.381
	1400	0.0149	0.535	0.0266	0.299
0.15	0	0.0090	0.885	0.0105	0.759
	700	0.0141	0.565	0.0260	0.306
	1400	0.0183	0.435	0.0345	0.231
0.20	0	0.0186	0.857	0.0118	0.675
	700	0.0155	0.514	0.0326	0.244
	1400	0.0228	0.349	0.0457	0.174

**Appendix K:**

**LIST OF PUBLICATIONS**

Green, T.D., Valverde, P., and Roy, S., *Anodic Reactions and the Corrosion of Copper in Deep Eutectic Solvents*. Journal of the Electrochemical Society, 2018. 165(9); p. D303-D320. (Corresponding to chapter 7).

Valverde, P, Green, T.D., and Roy, S., *Copper Electrodeposition from a Water-containing Choline Chloride-based Deep Eutectic Solvent*. ECS Transactions, 2017. 77(11); p.859-864. (Corresponding to a section of chapter 6).

Valverde, P, Green, T.D., and Roy, S., *Electrodeposition of Copper from Choline Chloride Ethylene Glycol Water-Containing Deep Eutectic Solvent*. In Manuscript. (Corresponding to chapter 6).

Valverde, P, Green, T.D., and Roy, S., *Effect of Water on the Physical-chemical and Electrochemical Properties of Copper Containing Deep Eutectic Solvent: Implications in Deposit Uniformity*. In Manuscript. (Corresponding to Chapter 5).

*Appendix L:*

**LIST OF ATTENDED CONFERENCES**

**2019 Scotland and North of England Electrochemistry Symposium (Butler Meeting).** (Oral presentation). April 2019. University of Edinburgh, United Kingdom.

**13<sup>th</sup> International Workshop on Electrodeposited Nanostructures “EDNANO XIII”.** (Oral presentation). August 2018. University of Bristol, United Kingdom.

**Strathwide 2018: 2<sup>nd</sup> Annual Strathclyde Research Conference.** (Oral presentation). June 2018. University of Strathclyde, United Kingdom.

**SCI Electrochemistry Postgraduate Conference 2018. “An ISE Regional Student Meeting”.** May 2018. (Oral presentation). University of Strathclyde, United Kingdom.

**22<sup>nd</sup> Topical Meeting of the International Society of Electrochemistry (ISE).** (Oral and poster presentation). April 2018. Waseda University, Japan.

**Royal Society of Chemistry Twitter Poster Conference.** (Poster presentation). March 2018. United Kingdom.

**Electrochem 2017.** (Oral presentation). September 2017. University of Birmingham, United Kingdom.

**Modern Electrochemical Technologies for Environment & Energy Conference.** (Poster presentation). June 2017. University of Strathclyde, United Kingdom.

**PGR ChemEng Departmental student’s seminars: PGR seminars 2017.** (Oral presentation). April 2017. University of Strathclyde, United Kingdom.

**European Academy of Surface Technology: EAST forum 2017.** (Oral presentation). April 2017. Germany.

**ChemEngUKDay 2017.** (Poster presentation). March 2017. University of Birmingham, United Kingdom.

**Research Celebration Day: Chemical and Process Engineering.** (Oral presentation). December 2016. University of Strathclyde, United Kingdom.

**Faculty of Engineering Research Presentation Day.** (Poster Presentation). June 2016. University of Strathclyde, United Kingdom.

**2016 Scotland and North England Electrochemistry Symposium: Butler Meeting.** (Poster presentation). April 2016. University of Glasgow, United Kingdom.



## References

1. Wilkes, J., *A short history of ionic liquids - from molten salts to neoteric solvents*. Green Chemistry, 2002. **4**: p. 74-80.
2. Hamann, C.H., Hamnett, A., and Vielstich, W. 1998, *Electrochemistry*. Germany: Wiley-Vch.
3. Sahami, S., and Osteryoung, R.A., *Voltammetric Determination of Water in an Aluminum Chloride-N-N-Butylpyridinium Chloride Ionic Liquid*. Analytical Chemistry, 1983. **55**(12): p. 1970-1973.
4. Abbott, A.P., Capper, G., Davies, D.L., Munro H.L., Rasheed, R.K., and Tambyrajah, V., *Preparation of Novel, Moisture-Stable, Lewis-Acidic Ionic Liquids Containing Quaternary Ammonium Salts with Functional Side Chains*. Chemical Communications, 2001: p. 2010-2011.
5. Smith, E., Abbott, A.P., and Ryder, K., *Deep Eutectic Solvents (DESs) and Their Applications*. Chemical Reviews, 2014. **114**: p. 11060-11082.
6. Garcia, A., and Aguilar, J., *Analysis of Water in Room Temperature Ionic Liquids by Linear Sweep, Differential Pulse and Square Wave Cathodic Stripping Voltammetries*. Electrochimica Acta, 2015. **182**: p. 238-246.
7. Qian, Q., Yu, P., Cheng, H., Wang, X., Yang, L., and Mao, L., *Electrochemical Quantification of Hygroscopicity of Ionic Liquids with Solution-Dissolved Potassium Ferricyanide as the Redox Probe*. Electroanalysis, 2011. **23**(12): p. 2870-2877.
8. Chen, Y., Cao, Y., Lu, X., Zhao, C., Yan, C., and Mu, T., *Water Sorption in Protic Ionic Liquids: Correlation Between Hygroscopicity and Polarity*. New Journal of Chemistry, 2013. **37**: p. 1959-1967.
9. Zhao, C., Bond, A.M., Lu, X., *Determination of Water in Room Temperature Ionic Liquids by Cathodic Stripping Voltammetry at a Gold Electrode*. Analytical Chemistry, 2012. **84**: p. 2784-2791.
10. Pianta, D., Frayret, J., Gleyzes, C., Cugnet, C., Dupin, J.C., and Hecho, I., *Determination of the Chromium(III) Reduction Mechanism During Chromium Electroplating*. Electrochimica Acta, 2018. **284**: p. 234-241.
11. Song, Y.B., and Chin, D.T., *Current Efficiency and Polarization Behavior of Trivalent Chromium Electrodeposition Process*. Electrochimica Acta, 2002. **48**: p. 349-356.
12. Goosey, M., *Cadmium Replacement Using Pulse Plating and Ionic Liquids (CRUPPAIL)*. Transactions of the Institute Metal Finishing, 2018. **96**(1): p. 1-6.
13. Welton, T., *Room Temperature Ionic Liquids. Solvents for Synthesis and Catalysis*. Chemical Reviews, 1999. **99**(8): p. 2071-2083.

14. Merrigan, T.L., Bates, E.D., Dorman, S.C. and Davis J.H., *New Fluorous Ionic Liquids Function as Surfactants in Conventional Room-Temperature Ionic Liquids*. Chemical Communications, 2000: p. 2051-2052.
15. Wasserscheid, P., and Welton, T. 2003, *Ionic Liquids in Synthesis*. Weinheim, Germany: Wiley-VCH.
16. Walden, P., *Molecular Weights and Electrical Conductivity of Several Fused Salts*. Bulletin de l'Académie Impériale des Sciences de Saint-Petersbourg, 1914. **8**: p. 405-422.
17. Hurley, F.H., and Wier T.P., *Electrodeposition of Metals from Fused Quaternary Ammonium Salts*. Journal of Electrochemical Society, 1951. **98**: p. 207.
18. Gale, R.J., Gilbert, B., and Osteryoung, R.A. , *Raman Spectra of Molten Aluminum Chloride: 1-Butylpyridinium Chloride Systems at Ambient Temperatures*. Inorganic Chemistry, 1978. **17**: p. 2728-2729.
19. Robinson, J., and Osteryoung, R.A., *An Electrochemical and Spectroscopic Study of Some Aromatic Hydrocarbons in the Room Temperature Molten Salt System Aluminum Chloride-n-Butylpyridinium Chloride*. Journal of the American Chemical Society, 1979. **101**(2): p. 323-327.
20. Wilkes, J.S., Levisky, J.A., Wilson, R.A., and Hussey, C.L., *Dialkylimidazolium Chloroaluminate Melts: A New Class of Room-Temperature Ionic Liquids for Electrochemistry, Spectroscopy and Synthesis*. Inorganic Chemistry, 1982. **21**(3): p. 1263-1264.
21. Fannin, A.A., Floreani, D.A., King, L.A., Landers, J.S., Piersma, B.J., Stech, D.J., Vaughn, R.L., Wilkes, J., and Williams J.L., *Properties of 1,3-Dialkylimidazolium Chloride-Aluminum Chloride Ionic Liquids. 2. Phase transitions, Densities, Electrical Conductivities, and Viscosities*. The Journal of Physical Chemistry, 1984. **88**: p. 2614-2621.
22. Wilkes, J.S., and Zaworotko, M.J., *Air and Water Stable 1-ethyl-3-Methylimidazolium Based Ionic Liquids*. Journal of Chemical Society, Chemical Communications, 1992(24): p. 2473-2670.
23. Endres, F., Abbott, A.P., and MacFarlane, D. 2008, *Electrodeposition from Ionic Liquids*. Germany: Wiley-Vch.
24. Hussey, C., Sun, I.W., Strubinger, S., and Barnard, P., *Some Observations about the Diffusion Coefficients of Anionic Transition Metal Halide Complexes in Room-Temperature Haloaluminate Ionic Liquids*. Journal of the Electrochemical Society, 1990. **137**(8): p. 2515-2516.
25. Dong, Q., Muzny, C., Chirico, R., Widegren, J., Diky V., Magee, J., Marsh, K., and Frenkel, M. 2005. IUPAC Ionic Liquids Database - (ILThermo) (Online). Available at: <https://www.nist.gov/publications/iupac-ionic-liquids-database-ilthermo> (Accessed: 14 Jan 2018).

26. Lei, Z., Chen, B., and Koo, Y.M., *Introduction: Ionic Liquids*. Chemical Reviews, 2017. **117**: p. 6633-6635.
27. Bier, M., and Dietrich, S. 2009, *Vapor Pressure of Ionic Liquids*. Molecular Physics, 2010. **108**(2): p. 211-214.
28. Yoshizawa, M., Xu, W., and Angell, A. , *Ionic Liquids by Proton Transfer: Vapor Pressure, Conductivity, and the Relevance of  $\Delta pK_a$  from Aqueous Solutions*. Journal of the American Chemical Society, 2003. **125**: p. 15411-15419.
29. MacFarlane, D.R., Pringle, J., Johansson, K.M., Forsyth, S.A., and Forsyth, M., *Lewis base Ionic Liquids*. Chemical Communications, 2006: p. 1905-1917.
30. Ohno, H., 2008. Physical Properties of Ionic Liquids for Electrochemical Applications. In: Endres, F., Abbott, A., and MacFarlane, D. eds. *Electrodeposition from Ionic Liquids*. Germany: Wiley-VCH, p. 47-82.
31. Holbrey, J.D., and Seddon, K.R., *The Phase Behaviour of 1-Alkyl-3-Methylimidazolium Tetrafluoroborates; Ionic Liquids and Ionic Liquid Crystals*. Journal of the Chemical Society, Dalton Transactions, 1999: p. 2133-2139.
32. Gordon, M.C., Holbrey, J.D., Kennedy, A.R., and Seddon, K.R. , *Ionic Liquid Crystals: Hexafluorophosphate Salts*. Journal of Materials Chemistry, 1998. **8**: p. 2627-2636.
33. Suga, T. In: Ohno, H. ed. *Ionic Liquid II-Marvelous Developments and Colorful Near Future*. CMC, Tokyo. p. 16-22.
34. Dzyuba, S.V., and Bartsch, R.A., *Influence of Structural Variations in 1-Alkyl(aralkyl)-3-Methylimidazolium Hexafluorophosphates and Bis(trifluoromethyl-sulfonyl)imides on Physical Properties of the Ionic Liquids*. Chemical Physics and Physical Chemistry, 2002(3).
35. Tsuzuki, S., *Factors Controlling the Diffusion of Ions in Ionic Liquids*. Chemical Physics and Physical Chemistry, 2012. **13**: p. 1664-1670.
36. Okoturo, O., and Vandernoot, T.J., *Temperature Dependence of Viscosity for Room Temperature Ionic Liquids*. Journal of Electroanalytical Chemistry, 2004. **568**: p. 167-181.
37. Bonhôte, P., Dias, A.P., Papageorgiou, N, Kalyanasundaram, K., and Gratzel, M., *Hydrophobic, Highly Conductive Ambient-Temperature Molten Salts*. Journal of Inorganic Chemistry, 1996. **35**: p. 1168-1175.
38. West, R.C., *CRC Handbook of Chemistry, and Physics, 70th Edition.*, Boca Raton, Florida: CRC Press.
39. Mcewen, A.B., Ngo, H.L., Lecompte, K., and Goldman, J.L., *Electrochemical Properties of Imidazolium Salt Electrolytes for*

- Electrochemical Capacitor Applications*. Journal of Electrochemical Society, 1999. **146**: p. 1687-1695.
40. Tokuda, H., Tsuzuki, S., Susan, A., Hayamizu, K., Watanabe, M., *How Ionic Are Room-Temperature Ionic Liquids? An Indicator of the Physicochemical Properties*. The Journal of Physical Chemistry B, 2006. **110**(39): p. 19593-19600.
  41. Buzzeo, M.C., Evans, R.G., and Compton, R.G., *Non-Haloaluminate Room-Temperature Ionic Liquids in Electrochemistry - A Review*. ChemPhysChem 2004. **5**: p. 1106-1120.
  42. MacFarlane, D.R., Meakin, P., Sun, J., Amini, N., and Forsyth, M., *Pyrrolidinium Imides: A New Family of Molten Salts and Conductive Plastic Crystal Phases*. Journal of Physical Chemistry B, 1999. **103**: p. 4164.
  43. Schroder, U., Wadhawan, J.D., Compton, R.G., Marken, F.S., Suarez, P.A., Consorti, C.S., de Souza, R.F., and Dupont, J., *Water-Induced Accelerated Ion Diffusion: Voltammetric Studies in 1-methyl-3-[2,6-(S)-dimethylocten-2-yl]imidazolium tetrafluoroborate, 1-butyl-3-methylimidazolium tetrafluoroborate and Hexafluorophosphate Ionic Liquids*. New Journal of Chemistry, 2000. **24**(12): p. 1009-1015.
  44. Abbott, A.P., Capper, G., Davies, D.L., Rasheed R.K., and Tambyrajah, V., *Novel Solvent Properties of Choline Chloride/Urea Mixtures*. Chemical Communications, 2003: p. 70-71.
  45. Plascencia, G., and Jaramillo, D. 2017, *Basic Thermochemistry in Materials Processing*. Gewerbestrasse, Switzerland: Springer Nature. 168-172.
  46. Abbott, A.P., Boothby, D., Capper, G., Davies, D.L., and Rasheed R., *Deep Eutectic Solvents Formed Between Choline Chloride and Carboxylic Acids: Versatile Alternatives to Ionic Liquids*. Journal of the American Chemical Society, 2004. **126**: p. 9142-9147.
  47. Abbott, A.P., Frisch, G., and Ryder, K.S., *Electroplating using Ionic Liquids*. Annual Review of Materials Research, 2013. **43**: p. 335-358.
  48. Shekaari, H., Zafarani, M.T., Shayanfar, Ali., and Mokhtarpour, M., *Effect of Choline Chloride/Ethylene Glycol or Glycerol as Deep Eutectic Solvents on the Solubility and Thermodynamic Properties of Acetaminophen*. Journal of Molecular Liquids, 2018. **249**: p. 1222-1235.
  49. Abbott, A.P., Barron, J.C., Ryder, K.S., and Wilson D., *Eutectic-Based Ionic Liquids with Metal-Containing Anions and Cations*. European Journal of Chemistry, 2007. **13**: p. 6495 – 6501.
  50. Abbott, A.P., Capper, G., Davies, D.L., and Rasheed, R., *Ionic Liquids Based upon Metal Halide/Substituted Quaternary Ammonium Salt Mixtures*. Inorganic Chemistry, 2004. **43**: p. 3447–3452.

51. Mantz, R.A., Trulove, P.C., Carlin, R.T., and Osteryoung, R.A., *ROESY NMR of Basic Ambient-Temperature Chloroaluminate Ionic Liquids*. Inorganic Chemistry, 1995. **34**: p. 3846.
52. Abbott, A.P., Capper, G., Davies, D.L., and Rasheed R.K., *Ionic Liquid Analogues Formed from Hydrated Metal Salts*. Chemistry - A European Journal, 2004. **10**: p. 3769-3774.
53. Matthey, J. *Chemical Processes - Process Description - Choline Chloride (Online)*. Available at: [www.jmprotech.com](http://www.jmprotech.com) (Accessed: 28 Jan 2018).
54. Lloyd, D., Vainikka, T., Murtomaki, L., Kontturi, K., and Ahlberg, *The Kinetics of the Cu<sup>2+</sup>/Cu<sup>+</sup> Redox Couple in Deep Eutectic Solvents*. Electrochimica Acta, 2011. **56**: p. 4922-4948.
55. Maugeri, Z., *'Deep Eutectic Solvents: Properties and Biocatalytic Applications' PhD thesis*. University of Aachen. Germany.
56. Troter, D.Z., Todorovic, Z.B., Dokic-Stojanovic, D.R., Dordevic, B.S., Todorovic, V.M., Konstantinovic, S.S., and Veljkovic, V.B., *The Physicochemical and Thermodynamic Properties of the Choline Chloride-based Deep Eutectic Solvents*. Journal of the Serbian Chemical Society, 2017. **82**(9): p. 1039-1052.
57. Garcia, G., Aparicio, S., Ullah, R., and Atilhan, M., *Deep Eutectic Solvents: Physicochemical Properties and Gas Separation Applications*. Energy and Fuels, 2015. **29**: p. 2616-2644.
58. Zhang, Q., DeOliveira, K., Royer, S., and Jerome, F., *Deep Eutectic Solvents: Synthesis, Properties and Applications*. Chemical Society Reviews, 2012. **41**: p. 7108-7146.
59. Taysun, M.B., Sert, E., and Atalay, F.S., *Effect of Hydrogen Bond Donor on the Physical Properties of Benzyltriethylammonium Chloride Based Deep Eutectic Solvents and their Usage in 2-Ethyl-Hexyl Acetate Synthesis as a Catalyst*. Journal of Chemical Engineering Data, 2017. **62**: p. 1173-1181.
60. Guo, W., Hou, Y., Ren, S., Tian, S., and Wu, W., *Formation of Deep Eutectic Solvents by Phenols and Choline Chloride and Their Physical Properties*. Journal of Chemical Engineering Data, 2013. **58**: p. 866-872.
61. Yusof, R., Abdulmalek, E., Sirat, K., and Rahman M.B., *Tetrabutylammonium Bromide (TBABr)-Based Deep Eutectic Solvents (DESs) and Their Physical Properties*. Molecules, 2014. **19**: p. 8011-8026.
62. Bahadori, L., Chakrabarti, M.H., Mjalli, M.F., AlNashef, I.M., Manane, N.S., and Hashim, M.A., *Physicochemical Properties of Ammonium-Based Deep Eutectic Solvents and Their Electrochemical Evaluation using Organometallic Reference Redox Systems*. Electrochimica Acta, 2013. **113**: p. 205-211.

63. Florindo, C., Oliveira, F.S., Rebelo, L.P., Fernandes, A.M., and Marrucho, I.M., *Insights Into the Synthesis and Properties of Deep Eutectic Solvents Based on Cholinium Chloride and Carboxylic Acids*. ACS Sustainable Chemical Engineering, 2014. **2**: p. 2416-2425.
64. Leron, R.B., and Li, M.H., *High-Pressure Density Measurements for Choline Chloride: Urea Deep Eutectic Solvent and its Aqueous Mixtures at  $T = (298.15 \text{ to } 323.15) \text{ K}$  and up to 50 MPa*. Journal of Chemical Thermodynamics, 2012. **54**: p. 293-301.
65. Jeffery, G.A., 1997, *An Introduction to Hydrogen Bonding*. Oxford: Oxford University Press.
66. Zhu, J., Yu, K., Zhu, Y., Zhu, R., Ye, F., Song, N., and Xu Y., *Physicochemical Properties of Deep Eutectic Solvents Formed by Choline Chloride and Phenolic Compounds at  $T=(293.15 \text{ to } 333.15) \text{ K}$ : The Influence of Electronic Effect of Substitution Group*. Journal of Molecular Liquids, 2017. **232**: p. 182-187.
67. Ghosh, S., Ryder, K., and Roy, S., *Electrochemical and Transport Properties of Ethaline Containing Copper and Tin Chloride*. Transactions of IMF, 2014. **92**: p. 41-46.
68. Shahbaz, K., Baroutian, S., Mjalli, F.S., Hashim, M.A., and Alnashef, I.M., *Densities of Ammonium and Phosphonium Based Deep Eutectic Solvents: Prediction Using Artificial Intelligence and Group Contribution Techniques*. Thermochemica Acta, 2012. **527**: p. 59-66.
69. Kareem, M., Mjalli, F.S., Hashim, M.A., Alnashef, I.M., *Phosphonium-Based Ionic Liquids Analogues and Their Physical Properties*. Journal of Chemical Engineering Data, 2010. **55**: p. 4632-4637.
70. Harris, R., 2008, *'Physical Properties of Alcohol Based Deep Eutectic Solvents' PhD Thesis*. University of Leicester. Leicester.
71. Shannon, R.D., *Revised Effective Ionic Radii and Systematic Studies of Interatomic Distances in Halides and Chalcogenides*. Acta Crystallographica Section A, 1976. **32**: p. 751-767.
72. Abbott, A.P., and Ryder, K., 2015. What Is An Ionic Liquid? In: Plechkova, N., and Seddon K.R. eds. Ionic Liquids Uncoiled; Critical expert overviews. Wiley. p. 413.
73. Bockris, J.O.M., and Reddy, A.K.N., 1970, *Modern Electrochemistry, Vol. 1*. New York: Plenum Press.
74. Hagiwara, R., Matsumoto, K., Nakamori, Y., Tsuda, T., Ito, Y., Matsumoto, H., and Momota, K., *Physicochemical Properties of 1,3-Dialkylimidazolium Fluorohydrogenate Room-Temperature Molten Salts*. Journal of the Electrochemical Society, 2003. **150**(12): p. D195-D199.

75. Bockris, J.O.M., and Reddy, A.K.N., 1970, *Modern Electrochemistry. Vol. 2*. New York: Plenum Publishing Corporation. p. 883-892, 910-922.
76. Fürth, R., *On the Theory of the Liquid State. II. The Hole Theory of the Viscous Flow of liquids*. Mathematical Proceedings of the Cambridge Philosophical Society, 1941. **37**: p. 281-290.
77. Bockris, J.O.M., and Hooper, G.W., Discussion of the Faraday Society, 1961. **32**: p. 218-236.
78. Abbott, A.P., Harris, R., and Ryder, K., *Application of Hole Theory to Define Ionic Liquids by their Transport Properties*. Journal of Physical Chemistry B, 2007. **111**: p. 4910-4913.
79. Abbott, A.P., *Application of Hole Theory to the Viscosity of Ionic and Molecular Liquids*. Chemical Physics and Physical Chemistry, 2004. **5**: p. 1242-1246.
80. Abbott, A.P., Capper, G., and Gray, S., *Design of Improved Deep Eutectic Solvents Using Hole Theory*. ChemPhysChem, 2006. **7**: p. 803-806.
81. Alomar, M.K., Hayyan, M., Alsaadi, M.A., Akib, S., Hayyan, A., and Hashim, M.A., *Glycerol-based Deep Eutectic Solvents: Physical Properties*. Journal of Molecular Liquids, 2016. **215**: p. 98-103.
82. Fuoss, R.M., *Properties of Electrolytic Solutions*. Chemical Reviews, 1935. **17**: p. 27-42.
83. Robinson, R.A., and Stokes, R.H., *Electrolyte Solutions*. 1959, Butterworths, London.
84. Pugsley, F.A., and Wetmore, F.E.W., *Molten Salts: Viscosity of Silver Nitrate*. Canadian Journal of Chemistry, 1954. **32**(9): p. 839-841.
85. Longinotti, M.P., and Corti, H.R., *Fractional Walden Rule for Electrolytes in Super-cooled Disaccharide Aqueous Solutions*. Journal of Physical Chemistry B, 2009. **113**: p. 5500-5507.
86. Koryta, J., Dvorak, J., Kavan, L. 1993, *Principles of Electrochemistry*. Chichester, England: John Wiley & Sons.
87. Abbott, A.P., *Model for the Conductivity of Ionic Liquids Based on an Infinite Dilution of Holes*. Chemical Physics and Physical Chemistry, 2005. **6**: p. 2502-2505.
88. Costa, R., Figueiredo, M., Pereira, C.M., and Silva, F., *Electrochemical Double Layer at the Interfaces of Hg/Choline Chloride Based Solvents*. Electrochimica Acta, 2010. **55**: p. 8916-8920.
89. Ghosh, S., and Roy, S., *Electrochemical Copper Deposition from an Ethaline-CuCl<sub>2</sub>·2H<sub>2</sub>O DES*. Surface and Coatings Technology, 2014. **238**: p. 165-173.

90. Bagh, F.S., Shahbaz, K., Mjalli, F.S., Hashima, M.A., and Alnashef, I.M., *Zinc (II) Chloride-Based Deep Eutectic Solvents for Application as Electrolytes: Preparation and Characterization*. Journal of Molecular Liquids, 2015. **204**: p. 76-83.
91. Temple, M., and Snowball, D. 2018. Health and Safety Executive. (Online). Available at: <http://www.hse.gov.uk/reach/> (Accessed: 3 Feb 2018).
92. Abbott, A.P., Ballantyne, A., Harris, R.C., Juma, J.A., Ryder, K.S., and Forrest, G., *A Comparative Study of Nickel Electrodeposition Using Deep Eutectic Solvents and Aqueous Solutions*. Electrochimica Acta, 2015. **176**: p. 718-726.
93. Hartley, J.M., Ip, C.M, Forrest, G.C., Singh, K., Gurman, S.J., Ryder, K.S., Abbott, A.P., and Frisch, G., *EXAFS Study into the Speciation of Metal Salts Dissolved in Ionic Liquids and Deep Eutectic Solvents*. 2014. **53**: p. 6280-6288.
94. Abbott, A.P., Ttaib, K.E., Ryder, K.S., and Smith, E.L., *Electrodeposition of Nickel Using Eutectic Based Ionic Liquids*. Transactions of the Institute Metal Finishing, 2008. **86**(4): p. 234-240.
95. Yang, H., Guo, X., Birbilis, N., Wu, G., and Ding, W., *Tailoring Nickel Coatings Via Electrodeposition from a Eutectic-based Ionic Liquid Doped with Nicotinic Acid*. Applied Surface Science, 2011. **257**: p. 9094-9102.
96. Bund, A., and Zschippang, E., *Nickel Electrodeposition from a Room Temperature Eutectic Melt*. ECS Transactions, 2007. **3**(35): p. 253-261.
97. Gu, C.D., and Tu, J.P, *Thermochromic Behavior of Chloro-Nickel(II) in Deep Eutectic Solvents and their Application in Thermochromic Composite Films*. RSC Advances, 2011. **1**: p. 1220-1227.
98. Biddulph, C., *Zinc Electroplating*, P. Inc., Editor. 2016. p. 141-149.
99. Krishnan, R.M., Nataralan, S.R., Muralidharan, V.S., and Singh, G., *Characteristics of a Non-Cyanide Alkaline Zinc Plating Bath*. Plating and Surface Finishing, 1992: p. 67-70.
100. Bapu, G.N., Devaraj, G., and Ayyapparaj, J., *Studies on Non-Cyanide Alkaline Zinc Electrolytes*. Journal of Solid State Electrochemical, 1998. **3**: p. 48-51.
101. Abbott, A.P., Capper, G., McKenzie, K.J., and Ryder, K.S., *Electrodeposition of Zinc-Tin Alloys from Deep Eutectic Solvents based on Choline Chloride*. Journal of Electroanalytical Chemistry 2007. **599**: p. 288-294.
102. Pollet, B., Hihn, J.Y., and Mason, T., *Sono-electrodeposition (20 and 850 kHz) of Copper in Aqueous and Deep Eutectic Solvents*. Electrochimica Acta, 2008. **53**: p. 4248-4256.



103. Laher, T.M., and Hussey, C.L., *Copper (I) and Copper (II) Chloro Complexes in the Basic Aluminum Chloride-1-Methyl-3-ethylimidazolium Chloride Ionic Liquid*. Inorganic Chemistry, 1983. **22**: p. 3247-3251.
104. Chen, P.Y., and Sun, I.W., *Electrochemical Study of Copper in a Basic 1-ethyl-3-methylimidazolium Tetrafluoroborate Room Temperature Molten Salt*. Electrochimica Acta, 1999. **45**: p. 441-450.
105. De Vreese, P., Brooks, N.R., Vanhecke, K., Meervelt, L.V., Mattheijs, E., Binnemans, K., and Vandeur, R., *Speciation of Copper(II) Complexes in an Ionic Liquid Based on Choline Chloride and in Choline Chloride/Water Mixtures*. Inorganic Chemistry, 2012. **51**: p. 4972-4981.
106. Abbott, A.P., Ttaib, K.E., Frisch, G., Mckenzie, K.J., and Ryder, K.S., *Electrodeposition of Copper Composites from Deep Eutectic Solvents Based on Choline Chloride*. Physical Chemistry Chemical Physics, 2009. **11**: p. 4269-4277.
107. Li, G., Camaioni, D.M., Amonette, J.E., Zhang, Z.C., Johnson, T.J., and Fulton, J.L., *[CuCl<sub>n</sub>]<sup>2-n</sup> Ion-Pair Species in 1-Ethyl-3-methylimidazolium Chloride Ionic Liquid-Water Mixtures: Ultraviolet-Visible, X-ray Absorption Fine Structure, and Density Functional Theory Characterization*. Journal of Physical Chemistry B, 2010. **114**: p. 12614-12622.
108. Tierney, B.J., Pitner, W.R., Mitchell, J.A., and Hussey, C., *Electrodeposition of Copper and Copper-Aluminum Alloys from a Room-Temperature Chloroaluminate Molten Salt*. Journal of the Electrochemical Society, 1998. **145**(9): p. 3110-3116.
109. Sebastian., P., Valles, E., and Gomez, E., *Copper Electrodeposition in a Deep Eutectic Solvent. First Stages Analysis Considering Cu (I) Stabilisation in Chloride Media*. Electrochimica Acta, 2014. **123**: p. 285-295.
110. De Leon, C.P., and Walsh, F.C., *Research and Development Techniques 1: Potentiodynamic Studies of Copper Metal Deposition*. Transactions of the Institute Metal Finishing, 2003. **81**(5): p. 95-100.
111. Popescu, A.M., Constantin, V., Cojocaru, A., and Olteanu, M., *Electrochemical Behaviour of Copper (II) Chloride in Choline Chloride-Urea Deep Eutectic Solvent*. Revista de Chimie Bucharest, 2011. **62**(2): p. 206-211.
112. Tsuda, T., Boyd, L., Kuwabata, S., and Hussey, C., *Electrochemistry of Copper (I) Oxide in the 66.7-33.3 mol % Urea-Choline Chloride Room-Temperature Eutectic Melt*. Journal of the Electrochemical Society, 2010. **157**(8): p. 96-103.
113. Gu, C.D., You, Y.H., Wang, X.L., and Tu, J.P., *Electrodeposition, Structural, and Corrosion Properties of Cu Films from a Stable Deep Eutectics System with Additive of Ethylene Diamine*. Surface and Coatings Technology, 2012. **209**: p. 117-123.

114. Dela Pena, E., '*Electrodeposition of Copper using Additive-containing Low Metal Ion Concentration Electrolytes for EnFACE Applications*' PhD Thesis. University of Strathclyde. Glasgow.
115. Haerens, K., Matthijs, E., Binnemans, K., and Bruggen V.B., *Electrochemical Decomposition of Choline Chloride Based Ionic Liquid Analogues*. Green Chemistry, 2009. **11**: p. 1357-1365.
116. Mares, M., Ciocirlan, O., Cojocaru, A., and Anicai, L., *Physico-chemical and Electrochemical Studies in Choline Chloride Based Ionic Liquid Analogues Containing Trivalent Chromium Chloride*. Revista de Chimie Bucharest, 2013. **64**: p. 815-824.
117. Kikyt, A.A., Shaiderov, D.A., Vasileva, E.A., Protsenko, V.S., and Danilov, F.I., *Choline Chloride Based Ionic Liquids Containing Nickel Chloride: Physicochemical Properties and Kinetics of Ni(II) Electroreduction*. Electrochimica Acta, 2017. **245**: p. 133-145.
118. Xing, S., Zanella, C., and Deflorian, F., *Effect of Pulse Current on the Electrodeposition of Copper from Choline Chloride-Ethylene Glycol*. Journal of Solid State Electrochemistry, 2014. **18**: p. 1657-1663.
119. Barron, C., '*The Electrochemistry of Zn in Deep Eutectic Solvents*' PhD Thesis. University of Leicester. Leicester.
120. Pletcher, D., 2009, *A First Course in Electrode Processes*. 2nd ed., United Kingdom: RSC Publishing.
121. Popov, K.I., Djokic, S.S., and Grgur, B.N. 2002, *Fundamental Aspects of Electrometallurgy*. New York: Kluwer Academic Publishers. p. 10-15.
122. Pletcher, D., Greff, R., Peat, R., Peter, L.M., and Robinson, J. 2011, *Instrumental Methods In Electrochemistry*. Southampton Electrochemistry Group. United Kingdom: Woodhead Publishing Limited.
123. Hine, F., 1985, *Electrode Processes and Electrochemical Engineering*. New York: Plenum Press. p. 20-25.
124. Paunovic, M., and Schlesinger, M. 2006, *Fundamentals of Electrochemical Deposition*. 2nd ed., United States of America: John and Wiley & Sons, Inc. p. 55-59.
125. Bard, A.J., and Faulkner, L.R., 2001, *Electrochemical Methods. Fundamentals and Applications*. New York: John Wiley & Sons, Inc. p. 22, 340-343.
126. Crow, D.R., 1974, *Principles and Applications of Electrochemistry*. London: Springer. p. 187-192.
127. Yeager, E., Bockris, J.O.M., Conway, B.E., and Sarangapani, S. 1983, *Comprehensive Treatise of Electrochemistry*. Vol. 6. New York: Plenum Press. 67-73.

128. Nernst, W., *Theory of Reaction Velocity in Heterogenous Systems*. Zeitschrift für Physikalische Chemie, 1904. **47**: p. 52-55.
129. Pletcher, D., and Walsh, F.C, 1993, *Industrial Electrochemistry*. Springer Science+Business Media, LLC. p. 2-10.
130. Brett, C., and Oliveira, A.M., 1993, *Electrochemistry: Principles, Methods, and Applications*. New York: Oxford University Press Inc. p. 93-98.
131. Oldham, K.B., Myland, J.C., and Bond, A.M. 2012, *Electrochemical Science and Technology*. Singapore: John Wiley & Sons, Ltd.
132. Karman, T.H., *Laminare and Tubulente Reibung*. Journal of Applied Mathematics and Mechanics, 1921. **1**(4): p. 233-252.
133. Cochran, B.A., *The Flow due to a Rotating Disk*. Mathematical Proceedings of the Cambridge Philosophical Society, 1934. **30**: p. 365-375.
134. Schmickler, W., and Santos, E., 2010, *Interfacial Electrochemistry*. 2nd ed., New York: Springer. p. 259-262.
135. Newman, J., *Current Distribution on a Rotating Disk Below the Limiting Current*. Journal of the Electrochemical Society, 1966. **113**(12): p. 1235-1241.
136. Smyrl, W., H., and Newman, J., *Limiting Current on a Rotating Disk with Radial Diffusion*. Journal of the Electrochemical Society, 1971. **118**(7): p. 1079-1081.
137. Newman, J., and Thomas, K.E., 2004, *Electrochemical Systems. Vol. 3*. John Wiley and Sons, Inc. p. 378-392, 419-424, 424-428.
138. Newman, J., *Resistance for Flow of Current to a Disk*. Journal of the Electrochemical Society, 1966. **113**: p. 501-502.
139. Pierini, P., Appel, P., and Newman, J., *Current Distribution on a Disk Electrode for Redox Reactions*. Journal of the Electrochemical Society, 1976. **123**(3): p. 366-369.
140. Marathe, V., and Newman, J., *Current Distribution on a Rotating Disk Electrode*. Journal of the Electrochemical Society, 1969. **116**(12): p. 1704-1707.
141. West, A.C., 2012, *Electrochemisstry and Electrochemical Engineering*. Columbia University, New York. p. 170-178.
142. *'Introduction to Karl Fischer Titration: KF Guide 1, The Techniques' 2012*. Global MarCom Switzerland: Switzerland.
143. *'Karl Fischer The Method at a Glance' 2012*, in *KF Guide 4 - An Overview*. Global MarCom Switzerland: Switzerland.

144. Meyer, A.S., and Boyd, C.M., *Determination of Water by Titration with Coulometrically Generated Karl Fischer Reagent*. Analytical Chemistry, 1959. **31**(2): p. 215-219.
145. Walter, C., and Rohner, R. 1998, '*Fundamentals of the Volumetric Karl Fischer Titration with 10 Selected Applications*'. Switzerland: Mettler-Toledo GmbH.
146. Bruttel, P., and Schlink, R., 2003, '*Water Determination by Karl Fischer Titration*'. Switzerland: Metrohm Ltd.
147. Stock, J.T., *Bipotentiometric Titration Microchemical and General Applications*. Microchemical Journal, 1971. **16**: p. 557-570.
148. Reich, G., *Near-Infrared Spectroscopy and Imaging: Basic Principles and Pharmaceutical Applications*. Advanced Drug Delivery Reviews, 2005. **57**: p. 1109-1143.
149. Burns, D.A., and Ciurczak, E.M. 2001, *Handbook of Near-Infrared Analysis, Second Edition, Revised and Expanded*. United States of America: Marcel Dekker.
150. Raghavachari, R., *Near-Infrared Applications in Biotechnology*. Madison, Wisconsin: Promega Corporation.
151. Davies, A.M.C., 2017. An Introduction to Near Infrared (NIR) Spectroscopy (Online). Available at: <http://www.impublications.com/content/introduction-near-infrared-nir-spectroscopy> (Accessed: 7 Jun 2018).
152. Greeves, N., 2008. Molecular Vibration - Infrared Spectroscopy (Online). Available at: <http://www.chemtube3d.com/vibrationsH2O.htm> (Accessed: 7 Jun 2018).
153. Guided Wave Process Analytical Systems. 2016. A Word or Two About Online NIR Water Measurements in Liquid Samples (Online). Available at: <http://guided-wave.com/application-notes/> (Accessed 5 Dec 2017).
154. Harris, D., *Quantitative Chemical Analysis*. W.H. Freeman and Company: New York.
155. Abbott, A.P., Albarzingjy, A.Z., Abbott, P.D., Frisch, G., Harris, R.C., Hartley, J., and Ryder, K.S., *Speciation, Physical and Electrolytic Properties of Eutectic Mixtures Based on CrCl<sub>3</sub>·6H<sub>2</sub>O and Urea*. Physical Chemistry Chemical Physics, 2014. **16**: p. 9047-9055.
156. Zhang, N., Zeng, D., Hefter, G., and Chen, Q., *Chemical Speciation in Concentrated Aqueous Solutions of CuCl<sub>2</sub> using thin-film UV-Visible Spectroscopy Combined with DFT calculations*. Journal of Molecular Liquids, 2014. **198**: p. 200-203.

157. Oelbner, W., Berthold, F., and Guth, U., *The iR Drop Well-known but often Underestimated in Electrochemical Polarisation Measurements and Corrosion Testing*. *Materials and Corrosion*, 2006. **57**(6): p. 455-465.
158. Roy, S., and Buckle, R., *The Recovery of Copper and Tin from Waste Tin Stripping Solution. Part II: Kinetic analysis*. *ECS Transactions*, 2009. **16**(36): p. 73-81.
159. Roy, S., and Buckle, R., *The Recovery of Copper and Tin from Waste Tin Stripping solution. Part II: Kinetic analysis of synthetic and real process waste*. *Separation and Purification Technology*, 2009. **68**: p. 185-192.
160. Fahlman, B.D., *Materials Chemistry*. United States of America: Springer.
161. Callister, W.D., and Rethwisch, D.G., 2012, *Fundamentals of Materials Science and Engineering. An Integrated Approach*. United States of America: John Wiley and Sons, Inc. p. 150-152.
162. Marturi, N., 2013, 'Vision and Visual Serving for Nanomanipulation and Nanocharacterization in Scanning Electron Microscope' *PhD Thesis*. University of Franche-Comte. France.
163. *Oxford Instruments, 2016. The Business of Science. EBSD Explained* (Online). Available at: <http://www.ebsd.com/ebsd-explained/basics-of-automated-indexing> (Accessed: 5 Jun 2018).
164. *ASTM International. 2013. Standard Test Methods for Determining Average Grain Size*. United States. p. 1-26.
165. Abbott, A.P., Frisch, G., Hartley, J., Karim, W.O., and Ryder, K.S., *Anodic Dissolution of Metals in Ionic Liquids*. *Progress in Natural Science Materials International*, 2015. **25**: p. 595-602.
166. Tran, C., Lacerda, S.H., and Oliveira, D., *Absorption of Water by Room Temperature Ionic Liquids: Effect of Anions on Concentration and State of Water*. *Applied Spectroscopy*, 2003. **57**(2): p. 152-157.
167. Du, C., Zhao, B., Chen, X.B., Birbilis, N., and Yang, H., *Effect of Water Presence on Choline Chloride-2 Urea Ionic Liquid and Coating Platings from the Hydrated Ionic Liquid*. *Scientific Reports*, 2016. **6**: p. 1-13.
168. Elleb, M., Meullemeestre, J., Weill, M.J., and Vierling, F. , *Spectrophotometric Study of Copper (II) Chloride Complexes in Propylene Carbonate and in Dimethyl Sulfoxide*. *Inorganic Chemistry*, 1982. **21**: p. 1477-1483.
169. Sasaki, T., Tada, M., Zhong, C., Kume, T., and Iwasawa, Y., *Immobilized Metal Ion-Containing Ionic Liquids: Preparation, Structure and Catalytic Performances in Kharasch Addition Reaction and Suzuki Cross-Coupling Reactions*. *Journal of Molecular Catalysis A: Chemical*, 2008. **279**: p. 200-209.

170. Schaltin, S., Nockemann, P., Thijs, B., Binnemans, K., and Fransaer, J., *Influence of the Anion on the Electrodeposition of Cobalt from Imidazolium Ionic Liquids*. *Electrochemical and Solid State Letters*, 2007. **10**(10): p. D104-D107.
171. Yadav, A., Kar, J., Verma, M., Naqvi, S., and Pandey, S., *Densities of Aqueous Mixtures of (Choline Chloride+Ethylene Glycol) and (Choline Chloride+Malonic Acid) Deep Eutectic Solvents in Temperature Range 283.15-363.15 K*. *Thermochimica Acta*, 2015. **600**: p. 95-101.
172. Mjalli, F., and Ahmad, O., *Density of Aqueous Choline Chloride-based Ionic Liquids Analogues*. *Thermochimica Acta*, 2017. **647**: p. 8-14.
173. Protsenko, V.S., Bobrova, L.S., and Danilov F.I., *Physicochemical Properties of Ionic Liquid Mixtures Containing Choline Chloride, Chromium (III) Chloride and Water: Effects of Temperature and Water Content*. *Ionics*, 2017. **23**: p. 637-643.
174. Shekaari, H., Taghi, M.T., and Mohammadi, B., *Thermophysical Characterization of Aqueous Deep Eutectic Solvent (Choline Chloride/Urea) Solutions in Full Ranges of Concentration at T = (293.15-323.15)*. *Journal of Molecular Liquids*, 2017. **243**: p. 451-461.
175. Yadav, A., and Pandey, S., *Densities and Viscosities of (Choline Chloride + Urea) Deep Eutectic Solvent and its Aqueous Mixtures in the Temperature Range 293.15 K to 363.15 K*. *Journal of Chemical & Engineering Data*, 2014. **59**: p. 2221-2229.
176. Shah, D., and Mjalli, F., *Effect of Water on the Thermo-Physical Properties of Reline: An Experimental and Molecular Simulation Based Approach*. *Physical Chemistry Chemical Physics*, 2014. **16**: p. 23900-23907.
177. Protsenko, V.S., Kityk, A.A., Shaiderov, D.A., and Danilov F.I., *Effect of Water Content on Physicochemical Properties and Electrochemical Behaviour of Ionic Liquids Containing Choline Chloride, Ethylene Glycol and Hydrated Nickel Chloride*. *Journal of Molecular Liquids*, 2015. **212**: p. 716-722.
178. Zhekenov, T., Toksanbayev, N., Kazakbayeva, Z., and Shab, D., *Formation of Type III Deep Eutectic Solvents and Effect of Water on their Intermolecular Interactions*. *Fluid Phase Equilibria*, 2017. **441**: p. 43-48.
179. Yadav, A., Trivedi, S., Rai, R., and Pandey, S., *Densities and Dynamic Viscosities of (Choline Chloride+Glycerol) Deep Eutectic Solvent and its Aqueous Mixtures in the Temperature Range (283.15-363.15) K*. *Fluid Phase Equilibria*, 2014. **367**: p. 135-142.
180. Gritzner, G., and Phillips, R.F., *Densities, Viscosities, and Vapor Pressures of Copper Chloride Solutions in Hydrochloric acid*. *Journal of Chemical and Engineering Data*, 1972. **17**(4): p. 425-428.

181. Hammond, O.S., Bowron, D.T., and Edler J.K., *The Effect of Water Upon Deep Eutectic Solvent Nanostructure: An Unusual Transition from Ionic Mixture to Aqueous Solution*. *Angew. Chem. Int. Ed.*, 2017. **56**: p. 9782-9785.
182. Vila, J., Gines, P., Rilo, E., Cabeza, O., and Varela, L.M., *Great Increase Of The Electrical Conductivity Of Ionic Liquids In Aqueous Solutions*. *Fluid Phase Equilibria*, 2006. **247**: p. 32-39.
183. Bobrova, L.S., Danilov, F.I., and Protsenko, V.S., *Effects of Temperature and Water Content on Physicochemical Properties of Ionic Liquids Containing  $CrCl_3 \cdot xH_2O$  and Choline Chloride*. *Journal of Molecular Liquids*, 2016. **223**: p. 48-53.
184. Wolf, A.V., *Aqueous Solutions and Body Fluids*. New York: Harper and Row.
185. Omahony, A.M., Silvester, D.S., Aldous, L., Hardacre, C., and Compton, R., *Effect of Water on the Electrochemical Window and Potential Limits of Room-Temperature Ionic Liquids*. *Journal of Chemical & Engineering Data*, 2008. **53**(12): p. 2884-2891.
186. Ru, J., Hua, Y., Wang, D., Xua, C., Li, J., Li, Y., Zhoua, Z., and Gong, K., *Mechanistic Insight of in Situ Electrochemical Reduction of Solid  $PbO$  to Lead in  $ChCl-EG$  Deep Eutectic Solvent*. *Electrochimica Acta*, 2015. **186**: p. 455-464.
187. Yue, D., Jia, Y., Yaoa, Y., Suna, J., and Jing, Y., *Structure and Electrochemical Behavior of Ionic Liquid Analogue Based on Choline Chloride and Urea*. *Electrochimica Acta*, 2012. **65**: p. 30-36.
188. Mandroyan, A., Mahmoud, M., Doche, M.L., and Hihn, J.Y., *Effects of Ultrasound and Temperature on Copper Electroreduction in Deep Eutectic Solvents (DES)*. *Ultrasonics Sonochemistry*, 2014. **21**: p. 2010-2019.
189. Lloyd, D., Vainikka, T., Schmachtel, S., Murtomaki, L, and Kontturi, K., *Simultaneous Characterisation of Electrode Kinetics and Electrolyte Properties in Ionic Liquids using a Rotating Disc Electrode*. *Electrochimica Acta*, 2012. **69**: p. 139-145.
190. Kiekens, P., Verbeeck, R.M.H., and Temmerman, E., *A Kinetic Study of the  $Cu(II)/Cu(I)$  System in  $Cl^-$  Media at the Glassy Carbon Electrode*. *Mikrochimica Acta*, 1981. **2**: p. 29-36.
191. Ribeiro, A.C., Estes, M.A., Lobo, V.M., Valente, A.J., Simoes, S.M., Sobral, A.J., and Burrows, H.D., *Diffusion Coefficients of Copper Chloride in Aqueous Solutions at 298.15 K and 310.15 K*. *Journal of Chemical Engineering Data*, 2005. **50**: p. 1986-1990.

192. Abbott, A.P., Frisch, G., Gurman, S.J., Hillman, A.R., Hartley, J., Holyoak, F., and Ryder, K.S., *Ionometallurgy: Designer Redox Properties for Metal Processing*. Chemical Communications, 2011. **47**: p. 10031-10033.
193. Hall, D., Larow, E., Schatz, R., Beck, J., and Lvov, S., *Electrochemical Kinetics of CuCl(aq)/HCl(aq) Electrolyzer for Hydrogen Production via a Cu-Cl Thermochemical Cycle*. Journal of the Electrochemical Society, 2015. **162**(1).
194. Figueiredo, M., Gomes, C., Costa, R., Martins, A., Pereira, C.M., and Silva, F., *Differential Capacity of a Deep Eutectic Solvent Based on Choline Chloride and Glycerol on Solid Electrodes*. Electrochimica Acta, 2009. **54**: p. 2630-2634.
195. Hammond, O.S., Li, H., Westermann, C., Almurshedi, A.Y., Endres, F., Abbott, A.P., Warr, G.G., Edler, K., and Atkin, R., *Nanostructure of the Deep Eutectic Solvent/Platinum Electrode Interface as a Function of Potential and Water Content*. Nanoscale Horizons, 2018.
196. Durbha, M., and Orazem, M.A., *Current Distribution on a Rotating Disk Electrode Below the Mass-Transfer-Limited Current*. Journal of the Electrochemical Society, 1998. **145**(6): p. 1940-1948.
197. Landau, U., 1982. In: Yeager, E., and Dortan, D. eds. *Electrochemistry in Industry*. New York: Plenum Press.
198. Barkey, D.P., Muller, R.H., and Tobias, C.W., *Roughness Development in Metal Electrodeposition*. Journal of the Electrochemical Society, 1989. **136**(8): p. 2199-2207.
199. Wasekar, N.P., Haridoss, P., Seshadri, S.K., and Sundararajan, G., *Influence of Mode of Electrodeposition, Current Density and Saccharin on the Microstructure and Hardness of Electrodeposited Nanocrystalline Nickel Coatings*. Surface and Coatings Technology. **291**: p. 130-140.
200. Rashidi, A.M., and Amadeh, A., *Effect of Electroplating Parameters on Microstructure of Nanocrystalline Nickel Coatings*. Journal of Materials Science Technology, 2009. **26**(1): p. 82-86.
201. Ho, C.E., Chen, C.C., Hsu, L.H., and Lu, M.K., *Electron Backscatter Diffraction Characterization of Electrolytic Cu Deposition in the Blind-Hole Structure: Current Density Effect*. Thin Solid Films, 2015. **584**: p. 78-84.
202. Chene, O., and Landolt, D., *The Influence of Mass Transport on the Deposit Morphology and the Current Efficiency in Pulse Plating of Copper*. Journal of Applied Electrochemistry, 1988. **19**: p. 188-194.
203. Zhao, F., Franz, S., Vincenzo, A., Cavallotti, P.L., Sansotera, M., and Navarrini, W., *Electrodeposition of Nanostructured Columnar Cobalt for Self-Lubricant Coatings*. Electrochimica Acta, 2011. **56**: p. 9644-9651.



204. Forrest, G.H., 2014, '*Electrochemistry and Galvanic Deposition of Group 10 & 11 Transition Metals Using Deep Eutectic Solvents*' PhD Thesis. Leicester University: Leicester.
205. Bernasconi, R., Zebarjadi, M., and Magagnin, L., *Copper Electrodeposition from a Chloride Free Deep Eutectic Solvent*. Journal of Electroanalytical Chemistry, 2015. **758**: p. 163-169.
206. Winand, R., *Electrodeposition of Metals and Alloys-New Results and Perspectives*. Electrochimica Acta, 1994. **39**(8/9): p. 1091-1105.
207. Winand, R., *Electrocrystallization-Theory and Applications*. Hydrometallurgy, 1992. **29**: p. 567-598.
208. Andrianne, P.A., Dubois, J.P., and Winand, R.F., *Electrocrystallization of Copper in Chloride Aqueous Solutions*. Metallurgical Transactions B, 1997. **8B**: p. 315-321.
209. Berube, L., and Esperance, G.L., *A Quantitative Method of Determining the Degree of Texture of Zinc Electrodeposits*. Journal of the Electrochemical Society, 1989. **136**(8): p. 2314-2315.
210. Ghosh, S., and Roy, S., *Codeposition of Cu-Sn from Ethaline Deep Eutectic Solvent*. Electrochimica Acta, 2015. **183**: p. 27-36.
211. Andrievski, R.A., *Twinned Boundaries in Nanomaterials*. Reviews on Advanced Material Science, 2016. **46**: p. 104-120.
212. Mahajan, S., Pande, C.S., Iman, M.A., Rath, B.B., *Formation of Annealing Twins in FCC Crystals*. Acta Metallurgica Inc., 1997. **46**(6): p. 2633-2638.
213. Lu, L., Shen, Y., Chen, X., Qian, L., and Lu, K., *Ultrahigh Strength and High Electrical Conductivity in Copper*. Science 2004. **304**: p. 422-426.
214. Chen, H.Y., Yang, K.H., Ouyang, F.Y. *Nanotwinned Cu Thin Film with Different Twin Boundary Orientations Deposited by Unbalanced Magnetron Sputtering*. in *ICEP-IAAC 2015 Proceedings*. 2015.
215. Wang, Y.S., Lee, W.H., Chang, S.C., Nian, J.N., and Wang, Y.L., *An Electroplating Method for Copper Plane Twin Boundary Manufacturing*. Thin Solid Films, 2013. **544**: p. 157-161.
216. Zhang, X., Misra, A., Wang, H., Shen, T.D., Nastasi, M., Mitchell, T.E., Hirth, J.P., Hoagland, R.G., and Embury, J.D., *Enhanced Hardening in Cu/330 Stainless Steel Multilayers by Nanoscale Twinning*. Acta Materialia, 2004. **52**: p. 995-1002.
217. Hughes, D.A., and Hansen, N., *High Angle Boundaries Formed by Grain Subdivision Mechanisms*. Acta Metallurgica Inc., 1997. **45**(9): p. 3871-3886.

218. Su, Y., Liu, J., Wang, R., Aisa, S., Cao, X., Li, S., Wang, B., and Zhou, Q., *Comproportionation Reaction of Cu(II)/Cu(0) in Ethaline-Water Mixed Solvents*. Journal of the Electrochemical Society, 2018. **165**(3).
219. Drazic, D.M., and Popic, J.P., *Anomalous Dissolution of Metals and Chemical Corrosion*. Journal of the Serbian Chemical Society, 2005. **70**(3): p. 489-511.
220. James, W.E., 1974. In: Fontana, M.G., and Staehle, R.W. eds. *Advances in Corrosion Science and Technology*. New York: Plenum Press, ed.
221. Doche, M.L., Mandroyan, A., Mahmoud, M.M., Moutarlier, V., and Hihn, J.Y., *An Ultrasonic-Assisted Process for Copper Recovery in a DES Solvent: Leaching and Re-Deposition*. Chemical Engineering and Processing 2017. **121**: p. 90-96.
222. Datta, M., *Anodic Dissolution of Metals at High Rates*. IBM Journal of Research and Development, 1993. **37**(2): p. 207.
223. Datta, M., and Landolt, D., *On the Role of Mass transport in High Rate Dissolution of Iron and Nickel in ECM Electrolytes - I. Chloride Solutions*. Electrochimica Acta, 1980. **25**: p. 1263.
224. Datta, M., and Landolt, D., *Stoichiometry of Anodic Nickel Dissolution in NaCl and NaClO<sub>3</sub> under Active and Transpassive Conditions*. Corrosion Science, 1973. **13**(3): p. 187-197.
225. Chen, K.W., and Chin, D.T., Journal of the Electrochemical Society, 1974. **121**: p. 191.
226. Green, T.A., Su, X., and Roy, S., *Pulse Plating of Copper from Deep Eutectic Solvents*. ECS Transactions, 2017. **77**(11): p. 1247-1253.
227. Fischer, J., Nagel, E., and Mann, M., *Investigations Concerning Chromium Plating from Electrolytes Containing Chromium-III Chloride and Ionic Liquid*. 2012, Report No. 120808. University of North Dakota.
228. Verpoort, P., and Gonzalez, E.D., *Joint Workshop on Ionic Liquids at Interfaces*. 2015: Belek, Turkey.
229. Bock, R., and Wulf, S.E., *Transactions of the Institute Metal Finishing*, 2009. **87**: p. 28.
230. Lloyd, D., Vainikka, T., Roinkainen, M., and Kontturi, K., *Characterisation and Application of the Fe (II)/Fe (III) Redox Reaction in an Ionic Liquid Analogue*. Electrochimica Acta, 2013. **109**: p. 843-851.
231. Miller, M.A., Wainright, J.S., and Savinell, R.F., *Iron Electrodeposition in a Deep Eutectic Solvent for Flow Batteries*. Journal of the Electrochemical Society, 2017. **164**(4): p. A796-A803.